UNIVERSITÀ
DEGLI STUDI
DI PADOVA

Head Office: Università degli Studi di Padova

Department of Geosciences

Ph.D. COURSE IN: EARTH SCIENCES
CURRICULUM:
SERIES XXXV

Geochemical modeling of soil-binder systems in stabilization/solidification applications

Thesis is written with the financial contribution of the China Scholarship Council.

Coordinator: Prof. Claudia Agnini
Supervisor: Prof. Gilberto Artioli
Co-Supervisor: Prof. Maria Chiara Dalconi and Dr. Simone Molinari

Ph.D. student: Yikai Liu

Contents

Abstract

Sustainable soil stewardship provides the basis for terrestrial ecosystems and geochemical cycles. However, the unprecedented urbanization in the last decades brought massive solid waste stockpiles worldwide, detrimental to soil health and the neighborhood flora and fauna. Herein, in-situ solidification/stabilization (S/S) has been proposed as a remediation strategy to prevent further pollution in the contaminated sites. But the challenges of substantial CO_2 emission and the sensitive durability attributed to the ordinary Portland cement (OPC), which is the most widely used binder in the S/S technique, place this strategy under scrutiny.

In this work, we examined the feasibility of mitigating or negating the use of OPC in the S/S process of pyrite ash and phosphogypsum, the primary hazardous solid wastes generated in the phosphate industry. One traditional binder (OPC) and five alternative low-carbon footprint binders (calcium aluminate cement, mayenite mixed with blast furnace slag, alkaline-activated blast furnace slag, commercial CEMENT III/B, and γ-Al_2O_3) were applied in the remediation process. After the physicochemical and mineralogical characterization of the stabilized products, we constructed the geochemical modeling to reveal the potential mechanisms of contaminant retention and ensure long-term environmental availability. Finally, we evaluated how integrating these innovative technologies could shed light on reducing greenhouse gas emissions and offer technical benefits in future field trials. The overall findings underscore the immobilization mechanisms of pollutants using different binder strategies and highlight the urgent need to bridge the zero-emission insights to sustainable S/S technologies. The constructed geochemical modeling, in tandem with the inclusion of more solid waste types and properties in the following models, will be pivotal in predicting the availability and efficiency of green and sustainable remediation strategies.

Sommario

La gestione sostenibile del suolo rappresenta la condizione primaria per garantire l'equilibrio degli ecosistemi terrestri e i cicli geochimici. La crescente urbanizzazione degli ultimi decenni ha portato alla produzione di enormi volumi di rifiuti solidi in tutto il mondo, particolarmente dannosi per la salute umana, della fauna e della flora circostante. Il processo di solidificazione/stabilizzazione in situ (S/S) è stata proposto come strategia di bonifica sostenibile al fine di prevenire la mobilizzazione degli inquinanti in siti contaminati. Di contro le problematiche legate all'utilizzo di cemento Portland (OPC), che rappresenta il legante idraulico più utilizzato nella tecnica S/S, quali elevate emissioni di CO_2 durante la sua produzione e la sua durabilità rappresentano un grande limite all'utilizzo di questa strategia di bonifica. In questo lavoro, è stata investigata la possibilità di superare queste problematiche riducendo al massimo l'utilizzo di OPC nel processo S/S nella bonifica di due rifiuti solidi particolarmente inquinati quali ceneri di pirite e fosfogesso ovvero i principali scarti di produzione dell'industria dei concimi fostatici. Nel processo di bonifica sono stati quindi investigati parallelamente il legante tradizionale (OPC) e cinque leganti alternativi a bassa impronta di CO_2 (cemento alluminoso, mayenite miscelata con loppa d'altoforno, loppa d'altoforno ad attivazione alcalina, un cemento di tipo III/B e γ-Al_2O_3). Il lavoro ha previsto una preliminare caratterizzazione fisico-chimica dei leganti idraulici e delle miscele legante idraulico/suolo inquinato ed una successivo modeling geochimico con il fine di identificare e quantificare i meccanismi di ritenzione dei contaminanti e garantire un riciclo del rifiuto solido efficace e sostenibile nel tempo. Infine, è stata eseguita una valutazione preliminare dell'integrazione di queste tecnologie innovative di bonifica accoppiata ad una alta efficienza di bonifica con contemporanea riduzione delle emissioni di gas serra e offrendo allo stesso tempo vantaggi tecnici nelle bonifiche di grandi volumi di rifiuti solidi. I risultati complessivi del lavoro hanno permesso l'identificazione dei principali meccanismi di immobilizzazione degli inquinanti e il loro grado di efficienza, ed hanno evidenziato come un approccio "CO_2 free" sia urgente per garantire la sostenibilità di tecnologie S/S. La modellazione geochimica costruita sulla base delle caratteristiche dei rifiuti solidi rappresenta uno step fondamentale per prevedere l'applicabilità ed efficienza delle diverse strategie di bonifica disponibili in termini di sostenibilità ambientale ed economica a lungo termine.

Chapter 1

General introduction

1. Aims of the study

Exposure to potentially toxic elements (PTEs) continues to be one of the biggest public health challenges worldwide, particularly in developing countries (Hou et al., 2020). Growing commitments to reach the 2030 agenda for 17 Sustainable Development Goals through careful in-situ or ex-situ management of PTEs is a critical step forward in delivering sustainable development in future grand climate changes (Sachs et al., 2019; Dooley et al., 2022). To date, the successful commercialization and industrialization of the in-situ solidification/stabilization (S/S) technologies in the management of PTEs have been assessed (Bonomo et al., 2009; Contessi et al., 2020; Wang et al., 2022c). However, the increasing focus attributed to the net-zero emissions and potential risks related to the conventional use of ordinary Portland cement (OPC) makes this methodology under denunciation (Wang et al., 2020a; Watari et al., 2022). Herein, developing alternative low-carbon and cost-effective binders is important for facilitating these traditional remediation technologies. Against these knowledge gaps, the primary objectives of this work include three aspects:

(1) comprehensive multi-approached investigation for the mineralogical and physicochemical information of the collected solid wastes (pyrite ash and phosphogypsum), aiming to reveal the potential PTEs bearing phases within the raw wastes and provide insights into the possible PTEs redistribution mechanisms with the interactions of weathering process;

(2) deploying lower-carbon emission and efficient alternative binders (cement III/B (CEM III/B), calcium aluminate cement (CAC), mayenite mixed with blast furnace slag (MAY), alkaline-activated blast furnace slag (ABS), and γ-Al_2O_3) to mitigate the use of OPC and reduce the mobility of PTEs in the stabilized pyrite ash and phosphogypsum. In addition, quantifying the carbon footprint and profitability of the proposed strategies with perspective to confirm their niche in the broad market and real engineering trails;

(3) developing applicable geochemical modeling to give a more comprehensive insight into revealing the potential PTEs retention mechanisms and predict the PTEs leaching behavior in the interaction between the stabilized products and environments.

2. Thesis outline

The main contents of this thesis are structured as five different sections, presented in **Chapters 2** to **6**, which have been published, submitted, or are ready for submission to a peer-reviewed scientific journal, and a general conclusion related to the overall findings in this thesis, presented in **Chapter 7**. The primary content of each chapter is briefly introduced below.

In **Chapter 2**, we proposed a methodology to construct a geochemical model that can directly provide a reliable prediction and mineralogical interpretation of contaminants leaching in multiple leaching scenarios by only considering the raw solid waste characterization without any additional processing. In this chapter, we characterized the contaminants-bearing phases in the collected pyrite ash wastes and determined the pH parallel leaching behavior of lead, zinc, and sulfates. With this bulk sample information, we used the PHREEQC to develop geochemical modeling, aiming to evaluate the mineralogical evidence that controls the release of the contaminants. The validation of the experimental observations illustrates that this approach is promising to provide a fundamental understanding of most essential retention mechanisms and, in most cases, adequately predict the leaching behavior. In addition, the results of this chapter set the basis for the forthcoming solidification/stabilization designs of pyrite ash.

In **Chapter 3**, with the perspective of validating the possibility of using a cement-free pathway to enhance PTEs retention, we used one traditional binder (OPC) and four alternative binders (CEM III/B, CAC, MAY, and ABS) to immobilize the pyrite ash. To date, although OPC is the most widely used and welcome commercially manufactured material in the S/S field trials, the use of OPC has been proven insufficient in cases with high lead concentrations. In addition, the production of OPC results in substantial carbon emissions, which puts this material under scrutiny. Herein, in this work, four different binders with lower-carbon footprints were applied in the pyrite ash remediation strategy design. After the S/S process, leaching tests and characterization experiments were applied to the stabilized products to investigate the PTEs retention capacity and the attributed immobilization mechanisms. Further, we quantified the CO_2 emissions and overall benefits of each binder scenario, highlighting the urgent need to bridge the zero-emission insights to sustainable in-situ S/S technologies.

In **Chapter 4**, we propose to characterize and simulate the retention and leaching behavior of fluorides and phosphates in OPC stabilized phosphogypsum. Multi-techniques, including the SEM/EDS, EPMA/WDS, XRD, XRF, and FT-IR, were implemented to deepen the mechanisms associated with fluorides and phosphates immobilization in the stabilized products. pH-dependent leaching tests were carried out to verify the solidification/stabilization effectiveness and reveal fluoride and phosphate leaching behavior. Afterward, the geochemical modeling was constructed as a promising tool to interpret experimental results with emphasis on the pH values influencing the leaching, aiming to establish the links between leaching

and mineralogy controls.

In **Chapter 5**, we highlight the S/S remediation of phosphogypsum toward minimizing the potential effect on the environment from dual concerns on pollutants remediation and carbon footprint. As stated in the previous section, the use of OPC is not qualified for phosphogypsum remediation under acid conditions. The presumption was given as it is a range of pH that is unsuitable for hydration products stability (approximately range from 9 to12), and the stabilized pollutants released consequently. Herein, in this work, a more climate-friendly and lower greenhouse gas emission binder, γ-Al_2O_3, was used as the supplementary material to partially replace the OPC fraction. To further understand the principles of γ-Al_2O_3 in the mixtures systems, we developed a geochemical model to reveal the leaching and phase transport processes.

In **Chapter 6**, the influence of fluoride and phosphate on the early age hydration and the subsequent CO_2 uptake capacity of the proposed S/S scenario is investigated through experimental observation and geochemical modeling analysis. This work is conducted based on the findings presented in Chapters 4 and 5, of which fluoride and phosphate play different roles in the S/S systems. In addition, the sponge effect of the S/S products, indicating the ability that reabsorbs the atmospheric CO_2 in the future, is explored by quantifying the precipitated calcium carbonates in the S/S products. A cradle-to-gate CO_2 emission and storage model was developed that shed an intimate view of the CO_2 balance along the phosphogypsum recycling cycle, which shares new insights with those envisaged in current technology roadmaps.

In **Chapter 7**, we summarized the main conclusions of this thesis and briefly introduced the primary future outlooks of our following works.

In **Appendices**, we shed light on using geochemical modeling (PHREEQC) and parameter fitting software (PEST++) to quantify the roles of different Pb retention mechanisms in OPC and CAC stabilized pyrite ash under the broad pH varial leaching tests.

3. Background

3.1. Solid waste generation and immobilization scenarios: concepts, evolutions, and mechanisms

Solid waste production has been an inevitable consequence of unprecedented economic development and urbanization in the last few decades (Vergara and Tchobanoglous, 2012). To date, the stockpile of solid wastes has consequently been a stinging and widespread problem in both urban and rural areas in many developed and developing countries that directly threatens public health and the environment surrounding it (Abdel-Shafy and Mansour, 2018; Khan et al., 2022a). The potentially toxic elements (PTEs) within the solid waste can intricately interact with the air, soil, and waterbody leading to the mobilization of PTEs due to the weathering process (Das et al., 2019). In Europe, it is estimated that over 340,000 contaminated sites need to be efficiently remediated (Ausili et al., 2020). Concurrently, in the United States, the existence of

hundreds of thousands of contaminated sites was confirmed, and it would take over 100 years to remediate all of these sites at the current pace of cleanup (Hou and O'Connor, 2020). Likewise, approximately 16% of the topsoil in China was found that exceed the enrichment limits of PTEs based on the national environmental standard (Jin et al., 2021). This proliferation of solid waste triggers governments and society to be charged with managing the waste in an economically, socially, and environmentally acceptable manner.

Nevertheless, to minimize the side effect of solid waste stockpiles, different remediation technologies and policies have been proposed over time (Fig.1), just as the governance of waste has evolved. From the 1970s to the 80s, the "remove-all" strategy has been historically employed in waste management. Open pit incineration and ground dumping were the most common methods during that period (Vergara and Tchobanoglous, 2012). However, in the middle of the 1990s, studies found that despite the "remove-all" methods being simple operation and relatively low-cost involvement, easy mismanagement or ineffective execution may be easily present, producing long-term environmental, social, and economic repercussions (Khan et al., 2022b). For instance, residents who live near the waste disposal yards may greatly increase the prevalence of suffering several diseases like malaria, dermatitis, and gastrointestinal disorders (De and Debnath, 2016; Das et al., 2019). Meanwhile, open burning has been confirmed that is a major source of carcinogenic substances emissions of multiple gaseous pollutants (such as dioxin, furans, carbon monoxide, and 1-hexene) into the atmosphere along with the incineration process (Kumari et al., 2017).

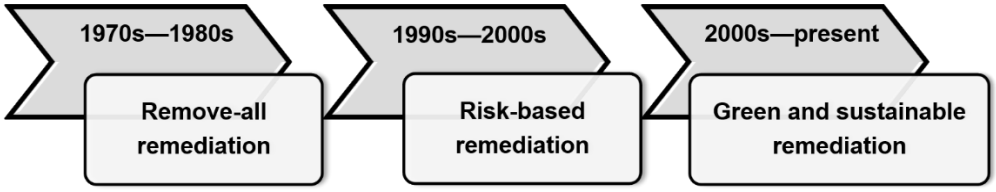

Figure.1. Different stages of solid waste remediation strategies from the 1970s to the present (Hou and O'Connor, 2020).

Therefore, an improved type of remediation method referred to as "risk-based remediation" has been practiced. This management is similar to ground dumping but built with some architectural upgrades such as multiple layers composed of cement, soil, and/or clay with the aim of reducing the seepage of toxic effluents (Zeng et al., 2005; Das et al., 2019). With the ongoing socio-economical development and stepped-up concerns about environmental pollution, the Sustainable Development Goals (SDGs) have been raised by the United Nations (Folke et al., 2002; Sachs et al., 2019), which induced the international community to eagerly seek new sustainable paradigm into the current waste management and innovative interventions to bring the solid waste back to beneficial use (Hák et al., 2016). Many in-situ or ex-situ green

and sustainable remediation approaches have been explored, such as biochemical conversion (Schnell et al., 2020), electrodialysis treatment (Pedersen et al., 2018), and pyrolysis technique (Xu et al., 2021). In the overall management trials of solid waste, stabilization/solidification (S/S) is one of the practicable and time-efficient approaches, which covers approximately 40% of the commercial treatment market (Chen et al., 2009; Xiong et al., 2019; Xue and Liu, 2021).

Given in Fig.2 is the framework of the high-performance S/S (HPSS®) process proposed by our co-workers (Bonomo et al., 2009; Contessi et al., 2020). After removing the large aggregates of the collected contaminants, the sieved sample and binder, primarily cementitious materials, are blended in a mechanical disc pelletizer with a predetermined amount of aqueous solution (water or alkaline solution). Then the pellets are cured in the air or atmosphere-isolated conditions for subsequent real-world use. This management is deemed to effectively convert the solid waste to a physicochemically stable solid assemblage that can long-term or permanently store contaminants in a relatively less mobile form (Chen et al., 2009). The potential PTEs retention mechanisms related to the S/S process are mainly attributed to two aspects: (1) adsorption and chemical bonding (surface complexation, precipitation, and co-precipitation) and (2) physical micro-and/or macro-encapsulation (Chen et al., 2009; Guo et al., 2017). Generally, these two mechanisms occur synchronously.

Figure.2. HPSS® process framework.

As one of the most widely used artificial materials in the industry (Habert et al., 2020), ordinary Portland cement (OPC) is herein extensively applied in the S/S process due to its unique properties and simplicity of use (Ouhadi et al., 2021). When the OPC binder reacts with the water, hydration products (e.g., ettringite, C−S−H gel, and portlandite) start to precipitate due to chemical reactions between clinker compounds, sulfates, and water. Simultaneously, the microstructural features of the mixtures get stiffer (Malviya and

Chaudhary, 2006). The hydration product precipitation usually leads to the adsorption and chemical bonding mechanisms of the available PTEs leading to their total retention. For example, many studies report that the sulfate molecules in ettringite are easily substituted by the heavy metal oxyanions with similar structure and radius (e.g., CrO_4^{2-}, SeO_4^{2-}, $VO_4^{2-}$and AsO_4^{3-}) (Chrysochoou and Dermatas, 2006; Chen et al., 2009; Contessi et al., 2021). For this reason, ettringite has been exploited to solidify the ions through chemical or physical adsorption (Wu and Liu, 2018; Hou et al., 2018). Regarding the C−S−H gel, its layered structures, which link through non-bridging oxygens to chains of silicate tetrahedra on both sides, give rise to a high surface area and a strong capacity for binding PTEs (Contessi et al., 2020; Chen et al., 2022). Vespa et al. (2014) summarized that three possible crystallographic positions in the C−S−H gel structures are responsible for the ions binding with reference to the tobermorite structure. For instance, it is reported that the Zn and Pb can be linked to a chain of silicate tetrahedra of C-S-H by Pb/Zn-O-Si linkage. In addition to sorption and chemical bonding, the precipitation of PTEs species with low solubility is another important fixation mechanism (Dijkstra et al., 2006, 2019; Jarošíková et al., 2017). Heavy metals can be precipitated as hydroxides, carbonates, and sulfates (Contessi et al., 2020; Ouhadi et al., 2021). Besides, the PTEs can react with the cations dissolved from the clinker phases and precipitate (Park et al., 2008; Bisone et al., 2017). For instance, fluoride would precipitate as sparingly soluble fluorite (CaF_2) and fluorapatite ($Ca_5(PO_4)_3F$) (Gerritse, 1993; Park et al., 2008; Gomes et al., 2012), and further, Cr^{3+} in a high calcium content would present as the form of calcium–chromium crystalline precipitates (Omotoso et al., 1998).

On the other hand, the physical micro-and/or macro-encapsulation refers to the capacity that prevents the PTEs from reacting with leaching media such as groundwater and rainfall (Chen et al., 2009). Theoretically, permeability and mechanical properties are the two significant parameters affecting encapsulation. But these two macro-scale properties, in turn, are susceptible to the degradation of mixtures during in-use conditions. The mixtures are attacked by CO_2, chloride, sulfate, and organic matter when exposed to air and waterbody, resulting in the dissolution of hydration products and other chemical reactions that deteriorates the solidified matrices (Dong et al., 2019).

Therefore, considering the challenges for the effective long-term remediation of PTEs, there is a need to investigate the following PTEs mobilization from the mixtures and reveal the mechanisms associated with the redistribution of the stabilized phases. However, the literature highlights that the phases associated with the PTEs are often amorphous, poorly crystalline mixtures, or trace content components at the nanometric scale (Chen et al., 2009; Jarošíková et al., 2017). The characterizations of these phases thus are very complicated. Few geochemical modeling studies have been published so far related the waste in the S/S regime (Dijkstra et al., 2006; Gomes et al., 2012; Chen et al., 2021b). Hopefully, this approach could provide a reliable prediction based on an in-depth mineralogical interpretation of contaminants mobility in

multiple leaching scenarios.

1.2. Alternative binder development: perspectives on PTEs remediation and carbon neutrality

In the 2015 Paris agreement, all major economic sectors worldwide committed to taking responsibility for the global CO_2 emission, which is estimated to be halved by 2030 and reach net zero by 2050, to limit the warming to around 1.5°C (Sachs et al., 2019; De Kleijne et al., 2022). The OPC is mainly composed of four components: alite (C_3S), belite (C_2S), tricalcium aluminate(C_3A), and tetracalcium aluminoferrite (C_4AF), which are primarily sourced from limestone ($CaCO_3$) calcination (Cao et al., 2020). Concurrently, during the OPC production, the raw limestone is excavated, crushed, and milled before being calcined in a rotary kiln at a temperature up to 1500 °C, which dissociates the limestone into CaO and CO_2 before the following reactions with aluminates and silicates (Hossain et al., 2020). The overall OPC production represents substantial greenhouse gas emissions, accounting for 8% of global CO_2 emissions (Andrew, 2018) and 36% of CO_2 released by construction activities (Bajželj et al., 2013). Based on the statistics, the predominant CO_2 emission source is attributed to the kilning stage in OPC production, although the grinding, excavation, packaging, and transportation (Fig.3) also have a minor contribution to the carbon footprint (De Kleijne et al., 2022; Chen et al., 2022; Yang et al., 2022). Therefore, the use of OPC is under critical scrutiny. In order to mitigate the carbon footprint of the S/S process, attempts to partially or entirely replace the OPC content have grown exponentially over the last decades (Habert et al., 2020; Hossain et al., 2020). Low-carbon supplementary cementitious materials (SCMs) and alternative binder solutions are promising routes to mitigate the environmental impacts relative to the conventional OPC.

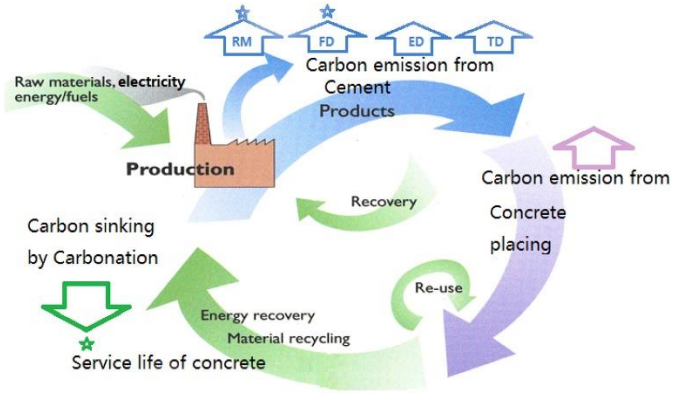

Figure.3. The life cycle process of cement (Shen et al., 2016).

According to the calcium-to-silica reactions, SCMs can be roughly classified into two groups: hydraulic materials (calcium-containing materials spontaneously reacting with H_2O) and pozzolanic materials (slight or no cementation value but chemically reacting with portlandite) (Wang et al., 2020a). To date, the applications of multiple SCMs, such as fly ash, ground granulated blast furnace slag, silica fume, and nano-

Al_2O_3, illustrate an alternative solution for partially replacing the use of OPC (Skibsted and Snellings, 2019). Fly ash and ground granulated blast furnace slag are both typical industrial by-products, which have been extensively studied by researchers worldwide and preliminarily used in the S/S process (Minnu et al., 2021; Wang et al., 2022a). Fly ash incorporated S/S mixtures showed high performance in heavy metals (As and Pb) retention due to its significant pozzolanic reaction that promotes the formation of C−S−H gel and micro-aggregate filling that optimizes the structures of the mixtures (Singh and Pant, 2006; Liang et al., 2020). The addition of ground granulated blast furnace slag favors the C−S−H gel precipitation and reduces the exorbitant pH variation while simultaneously benefits the PTEs remediation (Wang et al., 2018; Zhang et al., 2022; Wu et al., 2022). The silica fume contains as high as 99% reactive SiO_2, thus, facilitating the additional C−S−H gel formation in the stabilized products through the pozzolanic reactions (Siddique, 2011). Likewise, this promotion significantly enhances the durability and mechanical properties of the S/S mixtures for engineering applications and decreases the PTEs' leachability in the view of sustainability. The more environmentally friendly and lower carbon footprint agent, nano-Al_2O_3, is produced by kaolin calcination (the main constituent in kaolin is kaolinite mineral: $Al_2O_3 \cdot 2SiO_2 \cdot 2H_2O$), with the CO_2 emission amounts to approximately 60% of OPC production (Hosseini et al., 2011). Apart from the low carbon footprint, nano-Al_2O_3 has excellent adsorption capacity for both PTEs due to its large specific surface and high mass transfer efficiency (Moharami and Jalali, 2014a; Hafshejani et al., 2017). Meanwhile, the aluminate presents high compatibility with the contaminated soil remediation by bonding the PTEs (Wang et al., 2020a). With the incorporation of nano-Al_2O_3, the S/S products show reduced environmental impacts through the chemical and physical adsorption of hydration products and nano-Al_2O_3 (Wang and Sohn, 2021; Praveenkumar et al., 2021). Furthermore, the nano-Al_2O_3 can provide sufficient alkalinity to activate the reactions of the systems, which contributed to the high retention efficiencies of PTEs at the early-age hydration period (Valero et al., 2006; Yang et al., 2020).

Aside from the SCMs, the applications of alternative binders may be capable of achieving the ideal one-for-one replacement for the OPC, including calcium aluminate cement (CAC) (Calgaro et al., 2021), geopolymer (Guo et al., 2017; Sun et al., 2019), and magnesium-rich cement (MRC) (Naeem et al., 2021). CAC is an alternative cementitious material manufactured industrially from mixtures of limestone and materials (bauxites and laterites) with a high content of Al_2O_3 (Chen et al., 2021a; Zapata et al., 2022). It is considered eco-cements due to the reduced carbon emissions generated during its production, even though it suffers from a higher production cost than OPC (Zapata et al., 2022). Promising superior PTEs (i.e., Ni, Cu, and Cr) immobilization results obtained in the works of Abbaspour et al. (2016) and Ivanov et al. (2016) open possibilities for its use as an alternative binder to OPC in the S/S process (Calgaro et al., 2021). Meanwhile, its specific engineering properties, such as fast setting time and relatively high early mechanical strength, broaden the in-use conditions of the S/S applications, which is difficult to achieve with

conventional OPC-based technologies (Calgaro et al., 2021; Sun et al., 2022). Geopolymer is a binder that can be synthesized from various raw aluminosilicate sources, for instance, metakaolin, blast furnace slag, fly ash, and clays (Xia et al., 2019). Of which metakaolin is the most widely used raw material (Wang et al., 2020a). With the activation of alkaline agents, the metakaolin synthesized geopolymer presents enhanced physical properties and chemical corrosion resistance compared to the OPC-based S/S (Xia et al., 2019). Less leaching of PTEs (Pb, Cr, Zn, and Cu) is verified through the ion exchange with the amorphous content and the precipitation of the fewer solubility minerals (Guo et al., 2017; Wang et al., 2021). Noteworthy, it is within a pH range (9 to 12) that most of the PTEs species have the lowest solubility. MRC is considered an eco-friendly cementitious substitute for OPC but has relatively low raw materials availability (Wang et al., 2020a). The study shows that the generated magnesium silicate hydrate (M−S−H) gel has the potential to immobilize nuclear contaminations, such as plutonium-contaminated ash arising from nuclear operations and uranium-containing nuclear wastes (Walling and Provis, 2016). This is because the M−S−H gel has a lower equilibrium pH (10.5) than the conventional PC blends, suggesting that it can be advantageous in reducing aluminum-induced expansion and cracking in alkaline media and the low water requirement for the MRC binder reduces the availability of free water for corrosion (Pyo et al., 2021). But due to its low water resistance and unprofitability, the wide application of MRC is limited, and it is usually introduced to special conditions unsuitable for the OPC.

Although many works have been carried out on the use of SCMs and alternative binders during the past decades, the economic consumption, the availability of the raw materials, the not-well-established immobilization mechanisms systems, and most importantly, the confidence in the long-term PTEs retention capacity highlights that there is still no silver bullet for achieving the overall replacement the conventional OPC (Hou and O'Connor, 2020; Habert et al., 2020).

1.3. Geochemical modeling: a new vitality for the traditional and versatile S/S remediation

In the service life, stabilized products will inevitably come in contact with infiltrating water sooner or later, and constituents of PTEs could be remobilized (Contessi et al., 2020; Chen et al., 2022). Therefore, studying the fate and transportation of PTEs in solid wastes and stabilized products is of great significance to better understand the fate of contaminants and their interactions with the environment (Tiruta-Barna, 2008; Jarošíková et al., 2017; Khalidy and Santos, 2021). Concurrently the majority of the works mainly depend on direct evidence provided from the laboratory and field monitoring, for instance, the PTEs concentration in the leachate and the physiochemical characterization of bulk samples (Tiwari et al., 2015; Pietrzak, 2021). Despite these physical, chemical, and/or biological attempts successfully acquire pertinent information to assess the PTEs leaching in some cases, exploring the overall PTEs leaching controlling mechanisms is still challenging (Mahedi et al., 2020). During the past decade, geochemical modeling has

been one of the main driving forces in the ongoing global search for novel insights to chart the complex mechanisms that are responsible for the leaching behavior (Dijkstra et al., 2006; Appelo et al., 2014; Parkhurst and Wissmeier, 2015; Chen et al., 2021b).

PHREEQC (**pH** values, **Re**dox, **Eq**uilibrium, **C**++ programming language) (Parkhurst and Appelo, 2013; Appelo et al., 2014; Parkhurst and Wissmeier, 2015) is a computer program for simulating chemical reactions and transport processes in natural or polluted water. It is applicable to the study of the migration of heavy metals (e.g., Pb, Zn, and As) (Dijkstra et al., 2002; Halim et al., 2005; Tiruta-Barna, 2008), the spatial distribution of contaminants in the solid waste stockpile sites (Bisone et al., 2017), and the in the investigation of the PTEs/aquifers interactions (Chidambaram et al., 2012; Moharami and Jalali, 2014b; Appelo et al., 2014). Further, it can be used to determine the predominant hydrochemical processes controlling water quality and the occurrence of pharmaceuticals (Tomaszewska et al., 2018; Wątor et al., 2020; Pietrzak, 2021) and the sorption behavior of organic micropollutants (Yan et al., 2012; Mosai and Tutu, 2019).

In the projects of S/S application, Halim et al. (2005) simulated the long-term leaching behavior of Pb, Cd, As, and Cr from cementitious wastes. The model is mainly composed of four parts: (1) minerals equilibrium, (2) calcite-cerussite solid solution formation/dissolution, (3) organic surface complex, and (4) adsorption to hydroxides and silica gel. The results obtained in this work suggest that the minerals equilibrium is dominant in Pb and Cd leaching, of which carbonate and silicate species governed the solubility of Pb while carbonate, silicate, and hydroxide species governed the solubility of Cd. Likewise, the effectiveness of OPC at Cu, Pb, and Zn-contaminated soil immobilization was examined by PHREEQC (Navarro et al., 2011). In this work, both Pb and Zn demonstrate high mobility under basic conditions (pH > 12) based on the experimental observation. The PHREEQC simulation shows that the remobilization of Pb is attributed to the complexation with OH^-, Cl^-, CO_3^{2-}, and SO_4^{2-}, whereas the Zn leaching is associated with the OH^- and SO_4^{2-} species. Further, research has shown that PHREEQC can be applied to the investigations of the weathering process of S/S products (Vega-Garcia et al., 2021). For the pH-dependence leaching of stabilized PTEs, Martens et al. (2010) combined the mechanisms of minerals precipitation/dissolution, surface complexation, and solid solutions formation to reproduce the amphoteric Pb leaching. Nevertheless, all these findings indicate that the PHREEQC modeling is a promising route for revealing the possible PTEs retention mechanisms. However, the inverse modeling construction (Fig.4) relies on the thorough characterization of leachate (Martens et al., 2008; Navarro et al., 2011) and parameter fitting software (Vega-Garcia et al., 2021) to find the possible sets of mineral assemblages and aqueous species transfer. The model is calibrated by comparing the leaching data from the experiments and simulation back and forth and ends up with an acceptable compositional fit. This direct data acquisition

method is typically time- and cost-consuming. A series of tests must be carried out before reconstructing a convincing representation of reality.

On the other hand, studies also tried to use the forward model construction pathway to predict the leaching behavior of PTEs, aiming to simplify the laboratory measurement (Solpuker et al., 2014; Lupsea et al., 2014; Han et al., 2021). This methodology (Fig.4) is mainly based on the bulk S/S product characterization results as the initial input. With the calculation of minerals equilibrium, surface complexation, oxidation-reduction, etc., the modeling output (e.g., PTEs concentration in the solution and saturation index evolution of the initial input minerals) is taken as semiquantitative, or even qualitative, indicators of possible outcome (Khalidy and Santos, 2021).

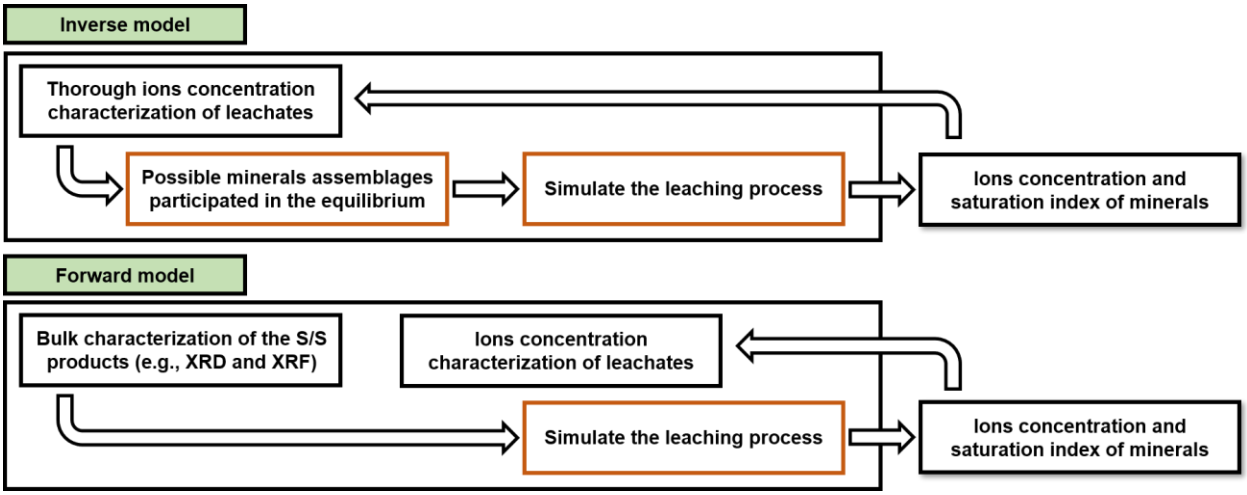

Figure.4. Inverse and forward PHREEQC model construction storylines.

The reported bulk characterization methods include X-ray diffraction (XRD) (Liu et al., 2020; Wang et al., 2020b), X-ray fluorescence (XRF) (Masindi et al., 2021), and scanning electron microscopy/energy dispersive X-ray spectroscopy (SEM/EDS) (Liu and Cheng, 2019). Without the parameter fitting process and the control of the specific PTEs input (e.g., the maximum PTEs leaching is based on experimental observation at harsh acid conditions instead of the bulk XRF or XRD quantification of the products), this direct pathway may bring larger variation between the simulation and experiments. But, in practice, the forward construction is simpler and less dependent on experimental or sampling data. If well constructed, it can still be valuable in many applied fields and at least can be utilized as semiquantitative or even qualitative indicators (Khalidy and Santos, 2021). Therefore, the considerable quantity of contaminants, the mineralogical composition of waste, the detailed investigation of the stockpile site, and the examination of the leaching behavior are fundamentally in the selection of management strategies. Nevertheless, experimental characterization is a typical straightforward method that can provide sufficient information for revealing the fate of contaminants. But this direct data acquisition method is typically time- and cost-

consuming. A series of tests must be carried out before reconstructing a convincing representation of reality. Consequently, geochemical modeling helps predict the future state of such a stockpile system and aids in the design of remedial strategies.

1.4. Literature review for the solid waste generated by the phosphorus fertilizer industry: generation, storage, and recycling of pyrite ash and phosphogypsum

As mentioned above, along with the rapid urbanization and industrialization that began in the last century, the global population was rising dramatically, posing an increasing demand for phosphates fertilizer for agricultural purposes (Villalba et al., 2008). Although the fertilizer industry plays an essential role in improving the social and economic status of human beings, the inappropriate dumping of million tons of waste by-products poses a threat to climate change and human health (Rashad, 2017; Saadaoui et al., 2017; Wang, 2020). In the production of phosphoric acid, an essential intermediate for the phosphate fertilizer, there are two processes commonly used: the wet process (wet phosphoric acid production) and the thermal process (thermal phosphoric acid production). Thermal acid is of a higher grade than wet acid and is thus used in the food industry and industrial phosphates, whereas wet acid mostly goes to fertilizer production (Villalba et al., 2008; Tayibi et al., 2009). Generally, the by-products closely related to wet phosphoric acid production are pyrite ash and phosphogypsum (Cordell et al., 2009; Scholz et al., 2013; Chernysh et al., 2021). From Fig.5, it can be seen that pyrite ash is the by-product generated by the roasting process of pyrite to extract the sulfur from SO_2 to sulphuric acid. It is basically composed of iron oxide (hematite) and a minor content of sulfates (Oliveira et al., 2012). Phosphogypsum, another solid waste residue from the overall wet process, is produced by the wet-chemical processing (sulphuric acid) of phosphate rock. The observed mineral phases of by-product phosphogypsum mainly consist of three sulfate species: gypsum, bassanite, and anhydrite, accompanied by minor content of silicates (Lieberman et al., 2020). The weight percentage of these mineralogical components is influenced by the employed wet-process phosphoric acid production (Tayibi et al., 2009).

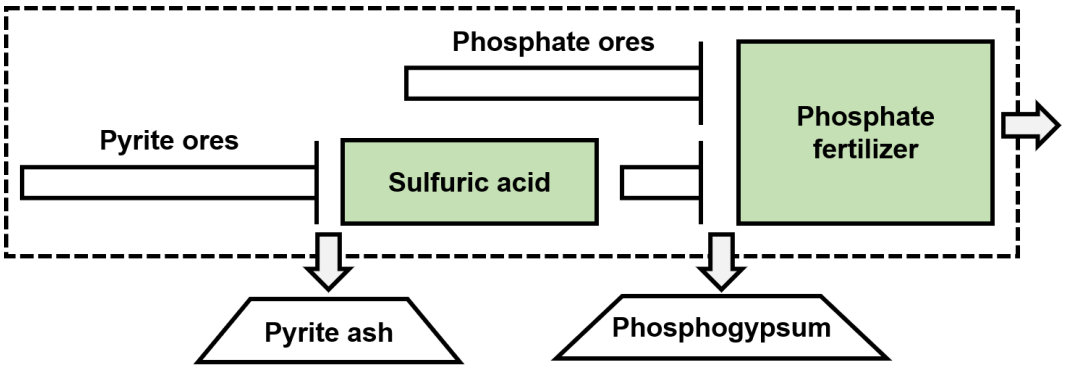

Figure.5. Solid waste generation related to the phosphates fertilizer industry.

Although the primary components in pyrite ash are hematite and calcium sulfates, which are naturally occurring minerals in the environment with low toxicity (Oliveira et al., 2012), along with the enrichment of the physicochemical process from the raw ores to business products, significant concentrations of PTEs are correspondingly presented in the residues. For instance, multiple heavy metals species (e.g., Pb, As, and Zn) and sulfides are observed in the pyrite ash residues (Gabarrón et al., 2018; Contessi et al., 2020). Regarding the phosphogypsum residues, the substantial presence of phosphates, fluorides, and radioactive elements components are explored (Tayibi et al., 2009; Zhang et al., 2017). Furthermore, due to the popular locus of historical management in the last century (risk-based remediation) and lacking efficient recycling strategy in recent decades, statistics report that 1 billion or more metric tons of pyrite ash and phosphogypsum have been accumulated so far (Villalba et al., 2008; Oliveira et al., 2012; Rashad, 2017). The interaction between weathering process and anthropogenic activities with the exposed residues deposits produces PTEs-rich leachates channeled back into the stockpile site, seriously affecting residues and the surrounding environment.

During the stockpile of pyrite ash, the oxidation of metal sulfides is a significant threat to the acidification in soils, which acts as a forerunner of heavy metal mobility (Hooda, 2010). For instance, the galena (PbS), a Pb host mineral in the pyrite ores, may oxidize to anglesite ($PbSO_4$) under acidic and oxidizing conditions (Gabarrón et al., 2018), thereby releasing huge amounts of Pb and sulfates into the environment being more soluble. Further, in pyrite oxidation, the porous texture of hematite with a high surface area can adsorb SO_2 and heavy metals (Oliveira et al., 2012; Contessi et al., 2020). When weathering occurs, the complex surface balance equilibrium is shifted, and the adsorbed SO_2 and heavy metals are released into the environment together with water infiltration. Similarly, the phosphogypsum storage not only occupies considerable land areas but also degrades groundwater quality by the PG leachates infiltration (Melki and Gueddari, 2018). The water-soluble phosphorous and fluorine, representing the primary phosphogypsum pollutants, and impurities of heavy metals (Ba, Cu, Pb, Zn) and toxic radionuclides (Ra^{226}, Pb^{210}, et al.) can be channeled back into the groundwater body through the weathering interactions (Lieberman et al., 2020). Hence, given the long history and vast scale of pyrite ores roasting and phosphate fertilizer production, the environmental risk management of areas affected by pyrite ash and phosphogypsum stockpile represents a major challenge worldwide (Oliveira et al., 2012; Liu et al., 2016; Soriano-Disla et al., 2018).

Concurrently, there are many research reports on the ex-situ utilization of pyrite ash disposal (Chun et al., 2011; Ma et al., 2021; Zhang et al., 2021). The majority (approximately 30 wt% of the total discarded) of the recycled pyrite cinder is attributed to an additive in brick-making, coating, and cement industry (Ma et al., 2021). Besides, techniques also have been used as a metal resource to recover Fe, Pb, and Zn from pyrite ash through magnetic and gravity separation (Li et al., 2018; Liu et al., 2022) and as an oxidation

catalyst to manage high-concentration refractory organics in wastewater (Song et al., 2022). Although these attempts presented a promising prospect of utilizing the pyrite cinder in a high-value and sustainable pathway, some drawbacks, such as energy-intensive, grievous environmental pollution, and serious equipment corrosion, are shown due to the pervasive intergrowth between the valuable resources and PTEs (Alp et al., 2009; Zhang et al., 2021). Up to date, some studies have tried to large-scale and efficiently remediate and recycle the pyrite ash through the S/S process (Wang et al., 2018; Contessi et al., 2020; Calgaro et al., 2021; Wang et al., 2022b). But the challenges refer to retention mechanisms of Pb to precisely control and track the release of PTEs and negative-emission binders to enable global climate change mitigation still needs further work to fill this gap.

Regarding phosphogypsum recycling, scholars tried to apply it to agricultural production (Abril et al., 2009; Soares et al., 2012), rare earth elements recovery (Cánovas et al., 2019), and building material manufacture (Değirmenci, 2008; Bagade and Satone, 2012; Tian et al., 2016; Yang et al., 2016; Liu et al., 2019). When reusing through the S/S process, the results depicted a gradual decline in workability and mechanical performance increased with the phosphogypsum content, which can be attributed to the presence of fluorine and phosphorus compounds. Therefore, studies for phosphogypsum purification pretreatment, for instance, water washings (Ölmez and Erdem, 1989; Singh et al., 1996), thermal treatments (Taher, 2007; Tayibi et al., 2009), hot aqueous ammonium sulfate solutions (Singh et al., 1993), and neutralization with lime (Al-Hwaiti, 2015), were accordingly conducted. However, the phosphogypsum itself also lacks adequate mechanical properties and durability for being used independently as a primary component in the mixtures (Potgieter et al., 2003; Huang et al., 2016; Nizevičienė et al., 2016). Besides, using complicated purification systems can increase extortionate costs. Therefore, the successful commercialization of recycling phosphogypsum has been consequently far from an apparent breakthrough, with particular emphasis on quality assurance, repeatability, processability, and safety.

4. Material and methods

In the thesis, the studied material (Fig.6a) of Chapters 2 to 4 was pyrite ash collected from the middle-east part of Italy (Ancona). This site was devoted to a pyrite ash storage place for an abandoned fertilizer production facility. Samples (Fig.6b) used in Chapters 5 to 7 were from a phosphogypsum stockpile site in China (Hubei), which was generated by fertilizer manufacturing and beneficiation of low-grade phosphate rock. The samples were excavated from the layer comprised in the depth interval between approximately 20 to 50 cm from the surface of a stockpile site and sieved through a 200 μm mesh. XRD, XRF, and Fourier transform infrared (FTIR) experiments were conducted to characterize the mineralogical and chemical composition of the collected samples with the aim of determining the PTEs bearing phases and the concentrations. Particle size distribution (PSD) tests were carried out to investigate the physical properties

of the bulk materials. Then, the detailed characterization SEM/EDS and Raman spectroscopy were applied to attain a better understanding of the PTEs distribution in the pyrite ash and phosphogypsum. Electron microprobe analyzer/wavelength dispersive elemental analysis (EMPA/WDS) was performed to characterize fluorine and iron to avoid overlapping of F *K*α and Fe *L*α lines obtained by SEM/EDS.

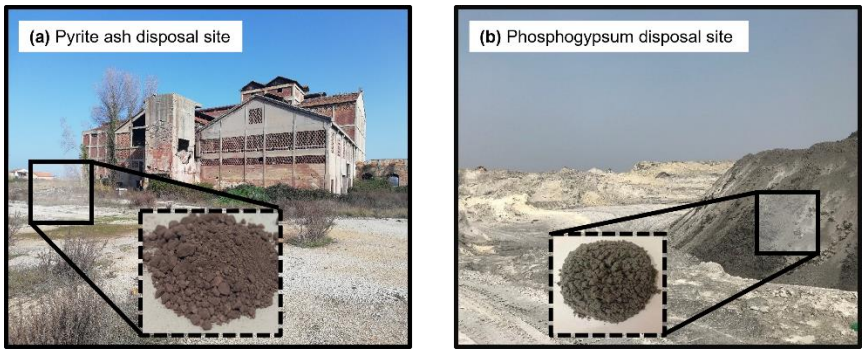

Figure.6. Sampling area. (a) pyrite ash disposal site in Ancona, Italy and (b) phosphogypsum storage site in Hubei, China.

After the raw material characterization, the samples were devoted to the S/S process. In the case of pyrite ash disposal, we preliminarily used multiple remediation strategies, including the traditional binders OPC and alternative binders CEM III/B, CAC, MAY, and ABS. Then pyrite ash, binders, and solution (water) were mixed and pelletized through the HPSS® as mentioned above (Fig.2). After 28 days of curing, the hardened pellets were sieved to a particle size ranging from 2 to 10 mm. With regards to the phosphogypsum remediation, we used the OPC and sustainable cementitious substitution of γ-Al_2O_3 as the binders. The mixtures were prepared using a plastic cylinder (5 cm in diameter and 10 cm in height). A series of physicochemical experiments were introduced to access the binder hydration process, PTEs species transformation, and mechanical properties of the S/S products. Toxicity characteristic leaching procedure (TCLP) and pH-dependent leaching tests were applied to determine the PTEs retention capacity of each S/S product. The details of the raw material and stabilized products characterization experiment and the acquired results are shown in the following chapters.

Reference

Abbaspour, A., Tanyu, B.F., and Cetin, B., 2016, Impact of aging on leaching characteristics of recycled concrete aggregate: Environmental Science and Pollution Research, v. 23, p. 20835–20852, doi:10.1007/S11356-016-7217-9/FIGURES/15.

Abdel-Shafy, H.I., and Mansour, M.S.M., 2018, Solid waste issue: Sources, composition, disposal, recycling, and valorization: Egyptian Journal of Petroleum, v. 27, p. 1275–1290, doi:10.1016/J.EJPE.2018.07.003.

Abril, J.M., García-Tenorio, R., Periáñez, R., Enamorado, S.M., Andreu, L., and Delgado, A., 2009, Occupational dosimetric assessment (inhalation pathway) from the application of phosphogypsum in agriculture in South West Spain: Journal of Environmental Radioactivity, v. 100, p. 29–34, doi:10.1016/j.jenvrad.2008.09.006.

Al-Hwaiti, M.S., 2015, Assessment of the radiological impacts of treated phosphogypsum used as the main constituent of building materials in Jordan: Environmental Earth Sciences, v. 74, p. 3159–3169, doi:10.1007/s12665-015-4354-2.

Alp, I., Deveci, H., Yazici, E.Y., Türk, T., and Süngün, Y.H., 2009, Potential use of pyrite cinders as raw material in cement production: Results of industrial scale trial operations: Journal of Hazardous Materials, v. 166, p. 144–149, doi:10.1016/J.JHAZMAT.2008.10.129.

Andrew, R.M., 2018, Global CO2 emissions from cement production: Earth System Science Data, v. 10, p. 195–217, doi:10.5194/ESSD-10-195-2018.

Appelo, C.A.J., Parkhurst, D.L., and Post, V.E.A., 2014, Equations for calculating hydrogeochemical reactions of minerals and gases such as CO2 at high pressures and temperatures: Geochimica et Cosmochimica Acta, v. 125, p. 49–67, doi:10.1016/J.GCA.2013.10.003.

Ausili, A., Bergamin, L., and Romano, E., 2020, Environmental Status of Italian Coastal Marine Areas Affected by Long History of Contamination: Frontiers in Environmental Science, doi:10.3389/fenvs.2020.00034.

Bagade, M.A., and Satone, S.R., 2012, An experimental investigation of partial replacement of cement by various percentage of Phosphogypsum in cement concrete: International Journal of Engineering Research and Applications, v. 2, p. 785–787.

Bajželj, B., Allwood, J.M., and Cullen, J.M., 2013, Designing climate change mitigation plans that add up: Environmental Science and Technology, v. 47, p. 8062–8069, doi:10.1021/ES400399H/SUPPL_FILE/ES400399H_SI_001.PDF.

Bisone, S., Gautier, M., Chatain, V., and Blanc, D., 2017, Spatial distribution and leaching behavior of pollutants from phosphogypsum stocked in a gypstack: Geochemical characterization and modeling: Journal of Environmental Management, doi:10.1016/j.jenvman.2017.02.055.

Bonomo, L., Careghini, A., Dastoli, S., De Propris, L., Ferrari, G., Gabellini, M., and Saponaro, S., 2009, Feasibility studies for the treatment and reuse of contaminated marine sediments: https://doi.org/10.1080/09593330902990105, v. 30, p. 817–823, doi:10.1080/09593330902990105.

Calgaro, L., Contessi, S., Bonetto, A., Badetti, E., Ferrari, G., Artioli, G., and Marcomini, A., 2021, Calcium aluminate cement as an alternative to ordinary Portland cement for the remediation of heavy metals contaminated soil: mechanisms and performance: Journal of Soils and Sediments, doi:10.1007/s11368-020-02859-x.

Cánovas, C.R., Chapron, S., Arrachart, G., and Pellet-Rostaing, S., 2019, Leaching of rare earth elements (REEs) and impurities from phosphogypsum: A preliminary insight for further recovery of critical raw materials: Journal of Cleaner Production, v. 219, p. 225–235, doi:10.1016/j.jclepro.2019.02.104.

Cao, Z., Myers, R.J., Lupton, R.C., Duan, H., Sacchi, R., Zhou, N., Reed Miller, T., Cullen, J.M., Ge, Q., and Liu, G., 2020, The sponge effect and carbon emission mitigation potentials of the global cement cycle: Nature Communications 2020 11:1, v. 11, p. 1–9, doi:10.1038/s41467-020-17583-w.

Chen, Q.Y., Tyrer, M., Hills, C.D., Yang, X.M., and Carey, P., 2009, Immobilisation of heavy metal in cement-based solidification/stabilisation: A review: Waste Management, doi:10.1016/j.wasman.2008.01.019.

Chen, L., Wang, Y.S., Wang, L., Zhang, Y., Li, J., Tong, L., Hu, Q., Dai, J.G., and Tsang, D.C.W., 2021a, Stabilisation/solidification of municipal solid waste incineration fly ash by phosphate-enhanced calcium aluminate cement: Journal of Hazardous Materials, v. 408, p. 124404, doi:10.1016/J.JHAZMAT.2020.124404.

Chen, L., Wang, L., Zhang, Y., Ruan, S., Mechtcherine, V., and Tsang, D.C.W., 2022, Roles of biochar in cement-based stabilization/solidification of municipal solid waste incineration fly ash: Chemical Engineering Journal, v. 430, p. 132972, doi:10.1016/J.CEJ.2021.132972.

Chen, Z., Zhang, P., Brown, K.G., Branch, J.L., van der Sloot, H.A., Meeussen, J.C.L., Delapp, R.C., Um, W., and Kosson, D.S., 2021b, Development of a Geochemical Speciation Model for Use in Evaluating Leaching from a Cementitious Radioactive Waste Form: Environmental Science and Technology, v. 55, p. 8642–8653, doi:10.1021/ACS.EST.0C06227/ASSET/IMAGES/LARGE/ES0C06227_0007.JPEG.

Chernysh, Y., Yakhnenko, O., Chubur, V., and Roubík, H., 2021, Phosphogypsum Recycling: A Review of Environmental Issues, Current Trends, and Prospects: Applied Sciences, doi:10.3390/app11041575.

Chidambaram, S., Anandhan, P., Prasanna, M. V., Ramanathan, A.L., Srinivasamoorthy, K., and Kumar, G.S., 2012, Hydrogeochemical Modelling for Groundwater in Neyveli Aquifer, Tamil Nadu, India, Using PHREEQC: A Case Study: Natural Resources Research, v. 21, p. 311–324, doi:10.1007/S11053-012-9180-6/FIGURES/11.

Chrysochoou, M., and Dermatas, D., 2006, Evaluation of ettringite and hydrocalumite formation for heavy metal immobilization: Literature review and experimental study: Journal of Hazardous Materials, doi:10.1016/j.jhazmat.2005.11.008.

Chun, T.J., Zhu, D.Q., and Pan, J., 2011, Influence of sulfur content in raw materials on oxidized pellets: Journal of Central South University of Technology 2011 18:6, v. 18, p. 1924–1929, doi:10.1007/S11771-011-0924-Y.

Contessi, S., Calgaro, L., Dalconi, M.C., Bonetto, A., Bellotto, M. Pietro, Ferrari, G., Marcomini, A., and Artioli, G., 2020, Stabilization of lead contaminated soil with traditional and alternative binders: Journal of Hazardous Materials, doi:10.1016/j.jhazmat.2019.120990.

Contessi, S., Dalconi, M.C., Pollastri, S., Calgaro, L., Meneghini, C., Ferrari, G., Marcomini, A., and Artioli, G., 2021, Cement-stabilized contaminated soil: Understanding Pb retention with XANES and Raman spectroscopy: Science of The Total Environment, v. 752, p. 141826, doi:10.1016/J.SCITOTENV.2020.141826.

Cordell, D., Drangert, J.O., and White, S., 2009, The story of phosphorus: Global food security and food for thought: Global Environmental Change, doi:10.1016/j.gloenvcha.2008.10.009.

Das, S., Lee, S.H., Kumar, P., Kim, K.H., Lee, S.S., and Bhattacharya, S.S., 2019, Solid waste management: Scope and the challenge of sustainability: Journal of Cleaner Production, v. 228, p. 658–678, doi:10.1016/J.JCLEPRO.2019.04.323.

De, S., and Debnath, B., 2016, Prevalence of Health Hazards Associated with Solid Waste Disposal- A Case Study of Kolkata, India: Procedia Environmental Sciences, v. 35, p. 201–208, doi:10.1016/J.PROENV.2016.07.081.

Değirmenci, N., 2008, Utilization of phosphogypsum as raw and calcined material in manufacturing of building products: Construction and Building Materials, v. 22, p. 1857–1862, doi:10.1016/j.conbuildmat.2007.04.024.

Dijkstra, J.J., Comans, R.N.J., Schokker, J., and van der Meulen, M.J., 2019, The geological significance of novel anthropogenic materials: Deposits of industrial waste and by-products: Anthropocene, v. 28, p. 100229, doi:10.1016/J.ANCENE.2019.100229.

Dijkstra, J.J., Van der Sloot, H.A., and Comans, R.N.J., 2002, Process identification and model development of contaminant transport in MSWI bottom ash: Waste Management, v. 22, p. 531–541, doi:10.1016/S0956-053X(01)00034-4.

Dijkstra, J.J., Van Der Sloot, H.A., and Comans, R.N.J., 2006, The leaching of major and trace elements from MSWI bottom ash as a function of pH and time: Applied Geochemistry, v. 21, p. 335–351, doi:10.1016/J.APGEOCHEM.2005.11.003.

Dong, Q., Liang, B., Jia, L., and Jiang, L., 2019, Effect of sulfide on the long-term strength of lead-zinc

tailings cemented paste backfill: Construction and Building Materials, v. 200, p. 436–446, doi:10.1016/j.conbuildmat.2018.12.069.

Dooley, K., Nicholls, Z., and Meinshausen, M., 2022, Carbon removals from nature restoration are no substitute for steep emission reductions: One Earth, v. 5, p. 812–824, doi:10.1016/j.oneear.2022.06.002.

Folke, C., Carpenter, S., Elmqvist, T., Gunderson, L., Holling, C.S., and Walker, B., 2002, Resilience and Sustainable Development: Building Adaptive Capacity in a World of Transformations: https://doi.org/10.1579/0044-7447-31.5.437, v. 31, p. 437–440, doi:10.1579/0044-7447-31.5.437.

Gabarrón, M., Babur, O., Soriano-Disla, J.M., Faz, A., and Acosta, J.A., 2018, Composition and risk assessment of roasted pyrite ash from fertiliser production: Chemosphere, v. 209, p. 277–285, doi:10.1016/J.CHEMOSPHERE.2018.06.109.

Gerritse, R.G., 1993, Prediction of travel times of phosphate in soils at a disposal site for wastewater: Water Research, doi:10.1016/0043-1354(93)90084-U.

Gomes, A.F.S., Lopez, D.L., and Ladeira, A.C.Q., 2012, Characterization and assessment of chemical modifications of metal-bearing sludges arising from unsuitable disposal: Journal of Hazardous Materials, doi:10.1016/j.jhazmat.2011.11.039.

Guo, B., Liu, B., Yang, J., and Zhang, S., 2017, The mechanisms of heavy metal immobilization by cementitious material treatments and thermal treatments: A review: Journal of Environmental Management, v. 193, p. 410–422, doi:10.1016/j.jenvman.2017.02.026.

Habert, G., Miller, S.A., John, V.M., Provis, J.L., Favier, A., Horvath, A., and Scrivener, K.L., 2020, Environmental impacts and decarbonization strategies in the cement and concrete industries: Nature Reviews Earth & Environment 2020 1:11, v. 1, p. 559–573, doi:10.1038/s43017-020-0093-3.

Hafshejani, L.D., Tangsir, S., Daneshvar, E., Maljanen, M., Lähde, A., Jokiniemi, J., Naushad, M., and Bhatnagar, A., 2017, Optimization of fluoride removal from aqueous solution by Al2O3 nanoparticles: Journal of Molecular Liquids, doi:10.1016/j.molliq.2017.04.104.

Hák, T., Janoušková, S., and Moldan, B., 2016, Sustainable Development Goals: A need for relevant indicators: Ecological Indicators, v. 60, p. 565–573, doi:10.1016/J.ECOLIND.2015.08.003.

Halim, C.E., Short, S.A., Scott, J.A., Amal, R., and Low, G., 2005, Modelling the leaching of Pb, Cd, As, and Cr from cementitious waste using PHREEQC: Journal of Hazardous Materials, v. 125, p. 45–61, doi:10.1016/j.jhazmat.2005.05.046.

Han, S.C., Jo, Y., and Yun, J. Il, 2021, Chemical degradation of fly ash blended concrete with the seasonal variation of rainwater in a radioactive waste repository: A thermodynamic modeling approach: Cement and Concrete Research, v. 141, p. 106326, doi:10.1016/J.CEMCONRES.2020.106326.

Hooda, P.S., 2010, Trace Elements in Soils: Trace Elements in Soils, doi:10.1002/9781444319477.

Hossain, M.U., Wang, L., Chen, L., Tsang, D.C.W., Ng, S.T., Poon, C.S., and Mechtcherine, V., 2020, Evaluating the environmental impacts of stabilization and solidification technologies for managing hazardous wastes through life cycle assessment: A case study of Hong Kong: Environment International, v. 145, p. 106139, doi:10.1016/J.ENVINT.2020.106139.

Hosseini, S.A., Niaei, A., and Salari, D., 2011, Production of γ-Al2O3 from Kaolin: Open Journal of Physical Chemistry, v. 01, p. 23–27, doi:10.4236/ojpc.2011.12004.

Hou, D., Li, T., Han, Q., and Zhang, J., 2018, Insight on the sodium and chloride ions adsorption mechanism on the ettringite crystal: Structure, dynamics and interfacial interaction: Computational Materials Science, v. 153, p. 479–492, doi:10.1016/J.COMMATSCI.2018.07.021.

Hou, D., and O'Connor, D., 2020, Green and sustainable remediation: past, present, and future developments: Sustainable Remediation of Contaminated Soil and Groundwater, p. 19–42, doi:10.1016/B978-0-12-817982-6.00002-1.

Hou, D., O'Connor, D., Igalavithana, A.D., Alessi, D.S., Luo, J., Tsang, D.C.W., Sparks, D.L., Yamauchi, Y., Rinklebe, J., and Ok, Y.S., 2020, Metal contamination and bioremediation of agricultural soils for food safety and sustainability: Nature Reviews Earth & Environment 2020 1:7, v. 1, p. 366–381, doi:10.1038/s43017-020-0061-y.

Huang, Y., Qian, J., Liang, J., Liu, N., Li, F., and Shen, Y., 2016, Characterization and calorimetric study of early-age hydration behaviors of synthetic ye'elimite doped with the impurities in phosphogypsum: Journal of Thermal Analysis and Calorimetry, v. 123, p. 1545–1553, doi:10.1007/s10973-015-5009-y.

Ivanov, R.C., Angulski da Luz, C., Zorel, H.E., and Pereira Filho, J.I., 2016, Behavior of calcium aluminate cement (CAC) in the presence of hexavalent chromium: Cement and Concrete Composites, v. 73, p. 114–122, doi:10.1016/J.CEMCONCOMP.2016.07.006.

Jarošíková, A., Ettler, V., Mihaljevič, M., Kříbek, B., and Mapani, B., 2017, The pH-dependent leaching behavior of slags from various stages of a copper smelting process: Environmental implications: Journal of Environmental Management, v. 187, p. 178–186, doi:10.1016/J.JENVMAN.2016.11.037.

Jin, Y. et al., 2021, Integrated Life Cycle Assessment for Sustainable Remediation of Contaminated Agricultural Soil in China: Environmental Science and Technology, v. 55, p. 12032–12042, doi:10.1021/ACS.EST.1C02535/ASSET/IMAGES/LARGE/ES1C02535_0006.JPEG.

Khalidy, R., and Santos, R.M., 2021, Assessment of geochemical modeling applications and research hot spots—a year in review: Environmental Geochemistry and Health 2021 43:9, v. 43, p. 3351–3374, doi:10.1007/S10653-021-00862-W.

Khan, S., Anjum, R., Raza, S.T., Ahmed Bazai, N., and Ihtisham, M., 2022a, Technologies for municipal solid waste management: Current status, challenges, and future perspectives: Chemosphere, v. 288, p. 132403, doi:10.1016/J.CHEMOSPHERE.2021.132403.

Khan, A.H., López-Maldonado, E.A., Khan, N.A., Villarreal-Gómez, L.J., Munshi, F.M., Alsabhan, A.H., and Perveen, K., 2022b, Current solid waste management strategies and energy recovery in developing countries - State of art review: Chemosphere, v. 291, p. 133088, doi:10.1016/J.CHEMOSPHERE.2021.133088.

De Kleijne, K., Hanssen, S. V, Van Dinteren, L., Huijbregts, M.A.J., Van Zelm, R., and De Coninck, H., 2022, Limits to Paris compatibility of CO 2 capture and utilization: One Earth, v. 5, p. 168–185, doi:10.1016/j.oneear.2022.01.006.

Kumari, K., Kumar, S., Rajagopal, V., Khare, A., and Kumar, R., 2017, Emission from open burning of municipal solid waste in India: https://doi.org/10.1080/09593330.2017.1351489, v. 40, p. 2201–2214, doi:10.1080/09593330.2017.1351489.

Li, H., Li, X., Xiao, T., Chen, Y., Long, J., Zhang, G., Zhang, P., Li, C., Zhuang, L., and Li, K., 2018, Efficient removal of thallium(I) from wastewater using flower-like manganese dioxide coated magnetic pyrite cinder: Chemical Engineering Journal, v. 353, p. 867–877, doi:10.1016/J.CEJ.2018.07.169.

Liang, S., Chen, J., Guo, M., Feng, D., Liu, L., and Qi, T., 2020, Utilization of pretreated municipal solid waste incineration fly ash for cement-stabilized soil: Waste Management, v. 105, p. 425–432, doi:10.1016/J.WASMAN.2020.02.017.

Lieberman, R.N. et al., 2020, The geochemical evolution of brines from phosphogypsum deposits in Huelva (SW Spain) and its environmental implications: Science of the Total Environment, doi:10.1016/j.scitotenv.2019.134444.

Liu, N., and Cheng, J., 2019, Geochemical effects of cement mineral variations on water–rock–CO2 interactions in a sandstone reservoir as an experiment and modeling study: Greenhouse Gases: Science and Technology, v. 9, p. 789–810, doi:10.1002/GHG.1897.

Liu, Y., Guo, D., Dong, L., Xu, Y., and Liu, J., 2016, Pollution Status and Environmental Sound Management (ESM) Trends on Typical General Industrial Solid Waste: Procedia Environmental Sciences, v. 31, p. 615–620, doi:10.1016/J.PROENV.2016.02.111.

Liu, R., Jing, N., Song, Y., Zhai, Q., Mao, Z., Zhou, Y., and Sun, W., 2022, Recovery of valuable elements from pyrite pyrolysis slag using magnetic separation-flotation technique: Separation and Purification Technology, v. 299, p. 121772, doi:10.1016/J.SEPPUR.2022.121772.

Liu, B., Li, J., Wang, Z., Zeng, Y., and Ren, Q., 2020, Long-term leaching characterization and geochemical modeling of chromium released from AOD slag: Environmental Science and Pollution Research, v. 27, p. 921–929, doi:10.1007/S11356-019-07008-7/TABLES/3.

Liu, S., Wang, L., and Yu, B., 2019, Effect of modified phosphogypsum on the hydration properties of the phosphogypsum-based supersulfated cement: Construction and Building Materials, v. 214, p. 9–16,

doi:10.1016/j.conbuildmat.2019.04.052.

Lupsea, M., Tiruta-Barna, L., and Schiopu, N., 2014, Leaching of hazardous substances from a composite construction product – An experimental and modelling approach for fibre-cement sheets: Journal of Hazardous Materials, v. 264, p. 236–245, doi:10.1016/J.JHAZMAT.2013.11.017.

Ma, Z., Liu, G., Zhang, H., Zhang, S., and Lu, Y., 2021, Evaluation of pyrite cinders from sulfuric acid production as oxygen carrier for chemical looping combustion: Energy, v. 233, p. 121079, doi:10.1016/J.ENERGY.2021.121079.

Mahedi, M., Cetin, B., and Dayioglu, A.Y., 2020, Effect of cement incorporation on the leaching characteristics of elements from fly ash and slag treated soils: Journal of Environmental Management, v. 253, p. 109720, doi:10.1016/J.JENVMAN.2019.109720.

Malviya, R., and Chaudhary, R., 2006, Factors affecting hazardous waste solidification/stabilization: A review: Journal of Hazardous Materials, v. 137, p. 267–276, doi:10.1016/J.JHAZMAT.2006.01.065.

Martens, E., Jacques, D., Van Gerven, T., Wang, L., and Mallants, D., 2010, Geochemical modeling of leaching of Ca, Mg, Al, and Pb from cementitious waste forms: Cement and Concrete Research, v. 40, p. 1298–1305, doi:10.1016/J.CEMCONRES.2010.01.007.

Martens, E., Jacques, D., Van Gerven, T., Wang, L., and Mallants, D., 2008, PHREEQC modelling of leaching of major elements and heavy metals from cementitious waste forms, *in* Materials Research Society Symposium Proceedings, doi:10.1557/proc-1107-475.

Masindi, V., Ramakokovhu, M.M., Osman, M.S., and Tekere, M., 2021, Advanced application of BOF and SAF slags for the treatment of acid mine drainage (AMD): A comparative study: Materials Today: Proceedings, v. 38, p. 934–941, doi:10.1016/J.MATPR.2020.05.422.

Melki, S., and Gueddari, M., 2018, Impact Assessment of Phosphogypsum Leachate on Groundwater of Sfax-Agareb (Southeast of Tunisia): Using Geochemical and Isotopic Investigation: Journal of Chemistry, doi:10.1155/2018/2721752.

Minnu, S.N., Bahurudeen, A., and Athira, G., 2021, Comparison of sugarcane bagasse ash with fly ash and slag: An approach towards industrial acceptance of sugar industry waste in cleaner production of cement: Journal of Cleaner Production, v. 285, p. 124836, doi:10.1016/J.JCLEPRO.2020.124836.

Moharami, S., and Jalali, M., 2014a, Effect of TiO2, Al2O3, and Fe3O4 nanoparticles on phosphorus removal from aqueous solution: Environmental Progress and Sustainable Energy, doi:10.1002/ep.11917.

Moharami, S., and Jalali, M., 2014b, Phosphorus leaching from a sandy soil in the presence of modified and un-modified adsorbents: Environmental Monitoring and Assessment, doi:10.1007/s10661-014-3874-7.

Mosai, A.K., and Tutu, H., 2019, The effect of crop exudates and EDTA on cadmium adsorption by

agricultural podsolic soil: implications on groundwater: International Journal of Environmental Science and Technology, v. 16, p. 3071–3080, doi:10.1007/S13762-018-1927-0/FIGURES/6.

Naeem, I., Masood, N., Turan, V., and Iqbal, M., 2021, Prospective usage of magnesium potassium phosphate cement combined with Bougainvillea alba derived biochar to reduce Pb bioavailability in soil and its uptake by Spinacia oleracea L: Ecotoxicology and Environmental Safety, doi:10.1016/j.ecoenv.2020.111723.

Navarro, A., Cardellach, E., and Corbella, M., 2011, Immobilization of Cu, Pb and Zn in mine-contaminated soils using reactive materials: Journal of Hazardous Materials, v. 186, p. 1576–1585, doi:10.1016/J.JHAZMAT.2010.12.039.

Nizevičienė, D., Vaičiukynienė, D., Vaitkevičius, V., and Rudžionis, 2016, Effects of waste fluid catalytic cracking on the properties of semi-hydrate phosphogypsum: Journal of Cleaner Production, v. 137, p. 150–156, doi:10.1016/j.jclepro.2016.07.037.

Oliveira, M.L.S., Ward, C.R., Izquierdo, M., Sampaio, C.H., de Brum, I.A.S., Kautzmann, R.M., Sabedot, S., Querol, X., and Silva, L.F.O., 2012, Chemical composition and minerals in pyrite ash of an abandoned sulphuric acid production plant: Science of The Total Environment, v. 430, p. 34–47, doi:10.1016/J.SCITOTENV.2012.04.046.

Ölmez, H., and Erdem, E., 1989, The effects of phosphogypsum on the setting and mechanical properties of Portland cement and trass cement: Cement and Concrete Research, doi:10.1016/0008-8846(89)90027-6.

Omotoso, O.E., Ivey, D.G., and Mikula, R., 1998, Hexavalent chromium in tricalcium silicate: Part II Effects of CrVI on the hydration of tricalcium silicate: Journal of Materials Science 1998 33:2, v. 33, p. 515–522, doi:10.1023/A:1004356805022.

Ouhadi, V.R., Yong, R.N., and Deiranlou, M., 2021, Enhancement of cement-based solidification/stabilization of a lead-contaminated smectite clay: Journal of Hazardous Materials, v. 403, p. 123969, doi:10.1016/J.JHAZMAT.2020.123969.

Park, J.Y., Byun, H.J., Choi, W.H., and Kang, W.H., 2008, Cement paste column for simultaneous removal of fluoride, phosphate, and nitrate in acidic wastewater: Chemosphere, doi:10.1016/j.chemosphere.2007.09.012.

Parkhurst, D.L., and Appelo, C.A.J., 2013, Description of Input and Examples for PHREEQC Version 3 — A Computer Program for Speciation , Batch-Reaction , One-Dimensional Transport , and Inverse Geochemical Calculations.: U.S. Geological Survey Techniques and Methods, book 6, chapter A43,.

Parkhurst, D.L., and Wissmeier, L., 2015, PhreeqcRM: A reaction module for transport simulators based on the geochemical model PHREEQC: Advances in Water Resources, v. 83, p. 176–189, doi:10.1016/J.ADVWATRES.2015.06.001.

Pedersen, K.B., Jensen, P.E., Ottosen, L.M., and Barlindhaug, J., 2018, Influence of electrode placement for mobilising and removing metals during electrodialytic remediation of metals from shooting range soil: Chemosphere, v. 210, p. 683–691, doi:10.1016/J.CHEMOSPHERE.2018.07.063.

Pietrzak, D., 2021, Modeling migration of organic pollutants in groundwater — Review of available software: Environmental Modelling & Software, v. 144, p. 105145, doi:10.1016/J.ENVSOFT.2021.105145.

Potgieter, J.H., Potgieter, S.S., McCrindle, R.I., and Strydom, C.A., 2003, An investigation into the effect of various chemical and physical treatments of a South African phosphogypsum to render it suitable as a set retarder for cement: Cement and Concrete Research, v. 33, p. 1223–1227, doi:10.1016/S0008-8846(03)00036-X.

Praveenkumar, T.R., Manigandan, S., Gemede, H.F., Prabu, V., Balamoorthy, D., Tadesse, G., and Rath, B., 2021, Effective utilization of waste textile sludge composite with Al2O3 nanoparticles as a value-added application: Applied Nanoscience (Switzerland), v. 1, p. 1–11, doi:10.1007/S13204-021-02001-4/FIGURES/5.

Pyo, J.Y., Um, W., and Heo, J., 2021, Magnesium potassium phosphate cements to immobilize radioactive concrete wastes generated by decommissioning of nuclear power plants: Nuclear Engineering and Technology, v. 53, p. 2261–2267, doi:10.1016/J.NET.2021.01.005.

Rashad, A.M., 2017, Phosphogypsum as a construction material: Journal of Cleaner Production, v. 166, p. 732–743, doi:10.1016/j.jclepro.2017.08.049.

Saadaoui, E., Ghazel, N., Ben Romdhane, C., and Massoudi, N., 2017, Phosphogypsum: potential uses and problems–a review: International Journal of Environmental Studies, doi:10.1080/00207233.2017.1330582.

Sachs, J.D., Schmidt-Traub, G., Mazzucato, M., Messner, D., Nakicenovic, N., and Rockström, J., 2019, Six Transformations to achieve the Sustainable Development Goals: Nature Sustainability 2019 2:9, v. 2, p. 805–814, doi:10.1038/s41893-019-0352-9.

Schnell, M., Horst, T., and Quicker, P., 2020, Thermal treatment of sewage sludge in Germany: A review: Journal of Environmental Management, v. 263, p. 110367, doi:10.1016/J.JENVMAN.2020.110367.

Scholz, R.W., Ulrich, A.E., Eilittä, M., and Roy, A., 2013, Sustainable use of phosphorus: A finite resource: Science of The Total Environment, v. 461–462, p. 799–803, doi:10.1016/j.scitotenv.2013.05.043.

Shen, W., Cao, L., Li, Q., Wen, Z., Wang, J., Liu, Y., Dong, R., Tan, Y., and Chen, R., 2016, Is magnesia cement low carbon? Life cycle carbon footprint comparing with Portland cement: Journal of Cleaner Production, v. 131, p. 20–27, doi:10.1016/J.JCLEPRO.2016.05.082.

Siddique, R., 2011, Utilization of silica fume in concrete: Review of hardened properties: Resources, Conservation and Recycling, v. 55, p. 923–932, doi:10.1016/J.RESCONREC.2011.06.012.

Singh, M., Garg, M., and Rehsi, S.S., 1993, Purifying phosphogypsum for cement manufacture: Construction and Building Materials, doi:10.1016/0950-0618(93)90018-8.

Singh, M., Garg, M., Verma, C.L., Handa, S.K., and Kumar, R., 1996, An improved process for the purification of phosphogypsum: Construction and Building Materials, v. 10, p. 597–600, doi:10.1016/S0950-0618(96)00019-0.

Singh, T.S., and Pant, K.K., 2006, Solidification/stabilization of arsenic containing solid wastes using portland cement, fly ash and polymeric materials: Journal of Hazardous Materials, v. 131, p. 29–36, doi:10.1016/J.JHAZMAT.2005.06.046.

Skibsted, J., and Snellings, R., 2019, Reactivity of supplementary cementitious materials (SCMs) in cement blends: Cement and Concrete Research, v. 124, p. 105799, doi:10.1016/J.CEMCONRES.2019.105799.

Soares, J.R., Cantarella, H., and Menegale, M.L. de C., 2012, Ammonia volatilization losses from surface-applied urea with urease and nitrification inhibitors: Soil Biology and Biochemistry, v. 52, p. 82–89, doi:10.1016/j.soilbio.2012.04.019.

Solpuker, U., Sheets, J., Kim, Y., and Schwartz, F.W., 2014, Leaching potential of pervious concrete and immobilization of Cu, Pb and Zn using pervious concrete: Journal of Contaminant Hydrology, doi:10.1016/j.jconhyd.2014.03.002.

Song, B., Zeng, Z., Almatrafi, E., Shen, M., Xiong, W., Zhou, C., Wang, W., Zeng, G., and Gong, J., 2022, Pyrite-mediated advanced oxidation processes: Applications, mechanisms, and enhancing strategies: Water Research, v. 211, p. 118048, doi:10.1016/J.WATRES.2022.118048.

Soriano-Disla, J.M., Spille, U., Gabarrón, M., Faz, Á., and Acosta, J.A., 2018, Evaluation of strategies for mitigating risks associated with metals in pyrite ash: Journal of Environmental Management, doi:10.1016/j.jenvman.2018.03.104.

Sun, Z., Vollpracht, A., and van der Sloot, H.A., 2019, pH dependent leaching characterization of major and trace elements from fly ash and metakaolin geopolymers: Cement and Concrete Research, v. 125, p. 105889, doi:10.1016/J.CEMCONRES.2019.105889.

Sun, J., Wang, L., Yu, J., Guo, B., Chen, L., Zhang, Y., Wang, D., Shen, Z., and Tsang, D.C.W., 2022, Cytotoxicity of stabilized/solidified municipal solid waste incineration fly ash: Journal of Hazardous Materials, v. 424, p. 127369, doi:10.1016/J.JHAZMAT.2021.127369.

Taher, M.A., 2007, Influence of thermally treated phosphogypsum on the properties of Portland slag cement: Resources, Conservation and Recycling, v. 52, p. 28–38, doi:10.1016/j.resconrec.2007.01.008.

Tayibi, H., Choura, M., López, F.A., Alguacil, F.J., and López-Delgado, A., 2009, Environmental impact and management of phosphogypsum: Journal of Environmental Management, v. 90, p. 2377–2386, doi:10.1016/j.jenvman.2009.03.007.

Tian, T., Yan, Y., Hu, Z., Xu, Y., Chen, Y., and Shi, J., 2016, Utilization of original phosphogypsum for the preparation of foam concrete: Construction and Building Materials, v. 115, p. 143–152, doi:10.1016/j.conbuildmat.2016.04.028.

Tiruta-Barna, L., 2008, Using PHREEQC for modelling and simulation of dynamic leaching tests and scenarios: Journal of Hazardous Materials, v. 157, p. 525–533, doi:10.1016/J.JHAZMAT.2008.01.028.

Tiwari, M.K., Bajpai, S., Dewangan, U.K., and Tamrakar, R.K., 2015, Suitability of leaching test methods for fly ash and slag: A review: Journal of Radiation Research and Applied Sciences, v. 8, p. 523–537, doi:10.1016/J.JRRAS.2015.06.003.

Tomaszewska, B., Kmiecik, E., Wątor, K., and Tyszer, M., 2018, Use of numerical modelling in the prediction of membrane scaling. Reaction between antiscalants and feedwater: Desalination, v. 427, p. 27–34, doi:10.1016/J.DESAL.2017.11.004.

Valero, M.C., Raybaud, P., and Sautet, P., 2006, Influence of the hydroxylation of γ-Al2O3 surfaces on the stability and diffusion of single Pd atoms: A DFT study: Journal of Physical Chemistry B, doi:10.1021/jp0554240.

Vega-Garcia, P., Schwerd, R., Schwitalla, C., Johann, S., Scherer, C., and Helmreich, B., 2021, Leaching prediction for vertical test panels coated with plaster and mortars exposed under real conditions by a PHREEQC leaching model: Chemosphere, v. 280, p. 130657, doi:10.1016/J.CHEMOSPHERE.2021.130657.

Vergara, S.E., and Tchobanoglous, G., 2012, Municipal Solid Waste and the Environment: A Global Perspective: Annual Review of Environment and Resources, v. 37, p. 277–309, doi:10.1146/ANNUREV-ENVIRON-050511-122532.

Vespa, M., Dähn, R., and Wieland, E., 2014, Competition behaviour of metal uptake in cementitious systems: An XRD and EXAFS investigation of Nd- and Zn-loaded 11 Å tobermorite: Physics and Chemistry of the Earth, Parts A/B/C, v. 70–71, p. 32–38, doi:10.1016/J.PCE.2014.01.001.

Villalba, G., Liu, Y., Schroder, H., and Ayres, R.U., 2008, Global Phosphorus Flows in the Industrial Economy From a Production Perspective: Journal of Industrial Ecology, v. 12, p. 557–569, doi:10.1111/J.1530-9290.2008.00050.X.

Walling, S.A., and Provis, J.L., 2016, Magnesia-Based Cements: A Journey of 150 Years, and Cements for the Future? Chemical Reviews, v. 116, p. 4170–4204, doi:10.1021/ACS.CHEMREV.5B00463/ASSET/IMAGES/LARGE/CR-2015-00463S_0024.JPEG.

Wang, J., 2020, Utilization effects and environmental risks of phosphogypsum in agriculture: A review: Journal of Cleaner Production, doi:10.1016/j.jclepro.2020.123337.

Wang, D.L., Chen, M.L., and Tsang, D.D.C.W., 2020a, Green remediation by using low-carbon cement-based stabilization/solidification approaches: Sustainable Remediation of Contaminated Soil and

Groundwater, p. 93–118, doi:10.1016/B978-0-12-817982-6.00005-7.

Wang, S., Jin, H., Deng, Y., and Xiao, Y., 2021, Comprehensive utilization status of red mud in China: A critical review: Journal of Cleaner Production, v. 289, p. 125136, doi:10.1016/J.JCLEPRO.2020.125136.

Wang, H., Ju, C., Zhou, M., Chen, J., Dong, Y., and Hou, H., 2022a, Sustainable and efficient stabilization/solidification of Pb, Cr, and Cd in lead-zinc tailings by using highly reactive pozzolanic solid waste: Journal of Environmental Management, v. 306, p. 114473, doi:10.1016/J.JENVMAN.2022.114473.

Wang, Z., and Sohn, I., 2021, Understanding the solidification and leaching behavior of synthesized Cr-containing stainless steel slags with varying Al2O3/SiO2 mass ratios: Ceramics International, v. 47, p. 10918–10926, doi:10.1016/J.CERAMINT.2020.12.211.

Wang, X., Wang, L., Qi, Y., and Chen, J., 2022b, Sustainable stabilization/solidification of mine wastes: Low Carbon Stabilization and Solidification of Hazardous Wastes, p. 227–242, doi:10.1016/B978-0-12-824004-5.00009-8.

Wang, D., Wang, Q., and Xue, J., 2020b, Reuse of hazardous electrolytic manganese residue: Detailed leaching characterization and novel application as a cementitious material: Resources, Conservation and Recycling, v. 154, p. 104645, doi:10.1016/J.RESCONREC.2019.104645.

Wang, L., Yu, K., Li, J.S., Tsang, D.C.W., Poon, C.S., Yoo, J.C., Baek, K., Ding, S., Hou, D., and Dai, J.G., 2018, Low-carbon and low-alkalinity stabilization/solidification of high-Pb contaminated soil: Chemical Engineering Journal, v. 351, p. 418–427, doi:10.1016/j.cej.2018.06.118.

Wang, L., Zhang, Y., and Tsang, D.C.W., 2022c, Future research directions for sustainable remediation: Low Carbon Stabilization and Solidification of Hazardous Wastes, p. 555–564, doi:10.1016/B978-0-12-824004-5.00013-X.

Watari, T., Cao, Z., Hata, S., and Nansai, K., 2022, Efficient use of cement and concrete to reduce reliance on supply-side technologies for net-zero emissions: Nature Communications 2022 13:1, v. 13, p. 1–9, doi:10.1038/s41467-022-31806-2.

Wątor, K., Dobrzyński, D., Sugimori, K., and Kmiecik, E., 2020, Redox potential research in the field of balneochemistry: case study on equilibrium approach to bioactive elements in therapeutic waters: International Journal of Biometeorology, v. 64, p. 815–826, doi:10.1007/S00484-020-01871-7/FIGURES/5.

Wu, R.J., and Liu, J.C., 2018, Removal of Phosphate Using Ettringite Synthesized from Industrial By-products: Water, Air, and Soil Pollution, doi:10.1007/s11270-018-3828-8.

Wu, F., Liu, S., Qu, G., Chen, B., Zhao, C., Liu, L., Li, J., and Ren, Y., 2022, Highly targeted solidification behavior of hazardous components in phosphogypsum: Chemical Engineering Journal Advances, v.

9, p. 100227, doi:10.1016/J.CEJA.2021.100227.

Xia, M., Muhammad, F., Zeng, L., Li, S., Huang, X., Jiao, B., Shiau, Y.C., and Li, D., 2019, Solidification/stabilization of lead-zinc smelting slag in composite based geopolymer: Journal of Cleaner Production, v. 209, p. 1206–1215, doi:10.1016/J.JCLEPRO.2018.10.265.

Xiong, X. et al., 2019, Potentially toxic elements in solid waste streams: Fate and management approaches: Environmental Pollution, v. 253, p. 680–707, doi:10.1016/J.ENVPOL.2019.07.012.

Xu, Z., Wan, Z., Sun, Y., Cao, X., Hou, D., Alessi, D.S., Ok, Y.S., and Tsang, D.C.W., 2021, Unraveling iron speciation on Fe-biochar with distinct arsenic removal mechanisms and depth distributions of As and Fe: Chemical Engineering Journal, v. 425, p. 131489, doi:10.1016/J.CEJ.2021.131489.

Xue, Y., and Liu, X., 2021, Detoxification, solidification and recycling of municipal solid waste incineration fly ash: A review: Chemical Engineering Journal, v. 420, p. 130349, doi:10.1016/J.CEJ.2021.130349.

Yan, W., Hu, S., and Jing, C., 2012, Enrofloxacin sorption on smectite clays: Effects of pH, cations, and humic acid: Journal of Colloid and Interface Science, v. 372, p. 141–147, doi:10.1016/J.JCIS.2012.01.016.

Yang, Z., Sui, S., Wang, L., Feng, T., Gao, Y., Mu, S., Tang, L., and Jiang, J., 2020, Improving the chloride binding capacity of cement paste by adding nano-Al2O3: The cases of blended cement pastes: Construction and Building Materials, doi:10.1016/j.conbuildmat.2019.117219.

Yang, J., Zeng, J., He, X., Zhang, Y., Su, Y., and Tan, H., 2022, Sustainable clinker-free solid waste binder produced from wet-ground granulated blast-furnace slag, phosphogypsum and carbide slag: Construction and Building Materials, v. 330, p. 127218, doi:10.1016/J.CONBUILDMAT.2022.127218.

Yang, L., Zhang, Y., and Yan, Y., 2016, Utilization of original phosphogypsum as raw material for the preparation of self-leveling mortar: Journal of Cleaner Production, v. 127, p. 204–213, doi:10.1016/j.jclepro.2016.04.054.

Zapata, J.F., Azevedo, A., Fontes, C., Monteiro, S.N., and Colorado, H.A., 2022, Environmental Impact and Sustainability of Calcium Aluminate Cements: Sustainability 2022, Vol. 14, Page 2751, v. 14, p. 2751, doi:10.3390/SU14052751.

Zeng, Y., Trauth, K.M., Peyton, R.L., and Banerji, S.K., 2005, Characterization of solid waste disposed at Columbia Sanitary Landfill in Missouri: Waste Management and Research, v. 23, p. 62–71, doi:10.1177/0734242X05050995.

Zhang, H., Chen, G., Cai, X., Fu, J., Liu, M., Zhang, P., and Yu, H., 2021, The leaching behavior of copper and iron recovery from reduction roasting pyrite cinder: Journal of Hazardous Materials, v. 420, p. 126561, doi:10.1016/J.JHAZMAT.2021.126561.

Zhang, Y., Ong, Y.J., and Yi, Y., 2022, Comparison between CaO- and MgO-activated ground granulated

blast-furnace slag (GGBS) for stabilization/solidification of Zn-contaminated clay slurry: Chemosphere, v. 286, p. 131860, doi:10.1016/J.CHEMOSPHERE.2021.131860.

Zhang, F., Wang, Q., Hong, J., Chen, W., Qi, C., and Ye, L., 2017, Life cycle assessment of diammonium- and monoammonium-phosphate fertilizer production in China: Journal of Cleaner Production, doi:10.1016/j.jclepro.2016.09.107.

Chapter 2

The leaching behaviors of potentially toxic lead, zinc, and sulfate in the pyrite ash: mineralogical assessments and environmental implications

Yikai Liu[1]; Simone Molinari[1,*]; Maria Chiara Dalconi[1]; Luca Valentini[1]; Giulia Ricci[1]; Claudio Carrer[2]; Giorgio Ferrari[3]; Gilberto Artioli[1]

[1] *Department of Geosciences and CIRCe Centre, University of Padua, via G. Gradenigo 6, 35129, Padua, Italy*

[2] *Magistrato alle Acque di Venezia Ufficio Tecnico Antinquinamento Laboratorio CSMO, Padova, Italy*

[3] *Mapei S.p.A., via Cafiero 22, 20158, Milan, Italy*

Graphical abstract

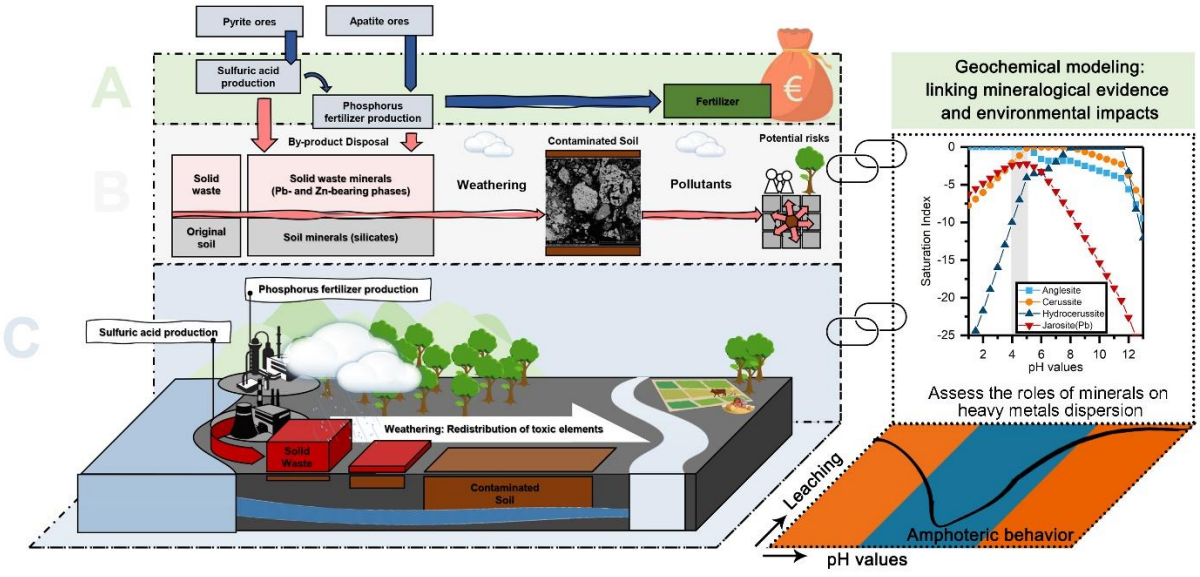

This manuscript is under review in Chemosphere

Abstract

High mobility of hazardous elements in pyrite ash can threaten the environment and human health. To avoid any inadvertent exposure, it is crucial to monitor the tendency of contaminant accumulation in the soil through adsorption, absorption, and precipitation. This study aims to profoundly investigate the critical role of soil mineralogy in contaminants release and to predict the geochemical behavior of toxic elements by exploiting the potential of the modeling approach. The investigated soil comes from a brownfield site devoted to fertilizers production. Hematite, jarosite, and gypsum are the major mineralogical phases. Zinc sulfate, anglesite, kintoreite, and Pb-bearing jarosite were identified as the dominant Pb and Zn phases. pH-dependent leaching tests in combination with geochemical modeling were used to reveal the potential leaching mechanisms and contaminants solubility-controlling phases at pH values ranging from 1 to 13. The experimental results demonstrated that Pb and Zn have an amphoteric leaching behavior, with the lowest leached concentrations presented at the pH value of 9.0, which are 0.38 and 0.03 μmol/L, respectively. The integrated geochemical analysis also ascertained a downward trend of leached concentrations towards the neutral/alkaline region around pH values from 8.0 to 10.0. The calculated saturation indexes suggest that Pb retention is controlled by anglesite, cerussite, and hydrocerussite. Zn retention is attributed to zinc carbonates and hydroxides. Further, jarosite and ferrihydrite may play a role in Pb and Zn retention. Overall, the geochemical modeling demonstrates an acceptable ability to simulate potentially toxic elements leaching and provides essential information to adequately manage present and historical pyrite ash disposal sites.

Keywords

pyrite ash, potentially toxic elements, solid waste, pH-dependent leaching, geochemical modeling

1. Introduction

Over the past decades, as a consequence of fast rates of urbanization and industrialization, the discharged potentially toxic elements (PTEs)-containing solid waste have been proven detrimental to soil health (Filippelli et al., 2012). The biological and geochemical cycles may play a critical role in the abundance and redistribution of PTEs in the stockpile sites, with the most commonly encountered trace metal contaminations, including Cd, As, Pb, and Zn, as well as sulfates (Abollino et al., 2002; Hou et al., 2020). The former may cause serious neurological diseases and life-threatening cancers (Hou et al., 2020), whereas the sulfate ions may cause taste impairment and laxative effects (Torres-Martínez et al., 2020). Noteworthy, many solid waste storage sites, such as pyrite ash (Oliveira et al., 2012), phosphogypsum (Bisone et al., 2017), and fly ash (Jambhulkar et al., 2018) stockpile regions, are generally more vulnerable because of their location (situated near sensitive aquatic ecosystems) and unstable nature (Hou et al., 2020). Although

many in- or ex-situ attempts have been adopted to limit and prevent the mobility of these toxic elements, finding applicable management options and overcoming the technical limits is still a challenge due to the presence of impurities which may deteriorate the properties and shorten the service life of the immobilized products (Kumpiene et al., 2019; Palansooriya et al., 2020). For instance, the presence of Pb and Zn is known for its negative influence on the rate of hydration in cementitious systems (Contessi et al., 2020). Hence, waste stockpiling is still a prevalent method that is still massively used in all countries, but the associated problems, including the degradation of soil and the resultant loss of crop yield, have aroused great concern in society (Hou et al., 2020). Previous publications suggest that over 340,000 contaminated sites in Europe require immediate treatment, with the most frequent contaminants being trace metals and mineral oils (Agnello et al., 2016; Ausili et al., 2020). Meanwhile, previous studies have confirmed that the deposited trace metals-bearing particulates would generate varied mineralogical structures containing sulfides, oxides, and silicates, during the stockpiling process, which are driven by the factors such as seasonal wet-dry cycles, geogenic differences, and anthropogenic activities (Hou et al., 2020; Obeng-Gyasi et al., 2021). Such processes tend to induce the trace metals to reach a dynamic equilibrium, with the bulk of trace metals may persist in the solid phases of the pedosphere for extended periods due to most of the trace metals remaining non-biodegradable in the soil (Tuhý et al., 2020; Kang et al., 2021; Izydorczyk et al., 2021). For example, Contessi et al. (2020) found that lead (Pb) in the pyrite ash disposal sites is likely to be hosted in the form of anglesite ($PbSO_4$) because of weathering-induced oxidation. Compared with pyrite, which is a relatively resistant mineral to both acidic and alkaline attacks, the oxidized products would promote the leaching and mobility of Pb. Fazle Bari et al. (2021) illustrated that the formation of tooeleite ($Fe_6(AsO_3)_4(SO_4)(OH)_4 \cdot 4H_2O$), identified as the dominant arsenic (As) containing minerals in abandoned mine soils, might enhance the solubility of As. Also, in the lead/zinc (Pb/Zn) smelter-contaminated soil, Zn incorporation into apatite ($Ca_5(PO_4)_3OH$), wollastonite ($CaSiO_3$), and kaolinite ($Al_2Si_2O_5(OH)_4$) structures and/or precipitated as pyroxene ($XY(Si, Al)_2O_6$, X represents Ca, Na, Fe, Mg, and Zn and Y represents ions of smaller size) and zinc oxide (ZnO) was observed (Xu et al., 2022). Therefore, contaminated soil can not only be considered a sink, but a source of pollution with a great potential to transfer pollutants to the groundwater, the food chain, and the human body (Poggio et al., 2009). Before deploying remediation technologies, it is crucial to study the origin and fate of PTEs in dynamic environmental conditions (Rakotonimaro et al., 2021).

To achieve this goal, detailed characterizations are necessary prerequisites to provide a fundamental understanding of the fate of hazardous contaminants. Concurrently, many laboratory works have been carried out to fill the knowledge gap in the mineralogy and chemistry of phases incorporating contaminants (Gabarrón et al., 2018; Deng et al., 2020; Xu et al., 2022). With the scope of simplifying the analysis process, some works attempted to use the experimental datasets required in prior literature to reconstruct the

transformation by simplified artificial systems (Zhou et al., 2020; Tabelin et al., 2020; Contessi et al., 2021), but the extrapolation from the laboratory findings to the real cases is usually far from satisfactory. Another major limitation is the detection limit of the routinely employed analytical techniques (Khan et al., 2020) (e.g., the XRD technique is not sensitive to trace elements in solid-solution phases or to ionic species adsorbed on mineral surfaces). Therefore, individual analytical methods are not always suitable or sufficient for overall knowledge of the fate and long-term behavior of mineral phases controlling toxic elements released in such a complex pollutants-soil system, especially since this dual system will suffer complex environmental impacts (Guo et al., 2020; Pękala and Musiał, 2021). Geochemical simulations could be the key to overcome the complexity of linking the potential release of hazardous chemical constituents with soil mineralogical and deeply understanding long-term environmental impacts that affect surrounding groundwater. Currently, several attempts have been conducted to explore how mineralogical factors control the leaching behaviors of toxic elements. In Bisone et al.'s work (2017), a geochemical assessment was used to characterize the spatial variability of toxic elements in stocked phosphogypsum at varying time and pH values. Other researchers also tried to reconstruct the leaching profiles of metals (e.g., Pb, Zn, Cu, and As) as a function of pH values (Cappuyns et al., 2014; Helser et al., 2022). The above geochemical assessments of leaching showed good consistency with experiments, but it is not a common practice to perform the geochemical modeling construction based on the bulk experimental characterization (e.g., XRD), even though this mineralogical information is of paramount importance in determining which minerals dissolved during the leaching procedures. Therefore, in this study, we tend to explore the role of dissolving/precipitating mineralogical phases through the bulk XRD characterization, which is a missing key element in understanding the factors controlling the dispersion of contaminants and overcoming the limitations of the demanding experimental procedures (Dijkstra et al., 2019; Wei et al., 2021).

The objective of the present study is to contribute to the knowledge of pH-dependent leaching characteristics and associated mineralogical information of Pb and Zn-rich pyrite ash. The chemical and mineralogical compositions of the pyrite ash were first characterized through a multi-technique approach based on XRD, XRF, SEM/EDS, and Raman analyses. Afterward, the pH-dependent leaching of hazardous (Pb, Zn, and sulfate) and major elements (Fe) was explicitly studied in the pH range of 1.02-12.02. In order to elucidate the impacts of mineralogical compositions on the partitioning of chemical species between the solid and aqueous phases at different pH values, geochemical modeling was performed to predict the leaching behavior. Meanwhile, the leaching residues were analyzed to give corroborating insight into the predominant solubility-controlling mechanisms. The combination of traditional characterization approaches with geochemical modeling may be helpful to better understand the influence of different parameters on environmental risks and provide a reliable, low-cost, and much less time-consuming instrument to evaluate suitable remediation and management techniques for pyrite ash disposal.

2. Materials and methods

2.1. Sampling process

The soil used in this work was excavated from an abandoned fertilizer production facility in Italy, which is now used as a storage site for the solid waste generated by pyrite roasting, sulfuric acid production, and phosphorus-based fertilizer production. The pyrite ash was collected following a systematic sampling grid from the surface to a 2.5 m depth covering the whole area of around 0.11 km^2. In this work, the soil was mainly composed of black pyrite ashes. The soil sample was placed in a polyethylene bag and then transported to the laboratory. Then the sample was air-dried, ground, and passed through a 2 mm mesh sieve prior to the following characterization experiments. The soil moisture content was calculated by drying the soil in an oven a 105 °C ± 5 °C according to UNI 12457-4:2004 (British Standards Institution, 2004) and resulted below 1 %.

2.2. Characterization methods

Prior to characterization, the sieved soil was divided by using coning and quartering to obtain a representative sample. The solid sample was digested following the procedure reported by (Bettiol et al., 2008). HF, HNO_3, HCl, and H_3BO_3 (AppliChem GmbH, Darmstadt, Germany) were used at high purity levels for trace metal analyses. Before the XRD analysis, the divided fraction was ground in an agate mortar and then micronized for 10 mins (McCrone micronizing mill, RETSCH Inc., Haan, Germany) in order to reduce the effect of the preferred crystallographic orientation (Gliozzo et al., 2009). The mineralogical composition of the micronized sample was determined by XRD Rietveld analysis (Rietveld, 1969). Diffraction measurements were performed using a Malvern Panalytical X'Pert Pro diffractometer operating in Bragg-Brentano geometry. The instrument setup is provided in Table.S1. Diffraction data were acquired from 3° to 84° 2θ, with a step interval of 0.017° and an equivalent counting time of 100 s per step. Known amounts of ZnO (ACS Reagent, Thermo Fisher Scientific Inc., Waltham, USA) were homogeneously mixed with the samples as an internal standard. Qualitative and quantitative analyses of the collected XRD patterns were executed using Highscore Plus and Profex (Doebelin and Kleeberg, 2015). The elemental composition of collected pyrite ash was determined with XRF (PW1480, Philips, USA). SEM/EDS investigation (CamScan MX3000, Applied Beams, USA) was performed on the polished and carbon-coated sections of pyrite ash. Detailed Raman investigation (DXR Raman microscope, Thermo Electron, USA) was conducted with a laser operating at 532 nm.

2.3. pH-dependent leaching tests

The pH-dependent leaching tests were performed on the sieved soil following the EN 14429:2015 (British Standards Institution, 2015) standard, consisting of a series of parallel batch extractions tests with

increasing pH values. The analytical reagent nitric acid (HNO_3) or sodium hydroxide (NaOH) was used to adjust the pH values of the leachate. The amount of used HNO_3 and NaOH are given in Fig.S3. Eluates were filtered at 0.45 μm and analyzed by inductively coupled plasma mass spectrometry (ELAN DRC II, Perkin, Elmer), atomic absorption spectrophotometry with flame (Varian, SpectrAA 220FS), and flameless atomization (Varian SpectrAA 240Z). The certified standard NIST-SRM 2711a (Montana II Soil) from NIST (National Institute of Standards and Technology, Gaithersburg, MD, USA) was used to validate the analytical methodology. All analyses were performed in triplicate.

2.4. Geochemical modeling

Geochemical simulations were conducted using the software PHREEQC (Parkhurst and Appelo, 2013) with two thermodynamic databases from MINTEQ (Gustafsson, 2011) and Lawrence Livermore National Laboratory (LLNL). The initial mineralogical input was based on XRD quantification and SEM/EDS characterization. Besides, additional mineral assemblages were given according to previous literature. The description of the initial input data is shown in Table.S2. The calculations (pH values range from 1~13) were based on the pH-dependent leaching tests, using NaOH and HNO_3 as the pH control agents. Meanwhile, the soil XRD result obtained was used as a starting point to select the set of mineral phases to take into account in the modeling approach. The XRD characterizations of the residues were used to constrain the maximum amount of minerals that can dissolve (Dijkstra et al., 2006; Bernasconi et al., 2022). Based on the quantification results of the residues at the overall pH range, the maximum amount of jarosite that would participate in the dissolution process was predictably assumed as 40 wt%.

3. Results

3.1. Characterization of the pyrite ash

The XRD mineralogical investigation (Fig.1) illustrates that hematite (Fe_2O_3) is the main crystalline phase present in the sample, with a concentration of 72.0 wt%. The high content of hematite is consistent with the findings of previous works on soils sampled in pyrite ash disposal sites (Oliveira et al., 2012; Contessi et al., 2020). The Pb-containing minerals are identified as anglesite (0.6 wt%) and kintoreite ($PbFe_3(PO_4)(SO_4)(OH)_6$, 1.7 wt%). The other observed minerals are mainly sulfates and silicates: gypsum ($CaSO_4 \cdot 2H_2O$, 15.3 wt%), jarosite ($KFe_3(SO_4)_2(OH)_6$, 7.6 wt%), and quartz (SiO_2, 2.8 wt%). The chemical composition from the XRF (Table.S3) shows Fe_2O_3 (83.1 wt%), CaO (8.6 wt%), and SiO_2 (6.4 wt%) as major elements, which validates the XRD characterization as the hematite, gypsum, and quartz being the principal components. The detected P_2O_5 (0.5 wt%) and K_2O (0.2 wt%) agree with the presence of kintoreite and jarosite. Minor contents of Al_2O_3 and Na_2O can be related to the clay minerals from the soil. The trace metal content of the collected sample is presented in Table.S4, showing a very high concentration of Pb

(11910 ± 714 mg/kg) and a minor content of Zn (582 ± 43 mg/kg).

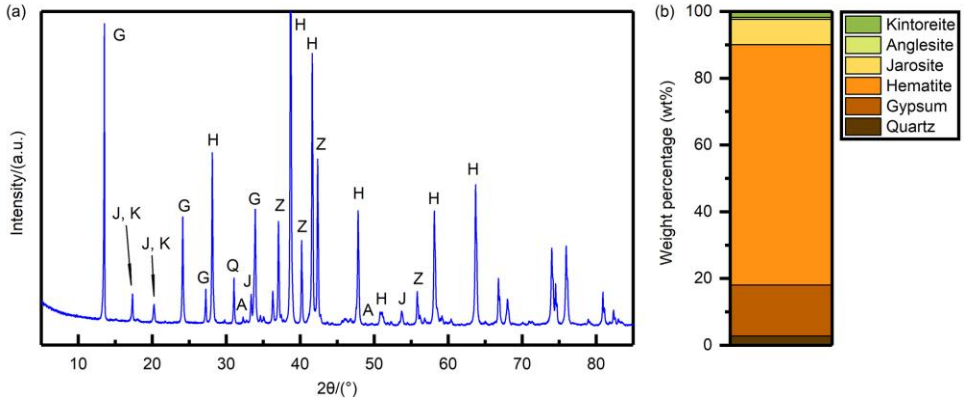

Figure.1. XRD pattern (a) and quantification results of studied soil (b). A: anglesite, G: gypsum, H: hematite, J: jarosite, K: kintoreite, Q: quartz, and Z: zincite (internal standard).

The SEM images (Fig.2a, b, and c) further evidence the presence of hematite, jarosite, gypsum, quartz, and anglesite. Besides forming sparingly soluble anglesite at acidic conditions, Pb was found in complex exsolution/intergrowths textures in amorphous Fe oxide phases (Fig.2d and e) and incorporated in the Fe-K-S-Pb oxide rims in a compact form along the edges of the structures (Fig.2f and g). A previous study also characterized the incorporation of Pb to Fe oxide phases (Contessi et al., 2020), and an adsorption mechanism was accordingly given to explain this observation. Therefore, the presence of Fe-K-S-Pb oxide rims could imply Pb incorporation within the jarosite crystal structure (Aguilar-Carrillo et al., 2018a; Shi et al., 2022). In addition, the fate of Zn was related to the formation of sulfur minerals, as a Zn-Fe-S assemblage was observed in Fig.2i. But as a minor component, it is hard to assess the exact origins of this assemblage, which could represent a residue of the primary ore or a precipitated secondary phase. To analyze the Pb distribution mechanisms in the pyrite ash, Raman spectroscopy was used to examine the area with high Pb concentration presented in Fig.2d and g. In addition to hematite (Fig.3a and b) confirmed by previous XRD, the Raman spectra show the presence of clear vibration bands that can be associated with different Pb-containing phases (Table.S5). In Fig.3c, the sulfate anion is characterized by the bands at 1160, 1100, 1004, 620, and 437 cm^{-1} (Frost et al., 2006b). The bands at 976, 557, and 335 cm^{-1} are assigned to the vibration of PO_4^{3-} (Frost et al., 2006a). Although previous studies have reported that four sharp bands can be observed at the wavenumber range from 420 to 480 cm^{-1} due to the ν_2 PO_4^{3-} bending modes, these bending modes could suffer the influence of overlap (Frost et al., 2006b). Hence the Pb concentrated area in Fig.2d and Fig.3a implies the presence of kintoreite. Whereas the band positions given in Fig.3b and d showed almost no changes to the standard K-jarosite (Frost et al., 2005). It is probable that the low concentration of Pb ions incorporated into the structure and the multiple overlapping bands due to the complexity of jarosite prevent any significant band shift related to Pb incorporation into jarosite (Frost et

al., 2006b; Chen et al., 2021).

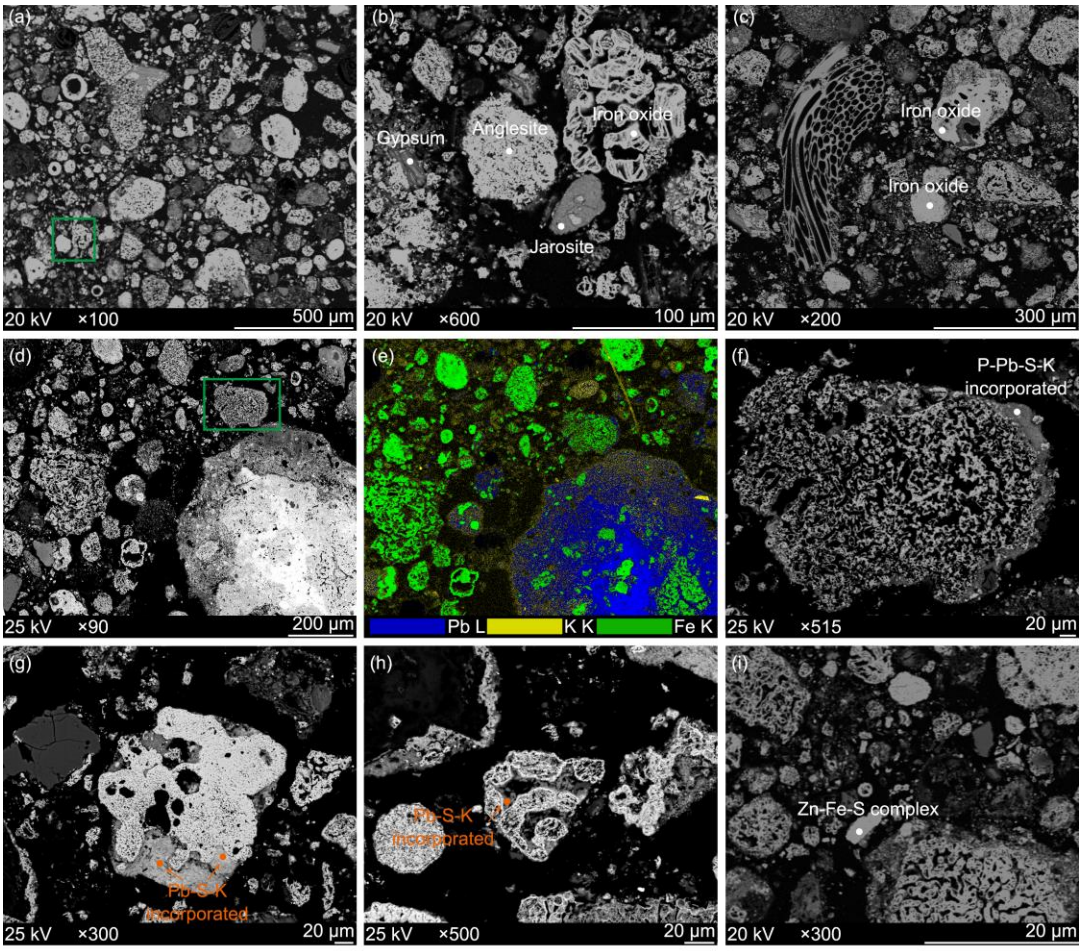

Figure.2. SEM micrographs of the sample. (a) backscattered scanning electron (BSE) microscopy image of pyrite ash; (b) BSE image showing the presence of anglesite;(c) BSE image implies the iron oxide; (d) BSE image demonstrates the distribution of Pb; (d) elemental mapping of lead, potassium, and iron attributing to image d; (f) the magnified BSE image corrected to the green rectangle marked area in image d, indicating a Pb-incorporated structure; (g) and (h) the compacted Pb-bearing assemblages; and (i) BSE image shows the Zn-Fe-sulfate assemblage.

In addition, another study has shown that incorporating Pb will significantly broaden the bandwidths of peaks at 1000 and 1005 cm^{-1} and raise three split bending modes at the low-wavenumber region (approximately at 436, 452, and 476 cm^{-1}) (Sasaki1 et al., 1998). However, these abovementioned vibration modes promiscuously overlapped with the SO_4^{2-} and O-Fe vibration profiles. Comparing the EDS point analysis (Fig.S1) with the Raman investigation, we inferred that the presence of Pb-bearing jarosite was entirely obscured by prevailing Raman bands of K-jarosite and hematite. Meanwhile, based on the optical microscopy and SEM images, it is likely that Pb species are combined with K-jarosite and hematite without

distinct boundaries. Although the literature suggests that the alunite-jarosite family could hypothetically function as collectors of Pb in the form of plumbojarosite ($Pb_{0.5}Fe_3(SO_4)_2(OH)$) (Forray et al., 2014), the Pb presence in our samples is more likely to be assigned by the co-existing mechanisms (adsorption on the surface and/or co-precipitation in the jarosite structure), because the characteristic peaks of plumbojarosite were not found in the XRD pattern (Fig.1a). Therefore, the occurrence of Pb (Fig.2d and e) may be related to the phase transformation (for instance, anglesite and K-jarosite) through the dissolution/precipitation process or solid-state recrystallization during the weathering process (Shi et al., 2022).

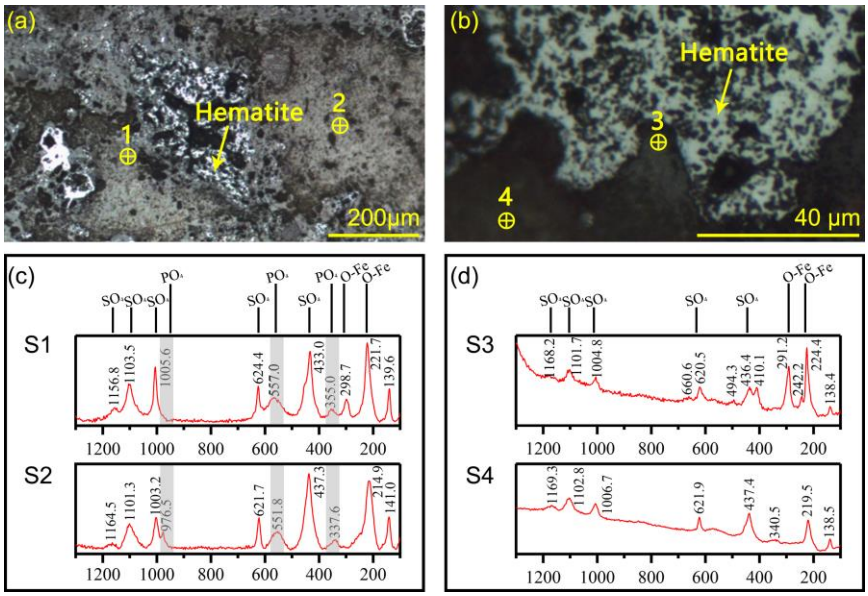

Figure.3. Raman spectra of the studied samples. (a) and (b) Optical microscope images of the tested area correlated to Fig.2d and g, respectively; (c) and (d) Raman spectra of the marked point, with the abbreviation S1 representing spot 1.

3.2. pH-dependent leaching tests

Fig. 4 illustrates the concentration of released Pb, Zn, Fe, and SO_4^{2-} with the acid/base addition to the solution in contact with pyrite ash. When using deionized water as the leachate (at pH 4.6), the leachability of the tested elements showed that the collected samples should be classified as hazardous waste, with all the concentrations being significantly higher than the limits established by Italian laws (Table.S6). The leaching of the studied trace metals (Pb, Zn, and Fe) showed a strong dependence on the pH values, indicating that the collected pyrite ash is susceptible to changing conditions of the stockpile. At the pH value of 1.98, the highest concentrations of Pb, Zn, and Fe in the leachate were reached at 1.59×10^{1}, 7.49×10^{1}, and 2.69×10^{2} μmol/L. The minimum release of Pb (0.38 μmol/L) and Zn (0.30×10^{-1} μmol/L) was found at the pH value of 9.04. However, with the increase in pH values, Pb and Zn showed an upward tendency in the release under alkaline conditions. These amphoteric Pb and Zn leaching profiles were also

observed in the research of Contessi et al. (2020), Cappuyns et al. (2014), and Jarošíková et al. (2017). The enhanced element release at basic conditions was due to the occurrence of specific dissolution of minerals (e.g., the transformation of Pb/Zn bearing carbonates to hydroxides) (Helser and Cappuyns, 2021) and desorption reactions of elements from reactive surfaces (e.g., Pb/Zn may desorb from Fe-oxides surfaces and favor the formation of hydroxyl-complexes). (Cappuyns et al., 2014). By contrast, the release of Fe at the neutral/alkaline conditions fluctuated approximately from 0.32 to 3.40 μmol/L, which was probably related to the formation of iron hydroxide (Cappuyns et al., 2014). Besides, the increasing leachability of SO_4^{2-} was only observed under alkaline conditions, with the concentrations being constant at around 10^4 μmol/L in the acidic and neutral region.

3.3. Mineral composition after leaching

To reveal the dissolution/precipitation of the mineralogical phases at different pH values, the solid residues after the leaching tests were collected for the mineralogical characterization. From quantitative phase analysis of the XRD patterns (Fig.S2 and 5), it can be seen that quartz and kintoreite are not affected by pH variation, with the concentration remaining approximately constant in the studied pH ranges. Despite a decrease in hematite appearing in the near-neutral region (Fig.5c and d), the mass fraction of hematite still dominates the total amount of phases. It is to note that the weight fraction variation obtained by Rietveld's quantitative analysis of the soil samples before and after leaching procedures can be directly compared only assuming that the solid mass of the sample stays constant. But during the leaching tests, part of the samples is dissolved, such that the constant mass assumption is invalid. Therefore, the weight fraction of the quantified minerals may interplay with the dissolution and precipitation of other phases (for instance, the hematite fraction quantified by the XRD patterns may be influenced by the dissolution of gypsum, thereby its weight percentage increased massively at acid conditions, see Fig.5a and b). Further, anglesite exhibits a higher solubility in the alkaline pH ranges. This observation is consistent with findings of previous works where anglesite is considered the most stable Pb-bearing phase when pH < 5.5 (Contessi et al., 2020; Nikkhou et al., 2020). Regarding gypsum, the XRD results illustrate that it is abundant at neutral pH values, with 4.2, 14.6, and 11.0 wt% being present at pH values of 1.26, 6.5, and 12.02, respectively. Jarosite was preserved at highly alkaline conditions, even though it was confirmed that it has a higher solubility when pH values > 4.5 (Kölbl et al., 2021). In the residues collected from the leachate at the pH of 12.02, 3.0 wt% of jarosite was quantified in the XRD pattern (Fig.5f), indicating that approximately 40% of jarosite dissolved. Previous work suggested that jarosite preservation at high pH values could be explained by the formation of nanoparticles of secondary iron oxide phases on the jarosite grain surfaces, which inhibits subsequent jarosite dissolution and does not resorb either K or SO_4 ions (Smith et al., 2006). Similar observations are also presented in the original soils (as shown in Fig.2g and h). Approximately 1.0 wt% of

calcite was characterized in the XRD pattern at pH values higher than 6.5. The occasionally found muscovite (pH 9.04, 0.6 wt%) could be related to the original soil from the stockpile site.

3.4. Geochemical modeling: the leaching profiles and phases equilibrium

To determine which processes and minerals control the release of hazardous contaminants, experimental results (the mineralogical composition of the residues and pH-dependent leaching tests) were combined with geochemical modeling. Based on the preliminary characterization, some basic modeling assumptions were adopted: (1) quartz is assumed insoluble during the studied pH range, as derived by quantitative analysis of XRD data indicating that this phase stays constant (Fig.5a and f); (2) since hematite formation is favored at high temperatures and low salinity (Han et al., 2018), the precipitation of this phase was not envisaged in the model; (3) in the first simulation (MO.1), jarosite was assumed to participate entirely in the dissolution/precipitation reactions and in the second approach (MO.2), a dissolution limitation coefficient, controlling the maximum amount of jarosite allowed to dissolve in the model, was set to simulate the effect of coating film (physical protection of iron oxide) mentioned in the previous sections. Based on the experiments (Fig.5a), the parameter was set as only 40 wt% of jarosite would participate in the dissolution/precipitation reactions; (4) due to lack of knowledge of the thermodynamic data of kintoreite, in this work, this mineral was assumed stable. Additionally, the saturation index (SI) was used to determine whether the solution is saturated (equilibrium, SI = 0) or undersaturated (mineral dissolution, SI < 0) with respect to the given Pb- and Zn-bearing minerals.

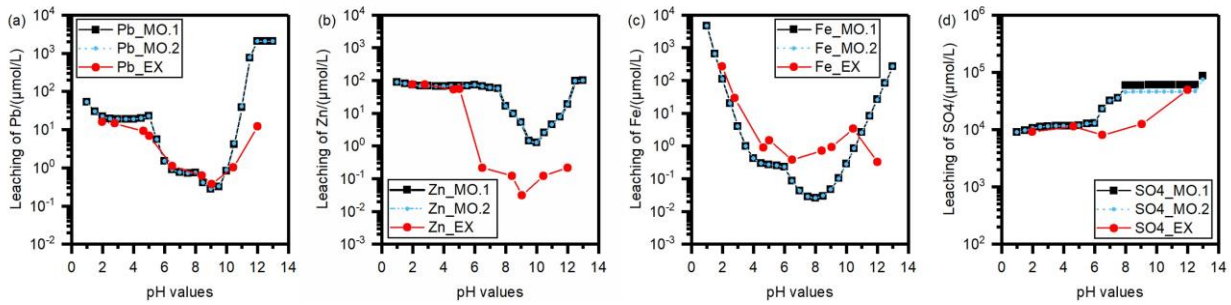

Figure.4. pH-dependent leaching results of Pb (a), Zn (b), Fe (c), and SO_4^{2-} (d) from experiments and simulations. The abbreviation EX means the experiments. MO.1 and MO.2 represent the geochemical modeling without or with jarosite dissolution limit.

The predicted Pb, Zn, and Fe leaching profiles (Fig.4a, b, and c) illustrate that both simulations can describe the pH-dependent leaching behavior of the tested systems. Noteworthy, compared to the acid conditions, the leaching of Pb and Zn in harsh alkaline conditions should be carefully investigated since a previous work demonstrated that the leaching of Pb under alkaline conditions (pH>11) could be several magnitudes higher than the acidic conditions (Contessi et al., 2020). From the predicted mineralogical composition

(Fig.5) and SI values (Fig.6a), from near-neutral to moderately alkaline conditions, the Pb retention is closely related to the equilibrium of anglesite, cerussite ($PbCO_3$), and hydrocerussite ($Pb_3(CO_3)_2(OH)_2$). In contrast, the plumbojarosite is undersaturated in the whole pH range. These observations ascertain the findings in previous research (Helser and Cappuyns, 2021).

The detected Pb release at this pH range can be explained by the formation of Pb-containing stable aqueous complexes (with CO_3^{2-}, $SO_4^{2-,}$ and OH^-). In contrast, at pH values over 12.5, all the Pb-bearing phases are undersaturated, indicating that Pb is prone to be preserved in the solution in the form of lead hydroxides complex (Navarro et al., 2011), which is consistent with the amphoteric leaching behavior. In Fig.6b, it can be seen that the retarded release of Zn at near-neutral conditions is due to the precipitation of carbonates (smithsonite and $ZnCO_3 \cdot H_2O$) and hydroxides ($Zn(OH)_2$). But at acid conditions, the aqueous Zn speciation is dominated by Zn^{2+} and $ZnSO_4$ instead of the zincosite precipitation. Similar to what was observed for Pb, Zn in the alkaline leachates occurred in the form of aqueous hydroxide species ($Zn(OH)_4^{2-}$ and $Zn(OH)_3^-$). In addition, the assumed limitation of jarosite dissolution (MO.2) reduced the deviation of SO_4^{2-} leaching data between the experimental and modeling results (Fig.4d), indicating that except for the gypsum and anglesite dissolution, the jarosite is also a predominant source of sulfate contaminants. Although the deviation of the SO_4^{2-} leaching was slightly improved by the assumption of limited jarosite dissolution, a significant difference still can be observed at the pH range from 7~12, which is not in agreement with the experimental findings. Hence, although the thermodynamic database used in this work is widely recommended, it is clear that the given log K value has overestimated the solubility of gypsum and tended to estimate sulfate concentrations that were two to three orders of magnitude higher than the experiments.

By comparing the predicted mineralogical compositions of the residues with the experimental results (Fig.5), the geochemical approach demonstrate a great potential to quantitatively describe the transformation of the minerals, with a good agreement between the phases characterized by XRD and the predicted minerals by geochemical modeling. A major discrepancy is detected in the gypsum estimation, as approximately 5.5 wt% of maximum deviation in the residues at particularly acid conditions (pH 1.26, Fig.5a). This discrepancy is slightly reduced at neutral and alkaline conditions, as shown in Fig.5c, with a difference between experimental and modeling results of 3.4 wt%. It is to note that geochemical modeling is capable of detecting such small variations of the PTEs-containing phases (< 1 wt%), which is hard to be revealed by the XRD mineralogical analysis. As shown in Fig.4a, when the pH increases to neutral conditions (pH values 6-9), which is unsuitable for the anglesite stability (Contessi et al., 2020) and the XRD characterization revealed the dissolution of anglesite (Fig.S2). The experimental XRD data did not identify mineralogical phases responsible for the retention of Pb at this pH range, with none of the lead-bearing crystalline phases being detected. The geochemical modeling results, along with previous

investigations (Vítková et al., 2009; Tangviroon et al., 2020; Redwan et al., 2021), suggest that the Pb-carbonate phases (hydrocerussite and cerussite) precipitate at neutral conditions (0.57 wt% at pH 6.5, Fig.5c) and then slightly dissolve (0.33 wt% at pH 11.52, Fig.5e) with the increase of pH. Similarly, about 0.010 wt% of Zn hydroxide was expected to precipitate in the residues at a pH of 9.04 (Fig.5d), then the weight percentage slightly decreased to 0.008 wt% (Fig.5e).

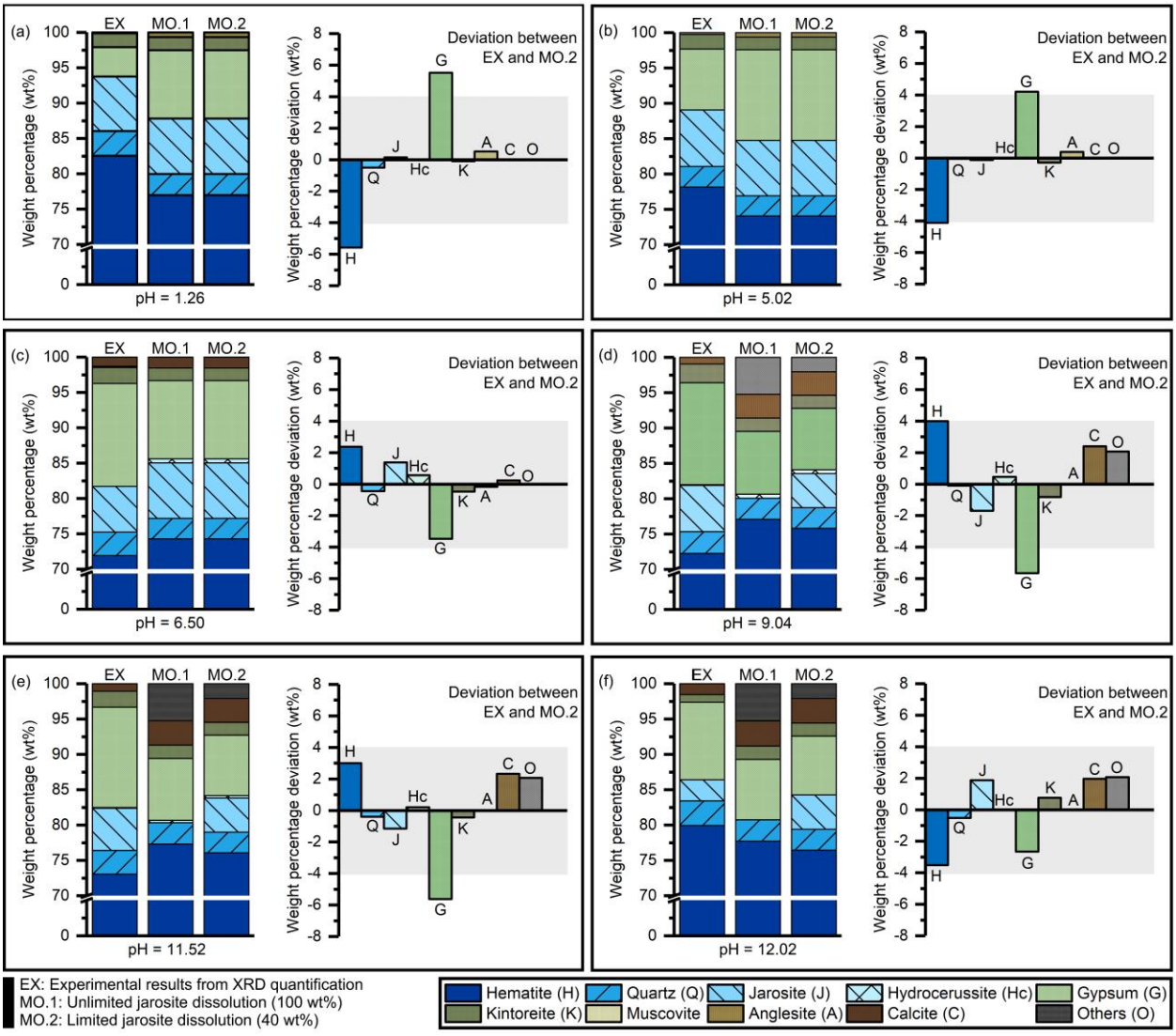

Figure.5. Quantified mineral assemblages of the residues from the XRD patterns and Phreeqc models and the correlated deviation. The leachate pH values at (a) 1.26, (b) 5.02, (c) 6.50, (d) 9.04, (e) 11.52, and (f) 12.02. The "Other" in the simulation is the weight percentage accumulation of $Fe(OH)_3$ and $Zn(OH)_2$ matrix. The marked gray rectangle represents the XRD limitation (±2 wt%). The predicted weight percentage of hydrocerussite is the accumulation of cerussite and hydrocerussite.

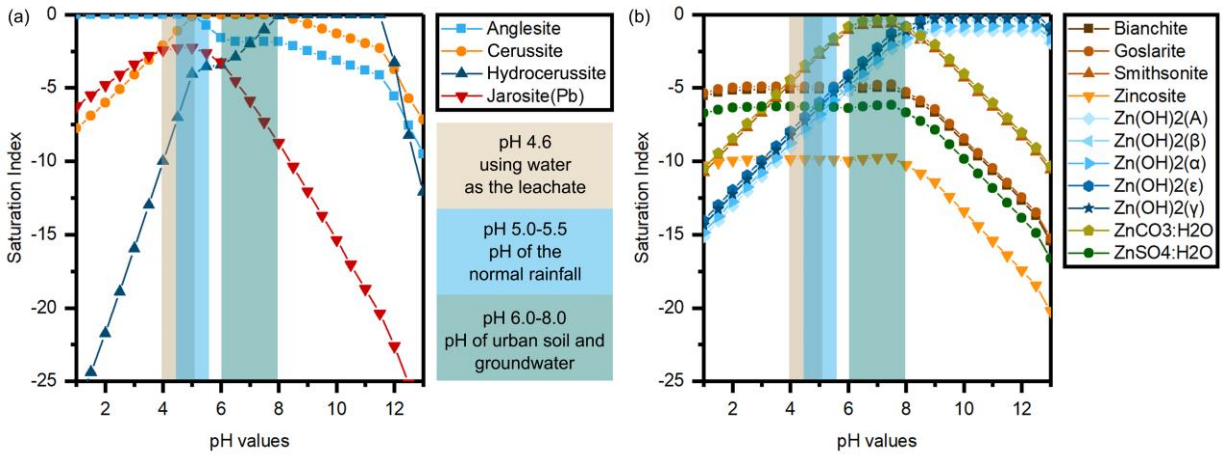

Figure.6. The SI of Pb-(a) and Zn-(b) bearing minerals from MO.2.

4. Discussion

4.1. Reconstruction of the mineral transformations from the fertilizer production and weathering process

With the previous mineralogical and chemical investigations, the distinct phases in the bulk soil provide valuable information to reconstruct the linkage between the stocked wastes and soil. In a typical P-fertilizer manufacturing chain (Fig.7a), the pyrite and apatite ores were used as the raw materials for sulfuric acid production and the following phosphorus fertilizer production (El Zrelli et al., 2018; Garbaya et al., 2021). The primary components in pyrite ash are hematite and calcium sulfates, which are naturally occurring minerals in the environment with low toxicity (Pérez-López et al., 2009; Oliveira et al., 2012). The concentrated pyrite ores are heated to 900 °C to extract the sulfur (mainly in the form of SO_2), leaving a residue consisting mainly of iron oxide (Oliveira et al., 2012). However, the generated by-products, iron oxide (hematite) and sulfates minerals (jarosite), would cover the unreacted pyrite and then preserve a partially reacted pyrite grain (Oliveira et al., 2012; Liu et al., 2016a). Compared to the other co-existing sulfides, the remained pyrite is readily weathered and promotes the oxidation and dissolution of galena (PbS), which is a significant Pb host in the pyrite ores (Contessi et al., 2020). Therefore, anglesite was present in the pyrite ash (Fig.1 and 2b) as a secondary oxidized product from the unreacted grains.

Lead was concentrated along the edges of iron oxides, as observed in Fig.2d, e, and f. The vibrations in the Raman spectra (Fig.3b and d) also show more complexity for these Pb-bearing phases. Previous works have ascertained the observation (Yang et al., 2009; Bendz et al., 2021) that Pb is partially released from the sulfide minerals as vapor during the roasting process. The volatilized Pb condensed on the external and interior surfaces of the porous iron oxide grains, which have high thermal stability, and formed sulfate precipitates (mainly $PbSO_4$). Then the free ferric ions formed by gradual dissolution are in contact with

$PbSO_4$, which are then hydrolyzed to generate Pb-rich jarosite (Qin et al., 2020). Further, the SI modeling illustrates that although the SI values of plumbojarosite are increasing and closely approach saturation equilibrium state in the water leaching condition (pH 4.64, Fig.6a), this phase is still undersaturated, and the formation of anglesite is favored. Experimental evidence confirmed that the formation of pure plumbojarosite hardly occurs in ambient conditions (air temperature and neutral pH conditions) (Shi et al., 2022). For instance, Forray et al. (2010) synthesized plumbojarosite by the reactions between the $Fe_2(SO_4)_3 \cdot 5H_2O$, $Pb(NO_3)_2$, and H_2SO_4 solutions at a temperature of 95 °C. In this case, the observed Pb (Fig.2f, g, and h) are not associated with the presence of plumbojarosite. The lead distribution in the soil can likely be explained by considering a combination of mechanisms such as incorporation and physicochemical mixtures (Forray et al., 2010; Shi et al., 2022). It has been established that Na- and K-jarosite can act as efficient carriers of Pb because they can incorporate Pb in their crystal structure (Aguilar-Carrillo et al., 2018b). Usually, jarosite forms as a product of pyrite oxidation under very acidic conditions. Accordingly, these co-precipitation processes may represent a likely mechanism for incorporating the metal cations present at the interfaces, which would have high mobility at this pH condition (as demonstrated in Fig.4a, approximately at pH>10) in the jarosite structure (Forray et al., 2014). Besides, apart from the formation of Pb/Na/K-jarosite compounds, Pb may preferentially precipitate as anglesite (Fig.6a) (Shi et al., 2022). The formed anglesite can serve as crystal nuclei for the subsequently precipitated jarosite. In this case, although Pb does not enter the jarosite structure, the anglesite is surrounded by jarosite forming small-scale mixtures. However, because of the complex speciation of Pb, it is hard to assert an exact interaction between the Pb and jarosite.

Regarding the characterized kintoreite, it is hard to ascertain if kintoreite is a gangue mineral originating from the ores or if it is a secondary mineral generated during fertilizer production. Many studies strongly emphasize that the occurrence and aggregation of kintoreite in the impacted soils is most likely a result of the acidity of the stockpile sites and the raw wastes (pH values from 3 to 4). The continuously leached Fe^{3+} and PO_4^{3-} combined with Pb (released mainly from galena) to form kintoreite (Munksgaard and Lottermoser, 2011; Schindler and Hochella, 2017; Li et al., 2020). But some field works also demonstrate that rare kintoreite is present in cavities of quartz gangue (Vrtiška Luboš et al., 2016; Mauro et al., 2021). Nevertheless, the quantified kintoreite weight fraction almost remained unchanged over the measured pH range (Fig.5), indicating it barely contributes to the Pb leaching profiles. This is also ascertained by the geochemical modeling (Fig.4a), as the assumption was given that the kintoreite will not participate in the precipitation/dissolution reactions, the simulated Pb leaching is still matched with the experiment results. Zinc that occurs in pyrite ash could mainly be in the minor phases of zinc sulfate (Fig.2i). The distribution of zinc sulfate is associated with the sphalerite present in pyrite ores, which can be oxidized by either dissolved molecular oxygen or ferric iron and then form secondary sulfates or other acid-exchangeable

species (Xuexin, 1984; Gabarrón et al., 2018). Meanwhile, with the time and climate conditions, the secondary zinc phases probably continue reacting at high humidity with the atmospheric CO_2 (the stockpile site in this study is a coastal city, as shown in Fig.7c) (Carrero et al., 2012; Tangviroon et al., 2020). The detected gypsum is a typical by-product generated from phosphorus fertilizer production (Garbaya et al., 2021). Unlike phases containing metals, gypsum residues are not dangerous for the environment, though the abundance of sulfate would accelerate the migration of metals (Yang et al., 2021). Further, with the increase of the pH values, the carbonates and hydroxide phases dominate the Pb and Zn retention.

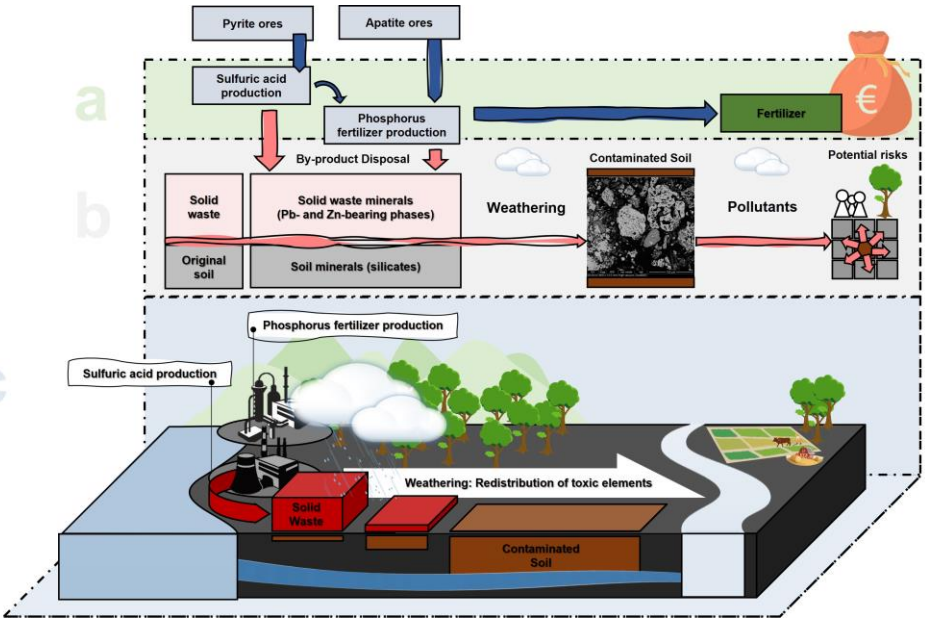

Figure.7. Schematic cartoon depicting solid waste generation due to industrial activities (a), the transformation of mineralogical phases from stockpiled solid waste and original soil during the long-term weathering process (b), and the overall geographical description of the studied sites (c).

4.2. Influence of pH values on the geochemical stability of toxic elements

As recognized by previous investigations (Contessi et al., 2020; Król et al., 2020), pH is one of the most important factors controlling changes in the mineralogical concentration and leachability of metals. Hence, the pH-dependent leaching tests can efficiently reveal the fundamental mechanisms, such as possible ion exchange/sorption, complexation, and precipitation/dissolution (Engelsen et al., 2010; Tian et al., 2018). The results of leaching tests (Fig.4) and the mineralogical study (Fig.5) illustrated that the addition of acid agents caused increased concentrations of Pb, Zn, and Fe in solutions. Noteworthy, over the acid pH range, Pb was preferentially precipitated as anglesite (Fig.6), but the leaching of Pb was still increased with the pH decrease. By checking the original (unnormalized) mineralogical compositions of the residues in the simulations, only 0.005wt% weight loss of anglesite was found at the pH value of 1.26 (from 0.621 wt% at

pH 5.02 to 0.616 wt% at pH 1.26), showing that the relatively small changes in weight percentage may cause an increase in the leachate concentration. Therefore, with continuously increased HNO_3 agent fraction in the system, anglesite is expected to dissolve partially and form ion pairs ($PbNO_3^{+}{}_{(aq)}$) (Rouff et al., 2005; Ettler et al., 2007). Further, Zn is mainly preserved in the acid solutions in the monatomic ion form, accompanied by the minor $ZnSO_{4(aq)}$ complex. At the pH range from 2 to 5, the slight deviation in leaching curves could be attributed to the Pb/Zn-substituted jarosite. There have been previous studies stating the strong affinity of Zn and Pb to Fe-minerals, suggesting that jarosite can efficiently immobilize metals by incorporating the metal ions in its crystal structure (Qin et al., 2020; Chen et al., 2021). Thus, the incorporated Pb and Zn should remain stable in the residues, with a relatively slow-releasing rate (Fig.6a). When the pH values increase to near-neutral conditions, Pb and Zn are preferentially precipitated as carbonates and hydroxides (Fig.5 and 6). But the simulated leaching profiles can only partly reflect the overall trends (Fig.4b), with minimum Pb and Zn leaching around a pH value of 10. Especially, the measured Zn concentration was one order of magnitude lower than what the model predicted (10^{-1} and 1 μmol/L, Fig.4b). This deviation could be partially explained by the high sorption ability and metal affinity of ferrihydrite (Reichert and Borg, 2008; Dijkstra et al., 2009; Ettler et al., 2020), which is a phase rarely exists as pure precipitation but a highly affinitive host for various foreign elements, such as Si, Al, and Mn (Ye et al., 2021). The additional modeling (Fig.S4) also verifies this hypothesis. With the assumption of Zn adsorption onto ferrihydrite, the estimated Zn leachability at pH values from 6 to 10 is slightly optimized compared to MO.1 and MO.2. Therefore, the adsorption competition among Pb, Zn, and other elements may play a crucial role in their mobility in the environment. However, this does not match experimental results since the amorphous content (ferrihydrite) is not observed in the quantification results. Besides, the preservation of Zn could also be related to the porous microstructure of hematite (Fig.2c and f). The Zn may be strongly bound to the crystalline structures of hematite and then preserved without a mineral phase change, which is associated with coupled O–Fe and protonated Fe vacancies (Gabarrón et al., 2018; Bylaska et al., 2019). In alkaline conditions (pH >10), despite the fact that ferrihydrite sorption mechanisms should theoretically display a role in the Pb and Zn retention, the increase of leaching profiles was observed in this work, also ascertained by previous investigations (Contessi et al., 2020; Helser and Cappuyns, 2021). The geochemical modeling shows that the increased leaching rate under alkaline conditions can be related to the formation of anionic hydroxo complexes such as $Zn(OH)_3^{-}$, $Zn(OH)_4^{2-}$, $Pb(OH)_3^{-}$, and $Pb(OH)_4^{2-}$, suggesting that the adsorped trace metal cations partially dissolved due to the anionic properties of the newly formed hydrolyzed species preclude their sorption onto the negative surface of the ferrihydrite. Similar results are reported by (Liu et al., 2016b) and (Jiao et al., 2016). Although an increasing trend of Pb and Zn concentrations was observed at this pH range (8 to 13), their relative leached amounts are still lower than those detected at acid conditions (pH 1 to 3, Fig.4a and b), which implies that other factors, such as

structural incorporation (isomorphous substitution and occupation of vacant sites of hematite and ferrihydrite), Pb-Fe solid solutions, and mechanical occlusion (Pb-bearing minerals could inevitably coprecipitate and interact with jarosite structure), may play a role in the releasing behavior (Shi et al., 2021). But further investigations are required to reveal the exact retention mechanism.

4.3 Environmental risk

As demonstrated in previous sections, the concentrations and leachabilities of PTEs are strongly influenced by the pH values due to the different geochemical stabilities of the PTEs-containing species. Numerous studies have indicated that the high solubility of PTEs represents a greater potential risk of contamination to plants and humans, especially during the rainy period when the washout of soluble phases may occur (Helser and Cappuyns, 2021; Pękala and Musiał, 2021). Significantly, the complexity of the studied area (Fig.7c, coastline city, stockpiled near the surface, and sparse vegetation cover) and the subsequent exposure of the contaminants to various environmental conditions (e.g., wind, erosion, acid rain, proximity to groundwater/surface water), makes it crucial to monitor the site and carefully take appropriate measures to minimize the risks (Helser et al., 2022).

From the pH-dependent leaching tests (Fig.4a and b), it can be concluded that the optimum pH for the lowest solubility of Pb and Zn is near the pH range of 8 to 10. This is due to the synergistic effects deriving from the remained jarosite, the formation of Pb/Zn-bearing carbonates, and the assumed ferrihydrite precipitation contributing to significantly lower concentrations of Pb and Zn in the leachates (pH 9.04, Fig.5d). If the storage system is kept at this pH range, a lower release of hazardous would be expected. Nonetheless, the concentrations of the released contaminants are still higher than the threshold limits (0.50×10^{-1} μmol/L for both Pb and Zn, from Decreto legislativo 3 aprile 2006, n. 152). In addition, field works in Italy revealed that the water from the rainfall and aquifers has a pH ranging from nearly neutral to slightly acidic (Madonia et al., 2021; Di Curzio et al., 2021), suggesting that the sorption/desorption of contaminants on ferrihydrite and carbonates may not govern the Pb and Zn retention in its natural stockpile state. Severe acid rain circumstances can also expose the risk of higher release of contaminants.

Hence, the outdated and improper stock is insufficient for the long-term disposal of pyrite ash, and efficient treatment is urgently needed for its management. Some works focused on the ex-situ immobilization technologies of these materials, for instance, ex-situ soil washing and filling (Liu et al., 2018), electrokinetic remediation (Pedersen et al., 2018), and chemical extraction (Zhang et al., 2021). For ex-situ treatment, it is fundamental to evaluate the advantages and disadvantages of the intervention and compare them with the scenario of leaving the pyrite ash in its current state. It has to be evaluated whether the environmental and human health risks outweigh the risks of re-opening the site, especially the potential secondary pollution caused by the excavation and transportation processes during the large-scale reprocessing plan. Alternative

approaches encompass in-situ remediation strategies, such as high-performance solidification/stabilization procedures (Contessi et al., 2020) and cemented paste backfill (Guo et al., 2021), that could be envisaged for this solid waste. However, based on the amphoteric leaching behavior revealed by the pH-dependent leaching test, the traditional binders (ordinary Portland cement or lime) might not be suitable for the management scenarios. It is because the high alkalinity provided by traditional binders might increase the mobility of Pb and Zn under alkaline conditions (pH>10). Therefore, additional studies need to be conducted on the mix design, the buffering capacity, and the leaching potential of metals.

5. Conclusion

This study focused on assessing the leaching behavior and potential environmental risks of soil contaminated by Pb and Zn, mainly based on the geochemical mobility investigation and mineralogical assessments of the hazardous contaminants. The overall results demonstrated that Pb, Zn, and SO_4^{2-} are the most abundant pollutants. These contaminants were also highly mobile in the studied pH ranges, and various mechanisms played a role in controlling the releasing behavior. With the aid of PHREEQC modeling, a more comprehensive mineralogical insight was provided into solid waste management. The forward model construction is feasible and capable of monitoring major and minor phases participating in metal retention. Overall, the combined use of geochemical modeling and experiments has prompted the possibility of an in-depth investigation for application to in-situ remediation in industrial sites. Moreover, this approach may integrate the experimental approach through a relatively uncomplicated pathway for monitoring the PTEs leaching behavior. The main findings are as follows:

(1) With the raw material characterization, the anglesite and kintoreite are the main Pb-bearing crystalline phases detected in the XRD patterns, which may be generated from the oxidation of remaining pyrite particles. The sulfates (jarosite) were confirmed as the trace metal-bearing phases, as the Pb/Zn-Fe sulfates were characterized along the edge of the hematite particles. The SI of the phases calculated by geochemical modeling suggests that Pb and Zn are associated with different phases and an adsorption mechanism is also active in the soil.

(2) The measured concentrations of contaminants in the leachates showed a strong dependence on the pH values of the contact solution. Both Pb and Zn releases exhibit an amphoteric behavior, with a downward trend towards the neutral/alkaline region around pH values from 8 to 10. The mineralogical information indicates that the solubility of trace metal compounds, especially in the form of oxides, hydroxides, and carbonates, significantly depends on the pH value. At acid conditions, the solubility of Pb is dominated by the dissolution of anglesite and the formation of Pb nitrate complexes, while Zn is controlled by Zn ions and Zn-sulfate complexes in solution. The decrease of trace metal leaching in the neutral/alkaline region is related to the precipitation of carbonates and the potential adsorption onto jarosite and ferrihydrite. When

the pH values move to strong alkaline conditions, the upward trend could be associated with the complexation of aqueous metal hydrates.

(3) The simulated and experimental results of leaching and mineralogical composition of the residues are in good agreement. The conceptual model, which combined processes of precipitation/dissolution and formation of solid solutions, gave a great reproduction of the amphoteric Pb and Zn leaching. The jarosite was preserved in the residues, which could be related to the formation of nanoparticles of secondary iron oxide phases. Although an erroneous estimate was demonstrated for the precipitation/dissolution of gypsum, due to its high solubility, the general estimation has progressed in the ability to predict the environmental fates of associated trace and hazardous elements.

(4) The pH-dependent mobility of contaminants is concerning because it clearly indicates that, even in its natural state, the collected pyrite ash poses a great environmental risk and strongly threatens human health, which only worsens under acidic or alkaline conditions. However, a more detailed in situ scenario design should be incorporated to understand the risks thoroughly before the large-scale application.

Acknowledgments

This study was conducted with financial support from the PRIN project “Mineral reactivity, a key to understand large-scale processes: from rock-forming environments to solid waste recovering/lithification” (No.2017L83S77) and a scholarship granted by the China Scholarship Council (No.CSC201906370062).

Author contributions

Yikai Liu: Conceptualization, Writing- Original Draft preparation, Investigation, Formal analysis

Simone Molinari: Conceptualization, Validation, Writing – Review & Editing, Visualization

Maria Chiara Dalconi: Validation, Investigation, Visualization, Writing – Review & Editing

Luca Valentini: Investigation, Validation, Visualization

Giulia Ricci: Investigation, Supervision

Claudio Carrer: Investigation, Validation

Giorgio Ferrari: Resources, Supervision

Gilberto Artioli: Conceptualization, Writing – Review & Editing, Project administration,

Resources, Supervision, Validation

All the authors discussed the data and agreed on their interpretations. All the co-authors contributed to the final polishing of the manuscript.

References

Abollino, O., Aceto, M., Malandrino, M., Mentasti, E., Sarzanini, C., and Petrella, F., 2002, Heavy metals in agricultural soils from Piedmont, Italy. Distribution, speciation and chemometric data treatment: Chemosphere, v. 49, p. 545–557, doi:10.1016/S0045-6535(02)00352-1.

Agnello, A.C., Bagard, M., van Hullebusch, E.D., Esposito, G., and Huguenot, D., 2016, Comparative bioremediation of heavy metals and petroleum hydrocarbons co-contaminated soil by natural attenuation, phytoremediation, bioaugmentation and bioaugmentation-assisted phytoremediation: Science of The Total Environment, v. 563–564, p. 693–703, doi:10.1016/J.SCITOTENV.2015.10.061.

Aguilar-Carrillo, J., Herrera, L., Gutiérrez, E.J., and Reyes-Domínguez, I.A., 2018a, Solid-phase distribution and mobility of thallium in mining-metallurgical residues: Environmental hazard implications: Environmental Pollution, v. 243, p. 1833–1845, doi:10.1016/J.ENVPOL.2018.10.014.

Aguilar-Carrillo, J., Villalobos, M., Pi-Puig, T., Escobar-Quiroz, I.N., and Romero, F.M., 2018b, Synergistic arsenic(v) and lead(ii) retention on synthetic jarosite. I. Simultaneous structural incorporation behaviour and mechanism: Environmental Science: Processes & Impacts, v. 20, p. 354–369, doi:10.1039/C7EM00426E.

Ausili, A., Bergamin, L., and Romano, E., 2020, Environmental Status of Italian Coastal Marine Areas Affected by Long History of Contamination: Frontiers in Environmental Science, doi:10.3389/fenvs.2020.00034.

Bendz, D., Tiberg, C., and Kleja, D.B., 2021, Mineralogical characterization and speciation of sulfur, zinc and lead in pyrite cinder from Bergvik, Sweden: Applied Geochemistry, v. 131, p. 105010, doi:10.1016/J.APGEOCHEM.2021.105010.

Bernasconi, D., Caviglia, C., Destefanis, E., Agostino, A., Boero, R., Marinoni, N., Bonadiman, C., and Pavese, A., 2022, Influence of speciation distribution and particle size on heavy metal leaching from MSWI fly ash: Waste Management, v. 138, p. 318–327, doi:10.1016/J.WASMAN.2021.12.008.

Bettiol, C., Stievano, L., Bertelle, M., Delfino, F., and Argese, E., 2008, Evaluation of microwave-assisted acid extraction procedures for the determination of metal content and potential bioavailability in sediments: Applied Geochemistry, v. 23, p. 1140–1151, doi:10.1016/J.APGEOCHEM.2007.11.008.

Bisone, S., Gautier, M., Chatain, V., and Blanc, D., 2017, Spatial distribution and leaching behavior of pollutants from phosphogypsum stocked in a gypstack: Geochemical characterization and modeling: Journal of Environmental Management, doi:10.1016/j.jenvman.2017.02.055.

British Standards Institution, 2004, Characterisation of Waste - Leaching - Compliance Test for Leaching

of Granular Waste Materials and Sludges - Part 4: One Stage Batch Test at a Liquid to Solid Ratio of 10 l/kg for Materials With Particle Size Below 10 Mm (without or With Size Reduction):

Bylaska, E.J., Catalano, J.G., Mergelsberg, S.T., Saslow, S.A., Qafoku, O., Prange, M.P., and Ilton, E.S., 2019, Association of Defects and Zinc in Hematite: Environmental Science and Technology, v. 53, p. 13687–13694, doi:10.1021/ACS.EST.9B04323/ASSET/IMAGES/LARGE/ES9B04323_0004.JPEG.

Cappuyns, V., Alian, V., Vassilieva, E., and Swennen, R., 2014, PH dependent leaching behavior of Zn, Cd, Pb, Cu and As from mining wastes and slags: Kinetics and mineralogical control: Waste and Biomass Valorization, v. 5, p. 355–368, doi:10.1007/S12649-013-9274-3/FIGURES/5.

Carrero, J.A., Goienaga, N., Olivares, M., Martinez-Arkarazo, I., Arana, G., and Madariaga, J.M., 2012, Raman spectroscopy assisted with XRF and chemical simulation to assess the synergic impacts of guardrails and traffic pollutants on urban soils: Journal of Raman Spectroscopy, v. 43, p. 1498–1503, doi:10.1002/JRS.4089.

Chen, K., Jin, X., Guo, C., He, C., Zhang, Y., Gao, K., Lu, G., and Dang, Z., 2021, Reductive dissolution of Pb-Zn jarosite under near-neutral conditions: Chemical Geology, v. 579, p. 120338, doi:10.1016/J.CHEMGEO.2021.120338.

Contessi, S., Calgaro, L., Dalconi, M.C., Bonetto, A., Bellotto, M. Pietro, Ferrari, G., Marcomini, A., and Artioli, G., 2020, Stabilization of lead contaminated soil with traditional and alternative binders: Journal of Hazardous Materials, doi:10.1016/j.jhazmat.2019.120990.

Contessi, S., Dalconi, M.C., Pollastri, S., Calgaro, L., Meneghini, C., Ferrari, G., Marcomini, A., and Artioli, G., 2021, Cement-stabilized contaminated soil: Understanding Pb retention with XANES and Raman spectroscopy: Science of The Total Environment, v. 752, p. 141826, doi:10.1016/J.SCITOTENV.2020.141826.

Di Curzio, D., Rusi, S., Di Giovanni, A., and Ferretti, E., 2021, Evaluation of Groundwater Resources in Minor Plio-Pleistocene Arenaceous Aquifers in Central Italy: Hydrology 2021, Vol. 8, Page 121, v. 8, p. 121, doi:10.3390/HYDROLOGY8030121.

Deng, J., Zhang, K., He, D., Zhao, H., Hakkou, R., and Benzaazoua, M., 2020, Occurrence of sesquioxide in a mid-low grade collophane-sedimentary apatite ore from guizhou, china: Minerals, doi:10.3390/min10111038.

Dijkstra, J.J., Comans, R.N.J., Schokker, J., and van der Meulen, M.J., 2019, The geological significance of novel anthropogenic materials: Deposits of industrial waste and by-products: Anthropocene, v. 28, p. 100229, doi:10.1016/J.ANCENE.2019.100229.

Dijkstra, J.J., Meeussen, J.C.L., and Comans, R.N.J., 2009, Evaluation of a generic multisurface sorption model for inorganic soil contaminants: Environmental Science and Technology, v. 43, p. 6196–6201, doi:10.1021/ES900555G/SUPPL_FILE/ES900555G_SI_001.PDF.

Dijkstra, J.J., Van Der Sloot, H.A., and Comans, R.N.J., 2006, The leaching of major and trace elements from MSWI bottom ash as a function of pH and time: Applied Geochemistry, v. 21, p. 335–351, doi:10.1016/J.APGEOCHEM.2005.11.003.

Doebelin, N., and Kleeberg, R., 2015, Profex: a graphical user interface for the Rietveld refinement program BGMN: urn:issn:1600-5767, v. 48, p. 1573–1580, doi:10.1107/S1600576715014685.

Engelsen, C.J., Van Der Sloot, H.A., Wibetoe, G., Justnes, H., Lund, W., and Stoltenberg-Hansson, E., 2010, Leaching characterisation and geochemical modelling of minor and trace elements released from recycled concrete aggregates: Cement and Concrete Research, v. 40, p. 1639–1649, doi:10.1016/J.CEMCONRES.2010.08.001.

Ettler, V., Mihaljevič, M., Šebek, O., and Grygar, T., 2007, Assessment of single extractions for the determination of mobile forms of metals in highly polluted soils and sediments—Analytical and thermodynamic approaches: Analytica Chimica Acta, v. 602, p. 131–140, doi:10.1016/J.ACA.2007.09.017.

Ettler, V., Štěpánek, D., Mihaljevič, M., Drahota, P., Jedlicka, R., Kříbek, B., Vaněk, A., Penížek, V., Sracek, O., and Nyambe, I., 2020, Slag dusts from Kabwe (Zambia): Contaminant mineralogy and oral bioaccessibility: Chemosphere, v. 260, p. 127642, doi:10.1016/J.CHEMOSPHERE.2020.127642.

Fazle Bari, A.S.M., Lamb, D., Choppala, G., Seshadri, B., Islam, M.R., Sanderson, P., and Rahman, M.M., 2021, Arsenic bioaccessibility and fractionation in abandoned mine soils from selected sites in New South Wales, Australia and human health risk assessment: Ecotoxicology and Environmental Safety, v. 223, p. 112611, doi:10.1016/J.ECOENV.2021.112611.

Filippelli, G.M., Morrison, D., and Cicchella, D., 2012, Urban Geochemistry and Human Health: Elements, v. 8, p. 439–444, doi:10.2113/GSELEMENTS.8.6.439.

Forray, F.L., Smith, A.M.L., Drouet, C., Navrotsky, A., Wright, K., Hudson-Edwards, K.A., and Dubbin, W.E., 2010, Synthesis, characterization and thermochemistry of a Pb-jarosite: Geochimica et Cosmochimica Acta, v. 74, p. 215–224, doi:10.1016/J.GCA.2009.09.033.

Forray, F.L., Smith, A.M.L., Navrotsky, A., Wright, K., Hudson-Edwards, K.A., and Dubbin, W.E., 2014, Synthesis, characterization and thermochemistry of synthetic Pb–As, Pb–Cu and Pb–Zn jarosites: Geochimica et Cosmochimica Acta, v. 127, p. 107–119, doi:10.1016/J.GCA.2013.10.043.

Frost, R.L., Weier, M.L., Martens, W., and Mills, S., 2006a, ThermoRaman spectroscopic study of kintoreite: Spectrochimica Acta Part A: Molecular and Biomolecular Spectroscopy, v. 63, p. 282–288, doi:10.1016/J.SAA.2005.05.011.

Frost, R.L., Wills, R.A., Weier, M.L., and Martens, W., 2005, Comparison of the Raman spectra of natural and synthetic K- and Na-jarosites at 298 and 77 K: Journal of Raman Spectroscopy, v. 36, p. 435–444, doi:10.1002/JRS.1317.

Frost, R.L., Wills, R.A., Weier, M.L., Martens, W., and Mills, S., 2006b, A Raman spectroscopic study of selected natural jarosites: Spectrochimica Acta Part A: Molecular and Biomolecular Spectroscopy, v. 63, p. 1–8, doi:10.1016/J.SAA.2005.03.034.

Gabarrón, M., Babur, O., Soriano-Disla, J.M., Faz, A., and Acosta, J.A., 2018, Composition and risk assessment of roasted pyrite ash from fertiliser production: Chemosphere, v. 209, p. 277–285, doi:10.1016/J.CHEMOSPHERE.2018.06.109.

Garbaya, H., Jraba, A., Khadimallah, M.A., and Elaloui, E., 2021, The development of a new phosphogypsum-based construction material: A study of the physicochemical, mechanical and thermal characteristics: Materials, v. 14, doi:10.3390/MA14237369.

Gliozzo, E., Dalconi, M.C., Cruciani, G., and Memmi, I.T., 2009, Application of the Rietveld method for the investigation of mortars: a case study on the archaeological site of Thamusida (Morocco): European Journal of Mineralogy, v. 21, p. 457–465, doi:10.1127/0935-1221/2009/0021-1905.

Guo, Z., Qiu, J., Jiang, H., Zhang, S., and Ding, H., 2021, Improving the performance of superfine-tailings cemented paste backfill with a new blended binder: Powder Technology, v. 394, p. 149–160, doi:10.1016/J.POWTEC.2021.08.029.

Guo, B., Xiong, Y., Chen, W., Saslow, S.A., Kozai, N., Ohnuki, T., Dabo, I., and Sasaki, K., 2020, Spectroscopic and first-principles investigations of iodine species incorporation into ettringite: Implications for iodine migration in cement waste forms: Journal of Hazardous Materials, v. 389, p. 121880, doi:10.1016/J.JHAZMAT.2019.121880.

Gustafsson, J.P., 2011, Visual MINTEQ 3.1 user guide: Department of Land and Water Recources, Stockholm, Sweden, p. 1–73.

Han, B. et al., 2018, Development of copper recovery process from flotation tailings by a combined method of high–pressure leaching–solvent extraction: Journal of Hazardous Materials, v. 352, p. 192–203, doi:10.1016/J.JHAZMAT.2018.03.014.

Helser, J., and Cappuyns, V., 2021, Trace elements leaching from PbZn mine waste (Plombières, Belgium)

and environmental implications: Journal of Geochemical Exploration, v. 220, p. 106659, doi:10.1016/J.GEXPLO.2020.106659.

Helser, J., Vassilieva, E., and Cappuyns, V., 2022, Environmental and human health risk assessment of sulfidic mine waste: Bioaccessibility, leaching and mineralogy: Journal of Hazardous Materials, v. 424, p. 127313, doi:10.1016/J.JHAZMAT.2021.127313.

Hou, D., O'Connor, D., Igalavithana, A.D., Alessi, D.S., Luo, J., Tsang, D.C.W., Sparks, D.L., Yamauchi, Y., Rinklebe, J., and Ok, Y.S., 2020, Metal contamination and bioremediation of agricultural soils for food safety and sustainability: Nature Reviews Earth & Environment 2020 1:7, v. 1, p. 366–381, doi:10.1038/s43017-020-0061-y.

Iannello, M. et al., 2021, Long-lasting effects of chronic exposure to chemical pollution on the hologenome of the Manila clam: Evolutionary Applications, v. 14, p. 2864–2880, doi:10.1111/EVA.13319.

Izydorczyk, G., Mikula, K., Skrzypczak, D., Moustakas, K., Witek-Krowiak, A., and Chojnacka, K., 2021, Potential environmental pollution from copper metallurgy and methods of management: Environmental Research, v. 197, p. 111050, doi:10.1016/J.ENVRES.2021.111050.

Jambhulkar, H.P., Shaikh, S.M.S., and Kumar, M.S., 2018, Fly ash toxicity, emerging issues and possible implications for its exploitation in agriculture; Indian scenario: A review: Chemosphere, v. 213, p. 333–344, doi:10.1016/J.CHEMOSPHERE.2018.09.045.

Jarošíková, A., Ettler, V., Mihaljevič, M., Kříbek, B., and Mapani, B., 2017, The pH-dependent leaching behavior of slags from various stages of a copper smelting process: Environmental implications: Journal of Environmental Management, v. 187, p. 178–186, doi:10.1016/J.JENVMAN.2016.11.037.

Jiao, F., Zhang, L., Dong, Z., Namioka, T., Yamada, N., and Ninomiya, Y., 2016, Study on the species of heavy metals in MSW incineration fly ash and their leaching behavior: Fuel Processing Technology, v. 152, p. 108–115, doi:10.1016/J.FUPROC.2016.06.013.

Kang, M.J., Yu, S., Jeon, S.W., Jung, M.C., Kwon, Y.K., Lee, P.K., and Chae, G., 2021, Mobility of metal(loid)s in roof dusts and agricultural soils surrounding a Zn smelter: Focused on the impacts of smelter-derived fugitive dusts: Science of The Total Environment, v. 757, p. 143884, doi:10.1016/J.SCITOTENV.2020.143884.

Khan, H., Yerramilli, A.S., D'Oliveira, A., Alford, T.L., Boffito, D.C., and Patience, G.S., 2020, Experimental methods in chemical engineering: X-ray diffraction spectroscopy—XRD: The Canadian Journal of Chemical Engineering, v. 98, p. 1255–1266, doi:10.1002/CJCE.23747.

Kölbl, A., Kaiser, K., Winkler, P., Mosley, L., Fitzpatrick, R., Marschner, P., Wagner, F.E., Häusler, W., and

Mikutta, R., 2021, Transformation of jarosite during simulated remediation of a sandy sulfuric soil: Science of The Total Environment, v. 773, p. 145546, doi:10.1016/J.SCITOTENV.2021.145546.

Król, A., Mizerna, K., and Bożym, M., 2020, An assessment of pH-dependent release and mobility of heavy metals from metallurgical slag: Journal of Hazardous Materials, v. 384, p. 121502, doi:10.1016/J.JHAZMAT.2019.121502.

Kumpiene, J., Antelo, J., Brännvall, E., Carabante, I., Ek, K., Komárek, M., Söderberg, C., and Wårell, L., 2019, In situ chemical stabilization of trace element-contaminated soil – Field demonstrations and barriers to transition from laboratory to the field – A review: Applied Geochemistry, v. 100, p. 335–351, doi:10.1016/J.APGEOCHEM.2018.12.003.

Li, R., Li, Q., Sun, X., Li, J., Shen, J., Han, W., and Wang, L., 2020, Removal of lead complexes by ferrous phosphate and iron phosphate: Unexpected favorable role of ferrous ions: Journal of Hazardous Materials, v. 392, p. 122509, doi:10.1016/J.JHAZMAT.2020.122509.

Liu, Y., Guo, D., Dong, L., Xu, Y., and Liu, J., 2016a, Pollution Status and Environmental Sound Management (ESM) Trends on Typical General Industrial Solid Waste: Procedia Environmental Sciences, v. 31, p. 615–620, doi:10.1016/J.PROENV.2016.02.111.

Liu, L., Li, W., Song, W., and Guo, M., 2018, Remediation techniques for heavy metal-contaminated soils: Principles and applicability: Science of the Total Environment, doi:10.1016/j.scitotenv.2018.03.161.

Liu, J., Zhu, R., Xu, T., Xu, Y., Ge, F., Xi, Y., Zhu, J., and He, H., 2016b, Co-adsorption of phosphate and zinc(II) on the surface of ferrihydrite: Chemosphere, v. 144, p. 1148–1155, doi:10.1016/J.CHEMOSPHERE.2015.09.083.

Madonia, P., Campilongo, G., Cangemi, M., Carapezza, M.L., Inguaggiato, S., Ranaldi, M., and Vita, F., 2021, Hydrogeological and Geochemical Characteristics of the Coastal Aquifer of Stromboli Volcanic Island (Italy): Water 2021, Vol. 13, Page 417, v. 13, p. 417, doi:10.3390/W13040417.

Mauro, D., Biagioni, C., and Zaccarini, F., 2021, A contribution to the mineralogy of Sicily, Italy – Kintoreite from the Tripi mine, Peloritani Mountains: occurrence and crystal structure: Mineralogical Magazine, v. 55, p. 1–9, doi:10.1180/MGM.2021.85.

Munksgaard, N.C., and Lottermoser, B.G., 2011, Fertilizer amendment of mining-impacted soils from broken hill, Australia: Fixation or release of contaminants? Water, Air, and Soil Pollution, v. 215, p. 373–397, doi:10.1007/S11270-010-0485-Y/FIGURES/11.

Navarro, A., Cardellach, E., and Corbella, M., 2011, Immobilization of Cu, Pb and Zn in mine-contaminated soils using reactive materials: Journal of Hazardous Materials, v. 186, p. 1576–1585,

doi:10.1016/J.JHAZMAT.2010.12.039.

Nikkhou, F., Xia, F., Knorsch, M., and Deditius, A.P., 2020, Mechanisms of Surface Passivation during Galena Leaching by Hydrogen Peroxide in Acetate and Citrate Solutions at 25-50 °c: ACS Sustainable Chemistry and Engineering, v. 8, p. 14407–14416, doi:10.1021/ACSSUSCHEMENG.0C04272/SUPPL_FILE/SC0C04272_SI_001.PDF.

Obeng-Gyasi, E., Roostaei, J., and Gibson, J.M., 2021, Lead Distribution in Urban Soil in a Medium-Sized City: Household-Scale Analysis: Environmental Science and Technology, v. 55, p. 3696–3705, doi:10.1021/ACS.EST.0C07317/SUPPL_FILE/ES0C07317_SI_001.PDF.

Oliveira, M.L.S., Ward, C.R., Izquierdo, M., Sampaio, C.H., de Brum, I.A.S., Kautzmann, R.M., Sabedot, S., Querol, X., and Silva, L.F.O., 2012, Chemical composition and minerals in pyrite ash of an abandoned sulphuric acid production plant: Science of The Total Environment, v. 430, p. 34–47, doi:10.1016/J.SCITOTENV.2012.04.046.

Palansooriya, K.N., Shaheen, S.M., Chen, S.S., Tsang, D.C.W., Hashimoto, Y., Hou, D., Bolan, N.S., Rinklebe, J., and Ok, Y.S., 2020, Soil amendments for immobilization of potentially toxic elements in contaminated soils: A critical review: Environment International, v. 134, p. 105046, doi:10.1016/J.ENVINT.2019.105046.

Parkhurst, D.L., and Appelo, C.A.J., 2013, Description of Input and Examples for PHREEQC Version 3 — A Computer Program for Speciation , Batch-Reaction , One-Dimensional Transport , and Inverse Geochemical Calculations.: U.S. Geological Survey Techniques and Methods, book 6, chapter A43,.

Pedersen, K.B., Jensen, P.E., Ottosen, L.M., and Barlindhaug, J., 2018, Influence of electrode placement for mobilising and removing metals during electrodialytic remediation of metals from shooting range soil: Chemosphere, v. 210, p. 683–691, doi:10.1016/J.CHEMOSPHERE.2018.07.063.

Pękala, A., and Musiał, M., 2021, Modelling the leachability of strontium and barium from stone building materials: Materials, v. 14, doi:10.3390/MA14123403.

Pérez-López, R., Sáez, R., Álvarez-Valero, A.M., Nieto, J.M., and Pace, G., 2009, Combination of sequential chemical extraction and modelling of dam-break wave propagation to aid assessment of risk related to the possible collapse of a roasted sulphide tailings dam: Science of The Total Environment, v. 407, p. 5761–5771, doi:10.1016/J.SCITOTENV.2009.07.031.

Poggio, L., Vrščaj, B., Schulin, R., Hepperle, E., and Ajmone Marsan, F., 2009, Metals pollution and human bioaccessibility of topsoils in Grugliasco (Italy): Environmental Pollution, v. 157, p. 680–689, doi:10.1016/J.ENVPOL.2008.08.009.

Qin, S.C., Jiang, K.X., Wang, H.B., Zhang, B.S., Wang, Y.F., and Zhang, X.D., 2020, Research on Behavior of Iron in the Zinc Sulfide Pressure Leaching Process: Minerals 2020, Vol. 10, Page 224, v. 10, p. 224, doi:10.3390/MIN10030224.

Rakotonimaro, T. V., Guittony, M., and Neculita, C.M., 2021, Compaction of peat cover over desulfurized gold mine tailings changes: Arsenic speciation and mobility: Applied Geochemistry, v. 128, p. 104923, doi:10.1016/J.APGEOCHEM.2021.104923.

Redwan, M., Rammlmair, D., and Berkh, K., 2021, Secondary minerals in a calcareous environment: an example from Um Gheig Pb/Zn mine site, Eastern Desert, Egypt: Environmental Earth Sciences, v. 80, p. 1–19, doi:10.1007/S12665-021-09590-X/FIGURES/10.

Reichert, J., and Borg, G., 2008, Numerical simulation and a geochemical model of supergene carbonate-hosted non-sulphide zinc deposits: Ore Geology Reviews, v. 33, p. 134–151, doi:10.1016/J.OREGEOREV.2007.02.006.

Rietveld, H.M., 1969, A profile refinement method for nuclear and magnetic structures: Journal of Applied Crystallography, v. 2, p. 65–71, doi:10.1107/S0021889869006558.

Rouff, A.A., Reeder, R.J., and Fisher, N.S., 2005, Electrolyte and pH effects on Pb(II)–calcite sorption processes: the role of the PbCO03(aq) complex: Journal of Colloid and Interface Science, v. 286, p. 61–67, doi:10.1016/J.JCIS.2005.01.053.

Sasaki1, K., Tanaike, O., and Konno, H., 1998, DISTINCTION OF JAROSITE-GROUP COMPOUNDS BY RAMAN SPECTROSCOPY: The Canadian Mineralogist, v. 36, p. 1225–1235.

Schindler, M., and Hochella, M.F., 2017, Sequestration of Pb–Zn–Sb- and As-bearing incidental nanoparticles by mineral surface coatings and mineralized organic matter in soils: Environmental Science: Processes & Impacts, v. 19, p. 1016–1027, doi:10.1039/C7EM00202E.

Shi, M. et al., 2021, Recent progress in understanding the mechanism of heavy metals retention by iron (oxyhydr)oxides: Science of The Total Environment, v. 752, p. 141930, doi:10.1016/J.SCITOTENV.2020.141930.

Shi, M., Min, X., Tian, C., Hao, T., Zhu, S., Ge, Y., Wang, Q., Yan, X., and Lin, Z., 2022, Mechanisms of Pb(II) coprecipitation with natrojarosite and its behavior during acid dissolution: Journal of Environmental Sciences, v. 122, p. 128–137, doi:10.1016/J.JES.2021.10.006.

Smith, A.M.L., Hudson-Edwards, K.A., Dubbin, W.E., and Wright, K., 2006, Dissolution of jarosite [KFe3(SO4)2(OH)6] at pH 2 and 8: Insights from batch experiments and computational modelling: Geochimica et Cosmochimica Acta, v. 70, p. 608–621, doi:10.1016/J.GCA.2005.09.024.

Tabelin, C.B., Corpuz, R.D., Igarashi, T., Villacorte-Tabelin, M., Alorro, R.D., Yoo, K., Raval, S., Ito, M., and Hiroyoshi, N., 2020, Acid mine drainage formation and arsenic mobility under strongly acidic conditions: Importance of soluble phases, iron oxyhydroxides/oxides and nature of oxidation layer on pyrite: Journal of Hazardous Materials, v. 399, p. 122844, doi:10.1016/J.JHAZMAT.2020.122844.

Tangviroon, P. et al., 2020, Immobilization of Lead and Zinc Leached from Mining Residual Materials in Kabwe, Zambia: Possibility of Chemical Immobilization by Dolomite, Calcined Dolomite, and Magnesium Oxide: Minerals 2020, Vol. 10, Page 763, v. 10, p. 763, doi:10.3390/MIN10090763.

Tian, Q., Guo, B., Nakama, S., and Sasaki, K., 2018, Distributions and Leaching Behaviors of Toxic Elements in Fly Ash: ACS Omega, v. 3, p. 13055–13064, doi:10.1021/ACSOMEGA.8B02096/ASSET/IMAGES/ACSOMEGA.8B02096.SOCIAL.JPEG_V03.

Torres-Martínez, J.A., Mora, A., Knappett, P.S.K., Ornelas-Soto, N., and Mahlknecht, J., 2020, Tracking nitrate and sulfate sources in groundwater of an urbanized valley using a multi-tracer approach combined with a Bayesian isotope mixing model: Water Research, v. 182, p. 115962, doi:10.1016/J.WATRES.2020.115962.

Tuhý, M., Hrstka, T., and Ettler, V., 2020, Automated mineralogy for quantification and partitioning of metal(loid)s in particulates from mining/smelting-polluted soils: Environmental Pollution, v. 266, p. 115118, doi:10.1016/J.ENVPOL.2020.115118.

Vítková, M., Ettler, V., Šebek, O., Mihaljevič, M., Grygar, T., and Rohovec, J., 2009, The pH-dependent leaching of inorganic contaminants from secondary lead smelter fly ash: Journal of Hazardous Materials, v. 167, p. 427–433, doi:10.1016/J.JHAZMAT.2008.12.136.

Vrtiška Luboš, Radana Malíková, and Jiří Sejkora, 2016, Zajímavý výskyt fosfátů v okolí Líštěnce u Votic (Česká republika): Bull. mineral.-petrolog. Odd. Nár. Muz. (Praha), v. 24, p. 114–131.

Wei, H., Liu, Y., Zhang, J., Li, S., Zhong, X., and Xiang, H., 2021, Leaching of simulated acid rain deteriorates soil physiochemical and mechanical properties in three agricultural soils: CATENA, v. 206, p. 105485, doi:10.1016/J.CATENA.2021.105485.

Xu, D.M., Fu, R.B., Wang, J.X., and An, B.H., 2022, The geochemical behaviors of potentially toxic elements in a typical lead/zinc (Pb/Zn) smelter contaminated soil with quantitative mineralogical assessments: Journal of Hazardous Materials, doi:10.1016/j.jhazmat.2021.127127.

Xuexin, S., 1984, Minor elements and ore genesis of the Fankou lead-zinc deposit, China: Mineralium Deposita 1984 19:2, v. 19, p. 95–104, doi:10.1007/BF00204667.

Yang, C., Chen, Y., Peng, P., Li, C., Chang, X., and Wu, Y., 2009, Trace element transformations and partitioning during the roasting of pyrite ores in the sulfuric acid industry: Journal of Hazardous Materials, v. 167, p. 835–845, doi:10.1016/J.JHAZMAT.2009.01.067.

Yang, C., Lu, G., Xie, Y., Guo, L., Chen, M., Ge, L., and Dang, Z., 2021, Sulfate migration and transformation characteristics in paddy soil profile affected by acid mine drainage: Environmental Research, v. 200, p. 111732, doi:10.1016/J.ENVRES.2021.111732.

Ye, C., Ariya, P.A., Fu, F., Yu, G., and Tang, B., 2021, Influence of Al(III) and Sb(V) on the transformation of ferrihydrite nanoparticles: Interaction among ferrihydrite, coprecipitated Al(III) and Sb(V): Journal of Hazardous Materials, v. 408, p. 124423, doi:10.1016/J.JHAZMAT.2020.124423.

Zhang, Y., Labianca, C., Chen, L., De Gisi, S., Notarnicola, M., Guo, B., Sun, J., Ding, S., and Wang, L., 2021, Sustainable ex-situ remediation of contaminated sediment: A review: Environmental Pollution, v. 287, p. 117333, doi:10.1016/J.ENVPOL.2021.117333.

Zhou, S., Li, X., Zhou, Y., Min, C., and Shi, Y., 2020, Effect of phosphorus on the properties of phosphogypsum-based cemented backfill: Journal of Hazardous Materials, doi:10.1016/j.jhazmat.2020.122993.

El Zrelli, R. et al., 2018, Characterization of phosphate rock and phosphogypsum from Gabes phosphate fertilizer factories (SE Tunisia): high mining potential and implications for environmental protection: Environmental Science and Pollution Research, v. 25, p. 14690–14702, doi:10.1007/s11356-018-1648-4.

Supporting information for Chapter 2

The leaching behaviors of potentially toxic lead, zinc, and sulfate in the pyrite ash: mineralogical assessments and environmental implications

Yikai Liu[1]; Simone Molinari[1,*]; Maria Chiara Dalconi[1]; Luca Valentini[1]; Giulia Ricci[1]; Claudio Carrer[2]; Giorgio Ferrari[3]; Gilberto Artioli[1]

[1] *Department of Geosciences and CIRCe Centre, University of Padua, via G. Gradenigo 6, 35129, Padua, Italy*

[2] *Magistrato alle Acque di Venezia Ufficio Tecnico Antinquinamento Laboratorio CSMO, Padova, Italy*

[3] *Mapei S.p.A., via Cafiero 22, 20158, Milan, Italy*

Table.S1. XRD instrument settings

Parameters	Settings
Radiation source	Cobalt
Detector	X'Celerator detector
Geometry	Bragg-Brentano geometry
Optics	Soller slits 0.04 rad.; Bragg-Brentano^{HD}
2θ range	3-84°
Step size	0.017°
Time per step	100 s

Table.S2. Modeling input

Elements	Minerals	Equilibrium equations	Log k	Initial assemblages (mol/100g)[a]
Ca	Gypsum	$CaSO_4 \cdot 2H_2O = Ca^{2+} + SO_4^{2-} + 2H_2O$	-4.6	0.08865
	Portlandite	$Ca(OH)_2 + 2H^+ = Ca^{2+} + 2H_2O$	22.7	0.00000
	Calcite	$CaCO_3 = CO_3^{2-} + Ca^{2+}$	-8.5	0.00000
Fe	Hematite	$Fe_2O_3 + 6H^+ = 2Fe^{3+} + 3H_2O$	-4.0	0.45074
	Schwermannite	$Fe_8O_8(OH)_{4.8}(SO_4)_{1.6} + 20.8H^+ = 8Fe^{3+} + 1.6SO_4^{2-} + 12.8H_2O$	18	0.00000
	Jarosite(K)	$KFe_3(SO_4)_2(OH)_6 + 6H^+ = 3Fe^{3+} + K^+ + 2SO_4^{2} + 6H_2O$	-14.8	0.01519(0.00608)[b]
	Iron hydroxide (amorphous)	$Fe(OH)_3 + 3H^+ = Fe^{3} + 3H_2O$	-4.9	0.00000
	Jarosite(Pb)	$Pb_{0.5}Fe_3(SO_4)_2(OH)_6 + 6H^+ = 3Fe^{3+} + 0.5Pb^{2+} + 2SO_4^{2-} + 6H_2O$	-8.1	0.00000
Zn	Hydrozincite	$Zn_5(CO_3)_2(OH)_6 + 6H^+ = 5Zn^{2+} + 2CO_3^{2-} + 6H_2O$	9.5	0.00000
	Zincosite	$ZnSO_4 = Zn^{2+} + SO_4^{2-}$	3.0	0.00010
	$ZnSO_4 \cdot H_2O$	$ZnSO_4 \cdot H_2O = Zn^{2+} + SO_4^{2-} + H_2O$	-0.6	0.00000
	Zinc hydroxide (amorphous)	$Zn(OH)_2 + 2H^+ = Zn^{2+} + 2H_2O$	12.5	0.00000
	Zinc hydroxide (α)	$Zn(OH)_2 + 2H^+ = Zn^{2+} + 2H_2O$	12.2	0.00000
	Zinc hydroxide (β)	$Zn(OH)_2 + 2H^+ = Zn^{2+} + 2H_2O$	11.8	0.00000
	Zinc hydroxide (γ)	$Zn(OH)_2 + 2H^+ = Zn^{2+} + 2H_2O$	11.7	0.00000
	Zinc hydroxide (ε)	$Zn(OH)_2 + 2H^+ = Zn^{2+} + 2H_2O$	11.4	0.00000
	Smithsonite	$ZnCO_3 = Zn^{2+} + CO_3^{2-}$	-10.0	0.00000
	$ZnCO_3{:}H_2O$	$ZnCO_3 \cdot H_2O = Zn^{2+} + CO_3^{2-} + H_2O$	-10.3	0.00000
	Bianchite	$ZnSO_4 \cdot 6H_2O = Zn^{2+} + SO_4^{2-} + 6H_2O$	-1.8	0.00000
	Goslarite	$ZnSO_4 \cdot 7H_2O = Zn^{2+} + SO_4^{2-} + 7H_2O$	-2.0	0.00000
Pb	Anglesite	$PbSO4 = Pb^{2+} + SO_4^{2-}$	-7.8	0.00207
	Cerrusite	$PbCO_3 + H^+ = HCO^{3-} + Pb^{2+}$	-3.2	0.00000
	Hydrocerussite	$Pb_3(CO_3)_2(OH)_2 + 4H^+ = 2H_2O + 2HCO^{3-} + 3Pb^{2+}$	1.9	0.00000
	Kintoreite	-[c]	-	0.00259
Si	Quartz	-	-	0.04616

Notes: [a] The mole concentration of the minerals for 100 grams of the soil; [b] The maximum mole content of the phase that can dissolve in the solution; [c] This phase is assumed to be stable in the simulation.

Table.S3. Chemical compositions of the Z1B samples.

Elements (wt%)	Original	Normalized
L.O.I	8.63	0.00
Na_2O	0.21	0.23
MgO	0.17	0.19
Al_2O_3	0.64	0.70
SiO_2	5.82	6.37
P_2O_5	0.45	0.49
K_2O	0.21	0.23
CaO	7.87	8.61
TiO_2	0.07	0.08
Fe_2O_3	75.94	83.11

Table.S4. Contamination level of the soil sample.

pH	UNI EN 12457-4:2004		4.6	±0.2
Alluminio	UNI EN ISO 16170 2016	mg/kg	978	±68.46
Arsenico	UNI EN ISO 16170 2016	mg/kg	246	±19.68
Bario	UNI EN ISO 16170 2016	mg/kg	192	±11.52
Berillio	UNI EN ISO 16170 2016	mg/kg	<2	-
Boro	UNI EN ISO 16170 2016	mg/kg	<5	-
Cadmio*	UNI EN ISO 15586:2004	mg/kg	1.98*	±0.28
Cobalto	UNI EN ISO 16170 2016	mg/kg	26	±1.82
Cromo	UNI EN ISO 16170 2016	mg/kg	20	±1.62
Ferro	UNI EN ISO 16170 2016	mg/kg	414500	±20725
Nichel	UNI EN ISO 16170 2016	mg/kg	3.1	±0.22
Piombo	UNI EN ISO 16170 2016	mg/kg	11910	±714.6
Rame	UNI EN ISO 16170 2016	mg/kg	340	±19.04
Selenio	UNI EN ISO 16170 2016	mg/kg	182	±11.83
Tallio	UNI EN ISO 16170 2016	mg/kg	<100	-
Vanadio	UNI EN ISO 16170 2016	mg/kg	6.6	±0.43
Zinco	UNI EN ISO 16170 2016	mg/kg	582	±42.49

**measured by atomic absorption spectroscopy (AAS)*

Table.S5. Possible assignments of the Raman spectra.

S1 (cm^{-1})	S2 (cm^{-1})	S3 (cm^{-1})	S4 (cm^{-1})	Possible assignments
221.7	214.9	222.4	219.5	O-Fe
-	-	242.9	-	
298.7	-	291.2	-	O-Fe
355.0	337.6	-	340.5	O-Fe
-	-	410.1	-	
433.0	437.3	436.4	437.4	O-Fe
557.0	551.8	-	-	$v_4\,PO_4^{3-}$
624.4	621.7	620.5	621.9	$v_4\,SO_4^{2-}$
-	976.5	-	-	$v_1\,PO_4^{3-}$
1005.6	1003.2	1004.8	1006.7	$v_1\,SO_4^{2}$
1103.5	1101.3	1101.7	1102.8	$v_3\,SO_4^{2-}$ or $v_3\,PO_4^{3-}$
1156.8	1164.5	1168.2	1169.3	$v_3\,SO_4^{2-}$ or $v_3\,PO_4^{3-}$

Table.S6. Results of pH-dependent leaching tests and the European standard

pH values / Elements	1.98	2.80	4.64	5.02	6.50	8.40	9.04	10.43	12.00	**Limit [a]**	**Limit [b]**
Pb^{2+}	0.015	0.014	0.009	0.006	0.001	0.000	0.000	0.001	0.012	**0.000**	**0.000**
(mmol/L)	93	48	17	76	11	63	38	01	07	**05**	**24**
Fe^{3+}	0.268	0.028	0.000	0.001	0.000	0.000	0.000	0.003	0.000	**0.003**	-
(mmol/L)	58	65	88	49	38	72	91	40	32	**58**	
Zn^{2+}	0.074	0.074	0.053	0.055	0.000	0.000	0.000	0.000	0.000	**0.000**	**0.000**
(mmol/L)	92	92	52	05	21	12	03	12	21	**05**	**05**
SO_4^{2-} (mmol/L)	9.06	-	11.45	-	8.02	-	12.49	-	48.93	**2.60**	**2.60**

Notes: [a] Standard based on Decreto legislativo 3 aprile 2006, n. 152, Norme in materia ambientale;

[b] Standard based on Decreto 5 aprile 2006, n. 186, Regolamento recante modifiche al decreto ministeriale 5 febbraio 1998.

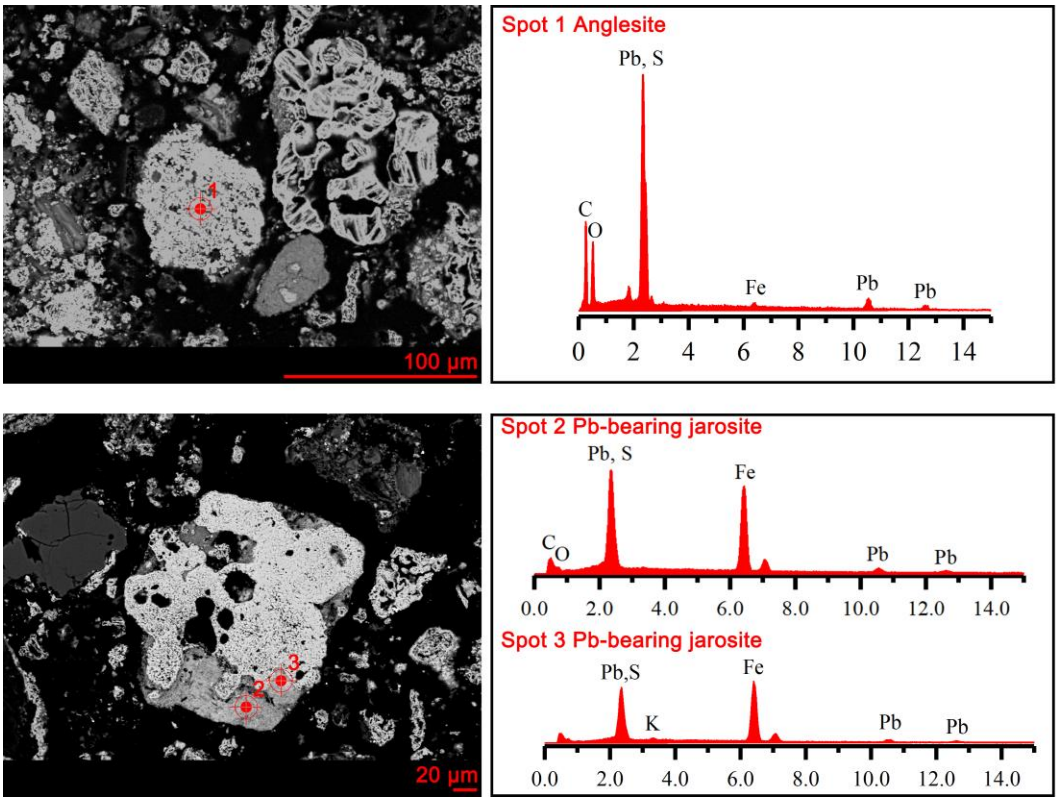

Figure.S1. EDS spectrum correlated to Fig.1

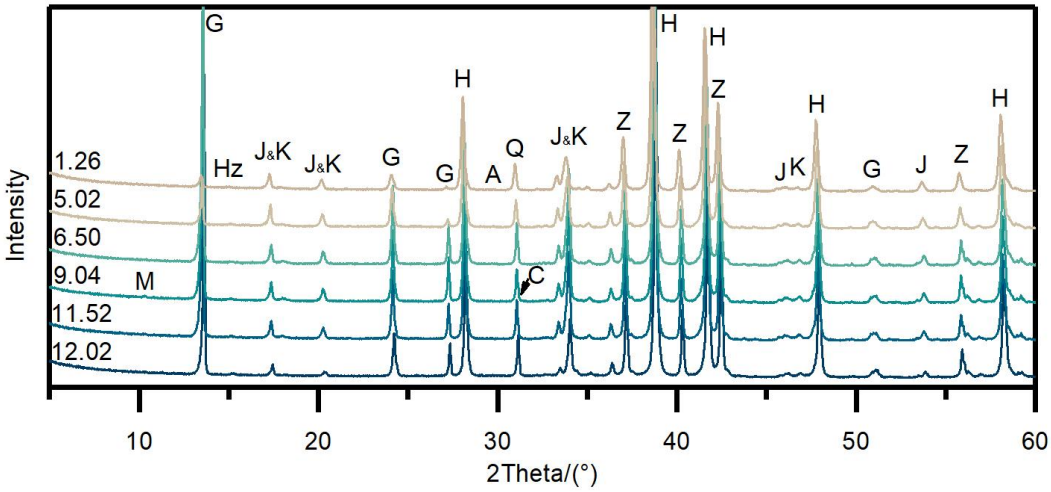

Figure.S2. XRD patterns of the residues after leaching. The number is marked to represent the pH values of the leachate. A: anglesite; C: calcite; G: gypsum; H: hematite; Hz: hydrozincite; J: jarosite; K: kintoreite; M: muscovite; Q: quartz; Z: zincite.

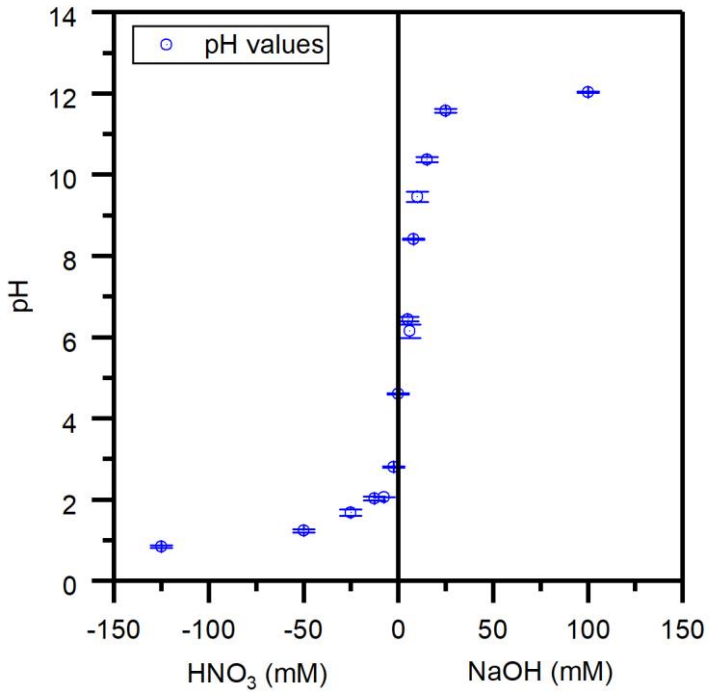

Figure.S3. Buffering capacity of the soil samples.

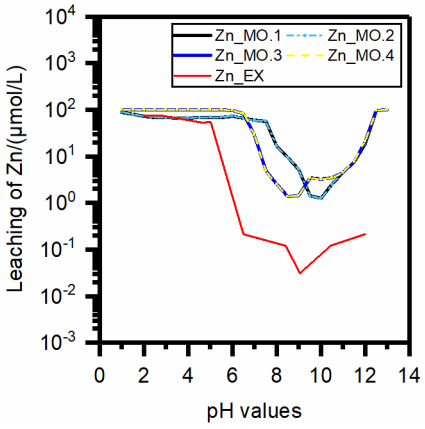

Figure.S4. The leaching behavior of Zn with or without adsorption assumption. Zn_Ex is the data from experiments, MO.1 and MO.2 are the same data as given in Fig.4b, and MO.3 (100 wt% jarosite) and MO.4 (40 wt% jarosite) indicate the modeling with ferrihydrite adsorption.

Chapter 3

Green in-situ remediation of pyrite ash: enhanced Pb retention through negative carbon binder strategies

Yikai Liu[1]; Simone Molinari[1,*]; Maria Chiara Dalconi[1]; Luca Valentini[1]; Maurizio Pietro Bellotto[2]; Giorgio Ferrari[3]; Roberto Pellay[4]; Graziano Rilievo[5]; Fabio Vianello[5]; Gabriella Salviulo[1]; Gilberto Artioli[1]

1 Department of Geosciences and CIRCe Centre, University of Padua, via G. Gradenigo 6, 35129, Padua, Italy

2 OPIGEO Srl, Montegalda, Vicenza, Italy

3 Mapei S.p.A., via Cafiero 22, 20158, Milan, Italy

4 TEVGroup S.r.l., via Romea 8, 30034, Mira (Venice), Italy

5 Department of Comparative Biomedicine and Food Science, University of Padova, Viale dell'Università 16, 35020 Legnaro, Italy

Graphical abstract

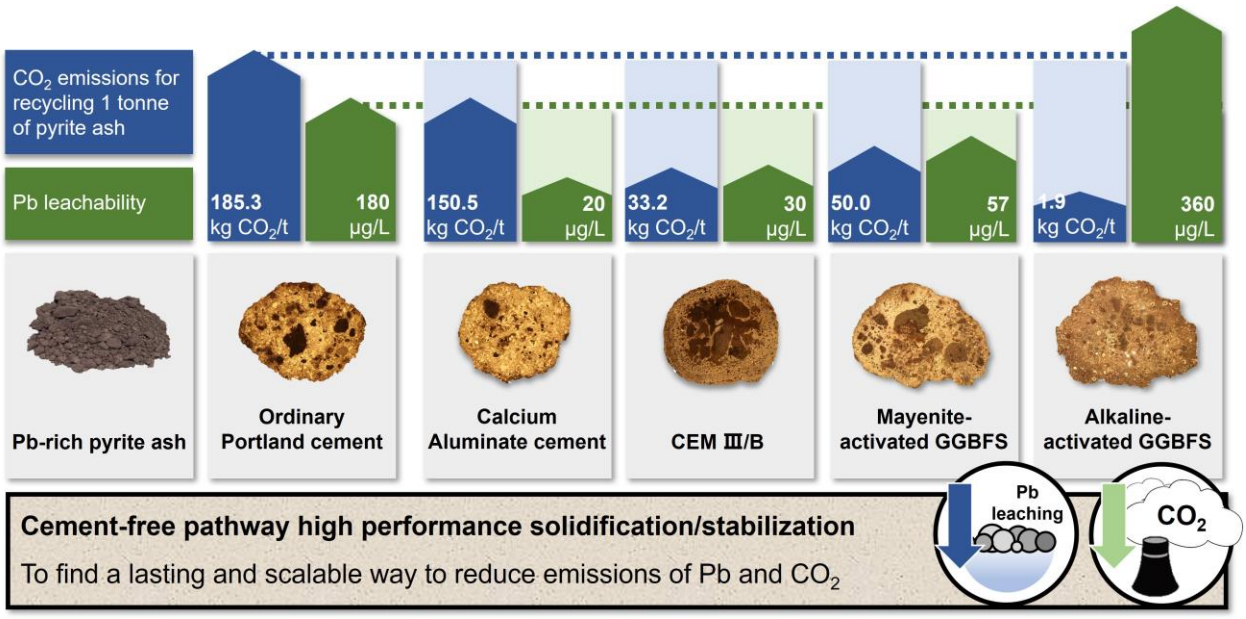

This chapter is in preparation

Abstract

Pyrite ash is a hazardous waste due to its high potential for releasing toxic elements into the natural environment, which requires careful stewardship to minimize the exposure risks. Although the use of ordinary Portland cement (OPC) has been proven a cost-effective binder for in-situ remediation of pyrite ash, the substantial greenhouse gas emission and durability concerns attributed to the OPC binder place strain on this strategy. To solve this issue, we tailored four alternative binders (CEM/IIIB, calcium aluminate cement, mayenite-ground-granulated blast-furnace slag mixture, and alkaline activated ground-granulated blast-furnace slag) as OPC-free/mitigation solutions to immobilize the pyrite ash, with the perspectives of promoting the toxic elements retention and mitigating the anthropogenic CO2 emissions. The comprehensive characterization of the stabilized products revealed the different interactions between the applied binder scenarios and pyrite ash, which clarifies the roles of hydration products and the microstructure of the binding systems to the Pb leachability. Further, we quantified the cradle-to-gate carbon footprint and cost analysis attributed to each binder-pyrite ash system, finding that the application of these alternative binders could be pivotal in the envisaged carbon-neutral world if the growth of the cement-free roadmap continues. The application of CEM/IIIB may offer a profitable and sustainable alternative to traditional OPC-based solidification/stabilization. The overall results underscore the potential immobilization mechanisms of Pb in multiple OPC-free/mitigation binder systems and highlight the urgent need to bridge the zero-emission insights to sustainable in-situ solidification/stabilization technologies.

Keywords

Lead, Pyrite ash, Solidification/stabilization, CO_2 mitigation, solid waste management

1. Introduction

Soil plays a critical role in supporting ecosystems and human society by providing a habitat for the earth's species and serving as a medium for crop production (Hou et al., 2020; He et al., 2022). However, the unprecedented urbanization rates and unparalleled anthropogenic activities in the last decades pose widespread soil contamination and degradation issues (Vergara and Tchobanoglous, 2012; Palansooriya et al., 2020; Chang et al., 2022). Potentially toxic element accumulation is a major threat to ensuring sustained soil management due to its toxicity, ubiquity, and non-biodegradability (Monterroso et al., 2014; Yin et al., 2018; Xue and Liu, 2021). Lead (Pb) is one of the most commonly encountered heavy metal contaminants in soils, accounting for 9% of all soil quality exceedances (Hou et al., 2020). Concurrently, technologies are being developed with the aim of recycling the Pb contaminants into value-added products to be used as additives in brick manufacturing (Ma et al., 2021)

and metal recycling through magnetic and gravity separation (Li et al., 2018; Liu et al., 2022). Although these attempts offer opportunities to utilize the Pb contamination in a high-value and sustainable pathway, some drawbacks, such as energy consumption, environmental pollution, and serious equipment corrosion, are shown due to the pervasive intergrowth between the valuable resources and toxic elements (Alp et al., 2009; Zhang et al., 2021a). Up to date, some studies have tried to efficiently remediate and recycle the Pb-rich solid wastes on a large scale through the in-situ solidification/stabilization (S/S) process (Navarro et al., 2011; Wang et al., 2018; Contessi et al., 2020; Calgaro et al., 2021). Typically, as one of the most widely used artificial materials in the industry (Habert et al., 2020; Bui Viet et al., 2020), ordinary Portland cement (OPC) is herein extensively applied in the S/S process due to its unique properties and simplicity of use (Pu et al., 2021; Ouhadi et al., 2021). This management is deemed to effectively convert the Pb-riched solid waste to a physico-chemically stable solid assemblage that can immobilize Pb in a relatively less mobile form through the mechanisms of adsorption, chemical bonding (surface complexation, precipitation, and coprecipitation), and physical micro-and/or macro-encapsulation (Chen et al., 2009; Guo et al., 2017).

However, a growing body of evidence has shown that the use of OPC is insufficient for Pb immobilization at high concentrations (Contessi et al., 2020; Pu et al., 2021). A previous study has already confirmed that using 20 wt% OPC to stabilize the contaminated soil with a 5000 mg/kg of Pb concentration cannot fulfill the engineering requirements both in the view of mechanical properties and Pb leachability (Pu et al., 2021). Further, the uncertain durability of OPC related to different environmental stresses questioned the long-term stability of the solidified matrix, which has the risk of Pb release and exposure (Guo et al., 2017; Sun et al., 2022). Especially in strongly acidic environments, the hydration products (e.g., C-S-H gel, ettringite, and portlandite) and hydroxide precipitates (e.g., $Pb(OH)_2$) that form in alkaline conditions are dissolved, increasing the vulnerability to Pb leaching (Halim et al., 2005; Du et al., 2014). Another growing issue is the greenhouse gas emission and energy consumption arising from OPC production (Habert et al., 2020; Miller et al., 2021). It is estimated that the overall CO_2 emission of the entire cement cycle accounts for 10% of total global energy-related emissions, around four gigatonnes per year (Watari et al., 2022). Many studies have described alternative binder technologies that can partially or entirely replace the use of OPC, moving the S/S process to the carbon neutrality vision (Chen et al., 2019, 2022a; Guo et al., 2021). For instance, blending binder within the binder is confirmed as a low-carbon strategy to promote the sustainability of the fly ash S/S process and ensure Pb retention of stabilized products (Chen et al., 2022a). The application of magnesium cement broadens the pH range of stabilized products to less alkaline conditions compared to the traditional OPC (Naeem et al., 2021; Wang et al., 2022b). In addition, industrial by-products, such as ground granulated blast furnace slag (GGBFS)

(Wang et al., 2022a), fly ash (Pu et al., 2021), and copper slag (Chen et al., 2021a), also demonstrate capabilities for enhancing the Pb immobilization. But considering the engineering concerns in the realistic conditions referring to the availability of raw materials, the most critical profitable issue, and the confidence in the long-term performance, further works related to the heavy metal retention mechanisms and the overall CO_2 emissions and economic value quantification are still required to fill these gaps (Shen et al., 2016; Habert et al., 2020).

In view of this, we used multiple pyrite ash-binder systems, a traditional binder (OPC) and four alternative binders (CEM III/B, calcium aluminate cement (CAC), mayenite-activated GGBFS (MBS), and alkaline-activated GGBFS (ABS), to immobilize the pyrite ash with high lead and sulfates contents. Mineralogical and microstructural characterization and leaching procedures were applied to investigate the S/S effectiveness of different scenarios. Subsequently, the CO_2 emission and potential economic cost of each binder strategy were quantified and elucidated. The primary objectives of this work are to provide scientific insights into (1) achieving net-zero emissions of the S/S process of pyrite ash with high Pb contaminant content without relying on the OPC and (2) elaborating different physico-chemical Pb stabilization mechanisms corresponding to the applied binders.

2. Material and methods

2.1. Materials sampling and pelletization process

The pyrite ash is collected from a phosphate fertilizer factory devoted to the pyrite roasting process for sulfuric acid production. Five different binders, OPC, CEM III/B, CAC, MBS, and ABS, are applied to the pelletization process (Scanferla et al., 2009; Contessi et al., 2020). The detailed mix proportions are given in Table.1.

Table.1. Mixtures component proportion.

Pellet labels	Binder (wt%)					Pyrite ash (wt%)	Water (wt%)
	OPC	CEM III/B	CAC	MBS[3]	ABS[4]		
CP[1]	16.4	-	-	-	-	65.2	18.4
CB[2]	-	25.0	-	-	-	75.0	25.8
CC[1]	-	-	16.3	-	-	64.9	18.8
MB[1]	-	-	-	16.3	-	64.6	19.1
AB[1]	-	-	-	-	16.5	61.4	19.2

Notes: [1] After the pelletization, the OP, CC, MB, and AB pellets were sealed in plastic bags with daily water spraying, [2] CB pellets were sealed in plastic bags but without additional water spraying, [3] the MBS binder is a mixture of ground granulated blast-furnace slag and mayenite, and [4] the ABS is composed by the ground granulated blast-furnace slag, sodium silicates, and a minor content of dispersant.

2.2. Characterization methods

The XRD measurements were conducted using a Malvern Panalytical X'Pert Pro diffractometer operating in Bragg-Brentano geometry, with a scan range from 3° to 84° 2θ and a step interval of 0.02° (Table.S1). To quantify the amorphous content of samples, known amounts of ZnO (ACS Reagent, Thermo Fisher Scientific Inc., Waltham, USA) were mixed with the powdered pellets as the internal standard. Profex (Doebelin and Kleeberg, 2015) and Highscore Plus were used for mineral phase detection and composition quantification. The SEM/EDS analyses (CamScan MX3000, Applied Beams, USA) were performed on the polished and carbon-coated sections of pellets. Before the experiments, all the pellets were dried at 105 ± 5°C.

2.3. Leaching procedures and ions concentration determination

The leaching tests were performed on the cured pellets following the standard UNI 12457-4:2004 (British Standards Institution, 2004). Before the Inductively Coupled Plasma Mass Spectrometry (ICP-MS) and Inductively Coupled Plasma Optical Emission Spectroscopy (ICP-OES) analysis, the eluates were filtered at 0.45 μm and then acidified to pH<2 by adding a proper amount of HNO_3 (Fluka, 65% pure grade). Al, Fe, and Pb were measured by ICP-MS (ELAN DRC II, Perkin, Elmer) following the method UNI EN ISO 17294-2 (2016). The limit of detection was 1, 5, and 0.1 μg $L^{-1,}$ respectively. Sulfate concentration was measured by ICP-OES (OPTIMA 2100 DV, Perkin, Elmer) following method CNR IRSA 5(2) (1985). The detection limit was 1 mg L^{-1}.

2.4. Quantifying the CO2 emission related to the preparation of the mixture

The CO_2 emissions for the S/S process were analyzed from a "cradle-to-gate" perspective of the environmental impacts of the engineered different scenarios (Cao et al., 2020; Chen et al., 2022b). The CO_2 emission associated with OPC production and water supply system is conventionally given as 852 kg CO_2/t (Ravikumar et al., 2021) and 2.50 kg CO2/m3 (Chang et al., 2012). The carbon footprint of commercial alternative binders, CEM III/B and CAC binder, are estimated as 213 (García-Segura et al., 2014) and 596 kg CO_2/t (Chen et al., 2021b; Seo et al., 2022), respectively. The MBS binder comprises the GGBFS and mayenite, which account for 52 and 412 kg CO_2/t emissions during their production (Ude, 2010; Fernández-González et al., 2018). To note, the mayenite used in this work is collected from the electric arc furnace slag, which is the by-product generated from steel production with a primary component of mayenite. Because of the lack of a reliable dataset to express the carbon footprint related to recycled mayenite, the carbon emissions data applied here is from synthetic mayenite. Herein, the overall CO_2 emissions associated with MBS are assumed as 195 CO_2/t. The ABS binder is mainly made of GGBFS and sodium silicates (Kwon and Wang, 2019; Santana-Carrillo et

al., 2022), of which the CO_2 emissions are assessed as 60 CO_2/t. Table.S2 displays the carbon footprint details related to each binder scenario and the parameters for product benefit. Noteworthy, the potential CO_2 capture of each binder scenario could be 100% in terms of all the available calcium oxide converted to calcium carbonates. But factors such as the physical porosity and chemical composition of the binding matrix would influence the maximum carbonation degree (Skocek et al., 2020). Especially this process would take years (Habert et al., 2020). Therefore, the sponge effect and CO_2 uptake capacity of the pellets are calculated based on the carbonates species quantified in the XRD characterization as the maximum carbonation that can be effectively achieved (Cao et al., 2020; Habert et al., 2020).

2.5. The estimation of sulfuric acid and pyrite ash production in the next decade and the calculation of Pb immobilization efficiency.

The annual generation of pyrite ash is estimated by the production of sulfuric acid, which is the main product produced from pyrite ores roasting. The annual sulfuric acid production is calculated based on the databases (National Minerals Information Center, 2022; Precedence Research, 2022), of which the primary sources for sulfuric acid include base metal smelters (36%), elemental sulfur (43%), pyrite ores (19%), and others (2%). The by-product-to-main product (pyrite ash to sulfuric acid, 0.8 t/t) ratio is derived from the literature (Zhang et al., 2018), with approximately 70 wt% of the generated pyrite ash being discarded on the ground (Ma et al., 2021). The calculated sulfuric acid production and pyrite ash generation in the next decade are given in Table.S3. The Pb immobilization efficiency is estimated through the leaching tests of unstabilized pyrite ash and stabilized products, using the difference of the leached Pb concentration divided by the calculated carbon footprint and financial expenses of different binder scenarios (section 2.4.). Subsequently, we examined the Pb concentrations variability in pyrite ash among 31 different records (Table.S4). The detected values range from 113 to 43198 mg/kg, with most records (>80%) lower than 5000 mg/kg.

3. Results

3.1. Pb retention in the traditional binder: characterization of CP pellets

In CP pellets, the typical crystalline hydration product, ettringite (5.5 wt%), and principal unhydrated clinker phases, alite and belite (1.6 wt%, in sum), were clearly detected in the XRD patterns (Fig.1a and b). Hematite (54.0 wt%), jarosite (2.1 wt%), and gypsum (6.7 wt%) were also present in the pellets. The amorphous content, primarily composed of C-S-H gel (Ouhadi et al., 2021; Yan et al., 2022), was quantified as 24.2 wt%. Portlandite was not observed in the XRD diffractogram. The absence of portlandite is possibly related to the carbonation with the atmospheric CO_2 because approximately 4.4

wt% of calcite was estimated (Du et al., 2019). SEM/EDS analysis (Fig.1c and d) gives an indication that the Pb is trapped within the cementitious matrix. The dark rims around the unhydrated cement clinker particles (Fig.1c) were considered to be the amorphous hydration products, C-S-H gel, because of the high Ca and Si fraction detected (Fig.1e and Fig.S1). The presence of Pb verifies the observation reported in Guo et al.'s work (2017) that Pb can be attached to the tetrahedral silicate chain of the C-S-H structure. In addition, Pb (Fig.1d) is presented in the pyrite ash phases adjacent to the iron oxide particles (the bright assemblage in the backscatter image).

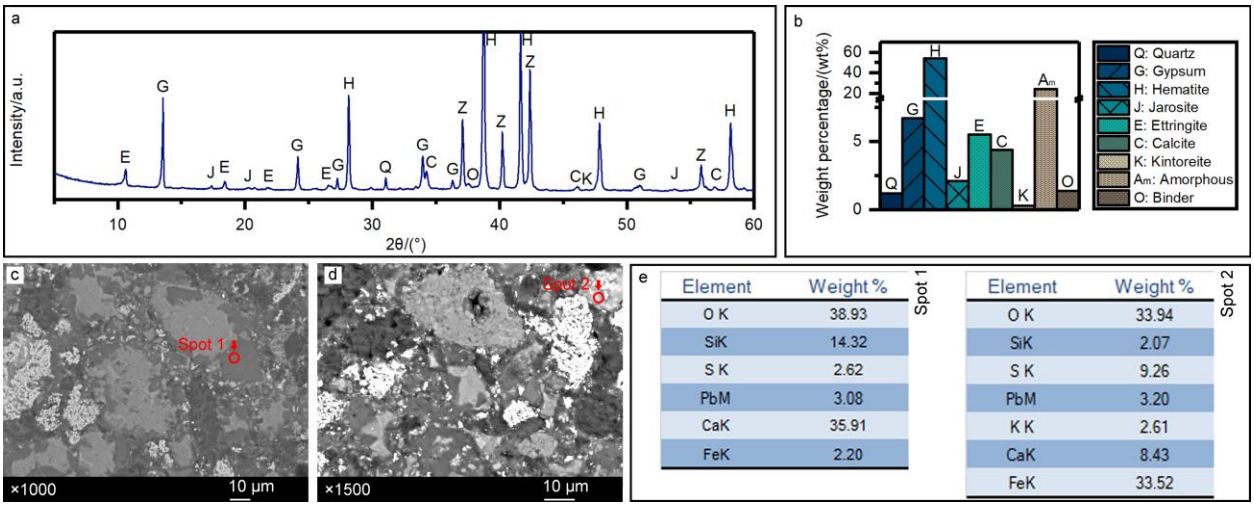

Figure.1. XRD and SEM/EDS results of the CP pellets. (a) XRD pattern of the pellets, (b) quantification results after subtracting the known amount of internal standard, (c) BSE image of CP pellets demonstrating the unhydrated cement particles and the cementitious matrix formed along their rims, (d) BSE image of CP pellets showing a mixture of hydrates and Pb-bearing phases, and (e) the correlated quantitative results of the spots marked in images c and d. The abbreviation O in image (a) means alite and belite.

3.2. Pb retention in the alternative binders: characterization of CB, CA, MB, and AB pellets

The XRD results of CB pellets (Fig.2a and b) illustrate that hematite is the main crystalline phase (52.0 wt%) detected. Meanwhile, the jarosite and gypsum, also originating from the pyrite ash, are observed at 4.4 and 9.2 wt%, respectively. The binder hydration products are ettringite (5.1 wt%) and amorphous phases (20.1 wt%) that mainly consist of C-(A)-S-H gel and amorphous aluminum hydroxide (Berthomier et al., 2021). Carbonates (vaterite and calcite) deriving from the carbonation of calcium species (e.g., portlandite and gypsum) at alkaline conditions (Morandeau et al., 2014; Yu et al., 2019) are quantified as 6.6 wt%. A minor proportion (0.5 wt%) of the crystalline Pb-bearing phase kintoreite is found, with the most pronounced diffraction peak being observed at 46.8° 2θ. The SEM/EDS images (Fig.2c-j) indicate that Pb preferentially distributes in the pyrite ash phases-rich

area (light grey matrix in Fig.2d, Fe and S enriched), with a trend toward dispersion throughout the cementitious matrix (Ca, Si, and Al area). Fig.2c shows that the porous iron oxide particles (hematite), along with the unreacted slag grains (unhydrated binder phases), remained in the pellets, which is well correlated with the XRD quantification results.

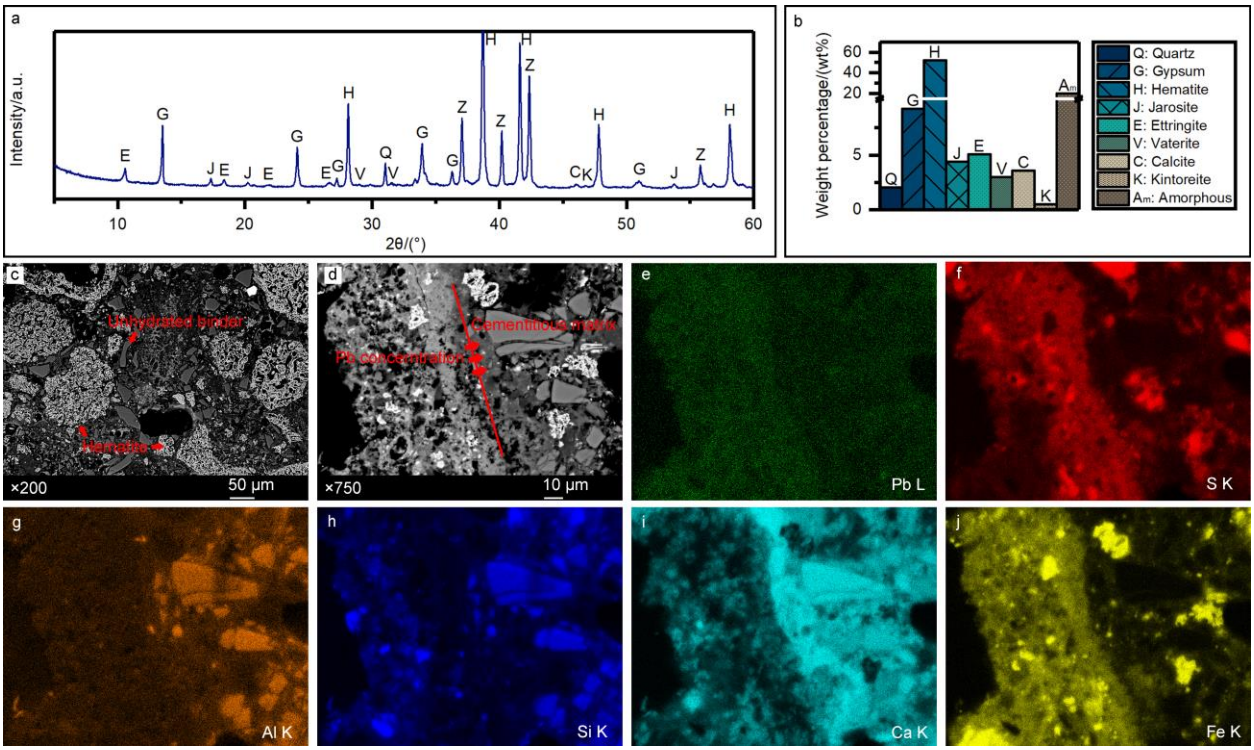

Figure.2. XRD and SEM/EDS results of the CB pellets. (a) XRD pattern of the pellets, (b) the quantification result related to the image (a), (c) BSE image of CB pellets illustrating the homogenous cementitious matrixes filled the space between the porous hematite particles and the unreacted slag particles, (d) BSE image of a Pb transition zone in CB pellets, indicating the Pb dissolved from the contaminated sample to the hydrates, and the elemental mapping of Pb (e), S (f), Al (g), Si (h), Ca (i), Fe (j).

XRD mineralogical analyses of the CA pellets (Fig.3a and b) show that the amount of precipitated ettringite (15.1 wt%) is approximately triple of the traditional binder samples (CP, 5.5 wt%). In turn, the amorphous content (10.7 wt%) is only half of the CP samples. This is because the CAC is mainly composed of $CaO{\cdot}Al_2O_3$ (CA), $CaO{\cdot}2Al_2O_3$ (CA2), and $12CaO{\cdot}7Al_2O_3$ (C12A7), therefore generating considerable ettringite, gibbsite (4.3 wt%), and metastable CAH hydrates species (e.g., CAH_{10}, C_2AH_8, and AH_3), instead of the C-S-H gel precipitation as the CP system (Hidalgo et al., 2009; Li et al., 2017). The sulfate phases (gypsum and jarosite) within the raw pyrite ash act as a sufficient supplier of sulfate ions at the early ages of hydration. However, as stated in the literature

(Chen et al., 2021b), the excessive dosage of ettringite formation may lead to unintended expansion and deteriorate the microstructures of the mixture. The cracks observed throughout the analyzed areas of CA pellets (Fig.3c) could be attributed to ettringite precipitation due to the drying process during the sample preparation (Bizzozero et al., 2014) and the high vacuum condition reached in the SEM experiments (Contessi et al., 2020). In Fig.3d, the areas rich in ettringite are characterized by small parallel cracks developing in a matrix of medium grey colors. Unlike the enrichment along the rims of unhydrated clinker particles in the CP pellets (Fig.1c), the presence of Pb in CA pellets (bright grey matrix) has a high correlation with the spatial distribution of Ca, Al, Fe, and S (Fig.3e and S2), inferring that Pb-bearing species are intermixed with ettringite through the adsorption and/or incorporation. Likewise, it is reported that the Pb, as a metal ion with similar sizes and charges, can substitute the divalent Ca cations in the ettringite structure and/or adsorption on charged surfaces (Vempati et al., 1995; Moon et al., 2013; Contessi et al., 2021).

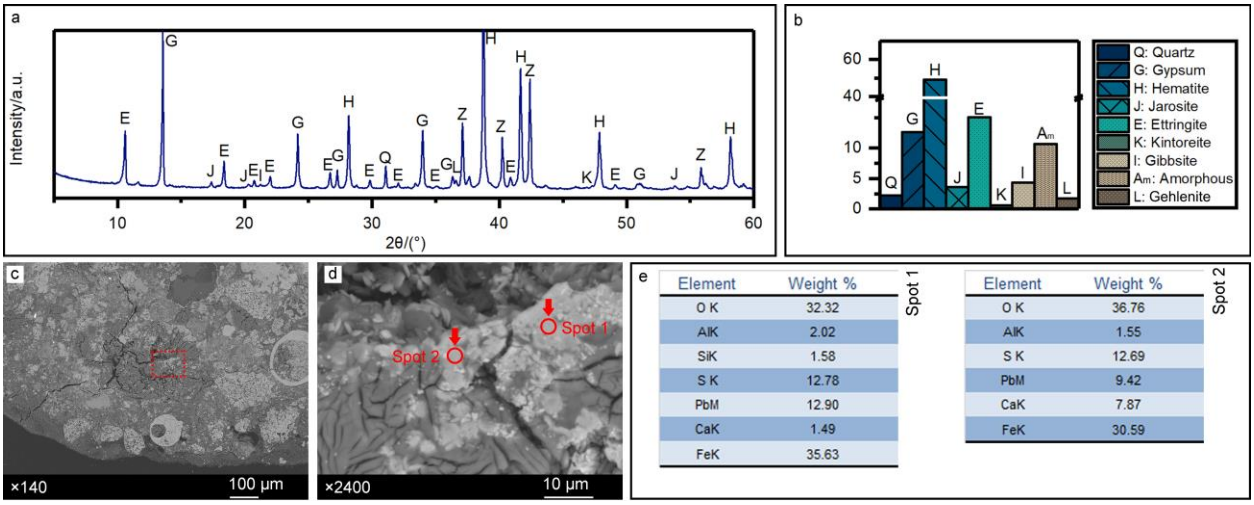

Figure.3. XRD and SEM/EDS results of the CA pellets. (a) the detected XRD spectra, (b) the quantification results, (c) the BSE images demonstrate the microstructures of CA pellets with several cracks being observed, (d) a higher magnification of the red dash rectangle marked area in image (c), and (e) the EDS analysis related to the spots marked in the image (d), illustrating the presence of Pb.

The pellets stabilized with MB binder present similar hydration products (Fig.4a and b) as the CP scenario, however, with more crystalline ettringite (14.7 wt%) and less amorphous components (16 wt%). Accordingly, the sulfate contents (gypsum 4.2 wt% and jarosite 5.3 wt%) are decreased. Further, although the mayenite and GGBFS are aluminate-rich materials like the CAC binder, the crystalline gibbsite is not observed in the XRD patterns. The carbonates species detected in CP and CB pellets (calcite and vaterite in Fig.1 and 2) are not present in the MB samples, indicating the low concentration

of calcium in the pore solutions, which is not conducive to the formation of portlandite and its subsequent carbonation. Noteworthy, the amorphous fraction can be partially attributed to unhydrated blast furnace slags, which are amorphous (Kirca et al., 2013; Gardner et al., 2015). SEM images evidence that the majority of the areas, showing a dense morphology, is mainly constituted by the aluminosilicates (Fig.4c and Fig.S4) and possibly C-(A)-S-H gel (Fig.4g, h, and i), with both unreacted slags and porous hematite particles (Fig.4e and j) being embedded within these binding matrices. The distribution of Pb in the hydration products is more likely to be homogeneously dispersed in the matrices, as the elemental maps reveal the dispersion of Pb in the Al, Ca, and Si enriched areas, which are typical elements deriving from cement. The high compatibility of Fe and Pb in the EDS analysis and elemental mapping (Fig.4f, j, and Fig.S3) evidence that the adsorption and coexistence of Pb in hematite still play a role in the Pb retention even at the cured MB pellets, which is ascertained previous findings that the Pb can be incorporated into defects or nanopores of hematite at basic conditions (Vu et al., 2013).

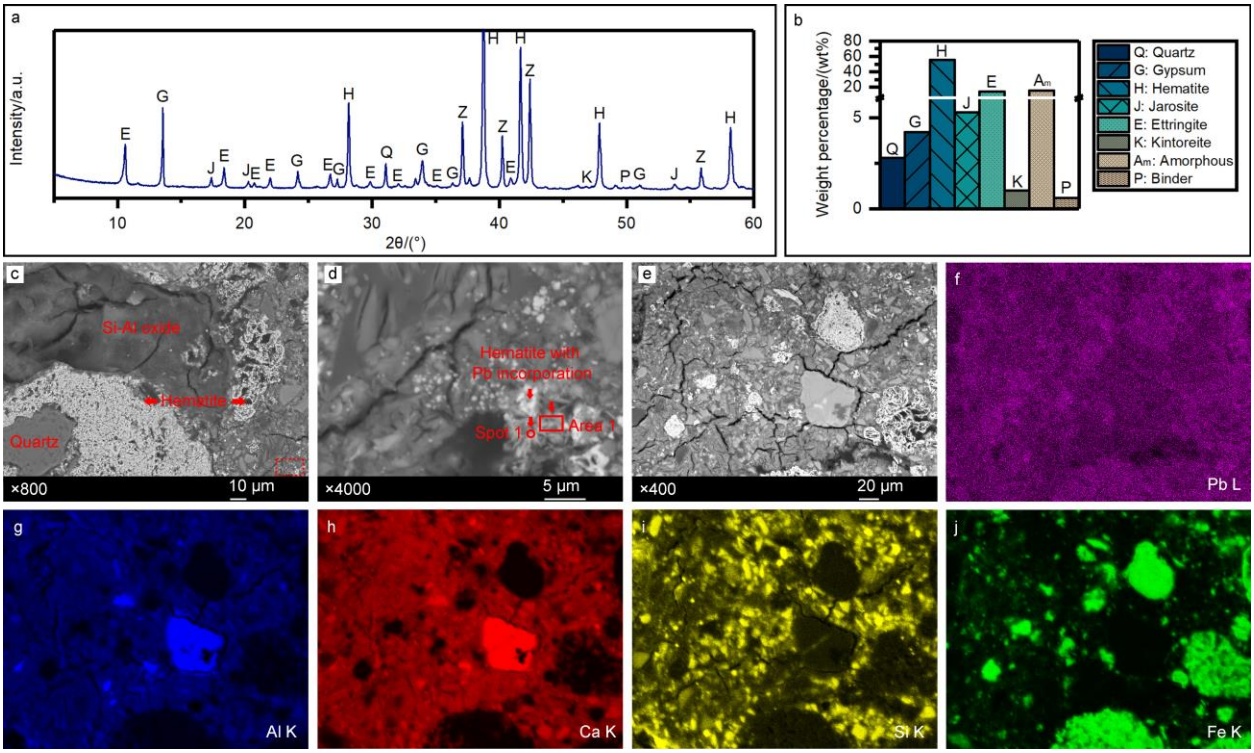

Figure.4. XRD results and SEM/EDS images for the MB pellets. (a) the XRD spectra of the detected pellets, (b) the correlated quantification results, (c, d, and e) the BSE images demonstrate the internal structures of MB pellets, (f) elemental mapping of Pb, (g) Al, (h) Ca, (i) Si, and (j) Fe.

XRD mineralogical analyses of the AB pellets show that the ettringite (0.3 wt%) formation is inhibited

in this system. The hematite (59.0 wt%), gypsum (10.9 wt%), jarosite (5.2 wt%), quartz (2.3 wt%), and kintoreite (0.9 wt%), which originate from the pyrite ash, account for over 78 wt% of the hydrated pellets fraction. Additionally, calcium carbonate (calcite in 2.1 wt%) is present in the system. However, the high fraction of angular light gray particles of various sizes rich in Ca, Al, and Si indicate that the starting slag has reacted to a low extent and contributes to a relatively substantial amorphous content (19.2 wt%). Furthermore, the Pb was preferentially distributed in Fe-rich areas, which could be associated with the alunite-jarosite family (e.g., K-jarosite, Na-jarosite, and kintoreite) observed in the raw pyrite ash. The overlapping of S (Fig.5m), Na (Fig.5l), K (Fig.5k), and P (Fig.5f) indicates that the Pb-rich assemblage might be a solid-solution series of jarosite group rather than an intermediate composition. But the incorporation trend towards the binding matrix (Ca, Si, and Al-rich area) is ongoing in the area neighboring the iron oxide particles, indicating that the dissolution and re-distribution of Pb have occurred along the dissolution and hydration of binder phases.

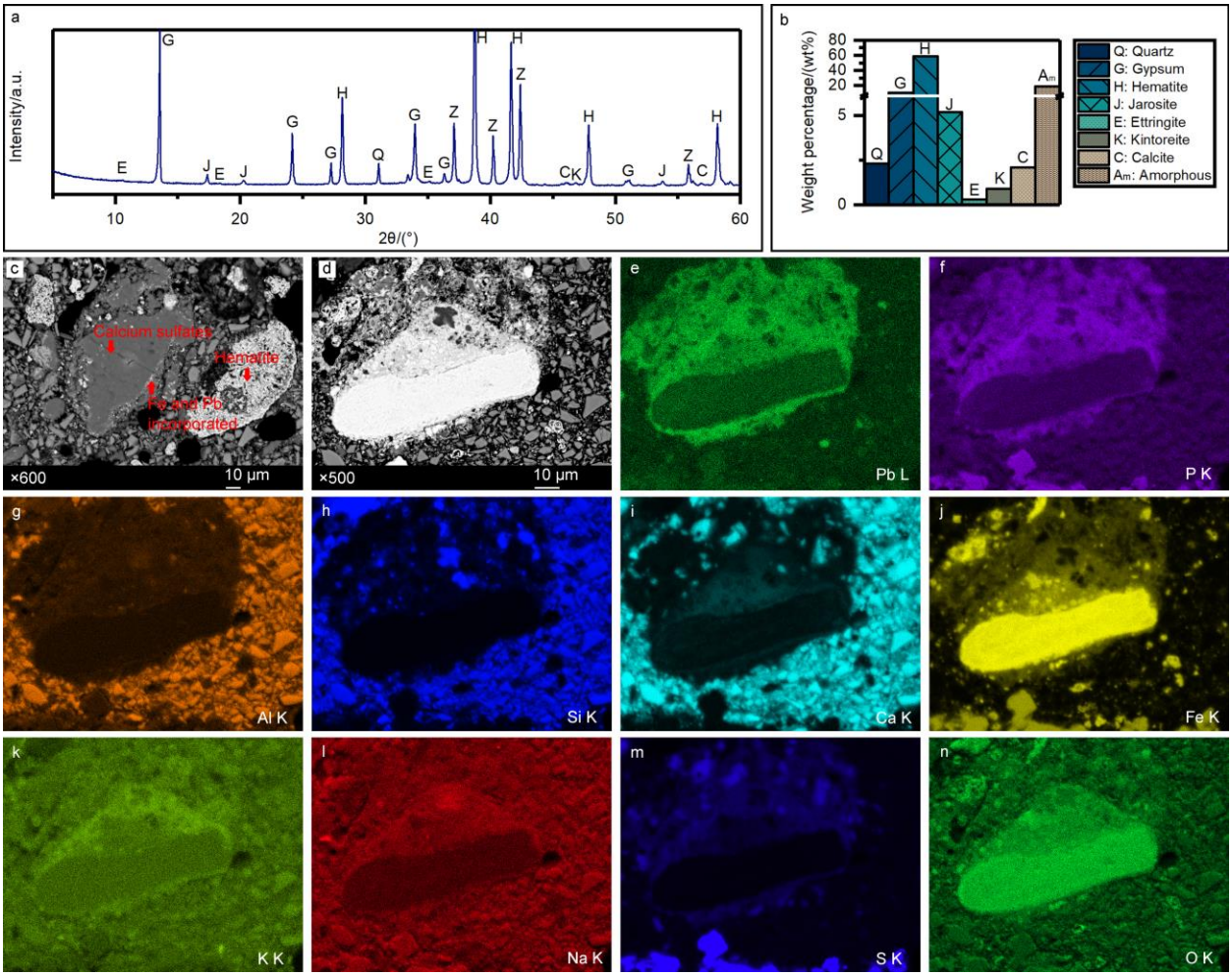

Figure.5. XRD characterization and SEM/EDS images for the AB pellets. (a) XRD spectra, (b) the quantification result, (c) BSE image of AB pellets illustrating the presence of unreacted slag

particles, (d) BSE image of a Pb transition zone in AB pellets, indicating the Pb dissolved from the iron oxides to the binding matrix, and the elemental mapping of Pb (e), P (f), Al (g), Si (h), Ca (i), Fe (j), K (k), Na (l), S (m), and O (n).

3.3. Leaching toxicity

The results of ultrapure water leaching (Fig.6) confirmed the immobilization efficiency of Pb, Al, Fe, and sulfates in the collected pyrite ash and applied binder scenarios. Without the HPSS process, the release of Pb in the pyrite ash is two orders of magnitude higher than the limitations (10 µg/L based on D.Lgs. n. 152/2006 and 50 µg/L based on D.M. n. 186). This means that any inadvertent ingestion, such as the ingestion of contaminated crops and the inhalation of Pb-contaminated soil dust, might bring health-threatening diseases to humans (Hou et al., 2020). The leaching of Fe is less sensitive to the immobilization process and binder selection, which varies from 19 to 68 µg/L. In the CP pellets, the Pb leachability (180 µg/L) far exceeded the concentration limit for on-site reuse (10 µg/L), which ascertained previous works that the OPC binder is insufficient when the Pb concentration is at a relatively high range (Contessi et al., 2020; Pu et al., 2021). With the pelletization treatment of CEM III/B, CAC, and MBS binders, the Pb leachability significantly decreased to 30, 20, and 57 µg/L, respectively. Accordingly, in the CAC and MBS, due to the presence of more ettringite, as confirmed in the XRD analyses (Fig.3a and Fig.4a), the Al leachability pellets increased to 9200 and 7800 µg/L compared with the concentration of 28 µg/L in CP pellets. Regarding the AB pellets, the Pb retention capacity deterioration is shown, with an approximately two-fold Pb concentration of 380 µg/L observed in comparison to the CP scenario. With regards to the sulfates leaching behavior, the incorporation of OPC and ABS binder increased the concentration from 715 mg/L in pyrite ash to 1600 and 2000 mg/L. Whereas in the CB, CA, and MB pellets, the sulfates concentrations are 800, 940, and 410 mg/L, respectively.

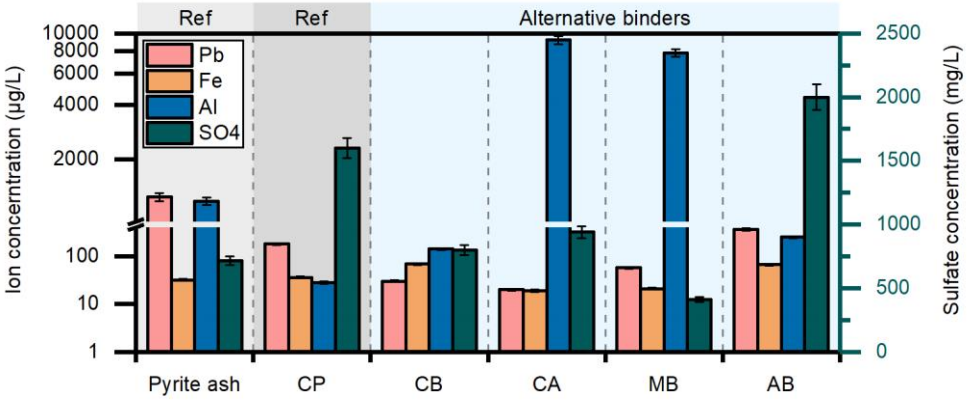

Figure.6. TCLP results of the pyrite ash, CP, CB, CA, MB, and AB pellets. The pH marked

indicates the pH values of the leachate after the leaching. Note that the leaching profile of pyrite ash presented here is multiplied by a parameter of 0.65 to present its weight percent in the pellets.

3.4. Carbon emissions and cost analysis related to the pellets preparation and Pb immobilization

Fig.7 summarizes the carbon emissions and the preparation cost associated with each binder scenario. In all the current cases studied, the CP pellets show the most significant carbon footprint as for recycling 1 tonne of pyrite ash, 215 kg of CO_2 would be released. Considering the CO_2 saving in view of the end life of applied binders at underuse (Habert et al., 2020), the following CP carbonation could eliminate 29.7 kg CO_2/t of the carbon footprint through the reaction with atmospheric CO_2, accounting for approximately 14% of the precursor pelletization process. Herein the overall cost for the CP pellets preparation could reach 30.8 €/t (17.8 from the binder and water supply and 13.0 from the estimated CO_2 tax in E.U.).

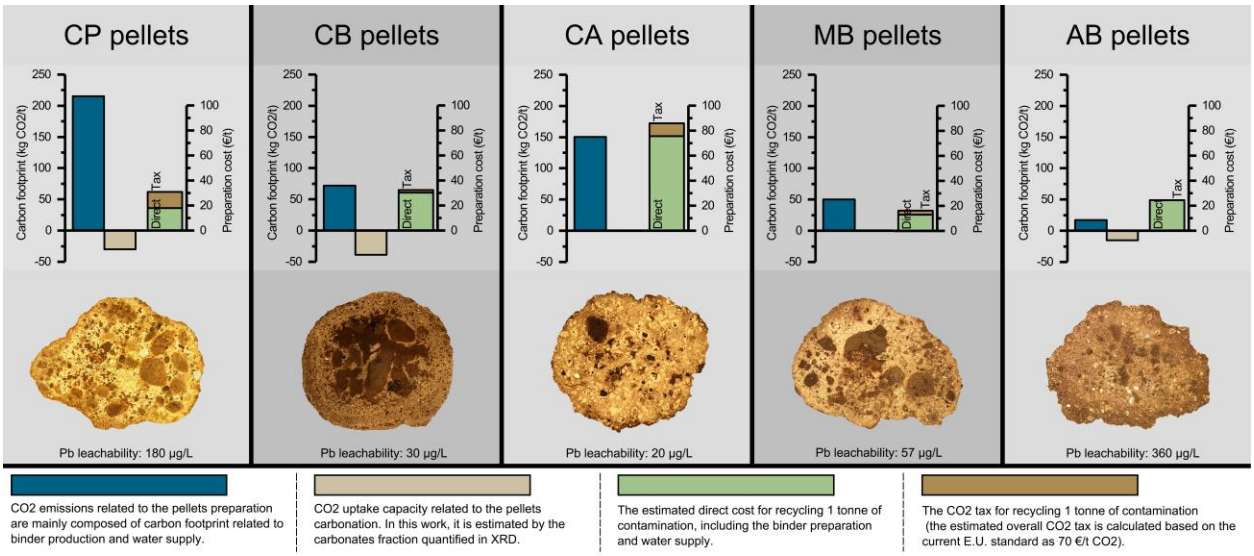

Figure.7. The optical microscope images and the related carbon footprint of the pellets preparation. The carbon uptake of CA and MB pellets is estimated to be 0 because the carbonates are not found in their XRD patterns. The "Direct" marked in the image represents the direct cost related to the pellets preparation and the "Tax" marked indicates the indirect cost of CO_2 tax.

The CO_2 benefit under the CB scenario is significantly optimized as the calculated CO_2 release and uptake are 71.9 and 38.7 kg CO_2/t, indicating over half of the CO_2 emission related to the binder production can be mitigated as a consequence of the sponge effect (Cao et al., 2020). Although the CB binder preparation cost (30.2 €/t) is higher than the CP pellets, the CO_2 tax (2.3 €/t) is much less than the traditional pathway. With regard to CA pellets, the overall cost (75.5 €/t) related to this binder

could be unprofitable because of the high price of CAC and its production is less carbon-negative, which may emit 150.5 kg CO_2/t. Further, the inhibited carbonation in CA pellets may bring less CO_2 tax benefit to this strategy. For the MB pellet, despite the carbonates (calcite and vaterite) are also not presented in this sample, its associated carbon footprint is only a quarter of the CP preparation at 50.0 kg CO_2/t. Meanwhile, because of the broad quantities and economics of GGBFS, the overall cost of the MB scenario is only 12.8 €/t. Noteworthy, the use of synthetic mayenite CO_2 emission data in the carbon footprint calculation may overestimate the overall CO_2 emission and tax costs of MB pellets, indicating that the overall economic benefits of the MB scenario are expected to decline further. The lowest carbon footprint corresponds to the cases of AB pellets, with the emission estimated as 16.9 kg CO_2/t. The following carbonation takes up 15 kg of CO_2 emissions.

Further, we quantified the relative CO_2 emission and financial costs attributed to the specific Pb immobilization efficiency of different binder strategies. From Fig.8a, the CP pellets nevertheless have the highest CO_2 emission burden, with approximately 1.68 kg CO_2 would be released for immobilizing 1 g of Pb in pyrite ash. However, owing to its large-scale use, the overall expense of the CP strategy is only 0.29 €/g Pb. Regarding the CA pellet, which has the most satisfactory Pb retention behavior (20 μg/L), its relative CO_2 emissions and financial costs are 1.19 kg CO_2/g Pb and 0.68 €/g Pb. The use of CB and AB pellets both significantly reduced the CO_2 footprint (0.26 and 0.02 kg CO_2/g Pb), but the related expenses (0.26 and 0.27 €/g Pb) are close to the traditional CP strategy.

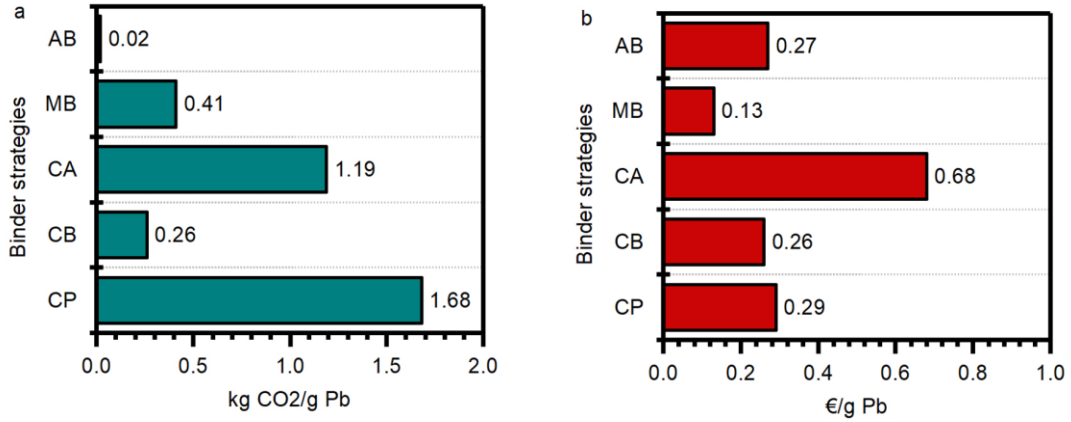

Figure.8. The relative CO_2 emissions (a) and financial costs (b) of the Pb immobilization efficiency attributed to the applied different binder strategies.

4. Discussion

4.1. Efficacy of cement-free S/S process for Pb immobilization

The leaching data (Fig.6) indicates a tight connection between the hydration products and the PTEs

leachability, with more hydration products precipitation (e.g., ettringite, C-(A)-S-H gel, and amorphous aluminum hydroxide) tending to offer more durable physical encapsulation of PTEs in dense cementitious matrices, as well as higher efficiencies of chemical immobilization through the adsorption and incorporation (Wang et al., 2018; Guo et al., 2021). Nevertheless, similar to the well-established Pb retention in the OPC systems (Navarro et al., 2011; Contessi et al., 2020). In the CP pellets, the Pb is well dispersed within the hydration products matrices along the unhydrated cement particles with a particular connection to the Ca and Si. Since the ionic radius of Pb^{2+} is only about 13% larger than Ca^{2+}, this ion exchange is plausible. However, similar to the investigations in the literature (Contessi et al., 2020; Zhang et al., 2021b; Ouhadi et al., 2021), the efficiency of the precipitated/stabilized lead components with OPC incorporation is high-potentially unsuccessful. This is because, despite the majority of Pb can be well-retained by the C-S-H gel and/or Pb hydroxide precipitation (Wang and Wang, 2022), the high pH conditions of OPC matrices due to the dissolution of clinker phases might adverse the solidifying/stabilizing of Pb contaminants. Previous works suggest that at highly alkaline conditions, the soluble Pb will be prone to present as soluble hydroxide complexes (preliminarily $Pb(OH)_3^-$) instead of the Pb hydroxides precipitation and Pb incorporation in C-S-H structures (Rose et al., 2000; Nimal Perera et al., 2001; Ouhadi et al., 2021).

The hydrates formation in the AB pellets is notably slower than in other cases, with a very low amount of ettringite found in XRD (Fig.5a) and massive unreacted slag present in the microstructure, as observed by SEM (Fig.5c). As a consequence of this slow hydration reaction, the Pb concentration in the leachates of AB pellets is twice to that of CP pellets. This slower hydration could be attributed to insufficient alkaline activation. Although sodium silicate can accelerate the calcium dissolution process and form additional C-S-H gel through pozzolanic reactions, the precipitated impermeable agglomerations coating would soon cover the unreacted particles (Mohan and Mini, 2018). Furthermore, the accelerated reactions also cause rapid water content consumption at the early ages and parts of the water may be enclosed in the coating layers (Langan et al., 2002; Zhang et al., 2022). Without the alkaline activation to solubilize the water-impermeable layer (Song et al., 2000; Zhang et al., 2020), the grains and water do not come into full contact resulting in less binder taking part in the hydration process. Therefore, although the Pb migration from the apparent enrichment along the iron oxide (possibly kintoreite) to the faint dispersal in the binding matrix is found in the SEM/EDS observations (Fig.5d), the lack of sufficient hydration products (such as C-(A)-S-H and ettringite) causes an increase in Pb leaching profile.

Likewise, the binders used in MB and CB pellets are also GGBFS-rich materials, whereas the incorporated mayenite and clinker phases promote the hydrates precipitation (Fig.3a and 4a), which

further reduces the leachability of PTEs (Fig.6). Regarding the former scenario, MB pellets, it is reported that mayenite is highly hydraulic and rapidly dissolve in the aqueous solutions and primarily forms C_2AH_8 (Adolfsson et al., 2011; Zhuang and Wang, 2021). However, unlike the coating film formed in AB pellets, the C_2AH_8 is not thermodynamically stable and would eventually convert to high-density C_3AH_6 as a final product (Adolfsson et al., 2011; Chen et al., 2021b). The conversion process can trigger subsequent reactions with slags herein would explain the enhanced hydrates precipitation in the MB pellets. Upon the CB pellets, although the GGBFS generally contains more Al_2O_3 than the OPC binder, which could supply sufficient alumina sources for ettringite precipitation, the quantified ettringite fraction is approximately equivalent to the CP samples but much lower than the MB samples. This differentiated latent hydraulic reaction is because the considerable proportion of $Ca(OH)_2$ produced during the cement clinker fraction dissolution is preferentially consumed by the silicate anions released from GGBFS and favors the C-S-H gel precipitation instead of the sulfate ions from the jarosite and gypsum (Osmanovic et al., 2018; Zhang et al., 2019; Dai et al., 2021). The previous thermodynamic calculations for OPC-GGBFS systems also ascertained this calcium competition through varying proportions of the low Ca/Si ratio C-(A)-S-H gel and ettringite precipitations (Lothenbach et al., 2011). The increasing content of GGBFS has an adverse effect on the ettringite precipitation, as more Al is bound in the bridging sites in the silicate chains of C-(A)-S-H (Lothenbach et al., 2011, 2012). Further, the lower Ca/Si ratio C-(A)-S-H gel increases the Pb uptake capacities (Mancini et al., 2021). Herein, although the overall fraction of hydration products in the CB pellets is lower than in the MB pellets, the Pb leachability is halved.

With the CAC pretreatment, the CA pellets demonstrate the minimum Pb leaching in all the cases. The SEM/EDS characterization (Fig.3d), along with previous works (Contessi et al., 2020, 2021), has highlighted the role of ettringite precipitation in Pb immobilization with a certain degree of substitution of Pb^{2+} for Ca^{2+}. In addition, unlike the incorporation in the C-(A)-S-H gel, literature confirmed the poor affinity of Pb^{2+} for calcium aluminate hydrates and the formation of oxo- and hydroxyl compounds (Duran et al., 2016). Therefore, such an enhanced immobilization performance could be partially attributed to the low alkalinity of the CAC system (pH = 10.1) due to the amphoteric properties of lead hydroxides, which are likely to appear as $Pb(OH)_2$ precipitates, acting as Pb solubility controlling phase at the faint alkaline environments as evidenced in the thermodynamic simulations (Wang and Wang, 2022). However, this tendency decreased with increasing pH, with the formation of Pb species in solution (e.g., $Pb(OH)_3^-$ and $Pb(OH)_4^{2-}$) are favored over $Pb(OH)_2$ at harsh alkaline conditions (Karlfeldt Fedje et al., 2010; Navarro-Blasco et al., 2013).

4.2. Views on carbon-zero emissions and practical implication

Although pollutant release is recognized as an important environmental issue that is faced in the S/S process, the recent most commonly discussed ecosystem impact is the high level of greenhouse gas emissions related to the cement industry (Habert et al., 2020; Miller et al., 2021). Based on the carbon footprint quantification results of all the binder strategies (Fig.7 and 8), it is clear that using cement-free pathways leads to substantial savings in terms of CO_2 emissions. The CB pellet is the most promising solution that can be realistically used in the scalable field trial concerning this case, cutting the Pb leaching to 17% (30μg/L) and the CO_2 emission to 18% (33.2 kg CO_2/tonne pyrite ash) of the CP pellet. Here, we expanded our data for the pyrite ash immobilization in a broader community to indicate their potential practical supply relative to demand in local/regional scenarios (Fig.9). The estimation shows that a doubling of pyrite ash annual production might be achieved between 2021 and 2030 (from 10.7 to 22.2 Mt, Fig.9a and Table.S3), driven by the growing demand of the fertilizer (Ma et al., 2021). Hence, the Pb concentration in these produced solid wastes is a crucial practical limitation for extrapolating the above-mentioned alternative binder scenarios since their different affinities to Pb retention have been investigated in previous sections. Fig.9b reveals the distribution of the collected Pb concentration records, with the mean concentration value being 4349 mg/kg. To further quantify the attributed CO_2 emissions and expenses for the subsequent in-situ remediation, we used the mean and maximum concentrations to represent the Pb enrichment within the newly generated pyrite ash. The results (Fig.9c and Fig.S5a) show that the substitution of alternative binders can play a much larger role in reducing CO_2 emissions, with reductions of up to 98.8% theoretically achievable by maximizing the utilization of the AB scenario globally. Although the AB pellets cannot preclude the risk of Pb exposure from being low enough at a high Pb concentration (for example, 11910 mg/kg in this work), this strategy may present an opportunity for efficiently immobilizing the pyrite ash wastes with less-enriched Pb concentrations since over 80% of records being lower 5000 mg/kg (Fig.9b). From the leaching examination, the CA pellets have the most promising control of Pb transportation. However, the CO_2 mitigation of CA pellets might reach a fairly limited upper bound (70.9% of CP pellets emissions, Fig.9c) due to the huge CO_2 emission associated with the dissociation of limestone during the clinker manufacturing process (Bharati et al., 2020). In addition, the wide use of CA pellets would require the following significant financial barriers to be overcome, with its expenses 2.4 times higher than the traditional CP strategy. This is because of the limited supply of bauxite, the main aluminum source of CAC production (Zapata et al., 2022), making it insufficient to bridge such a great gap in the current market demand (Habert et al., 2020). Nonetheless, some works tried to use aluminum-rich solid waste (ladle slag) to partially replace the aluminum sources of CAC and reduce manufacturing costs (Zapata et al., 2022). However, the introduction of new materials in CAC production has difficulty finding acceptance in the construction industry and field cases, as these

sectors are fragmented with multiple stakeholders (Habert et al., 2020). Such issues may delay the large-scale implementation of the CAC binder. Notwithstanding, the CB pellets are likely less affected by the raw material availability and capital expenditure issues, which critically affect the exploitation of cement-free Pb remediation approaches (Miller et al., 2021; Sun et al., 2022). The use of an aluminosilicate precursor, which has been discussed as a potential alternative that can entirely replace the use of OPC, is hindered by the issue of limited availability, making the implementation challenging (Habert et al., 2020). Concurrently, the production of commercial CEM III/B binder envisages the use of GGBFS, obtained as a by-product in the production of pig iron with a 330 Mt/year of global annual production, to make up the clinker phases in a proportion ranging from 66-80 wt% (Osmanovic et al., 2018; Nocuń-Wczelik et al., 2021).

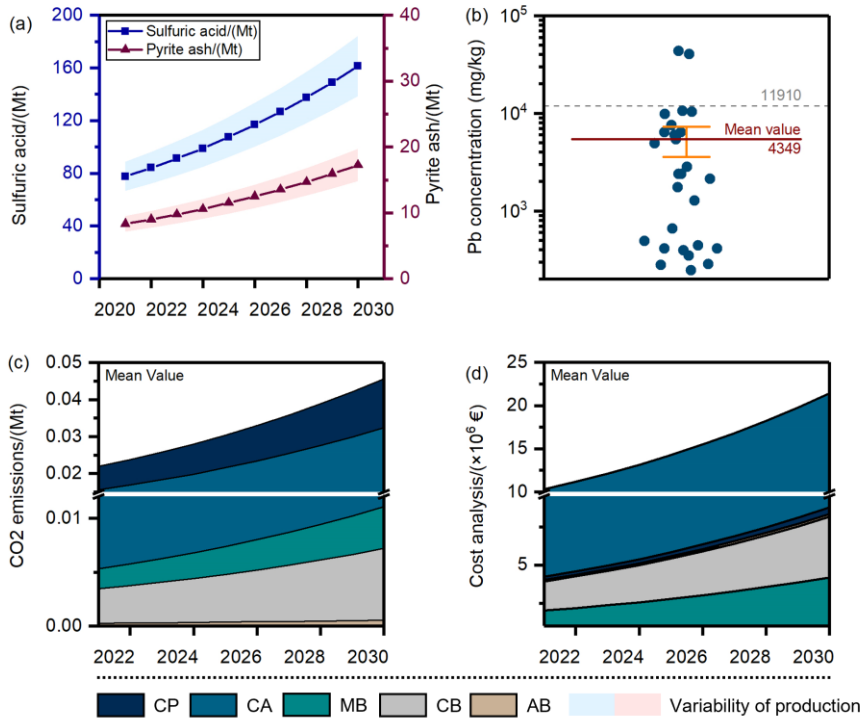

Figure.9. CO_2 mitigation and cost analysis regard to the application of alternative binder strategies. (a) Estimated sulfuric acid production and discarded pyrite ash from 2021-2030, (b) the Pb concentrations in pyrite ash, with 11910 indicating the sample we used in this work and 4349 representing the calculated mean Pb concentration, (c) the CO_2 carbon footprint attributed to the in-situ remediation of pyrite ash, and (d) the financial expense analysis attributed to the in-situ remediation of pyrite ash.

Therefore, the application of the CEM III/B binder could save a significant amount of historically wasted and newly generated GGBFS, which also represents a substantial contribution to the overall

benefit. The results show that applying alternative binders to one-for-one replace the OPC binder could reduce the carbon footprint and be financially and strategically rewarding, fostering the green economy and accelerating the trend toward carbon neutrality (Wang et al., 2021).

5. Conclusions

This work proposes the sustainable in-situ remediation of hazardous pyrite ash using the S/S process using binders with different levels of OPC replacement. The overall findings shed light on the understanding of Pb immobilization and transition in multiple alternative binders, highlighting the significance of the perspectives of carbon neutrality in the S/S applications and providing new insights into the highly efficient S/S of Pb-contaminated wastes. The main conclusions drawn from this study are:

(1) Although the results demonstrate the Pb incorporation into the OPC-based cementitious matrix, the high alkaline conditions resulting from the dissolution of clinker phases may interfere with the Pb immobilization efficiency in the CP pellets. Consequently, the Pb leachability is over three times higher than the limits. Herein, the traditional OPC binder exhibits low compatibility with Pb-rich pyrite ash wastes, both from the standpoints of insufficient Pb retention capacity and the colossal carbon footprint.

(2) The CAC binder displays significant potential for improving Pb immobilization in all the studied binder strategies due to the facilitated formation of hydration products (ettringite, $Al(OH)_3$, and C-(A)-S-H gel), which provide a stronger physical encapsulation and chemical immobilization. Further, the less-alkaline conditions of CA pellets also resulted in the formation of lead hydroxide species favoring Pb retention. However, the ecological benefits of the CAC binder application are less satisfactory. Although the associated carbon footprint is slightly optimized compared to the OPC strategy, it is not likely to lead to sufficient emission abatements under currently proposed production procedures.

(3) The use of CB pellets is an ideal alternative binder due to its excellent compatibility with Pb and relative low-carbon nature. The low Ca/Si ratio C-(A)-S-H enhanced the Pb incorporation within the binding matrix, fulfilling the Pb leachability requirements for reuse as S/S material. In addition, the sponge effect of the CB pellets, as well as the low-carbon footprint related to the CEM III/B production, would promote the achievement of carbon neutrality.

(4) Overall, our study provided useful guidance for improving the design and application of sustainable pathways to solid waste amendment, which bridged the gap between carbon-neutral world rhetoric and the reality of solid waste remediation applications. The carbon budget calculation based on each binder strategy is an important basis for future S/S management decision-making with the perspective

of carbon peak and carbon neutralization. Nevertheless, future works will be required to reveal uncertainties in the stability of disrupted S/S products and potential eco-toxicity after long-term adopted practices in diverse regional soil hydrology environments.

Acknowledgments

This study was conducted with financial support from the PRIN project “Mineral reactivity, a key to understand large-scale processes: from rock-forming environments to solid waste recovering/lithification” (No.2017L83S77) and a scholarship granted by the China Scholarship Council (No.CSC201906370062).

Author contributions

Yikai Liu: Conceptualization, Writing- Original Draft preparation, Investigation, Formal analysis;

Simone Molinari: Conceptualization, Validation, Writing – Review & Editing, Investigation, Visualization;

Maria Chiara Dalconi: Validation, Investigation, Visualization, Writing – Review & Editing;

Luca Valentini: Investigation, Validation, Visualization, Writing – Review & Editing;

Maurizio Pietro Bellotto: Resources, Investigation;

Giorgio Ferrari: Resources, Supervision;

Roberto Pellay: Resources, Investigation;

Graziano Rilievo: Writing – Review & Editing;

Fabio Vianello: Investigation, Writing – Review & Editing;

Gabriella Salviulo: Validation, Investigation;

Gilberto Artioli: Conceptualization, Writing – Review & Editing, Project administration, Resources, Supervision, Validation.

All the authors discussed the data and agreed on their interpretations. All the co-authors contributed to the final polishing of the manuscript.

Reference

Adolfsson, D., Robinson, R., Engström, F., and Björkman, B., 2011, Influence of mineralogy on the hydraulic properties of ladle slag: Cement and Concrete Research, v. 41, p. 865–871, doi:10.1016/J.CEMCONRES.2011.04.003.

Alp, I., Deveci, H., Yazici, E.Y., Türk, T., and Süngün, Y.H., 2009, Potential use of pyrite cinders as raw material in cement production: Results of industrial scale trial operations: Journal of Hazardous Materials, v. 166, p. 144–149, doi:10.1016/J.JHAZMAT.2008.10.129.

Berthomier, M., Lors, C., Damidot, D., De Larrard, T., Guérandel, C., and Bertron, A., 2021, Leaching of CEM III paste by demineralised or mineralised water at pH 7 in relation with aluminium release in drinking water network: Cement and Concrete Research, v. 143, doi:10.1016/J.CEMCONRES.2021.106399.

Bharati, S., Sah, R., and Sambandam, M., 2020, Green Castable Using Steelmaking Slags: A Sustainable Product for Refractory Applications: Journal of Sustainable Metallurgy, v. 6, p. 113–120, doi:10.1007/S40831-019-00261-7/FIGURES/8.

Bizzozero, J., Gosselin, C., and Scrivener, K.L., 2014, Expansion mechanisms in calcium aluminate and sulfoaluminate systems with calcium sulfate: Cement and Concrete Research, v. 56, p. 190–202, doi:10.1016/J.CEMCONRES.2013.11.011.

British Standards Institution, 2004, Characterisation of Waste - Leaching - Compliance Test for Leaching of Granular Waste Materials and Sludges - Part 4: One Stage Batch Test at a Liquid to Solid Ratio of 10 l/kg for Materials With Particle Size Below 10 Mm (without or With Size Reduction):

Bui Viet, D., Chan, W.P., Phua, Z.H., Ebrahimi, A., Abbas, A., and Lisak, G., 2020, The use of fly ashes from waste-to-energy processes as mineral CO2 sequesters and supplementary cementitious materials: Journal of Hazardous Materials, v. 398, p. 122906, doi:10.1016/J.JHAZMAT.2020.122906.

Calgaro, L., Contessi, S., Bonetto, A., Badetti, E., Ferrari, G., Artioli, G., and Marcomini, A., 2021, Calcium aluminate cement as an alternative to ordinary Portland cement for the remediation of heavy metals contaminated soil: mechanisms and performance: Journal of Soils and Sediments, doi:10.1007/s11368-020-02859-x.

Cao, Z., Myers, R.J., Lupton, R.C., Duan, H., Sacchi, R., Zhou, N., Reed Miller, T., Cullen, J.M., Ge, Q., and Liu, G., 2020, The sponge effect and carbon emission mitigation potentials of the global cement cycle: Nature Communications 2020 11:1, v. 11, p. 1–9, doi:10.1038/s41467-020-17583-w.

Chang, J.-S., Cho, Y.-C., and Lin, Y.-P., 2022, Regeneration of heavy metal contaminated soils for cement

production by cement kiln co-processing: Resources, Conservation and Recycling, doi:10.1016/j.resconrec.2021.105909.

Chang, N. Bin, Qi, C., and Yang, Y.J., 2012, Optimal expansion of a drinking water infrastructure system with respect to carbon footprint, cost-effectiveness and water demand: Journal of Environmental Management, v. 110, p. 194–206, doi:10.1016/j.jenvman.2012.06.004.

Chen, Q., Tao, Y., Feng, Y., Zhang, Q., and Liu, Y., 2021a, Utilization of modified copper slag activated by Na2SO4 and CaO for unclassified lead/zinc mine tailings based cemented paste backfill: Journal of environmental management, doi:10.1016/j.jenvman.2021.112608.

Chen, Q.Y., Tyrer, M., Hills, C.D., Yang, X.M., and Carey, P., 2009, Immobilisation of heavy metal in cement-based solidification/stabilisation: A review: Waste Management, doi:10.1016/j.wasman.2008.01.019.

Chen, L., Wang, L., Cho, D.W., Tsang, D.C.W., Tong, L., Zhou, Y., Yang, J., Hu, Q., and Poon, C.S., 2019, Sustainable stabilization/solidification of municipal solid waste incinerator fly ash by incorporation of green materials: Journal of Cleaner Production, v. 222, p. 335–343, doi:10.1016/J.JCLEPRO.2019.03.057.

Chen, L., Wang, Y.S., Wang, L., Zhang, Y., Li, J., Tong, L., Hu, Q., Dai, J.G., and Tsang, D.C.W., 2021b, Stabilisation/solidification of municipal solid waste incineration fly ash by phosphate-enhanced calcium aluminate cement: Journal of Hazardous Materials, v. 408, p. 124404, doi:10.1016/J.JHAZMAT.2020.124404.

Chen, L., Wang, L., Zhang, Y., Ruan, S., Mechtcherine, V., and Tsang, D.C.W., 2022a, Roles of biochar in cement-based stabilization/solidification of municipal solid waste incineration fly ash: Chemical Engineering Journal, v. 430, p. 132972, doi:10.1016/J.CEJ.2021.132972.

Chen, L., Zhang, Y., Wang, L., Ruan, S., Chen, J., Li, H., Yang, J., Mechtcherine, V., and Tsang, D.C.W., 2022b, Biochar-augmented carbon-negative concrete: Chemical Engineering Journal, v. 431, p. 133946, doi:10.1016/j.cej.2021.133946.

Contessi, S., Calgaro, L., Dalconi, M.C., Bonetto, A., Bellotto, M. Pietro, Ferrari, G., Marcomini, A., and Artioli, G., 2020, Stabilization of lead contaminated soil with traditional and alternative binders: Journal of Hazardous Materials, doi:10.1016/j.jhazmat.2019.120990.

Contessi, S., Dalconi, M.C., Pollastri, S., Calgaro, L., Meneghini, C., Ferrari, G., Marcomini, A., and Artioli, G., 2021, Cement-stabilized contaminated soil: Understanding Pb retention with XANES and Raman spectroscopy: Science of The Total Environment, v. 752, p. 141826,

doi:10.1016/J.SCITOTENV.2020.141826.

Dai, X., Aydin, S., Yücel Yardimci, M., Qiang, R.E.N., Lesage, K., and De Schutter, G., 2021, Rheology, early-age hydration and microstructure of alkali-activated GGBFS-Fly ash-limestone mixtures: Cement and Concrete Composites, v. 124, p. 104244, doi:10.1016/J.CEMCONCOMP.2021.104244.

Doebelin, N., and Kleeberg, R., 2015, Profex: a graphical user interface for the Rietveld refinement program BGMN: urn:issn:1600-5767, v. 48, p. 1573–1580, doi:10.1107/S1600576715014685.

Du, B., Li, J., Fang, W., and Liu, J., 2019, Comparison of long-term stability under natural ageing between cement solidified and chelator-stabilised MSWI fly ash: Environmental Pollution, v. 250, p. 68–78, doi:10.1016/J.ENVPOL.2019.03.124.

Du, Y.J., Wei, M.L., Reddy, K.R., Liu, Z.P., and Jin, F., 2014, Effect of acid rain pH on leaching behavior of cement stabilized lead-contaminated soil: Journal of Hazardous Materials, v. 271, p. 131–140, doi:10.1016/J.JHAZMAT.2014.02.002.

Duran, A., Sirera, R., Pérez-Nicolás, M., Navarro-Blasco, I., Fernández, J.M., and Alvarez, J.I., 2016, Study of the early hydration of calcium aluminates in the presence of different metallic salts: Cement and Concrete Research, v. 81, p. 1–15, doi:10.1016/J.CEMCONRES.2015.11.013.

Fernández-González, D., Prazuch, J., Ruiz-Bustinza, I., González-Gasca, C., Piñuela-Noval, J., and Verdeja, L.F., 2018, Solar synthesis of calcium aluminates: Solar Energy, v. 171, p. 658–666, doi:10.1016/J.SOLENER.2018.07.012.

García-Segura, T., Yepes, V., and Alcalá, J., 2014, Life cycle greenhouse gas emissions of blended cement concrete including carbonation and durability: International Journal of Life Cycle Assessment, v. 19, p. 3–12, doi:10.1007/S11367-013-0614-0/TABLES/8.

Gardner, L.J., Bernal, S.A., Walling, S.A., Corkhill, C.L., Provis, J.L., and Hyatt, N.C., 2015, Characterisation of magnesium potassium phosphate cements blended with fly ash and ground granulated blast furnace slag: Cement and Concrete Research, v. 74, p. 78–87, doi:10.1016/J.CEMCONRES.2015.01.015.

Guo, B., Liu, B., Yang, J., and Zhang, S., 2017, The mechanisms of heavy metal immobilization by cementitious material treatments and thermal treatments: A review: Journal of Environmental Management, v. 193, p. 410–422, doi:10.1016/j.jenvman.2017.02.026.

Guo, B., Tan, Y., Wang, L., Chen, L., Wu, Z., Sasaki, K., Mechtcherine, V., and Tsang, D.C.W., 2021, High-efficiency and low-carbon remediation of zinc contaminated sludge by magnesium oxysulfate cement: Journal of Hazardous Materials, v. 408, p. 124486, doi:10.1016/J.JHAZMAT.2020.124486.

Habert, G., Miller, S.A., John, V.M., Provis, J.L., Favier, A., Horvath, A., and Scrivener, K.L., 2020, Environmental impacts and decarbonization strategies in the cement and concrete industries: Nature Reviews Earth & Environment 2020 1:11, v. 1, p. 559–573, doi:10.1038/s43017-020-0093-3.

Halim, C.E., Short, S.A., Scott, J.A., Amal, R., and Low, G., 2005, Modelling the leaching of Pb, Cd, As, and Cr from cementitious waste using PHREEQC: Journal of Hazardous Materials, v. 125, p. 45–61, doi:10.1016/j.jhazmat.2005.05.046.

He, M., Xu, Z., Hou, D., Gao, B., Cao, X., Ok, Y.S., Rinklebe, J., Bolan, N.S., and Tsang, D.C.W., 2022, Waste-derived biochar for water pollution control and sustainable development: Nature Reviews Earth & Environment 2022 3:7, v. 3, p. 444–460, doi:10.1038/s43017-022-00306-8.

Hidalgo, A., García Calvo, J.L., Alonso, M.C., Fernández, L., and Andrade, C., 2009, Microstructure development in mixes of calcium aluminate cement with silica fume or fly ash: Journal of Thermal Analysis and Calorimetry, v. 96, p. 335–345, doi:10.1007/S10973-007-8439-3.

Hou, D., O'Connor, D., Igalavithana, A.D., Alessi, D.S., Luo, J., Tsang, D.C.W., Sparks, D.L., Yamauchi, Y., Rinklebe, J., and Ok, Y.S., 2020, Metal contamination and bioremediation of agricultural soils for food safety and sustainability: Nature Reviews Earth & Environment 2020 1:7, v. 1, p. 366–381, doi:10.1038/s43017-020-0061-y.

Ismail, I., Bernal, S.A., Provis, J.L., San Nicolas, R., Hamdan, S., and Van Deventer, J.S.J., 2014, Modification of phase evolution in alkali-activated blast furnace slag by the incorporation of fly ash: Cement and Concrete Composites, v. 45, p. 125–135, doi:10.1016/J.CEMCONCOMP.2013.09.006.

Karlfeldt Fedje, K., Ekberg, C., Skarnemark, G., and Steenari, B.M., 2010, Removal of hazardous metals from MSW fly ash—An evaluation of ash leaching methods: Journal of Hazardous Materials, v. 173, p. 310–317, doi:10.1016/J.JHAZMAT.2009.08.094.

Kirca, Ö., Özgür Yaman, I., and Tokyay, M., 2013, Compressive strength development of calcium aluminate cement–GGBFS blends: Cement and Concrete Composites, v. 35, p. 163–170, doi:10.1016/J.CEMCONCOMP.2012.08.016.

Kwon, S.J., and Wang, X.Y., 2019, Optimization of the mixture design of low-CO2 high-strength concrete containing silica fume: Advances in Civil Engineering, v. 2019, doi:10.1155/2019/7168703.

Langan, B.W., Weng, K., and Ward, M.A., 2002, Effect of silica fume and fly ash on heat of hydration of Portland cement: Cement and Concrete Research, v. 32, p. 1045–1051, doi:10.1016/S0008-8846(02)00742-1.

Li, H., Li, X., Xiao, T., Chen, Y., Long, J., Zhang, G., Zhang, P., Li, C., Zhuang, L., and Li, K., 2018,

Efficient removal of thallium(I) from wastewater using flower-like manganese dioxide coated magnetic pyrite cinder: Chemical Engineering Journal, v. 353, p. 867–877, doi:10.1016/J.CEJ.2018.07.169.

Li, G., Zhang, A., Song, Z., Shi, C., Wang, Y., and Zhang, J., 2017, Study on the resistance to seawater corrosion of the cementitious systems containing ordinary Portland cement or/and calcium aluminate cement: Construction and Building Materials, v. 157, p. 852–859, doi:10.1016/J.CONBUILDMAT.2017.09.175.

Liu, R., Jing, N., Song, Y., Zhai, Q., Mao, Z., Zhou, Y., and Sun, W., 2022, Recovery of valuable elements from pyrite pyrolysis slag using magnetic separation-flotation technique: Separation and Purification Technology, v. 299, p. 121772, doi:10.1016/J.SEPPUR.2022.121772.

Lothenbach, B., Le Saout, G., Ben Haha, M., Figi, R., and Wieland, E., 2012, Hydration of a low-alkali CEM III/B–SiO2 cement (LAC): Cement and Concrete Research, v. 42, p. 410–423, doi:10.1016/J.CEMCONRES.2011.11.008.

Lothenbach, B., Scrivener, K., and Hooton, R.D., 2011, Supplementary cementitious materials: Cement and Concrete Research, v. 41, p. 1244–1256, doi:10.1016/J.CEMCONRES.2010.12.001.

Lu, Y., Hu, S., Liang, Z., Zhu, M., Wang, Z., Wang, X., Liang, Y., Dang, Z., and Shi, Z., 2020, Incorporation of Pb(ii) into hematite during ferrihydrite transformation: Environmental Science: Nano, v. 7, p. 829–841, doi:10.1039/C9EN01355E.

Ma, Z., Liu, G., Zhang, H., Zhang, S., and Lu, Y., 2021, Evaluation of pyrite cinders from sulfuric acid production as oxygen carrier for chemical looping combustion: Energy, v. 233, p. 121079, doi:10.1016/J.ENERGY.2021.121079.

Mancini, A., Wieland, E., Geng, G., Lothenbach, B., Wehrli, B., and Dähn, R., 2021, Fe(II) interaction with cement phases: Method development, wet chemical studies and X-ray absorption spectroscopy: Journal of Colloid and Interface Science, v. 588, p. 692–704, doi:10.1016/J.JCIS.2020.11.085.

Miller, S.A., Habert, G., Myers, R.J., and Harvey, J.T., 2021, Achieving net zero greenhouse gas emissions in the cement industry via value chain mitigation strategies: One Earth, v. 4, p. 1398–1411, doi:10.1016/J.ONEEAR.2021.09.011.

Mohan, A., and Mini, K.M., 2018, Strength and durability studies of SCC incorporating silica fume and ultra fine GGBS: Construction and Building Materials, v. 171, p. 919–928, doi:10.1016/J.CONBUILDMAT.2018.03.186.

Monterroso, C., Rodríguez, F., Chaves, R., Diez, J., Becerra-Castro, C., Kidd, P.S., and Macías, F., 2014,

Heavy metal distribution in mine-soils and plants growing in a Pb/Zn-mining area in NW Spain: Applied Geochemistry, doi:10.1016/j.apgeochem.2013.09.001.

Moon, D.H., Park, J.W., Cheong, K.H., Hyun, S., Koutsospyros, A., Park, J.H., and Ok, Y.S., 2013, Stabilization of lead and copper contaminated firing range soil using calcined oyster shells and fly ash: Environmental Geochemistry and Health, v. 35, p. 705–714, doi:10.1007/S10653-013-9528-9/FIGURES/3.

Morandeau, A., Thiéry, M., and Dangla, P., 2014, Investigation of the carbonation mechanism of CH and C-S-H in terms of kinetics, microstructure changes and moisture properties: Cement and Concrete Research, v. 56, p. 153–170, doi:10.1016/J.CEMCONRES.2013.11.015.

Naeem, I., Masood, N., Turan, V., and Iqbal, M., 2021, Prospective usage of magnesium potassium phosphate cement combined with Bougainvillea alba derived biochar to reduce Pb bioavailability in soil and its uptake by Spinacia oleracea L: Ecotoxicology and Environmental Safety, doi:10.1016/j.ecoenv.2020.111723.

National Minerals Information Center, 2022, Mineral commodity summaries 2022:, doi:10.3133/MCS2022.

Navarro-Blasco, I., Duran, A., Sirera, R., Fernández, J.M., and Alvarez, J.I., 2013, Solidification/stabilization of toxic metals in calcium aluminate cement matrices: Journal of Hazardous Materials, v. 260, p. 89–103, doi:10.1016/J.JHAZMAT.2013.04.048.

Navarro, A., Cardellach, E., and Corbella, M., 2011, Immobilization of Cu, Pb and Zn in mine-contaminated soils using reactive materials: Journal of Hazardous Materials, v. 186, p. 1576–1585, doi:10.1016/J.JHAZMAT.2010.12.039.

Nimal Perera, W., Hefter, G., and Sipos, P.M., 2001, An investigation of the Lead(II)-hydroxide system: Inorganic Chemistry, v. 40, p. 3974–3978, doi:10.1021/IC001415O/SUPPL_FILE/IC001415O_S.PDF.

Nocuń-Wczelik, W., Pacierpnik, W., and Kapeluszna, E., 2021, Application of calorimetry and other thermal methods in the studies of granulated blast furnace slag from the old storage yards as supplementary cementitious material: Journal of Thermal Analysis and Calorimetry, v. 147, p. 8157–8168, doi:10.1007/S10973-021-11161-Y/FIGURES/12.

Osmanovic, Z., Haračić, N., and Zelić, J., 2018, Properties of blastfurnace cements (CEM III/A, B, C) based on Portland cement clinker, blastfurnace slag and cement kiln dusts: Cement and Concrete Composites, v. 91, p. 189–197, doi:10.1016/J.CEMCONCOMP.2018.05.006.

Ouhadi, V.R., Yong, R.N., and Deiranlou, M., 2021, Enhancement of cement-based

solidification/stabilization of a lead-contaminated smectite clay: Journal of Hazardous Materials, v. 403, p. 123969, doi:10.1016/J.JHAZMAT.2020.123969.

Palansooriya, K.N., Shaheen, S.M., Chen, S.S., Tsang, D.C.W., Hashimoto, Y., Hou, D., Bolan, N.S., Rinklebe, J., and Ok, Y.S., 2020, Soil amendments for immobilization of potentially toxic elements in contaminated soils: A critical review: Environment International, v. 134, p. 105046, doi:10.1016/J.ENVINT.2019.105046.

Precedence Research, 2022, Sulfuric Acid Market Size, Growth, Trends, Report 2022-2030:, https://www.precedenceresearch.com/sulfuric-acid-market (accessed October 2022).

Pu, S., Zhu, Z., Song, W., Wang, H., Huo, W., and Zhang, J., 2021, A novel acidic phosphoric-based geopolymer binder for lead solidification/stabilization: Journal of Hazardous Materials, doi:10.1016/j.jhazmat.2021.125659.

Ravikumar, D., Zhang, D., Keoleian, G., Miller, S., Sick, V., and Li, V., 2021, Carbon dioxide utilization in concrete curing or mixing might not produce a net climate benefit: Nature Communications, v. 12, p. 1–13, doi:10.1038/s41467-021-21148-w.

Rose, J., Moulin, I., Hazemann, J.L., Masion, A., Bertsch, P.M., Bottero, J.Y., Mosnier, F., and Haehnel, C., 2000, X-ray absorption spectroscopy study of immobilization processes for heavy metals in calcium silicate hydrates: 1. Case of lead: Langmuir, v. 16, p. 9900–9906, doi:10.1021/LA0005208/ASSET/IMAGES/LARGE/LA0005208F00006.JPEG.

Santana-Carrillo, J.L., Burciaga-Díaz, O., and Escalante-Garcia, J.I., 2022, Blended limestone-Portland cement binders enhanced by waste glass based and commercial sodium silicate - Effect on properties and CO2 emissions: Cement and Concrete Composites, v. 126, p. 104364, doi:10.1016/J.CEMCONCOMP.2021.104364.

Scanferla, P., Ferrari, G., Pellay, R., Volpi Ghirardini, A., Zanetto, G., and Libralato, G., 2009, An innovative stabilization/solidification treatment for contaminated soil remediation: Demonstration project results, *in* Journal of Soils and Sediments, doi:10.1007/s11368-009-0067-z.

Seo, J., Nawaz, A., Jang, J.G., and Lee, H.K., 2022, Modifications in hydration kinetics and characteristics of calcium aluminate cement upon blending with calcium sulfoaluminate cement: Construction and Building Materials, v. 342, p. 127958, doi:10.1016/J.CONBUILDMAT.2022.127958.

Shen, W., Cao, L., Li, Q., Wen, Z., Wang, J., Liu, Y., Dong, R., Tan, Y., and Chen, R., 2016, Is magnesia cement low carbon? Life cycle carbon footprint comparing with Portland cement: Journal of Cleaner Production, v. 131, p. 20–27, doi:10.1016/J.JCLEPRO.2016.05.082.

Skocek, J., Zajac, M., and Ben Haha, M., 2020, Carbon Capture and Utilization by mineralization of cement pastes derived from recycled concrete: Scientific Reports 2020 10:1, v. 10, p. 1–12, doi:10.1038/s41598-020-62503-z.

Song, S., Sohn, D., Jennings, H.M., and Mason, T.O., 2000, Hydration of alkali-activated ground granulated blast furnace slag: Journal of Materials Science 2000 35:1, v. 35, p. 249–257, doi:10.1023/A:1004742027117.

Sun, J., Wang, L., Yu, J., Guo, B., Chen, L., Zhang, Y., Wang, D., Shen, Z., and Tsang, D.C.W., 2022, Cytotoxicity of stabilized/solidified municipal solid waste incineration fly ash: Journal of Hazardous Materials, v. 424, p. 127369, doi:10.1016/J.JHAZMAT.2021.127369.

Ude, S.N., 2010, The Synthesis and Crystal Chemistry of Ca12Al14O33 doped with Fe2O3:, https://trace.tennessee.edu/utk_gradthes/755 (accessed August 2022).

Vempati, R.K., Mollah, M.Y.A., Chinthala, A.K., Cocke, D.L., and Beeghly, J.H., 1995, Solidification/stabilization of toxic metal wastes using coke and coal combustion by-products: Waste Management, v. 15, p. 433–440, doi:10.1016/0956-053X(95)00050-A.

Vergara, S.E., and Tchobanoglous, G., 2012, Municipal Solid Waste and the Environment: A Global Perspective: Annual Review of Environment and Resources, v. 37, p. 277–309, doi:10.1146/ANNUREV-ENVIRON-050511-122532.

Vu, H.P., Shaw, S., Brinza, L., and Benning, L.G., 2013, Partitioning of Pb(II) during goethite and hematite crystallization: Implications for Pb transport in natural systems: Applied Geochemistry, v. 39, p. 119–128, doi:10.1016/J.APGEOCHEM.2013.10.001.

Wang, F. et al., 2021, Technologies and perspectives for achieving carbon neutrality: The Innovation, v. 2, p. 100180, doi:10.1016/J.XINN.2021.100180.

Wang, D.L., Chen, M.L., and Tsang, D.D.C.W., 2020, Green remediation by using low-carbon cement-based stabilization/solidification approaches: Sustainable Remediation of Contaminated Soil and Groundwater, p. 93–118, doi:10.1016/B978-0-12-817982-6.00005-7.

Wang, H., Ju, C., Zhou, M., Chen, J., Dong, Y., and Hou, H., 2022a, Sustainable and efficient stabilization/solidification of Pb, Cr, and Cd in lead-zinc tailings by using highly reactive pozzolanic solid waste: Journal of Environmental Management, v. 306, p. 114473, doi:10.1016/J.JENVMAN.2022.114473.

Wang, D., and Wang, Q., 2022, Clarifying and quantifying the immobilization capacity of cement pastes on heavy metals: Cement and Concrete Research, v. 161, p. 106945,

doi:10.1016/J.CEMCONRES.2022.106945.

Wang, L., Yu, K., Li, J.S., Tsang, D.C.W., Poon, C.S., Yoo, J.C., Baek, K., Ding, S., Hou, D., and Dai, J.G., 2018, Low-carbon and low-alkalinity stabilization/solidification of high-Pb contaminated soil: Chemical Engineering Journal, v. 351, p. 418–427, doi:10.1016/j.cej.2018.06.118.

Wang, L., Zhang, Y., and Tsang, D.C.W., 2022b, Future research directions for sustainable remediation: Low Carbon Stabilization and Solidification of Hazardous Wastes, p. 555–564, doi:10.1016/B978-0-12-824004-5.00013-X.

Watari, T., Cao, Z., Hata, S., and Nansai, K., 2022, Efficient use of cement and concrete to reduce reliance on supply-side technologies for net-zero emissions: Nature Communications 2022 13:1, v. 13, p. 1–9, doi:10.1038/s41467-022-31806-2.

Xue, Y., and Liu, X., 2021, Detoxification, solidification and recycling of municipal solid waste incineration fly ash: A review: Chemical Engineering Journal, v. 420, p. 130349, doi:10.1016/J.CEJ.2021.130349.

Yan, Y., Yang, S.Y., Miron, G.D., Collings, I.E., L'Hôpital, E., Skibsted, J., Winnefeld, F., Scrivener, K., and Lothenbach, B., 2022, Effect of alkali hydroxide on calcium silicate hydrate (C-S-H): Cement and Concrete Research, v. 151, p. 106636, doi:10.1016/J.CEMCONRES.2021.106636.

Yin, K., Ahamed, A., and Lisak, G., 2018, Environmental perspectives of recycling various combustion ashes in cement production – A review: Waste Management, v. 78, p. 401–416, doi:10.1016/J.WASMAN.2018.06.012.

Yu, L., Daniels, L.M., Mulders, J.J.P.A., Saldi, G.D., Harrison, A.L., Liu, L., and Oelkers, E.H., 2019, An experimental study of gypsum dissolution coupled to CaCO3 precipitation and its application to carbon storage: Chemical Geology, doi:10.1016/j.chemgeo.2019.08.005.

Zapata, J.F., Azevedo, A., Fontes, C., Monteiro, S.N., and Colorado, H.A., 2022, Environmental Impact and Sustainability of Calcium Aluminate Cements: Sustainability 2022, Vol. 14, Page 2751, v. 14, p. 2751, doi:10.3390/SU14052751.

Zhang, Y., Chang, J., Zhao, Q., Lam, W.L., Shen, P., Sun, Y., Zhao, D., and Poon, C.S., 2022, Effect of dosage of silica fume on the macro-performance and micro/nanostructure of seawater Portland cement pastes prepared with an ultra-low water-to-binder ratio: Cement and Concrete Composites, v. 133, p. 104700, doi:10.1016/J.CEMCONCOMP.2022.104700.

Zhang, H., Chen, G., Cai, X., Fu, J., Liu, M., Zhang, P., and Yu, H., 2021a, The leaching behavior of copper and iron recovery from reduction roasting pyrite cinder: Journal of Hazardous Materials, v. 420, p. 126561, doi:10.1016/J.JHAZMAT.2021.126561.

Zhang, J., Tan, H., He, X., Yang, W., Deng, X., Su, Y., and Yang, J., 2019, Compressive strength and hydration process of ground granulated blast furnace slag-waste gypsum system managed by wet grinding: Construction and Building Materials, v. 228, p. 116777, doi:10.1016/J.CONBUILDMAT.2019.116777.

Zhang, J., Yan, Y., Hu, Z., Fan, X., and Zheng, Y., 2018, Utilization of low-grade pyrite cinder for synthesis of microwave heating ceramics and their microwave deicing performance in dense-graded asphalt mixtures: Journal of Cleaner Production, v. 170, p. 486–495, doi:10.1016/J.JCLEPRO.2017.09.175.

Zhang, W. lu, Zhao, L. yang, Yuan, Z. jian, Li, D. qiang, and Morrison, L., 2021b, Assessment of the long-term leaching characteristics of cement-slag stabilized/solidified contaminated sediment: Chemosphere, doi:10.1016/j.chemosphere.2020.128926.

Zhang, T., Zhi, S., Li, T., Zhou, Z., Li, M., Han, J., Li, W., Zhang, D., Guo, L., and Wu, Z., 2020, Alkali activation of copper and nickel slag composite cementitious materials: Materials, doi:10.3390/ma13051155.

Zhuang, S., and Wang, Q., 2021, Inhibition mechanisms of steel slag on the early-age hydration of cement: Cement and Concrete Research, v. 140, p. 106283, doi:10.1016/J.CEMCONRES.2020.106283.

Supporting information for Chapter 3

Green in-situ remediation of pyrite ash: enhanced Pb retention through negative carbon binder strategies

Yikai Liu[1]; Simone Molinari[1,*]; Maria Chiara Dalconi[1]; Luca Valentini[1]; Maurizio Pietro Bellotto[2]; Giorgio Ferrari[3]; Roberto Pellay[4]; Graziano Rilievo[5]; Fabio Vianello[5]; Gabriella Salviulo[1]; Gilberto Artioli[1]

1 Department of Geosciences and CIRCe Centre, University of Padua, via G. Gradenigo 6, 35129, Padua, Italy

2 OPIGEO Srl, Montegalda, Vicenza, Italy

3 Mapei S.p.A., via Cafiero 22, 20158, Milan, Italy

4 TEVGroup S.r.l., via Romea 8, 30034, Mira (Venice), Italy

5 Department of Comparative Biomedicine and Food Science, University of Padova, Viale dell'Università 16, 35020 Legnaro, Italy

Table.S1. XRD instrument settings

Parameters	**Settings**
Radiation source	Cobalt
Detector	X'Celerator detector
Geometry optics	Bragg-Brentano geometry Soller slits 0.04 rad.; Bragg-Brentano^{HD}
2θ range	3-84°
Step size	0.017°
Time per step	100 s

Table.S2. The estimated carbon footprint and cost analysis of the applied binder strategies.

Parameters	CO_2 (kg/t)	Reference	Cost (€/t)	Reference
OPC	852	D Ravikumar, 2021	70	Average commercial price
CAC	596	J Seo, 2022	300	Average commercial price
CEM III/B	213	T García-Segura, 2014	90	Average commercial price
MAY	195	Estimated[1]	50	Average commercial price
ABS	107	Estimated[1]	90	Average commercial price
Na_2SiO_3	232	J.L.Santana-Carrillo, 2022	-	
Mayenite	412	D Fernández-González, 2018	-	
GGBFS	52	SJ Kwon, 2019	-	
Water	2.5	NB Chang, 2012	0.6	Upadhyaya 2022

Note: [1] The carbon footprint was evaluated based on the mix proportion of the raw materials. (e.g., the MAY is composed of mayenite and GGBFS and the ABS is primarily composed of GGBFS and Na_2SiO_3)

Table.S3. The estimated H_2SO_4 and pyrite ash production in the next decade

Year	Sulfuric acid production (Mt)	Pyrite ash production (Mt)	Discarded pyrtie ash (Mt)
2021	77.66	11.87	8.31
2022	84.18	12.86	9.00
2023	91.23	13.94	9.76
2024	98.84	15.10	10.57
2025	107.53	16.43	11.50
2026	116.76	17.84	12.49
2027	126.53	19.33	13.53
2028	137.40	20.99	14.70
2029	148.80	22.74	15.92
2030	161.29	24.65	17.25

Table.S4. The Pb concentrations (mg/kg) were collected from multiple publications.

No.	Concentration	Sources	No.	Concentration	Sources
1	40430	(Contessi et al., 2020)	17	126	(Sierra et al., 2010)
2	10352	(Gabarrón et al., 2018)	18	113	(Sierra et al., 2010)
3	5399	(Gabarrón et al., 2018)	19	278	(Fellet et al., 2007)
4	2394	(Boente et al., 2017)	20	2376	(Fernández-Caliani, 2012)
5	7550	(Soriano-Disla et al., 2018)	21	1269	(Fernández-Caliani, 2012)
6	10600	(Bendz et al., 2021)	22	6385	(Fernández-Caliani, 2012)
7	6360	(Bendz et al., 2021)	23	1749	(Fernández-Caliani, 2012)
8	43198	(Wang et al., 2018)	24	2825	(Fernández-Caliani, 2012)
9	9838	(Grantcharova and Fernandez-Caliani, 2021)	25	247	(Fernández-Caliani, 2012)
10	2130	(Becelic-Tomin et al., 2014)	26	137	(Fernández-Caliani, 2012)
11	395	(Oliveira et al., 2012)	27	493	(Vamerali et al., 2011)
12	443	(Oliveira et al., 2012)	28	410	(Corsini et al., 2010)
13	349	(Oliveira et al., 2012)	29	410	(Corsini et al., 2011)
14	284	(Oliveira et al., 2012)	30	144	(Matzen et al., 2020)
15	658	(Oliveira et al., 2012)	31	5998	(Pérez-Sirvent et al., 2011)
16	4890	(López et al., 2008)			
Mean value (mg/kg)			4396		

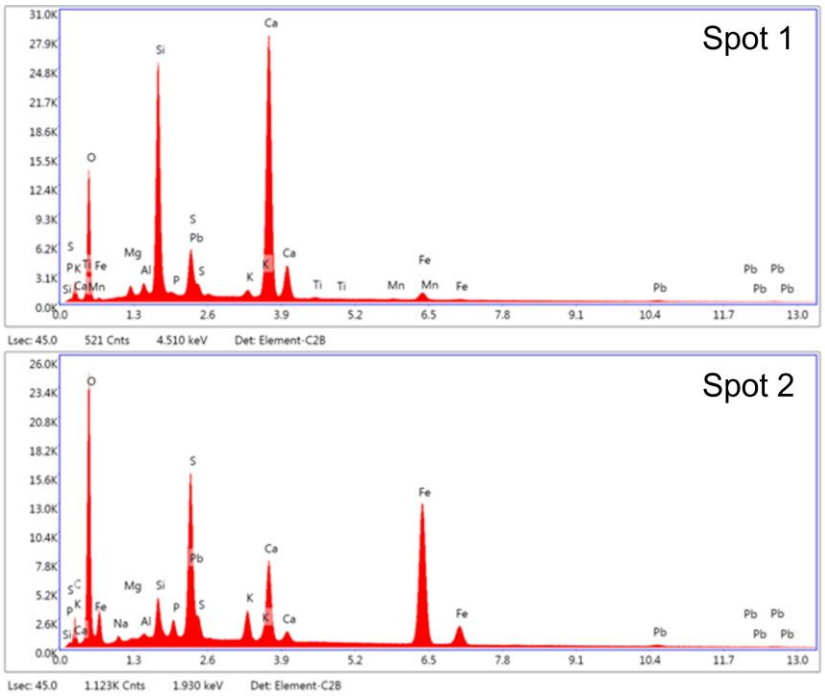

Figure.S1. The EDS spectra attributed to spots 1 and 2 (CP pellets) are marked in Fig.1

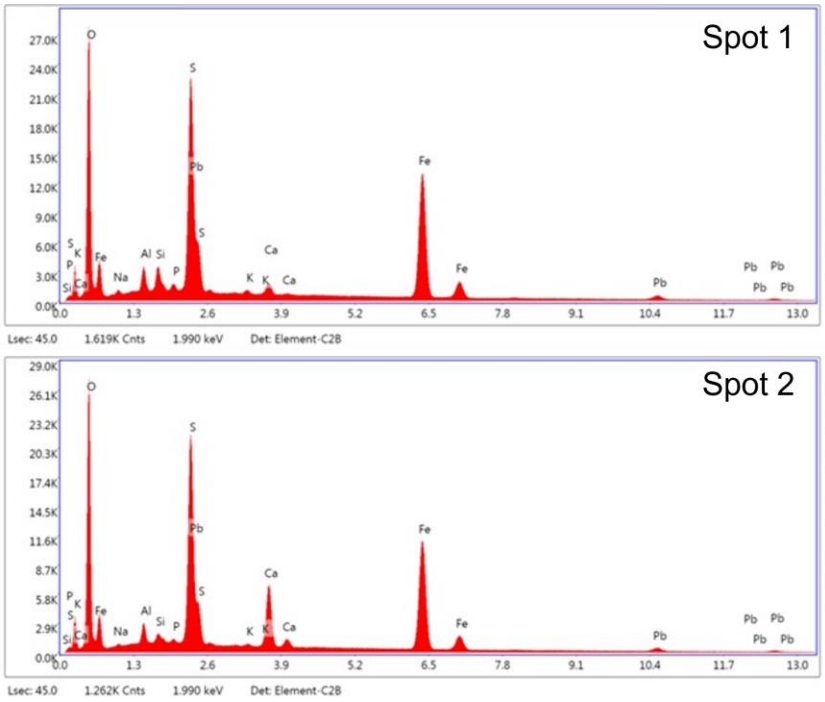

Figure.S2. The EDS spectra attributed to spots 1 and 2 (CA pellets) are marked in Fig.3.

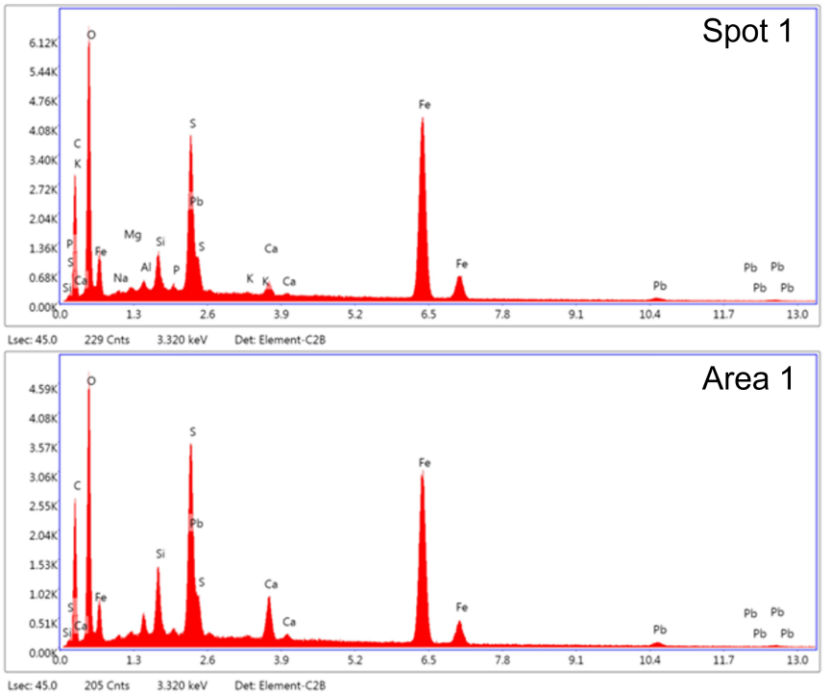

Figure.S3. The EDS spectra attributed to spots 1 and area 1 (MB pellets) are marked in Fig.4.

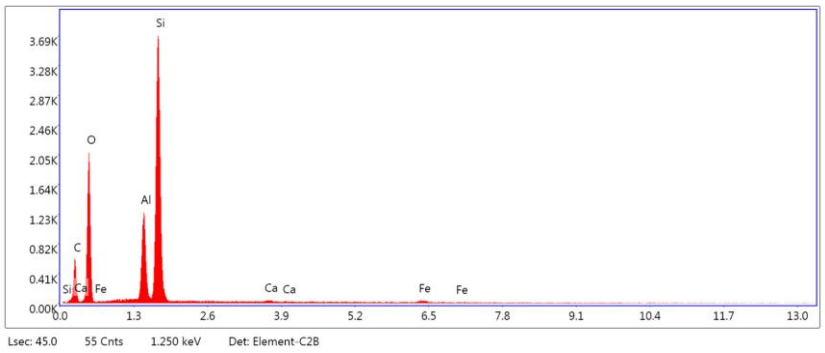

Figure.S4. The EDS spectra indicate the presence of aluminosilicates (MB pellets) are marked in Fig.4.

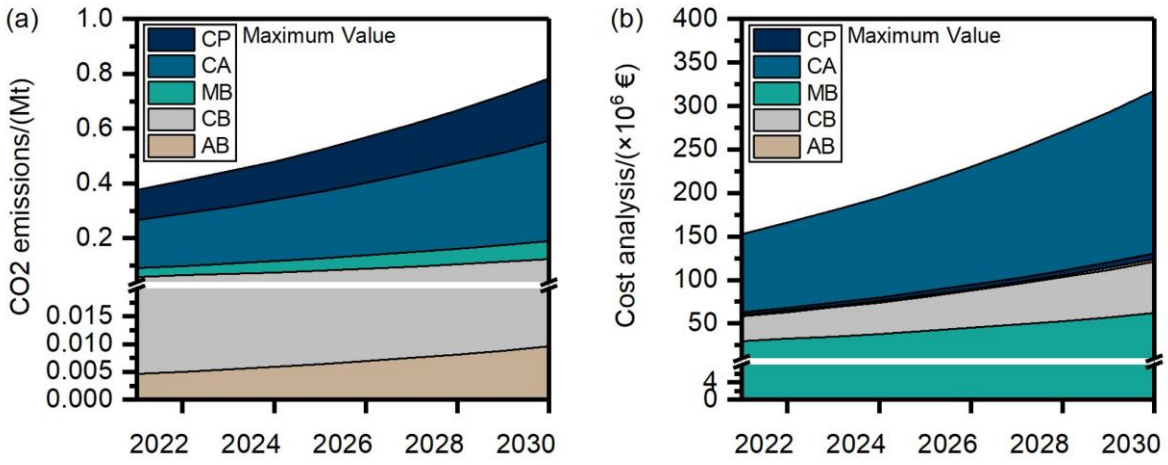

Figure.S5. The CO2 carbon footprint (a) and financial expense analysis (b) attributed to the in-situ remediation of pyrite ash with a Pb concentration of 43198 mg/kg.

References

Becelic-Tomin, M., Dalmacija, B., Rajic, L., Tomasevic, D., Kerkez, D., Watson, M., and Prica, M., 2014, Degradation of anthraquinone dye reactive blue 4 in pyrite ash catalyzed fenton reaction: The Scientific World Journal, v. 2014, doi:10.1155/2014/234654.

Bendz, D., Tiberg, C., and Kleja, D.B., 2021, Mineralogical characterization and speciation of sulfur, zinc and lead in pyrite cinder from Bergvik, Sweden: Applied Geochemistry, v. 131, p. 105010, doi:10.1016/J.APGEOCHEM.2021.105010.

Boente, C., Sierra, C., Rodríguez-Valdés, E., Menéndez-Aguado, J.M., and Gallego, J.R., 2017, Soil washing optimization by means of attributive analysis: Case study for the removal of potentially toxic elements from soil contaminated with pyrite ash: Journal of Cleaner Production, v. 142, p. 2693–2699, doi:10.1016/J.JCLEPRO.2016.11.007.

Contessi, S., Calgaro, L., Dalconi, M.C., Bonetto, A., Bellotto, M. Pietro, Ferrari, G., Marcomini, A., and Artioli, G., 2020, Stabilization of lead contaminated soil with traditional and alternative binders: Journal of Hazardous Materials, doi:10.1016/j.jhazmat.2019.120990.

Corsini, A., Cavalca, L., Crippa, L., Zaccheo, P., and Andreoni, V., 2010, Impact of glucose on microbial community of a soil containing pyrite cinders: Role of bacteria in arsenic mobilization under submerged condition: Soil Biology and Biochemistry, v. 42, p. 699–707, doi:10.1016/J.SOILBIO.2009.12.010.

Corsini, A., Cavalca, L., Zaccheo, P., Crippa, L., and Andreoni, V., 2011, Influence of microorganisms on arsenic mobilization and speciation in a submerged contaminated soil: Effects of citrate: Applied Soil Ecology, v. 49, p. 99–106, doi:10.1016/J.APSOIL.2011.06.010.

Fellet, G., Marchiol, L., Perosa, D., and Zerbi, G., 2007, The application of phytoremediation technology in a soil contaminated by pyrite cinders: Ecological Engineering, v. 31, p. 207–214, doi:10.1016/J.ECOLENG.2007.06.011.

Fernández-Caliani, J.C., 2012, Risk-based assessment of multimetallic soil pollution in the industrialized peri-urban area of Huelva, Spain: Environmental Geochemistry and Health, v. 34, p. 123–139, doi:10.1007/S10653-011-9396-0/TABLES/6.

Gabarrón, M., Babur, O., Soriano-Disla, J.M., Faz, A., and Acosta, J.A., 2018, Composition and risk assessment of roasted pyrite ash from fertiliser production: Chemosphere, v. 209, p. 277–285, doi:10.1016/J.CHEMOSPHERE.2018.06.109.

Grantcharova, M., and Fernandez-Caliani, J.C., 2021, Geochemical and mineralogical reactions driven by

acid generation and metal release from pyritic wastes improperly disposed on estuarine marsh soils:, doi:10.7185/GOLD2021.4050.

López, M., González, I., and Romero, A., 2008, Trace elements contamination of agricultural soils affected by sulphide exploitation (Iberian Pyrite Belt, Sw Spain): Environmental Geology, v. 54, p. 805–818, doi:10.1007/S00254-007-0864-X/FIGURES/9.

Matzen, S., Fakra, S., Nico, P., and Pallud, C., 2020, Pteris vittata Arsenic Accumulation Only Partially Explains Soil Arsenic Depletion during Field-Scale Phytoextraction: Soil Systems 2020, Vol. 4, Page 71, v. 4, p. 71, doi:10.3390/SOILSYSTEMS4040071.

Oliveira, M.L.S., Ward, C.R., Izquierdo, M., Sampaio, C.H., de Brum, I.A.S., Kautzmann, R.M., Sabedot, S., Querol, X., and Silva, L.F.O., 2012, Chemical composition and minerals in pyrite ash of an abandoned sulphuric acid production plant: Science of the Total Environment, doi:10.1016/j.scitotenv.2012.04.046.

Pérez-Sirvent, C., García-Lorenzo, M.L., Martínez-Sánchez, M.J., Molina-Ruiz, J., Marimon, J., and Navarro, M.C., 2011, Use of marble cutting sludges for remediating soils and sediments contaminated by heavy metals: Environmental Progress & Sustainable Energy, v. 30, p. 533–539, doi:10.1002/EP.10502.

Sierra, C., Gallego, J.R., Afif, E., Menéndez-Aguado, J.M., and González-Coto, F., 2010, Analysis of soil washing effectiveness to remediate a brownfield polluted with pyrite ashes: Journal of Hazardous Materials, v. 180, p. 602–608, doi:10.1016/J.JHAZMAT.2010.04.075.

Soriano-Disla, J.M., Spille, U., Gabarrón, M., Faz, Á., and Acosta, J.A., 2018, Evaluation of strategies for mitigating risks associated with metals in pyrite ash: Journal of Environmental Management, v. 217, p. 403–410, doi:10.1016/J.JENVMAN.2018.03.104.

Vamerali, T., Bandiera, M., Hartley, W., Carletti, P., and Mosca, G., 2011, Assisted phytoremediation of mixed metal(loid)-polluted pyrite waste: Effects of foliar and substrate IBA application on fodder radish: Chemosphere, v. 84, p. 213–219, doi:10.1016/J.CHEMOSPHERE.2011.04.052.

Wang, L., Yu, K., Li, J.S., Tsang, D.C.W., Poon, C.S., Yoo, J.C., Baek, K., Ding, S., Hou, D., and Dai, J.G., 2018, Low-carbon and low-alkalinity stabilization/solidification of high-Pb contaminated soil: Chemical Engineering Journal, v. 351, p. 418–427, doi:10.1016/j.cej.2018.06.118.

Chapter 4

Retention of phosphorus and fluorine in phosphogypsum for cemented paste backfill: Experimental and numerical simulation studies

Yikai Liu[1]; Qiusong Chen[2, 3]; Maria Chiara Dalconi[1]; Simone Molinari[1]; Luca Valentini[1]; Yunmin Wang[2,3]; Shiyuan Sun[3]; Peishen Wang[3]; Gilberto Artioli[1]

[1] *Department of Geosciences and CIRCe Centre, University of Padua, via G. Gradenigo 6, 35129, Padua, Italy*

[2] *Sinosteel Maanshan General Institute of Mining Research Co., Ltd., Maanshan, 24300, China;*

[3] *School of Resources and Safety Engineering, Central South University, Lushan South Road 932, 410083, Hunan, China*

Graphical abstract

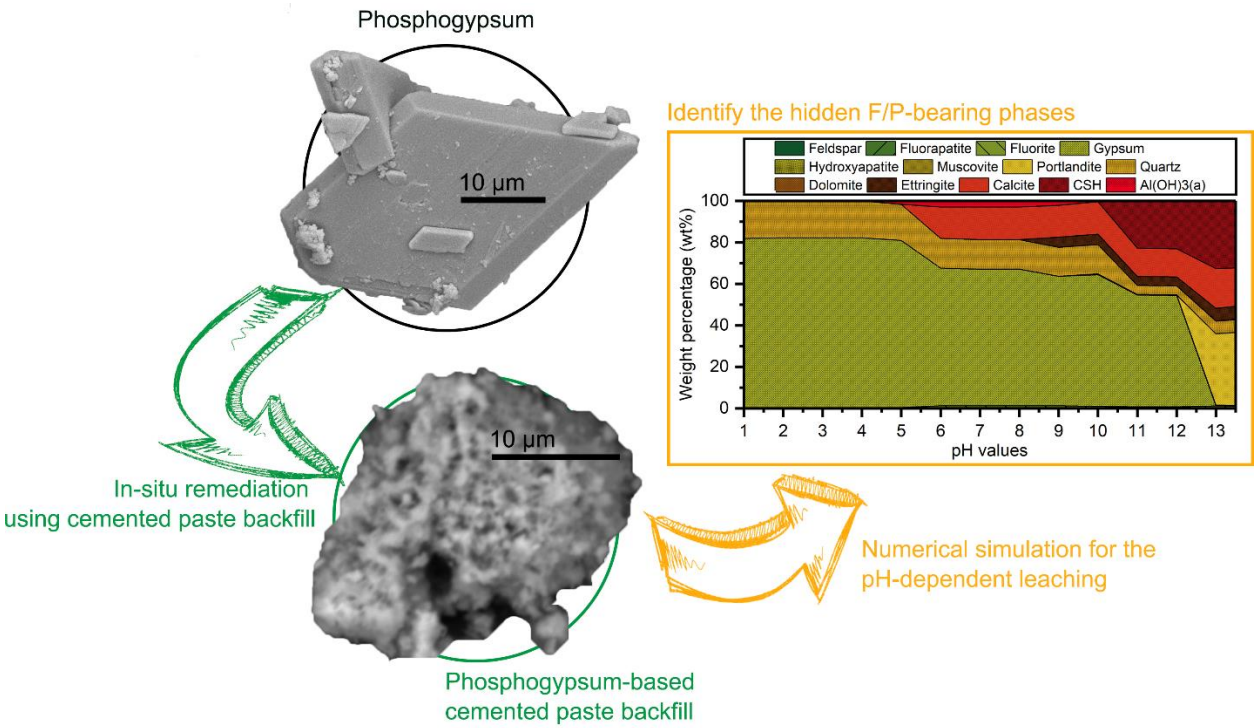

This chapter is published in Environmental Research, Volume 214, Part 1, 113775

Abstract

The solidification/stabilization of phosphogypsum using cemented paste backfill (OCPB) provides a low-cost and alternative in-situ technique for recycling phosphogypsum stockpiles. But the OCPB is far from obtaining steady states in which the pollutants would redistribute as a response to dynamic environmental conditions. Further, the associated chemical interactions and the mineralogy information of the solubility-controlling phases of contaminants (fluorine and phosphorus) have not been thoroughly studied or fully understood. In this study, a framework coupling the chemical, mineralogical, and morphological analyses is used to determine the fluoride and phosphate retention mechanisms of immobilized OCPB. Then the pH-dependent leaching tests and numerical simulation is applied as a useful tool to identify the minerals controlling stabilized OCPB leaching behavior. The overall findings proved that aluminate-rich calcium silicate hydrates play an essential role in fluoride and phosphate retention. Both experimental and simulational acid neutralization and leaching curves indicate that the cementitious matrix works as a strong buffering material ensuring high pH conditions that are necessary for fluorine and phosphorus retention. Although discrepancies were observed in absolute fluorine and phosphorus leaching values at highly acidic conditions, the simulations are able to describe highly amphoteric leaching behavior. The simulation suggests that the aluminum species and calcium phosphates governed the solubility of fluorine and phosphorus, respectively. The results of this work would have implications for predicting the leaching behavior of OCPB in detrimental and multiple environments.

Keywords

Phosphogypsum, cemented paste backfill, solidification/stabilization, leaching behavior,

waste management

1. Introduction

With the increasing demand for phosphoric fertilizers, phosphogypsum (PG) stacking and discharging is becoming a serious global environmental issue (Chernysh et al., 2021). As a typical by-product generated from the acidification process of phosphoric fertilizers production, the current worldwide generation of PG was estimated at 200-250 million tons per year (Rashad, 2017), with approximately 70 million tons of annual production in China (Zeng et al., 2021). Noteworthy, the major part of PG is still dumped in large stockpiles without any treatment because of the high remediation costs (Zhou et al., 2020), coupled with the risk of secondary contamination (Jiang et al., 2018) and transportation restrictions (Wei et al., 2021). The discarded PG not only occupies considerable land areas but also degrades groundwater quality by the PG leachates infiltration (Melki and Gueddari, 2018). In particular, water-soluble phosphorous and fluorine, which represent the primary PG pollutants, and impurities of heavy metals (Ba, Cu, Pb, Zn) and toxic

radionuclides (Ra226, Pb210, Po210, U238, et al.) can be concentrated in PG wastes (Bisone et al., 2017) thus increasing PG remediation complexity (Rashad, 2017; Yang et al., 2020). The phosphorus concentration can lead to the extensive growth of harmful algae and eutrophication of water bodies (Tong et al., 2017), while high fluoride intake can increase the risk of chronic toxicity and cancer in humans, especially children (Adimalla et al., 2020). For all the abovementioned factors, the persistence of PG-associated groundwater pollution represents the most demanding issue. Only about 15% of PG is recycled in the ex-situ forms of agricultural fertilizer (Hentati et al., 2015), road base (Amrani et al., 2020), set retarder (Akin Altun and Sert, 2004), and soil stabilization amendments (Degirmenci et al., 2007). Therefore, considering the high accumulation rate of pollutants and acidity in the disposal sites (Bisone et al., 2017), finding a sustainable environmental-economic equilibrium solution for PG is in pressing need. The use of cemented paste backfill (CPB) for underground disposal of industrial by-products was accordingly introduced as a practical and affordable in-situ solution for PG management (Chen et al., 2017; Li et al., 2017a). The incorporation and stabilization of chemicals in the cementitious matrix represent a common practice for treating industrial solid wastes. However, the field application of this technology in PG remediation still needs to be optimized to prevent the pollutants released from recycled materials (Behera et al., 2021).

Nevertheless, the PG-based CPB (OCPB) will sooner or later intercept more acidic or basic groundwater. In accordance with the different durabilities of the applied binding strategies and formulations, the partial remobilization of toxic elements might be a source of secondary environmental risk (Li et al., 2020; Shi et al., 2021) making it essential to understand the elution process of the different elements. In particular, the mechanisms controlling the phosphates and fluoride immobilization in OCPB systems are still not well established (Li et al., 2017a). With the ordinary Portland cement (OPC) stabilization, phosphorus was found would precipitate as calcium-phosphate (Tan et al., 2017; Zhou et al., 2020) or adsorb by calcium silicate hydrates (CSH) (Shi et al., 2021) and ettringite (Wu and Liu, 2018). Besides, fluoride was reported as sparingly soluble fluorite (CaF2) (Park et al., 2008; Gomes et al., 2012). Although the solubility of these stabilized mineral phases is strongly affected by the pH conditions, only a few studies performed leaching experiments by the acid attack (Li et al., 2017b). Many scholars only investigated the evolution of the system and determined the stabilization efficiency by the simple interaction with deionized water (Xue et al., 2019; Shi et al., 2021). To reveal the mechanisms of the leaching behavior and the mobility of the abovementioned contaminants, previous studies formulated several hypotheses, mainly relying on the experimental results. For instance, Gijbels et al.'s work (2020) identifies the mineral phases involved in the dissolution process by inversely determining the leached ions in the solution. However, they can hardly be confirmed due to the limitation of detection technics (for instance, the X-ray diffraction is more sensitive to the phase with more than 1 wt%) and the preparation of laborious large-scale experiments (time- and

expense-consuming).

Therefore, a convincing simulation is equally important and urgently required as a useful tool to estimate the release of pollutants from the stabilized mixtures. In some cases, scholars attempt to represent the leaching behavior of stabilized PG using a correlation analysis model (Zhou et al., 2020). This approach does not give a direct indication of chemical species controlling the release. But several models have been developed to describe the leaching behavior of heavy metals. Halim et al. (2005) modeled the leaching behavior of heavy metals from cementitious waste in the presence of two acid contents merchants and deionized water. Solpuker et al. (2014) simulated the leaching potential of pervious concrete and its capacity for immobilizing Cu, Pb, and Zn across a pH range from 4 to 12. These models are able to predict the theoretical response of minerals in various geochemical contexts. Herein, the simulation approach could be a promising tool for predicting the pollutants releasing behavior of the OCPB. To the best of our knowledge, the detailed investigation of coupling the F and P retention mechanisms and the impact of multiple leachates on the equilibrium of the reacting minerals in the OCPB systems have not been established well.

Thereby, the present study aims to assess the retention mechanisms and releasing behavior of fluorine and phosphorus over a wide range of pH through a combination of laboratory experiments and geochemical modeling. The mineralogical and chemical composition and morphology of PG and OCPB were investigated by X-ray fluorescence spectroscopy (XRF), X-ray diffraction (XRD), scanning electron microscope coupled with energy dispersive spectrometer (SEM/EDS), and electron microprobe analysis with wavelength-dispersive spectroscopy (EPMA/WDS). The solidification/stabilization effectiveness was verified by studying the leaching of fluorine and phosphorus from the PG and OCPB to the aqueous solution. Based on the characterization of PG and OCPB, geochemical modeling is proposed as an aid tool to identify and quantify the chemical reactions which are resulted from the interaction between the assemblages and the leachates. This combination of the experiments and modeling approaches gives a more comprehensive insight into the speciation of fluorine and phosphorus in the solid and solution, which can be used for optimizing the selection of remediation scenarios of PG in real cases. These findings can enrich the research to bridge the gap between the leaching behavior and the mineralogical controls, which has guiding significance for properly addressing the complex reality of the areas suffering from PG storage-related pollution.

2. Materials and methods

2.1. Sampling and OCPB preparation

PG used in this work was excavated from the layer comprised in the depth interval between approximately 20 to 50 cm from the surface of a stockpile site that was devoted to storage PG generated by fertilizer

manufacturing and beneficiation of low-grade phosphate rock (Fig.S1). The excavated PG samples used for the experiments were sieved through a 200 μm mesh and then dried at 55±5 °C to determine the moisture content. OCPB samples were prepared at a PG: cement: water ratio of 2:1:1, using M32.5 Portland cement (Xiangping Co. Ltd, GB/T3183-2017) as the binder. The PG, cement, and water were homogeneously mixed, then poured into plastic cylinders (5 cm in diameter and 10 cm in height), then cured for 28 days in a box at a relative humidity of 90% and temperature of 25 ± 2 ℃. Before the subsequent characterization experiments, PG and OCPB samples were dried at 55 ± 5℃ for 48 h and stored in a vacuum dryer to avoid further hydration of cement phases and dissolution of soluble species.

2.2. Physical, microstructural, spectroscopic, and chemical analysis

XRD patterns were recorded in an automated diffractometer (D8 Advance, Bruker Co. Ltd, Germany) employing Cu-Kα as the radiation source at 40 kV and 40 mA. The scan range was from 4° to 80° 2θ with a step width of 0.02° 2θ. The mineralogical composition of the powdered sample was determined quantitatively by Rietveld analysis. Highscore Plus 3.0e and Topas 2.1 were applied for identification and quantification. The measurement details are reported in Table.S1. To quantify the amorphous fractions in the samples, 20 wt.% of ZnO (zincite) internal standard (ACS Reagent) were mixed with the powder. The bulk elemental composition of the raw materials was determined with wavelength dispersive XRF spectrometry (AXS S4 Pioneer, Bruker Co. Ltd, Germany). About 400 mg powders were pressed (30 MPa, Zhonghe ZHY-401B, Beijing Zhonghechuangye Co., Ltd., China) as a double layer on a boric acid backing pellet. FTIR spectra were obtained by a spectrometer (Nicolet iS50, Thermo Fisher, Madison, USA) with a sample to KBr powder ratio of 1/100. The spectra were obtained in the range of 400 to 4000 cm^{-1} at a resolution of 4 cm^{-1} averaging 32 scans for each measurement. Microstructural investigation on polished and carbon-coated PG and cured OCPB were performed using SEM (JSM-7900F, JEOL Ltd., Japan) equipped with an EDS spectrometer. EMPA/WDS (JJXA-8230, JEOL Ltd., Japan) was performed to characterize fluorine and iron to avoid the overlap of F *K*α and Fe *L*α lines obtained by SEM/EDS.

2.3. Leachate assessment of fluoride and phosphate

The mobilization of toxic elements was assessed according to the standard for leaching toxicity of solid wastes (GB/5086.1; 1997, Jing et al., 2013). The OCPB samples were preliminary broken into particles less than 5 mm in diameter. Aliquots of 10 g were placed in contact with 100 ml solutions containing an increasing amount of HCl or NaOH. Each concentration of the acid/base solution was triplicate tested. After being immersed for 18 h using a rotary shaker at 30 rpm, the leachates were filtered through 0.45 μm filter paper and used for further analysis. The sampled solution for fluoride and phosphorus analysis was tested through the national standard of China for the determination of fluoride (ion-selective electrode method, GB/7484-87, 1987) and phosphate (inductively coupled plasma optical emission spectrometry HJ/776,

2015). The fluoride was tested by a fluoride ion detector (PF-202, INESA Scientific Instrument Co., Ltd, Shanghai, China) with a detection limit from 10-1 to 10-6 mol/L. To eliminate the influence of fluoro complex, sodium acetate (CH3COONa) or HCl was applied to modify the pH values of leachates from 5 to 7. The remained residues after leaching were collected and then dried at temperatures of 55 ± 5℃.

2.4. Geochemical modeling

The U.S. Geological Survey (USGS) program Phreeqc Interactive 3.0.6 (Parkhurst and Appelo, 2013) was used to determine the mineralogical species that most significantly affect the PG and OCPB leaching in different solutions. No kinetic was considered in reactions. Thus it was assumed that equilibrium between liquid and solid was reached. The Lawrence Livermore national library and Phreeqc thermodynamic database were used for solubility products and dissolution reactions of mineral phases.

The initial mineralogy inputs of the model simulation are based on the previous characterization. In the PG model, hydrofluoric acid (HF), phosphoric acid (H_3PO_4), and sulfuric acid (H_2SO_4) are introduced into the solution to representing the residual acids from the industrial process (Pérez-López et al., 2010; Bisone et al., 2017; Kandil et al., 2017). Considering that, on one side, scorzalite could be a gangue mineral that has already experienced very harsh acidic conditions and no thermodynamic data are available, this phase was assumed to be stable during the experimental leaching procedures. In the OCPB model, the stabilized phosphorus and fluoride were assumed in the form of calcium phosphate ($Ca_3(PO_4)_2$) and fluorite (CaF_2). Portlandite is introduced into the solution to simulate the alkalinity of the OCPB assemblage. Based on the aluminum-rich-CSH gel structure that is observed, the amorphous content quantified by XRD analysis is classified into CSH matrix and amorphous aluminum hydroxide ($Al(OH)_3$). The Ca/Si ratio of the CSH matrix is assumed to be 1.5, and the dissolution reaction and equilibrium constant is from Diaz Caselles et al. (2021). According to a previous study (Halim et al., 2005), an average surface area of 70 m^2/g was attributed to the CSH matrix. The amorphous aluminum hydroxide is found that, with the acid attack, can present in the framework silicates and single silanol groups (Gutberlet et al., 2015). Clinker phases (C_2S, C_3S, C_3A, and C_4AF) were not included in the database because no log *K* values of their dissolution can be found in the literature. Moreover, since the surface characteristics for describing fluoride adsorption are not well-established, two simulations were given: (1) OCPB_S1: only dissolution and precipitation reactions are included; (2) OCPB_S2: the data of chloride surface complexation on CSH is applied to represent the fluoride adsorption (Yoshida et al., 2021).

3. Results and discussion

3.1. Phase assemblage of the PG and OCPB samples

Quantitative phase analysis of XRD data highlighted that the PG is mainly composed of gypsum

($CaSO_4 \cdot 2H_2O$), bassanite ($CaSO_4 \cdot 0.5H_2O$), and anhydrite ($CaSO_4$), representing the 90.4wt% of the whole sample (Fig.1a,b). The other components in the PG sample consist of quartz (SiO_2), muscovite ($KAl_2(AlSi_3O_{10})(OH)_2$), and feldspar ($KAlSi_3O_8$). Besides, minor content of phosphorus compound (scorzalite, $FeAl(PO_4)(OH)_2$) was detected in the XRD pattern. The three calcium sulfate species were produced from the acidulation process in the phosphoric acid plant and the following recrystallization in the storage sites (Lieberman et al., 2020). Quartz, muscovite, and feldspar are common gangue minerals (impurities) in phosphate rocks and would remain in the PG by-product based on the applied beneficiation procedures (Li et al., 2019; Deng et al., 2020). Results of chemical analysis (Table.S2) corroborate the mineralogical results, indicating SO_3 and CaO as the main constituents representing around 90 wt% of the total sample weight (53.69 wt% and 37.07 wt%, respectively). The third main constituent is SiO_2 (5.28 wt%) which belongs primarily to quartz and a lesser extent, together with Ba, Na, K, and Ti, could confirm the presence of residual feldspar minerals (Rock, 1987), even though many authors indicate the possible presence of clay minerals (Rutherford et al., 1994; Arocena et al., 1995).

By comparing the XRD results with XRF analysis reporting P, Fe, Mg, and Al (1.07, 0.63, 0.08, and 0.70 wt%, respectively), it is presumable that all these elements belong to the mineral scorzalite, probably representing a residual unreacted phase from the feedstock ore. However, considering that the phosphorus rock ore used in the industrial process did not belong to just one mining site, it is difficult to confirm scorzalite origin. For this reason, the possibility of scorzalite as a secondary phase crystallized after the industrial process cannot be excluded. Meanwhile, the quantified P_2O_5 in PG is reported in many forms, such as phosphoric acid, $Ca(H_2PO_4)_2 \cdot H_2O$, $Ca_3(PO_4)_2$, or apatite (Mashifana, 2019; Chernysh et al., 2021). Further, it should be considered that coprecipitation with SO_4^{2-}/HPO_4^{2-} exchange in gypsum cannot be ruled out as the potential source of P, as suggested by FTIR analysis of the band at 837 cm^{-1} (Fig.S2 and Table.S3) characteristic of HPO_4^{2-} (Ennaciri et al., 2016). Moreover, it should also be stressed that a certain amount of phosphate could belong to surface complexed HPO_4^{2-} on silicates, especially feldspars and muscovite, which contribute becomes relevant, especially at acidic conditions as in the PG system (Fox and Malati, 1993; Priyantha and Perera, 2000). Finally, the fluorine weight percentage (0.8 wt%) in PG detected by XRF may be in the forms of acids, like HF and H_2SiF_6, and fluorosilicate complexes (Rashad, 2017; Ennaciri et al., 2020).

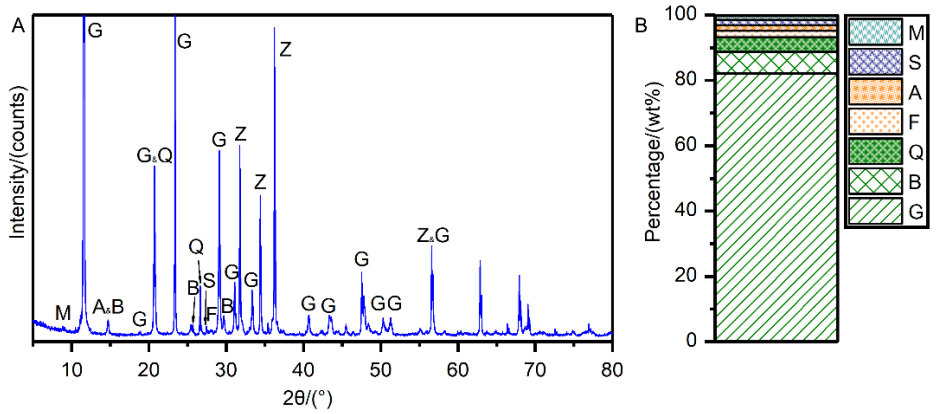

Figure.1 Mineralogical characterization of PG sample. (A) XRD pattern, (B) quantitative mineralogical composition obtained by Rietveld method. (A: Anhydrite, B: Bassanite, F: Feldspar, G: Gypsum, M: Muscovite, Q: Quartz, S: Scorzalite, Z: Zincite)

After 28 days of curing, the binder in the OCPB specimens is not entirely hydrated in both scenarios, with diffraction peaks of cement phases (C_3A, C_3S, and C_2S) still observed (Fig.2a,b). Phosphorus or fluoride-containing crystalline phases are not detected in cured OCPB samples. Portlandite ($Ca(OH)_2$), which usually forms after C_3S hydration, is not found in OCPB. This could be due to as fluorine is released into the system, portlandite acts as a pH buffer and dissolves completely, releasing Ca^{2+} in solution, forming calcite by reaction with atmospheric CO_2. Besides, gypsum, bassanite, and anhydrite from PG dissolved readily at the first stage of hydration and subsequentially provided Ca^{2+}, further accelerating the reaction. In the PC system, AFm is identified in the XRD pattern, which is usually formed in cement paste when the effective molar ratio of SO_3 to Al_2O_3 is <3 (Christensen et al., 2004). In comparison, ettringite is already found in the 7d OCPB sample (2.5 wt%) as a result of the appreciable sulfate content from gypsum (Hewlett, 2003). It should be noted that ettringite usually incorporates different pollutants in its structure (Chrysochoou and Dermatas, 2006; Contessi et al., 2020; Molinari et al., 2021). Moreover, being already reported the potential incorporation of fluorine (Gomes et al., 2012; Kamei et al., 2015) and phosphorus (Wu and Liu, 2018) in ettringite, its crystallization should be accompanied by a reduction in the above-mentioned pollutants solubility and mobility. In addition to the precipitation of P/F-bearing crystalline phases, the OPCB amorphous content can play a key role in fluorine and phosphorous fate. In fact, amorphous calcium silicate hydrates (CSH) is reported as one of the major phase incorporating/absorbing these pollutants in cementitious systems (Xu et al., 2017; Shi et al., 2021). To quantify the amount of CSH present in the system, an internal standard, consisting of zincite, was used in the XRD measurements. The results show that 25 and 21 wt% of amorphous content were found in 7 and 28 days cured OCPB (Fig.2b). The FT-IR spectra and corresponding possible assignments (Fig.S3 and Table.S4) of PC and OCPB corroborate the XRD quantification (Cai et al., 2018).

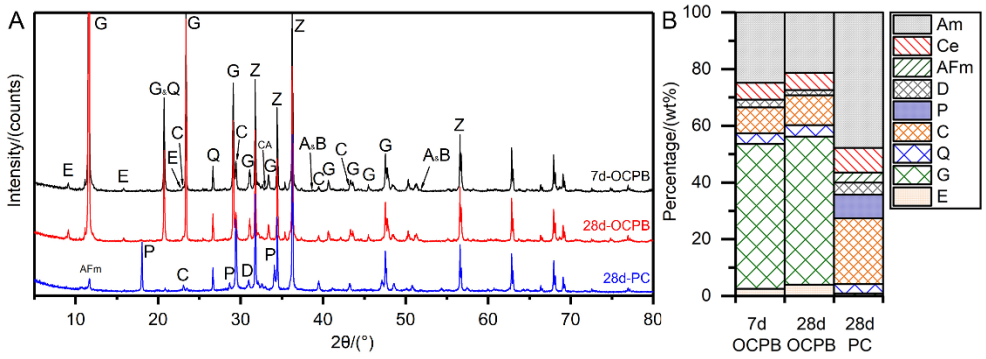

Figure.2. XRD quantification results of cured PC and OCPB samples. (A) XRD patterns of PC and OCPB (B) the quantitative mineralogical composition obtained by the Rietveld method of OCPB and PC at different curing ages (A: Alite, B: Belite, C: Calcite, D: dolomite, E: ettringite, G: gypsum, P: portlandite, Q: Quartz, Z: zincite, AFm: Monocarboaluminate, CA: calcium aluminate, Ce: the accumulation of Alite, Belite, and calcium aluminate, Am: amorphous).

3.2. Microstructural characterization of the PG and OCPB samples

The SEM imaging of PG reveals the presence of gypsum with its typical habit (Fig.3a and b). The SEM micrographs (Fig.3c) and the associated elemental map (Fig.3d~i) show the presence of iron sulfide particles and needle-like Al-Si-F-P-O complex, which were not detected in the previous bulk analysis. The presence of iron sulfide could be related to residual pyrite in the phosphate ores (Rentería-Villalobos et al., 2010; Deng et al., 2020). It should be noted that the fine matrix of the PG sample is mainly composed of aluminosilicates, probably muscovite, based on Al, O, Si, and K distribution (Fig.3h, j, k, and l). Interestingly, the results of P and F distributions substantiated the active role of silicates in the incorporation/complexation of these two contaminants, as demonstrated in the XRD and XRF analysis (Fig.1 and Table.S2). In addition, the formation of the Al-Si-F-P-O complex (Fig.3c) could be attributed to the weathering of aluminosilicates (Rutherford et al., 1995), thus representing a crucial problem for the PG repositories due to the fluorine mobilization with the clay soils or clay liners.

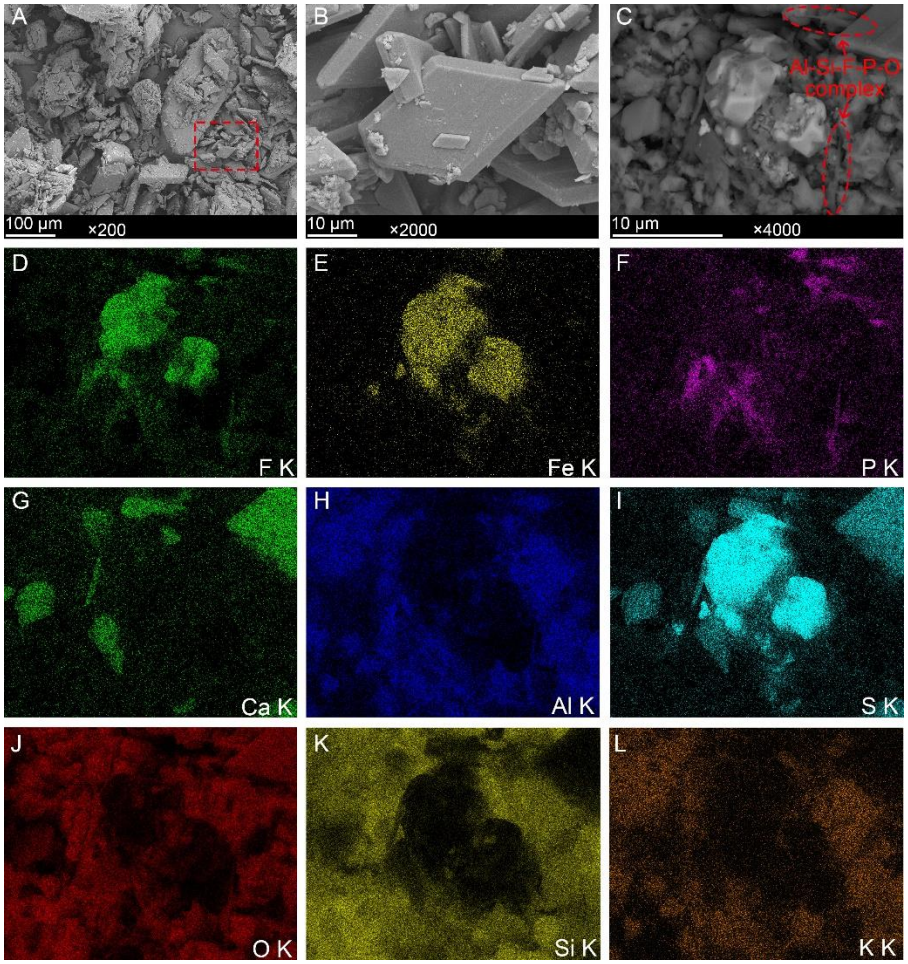

Figure.3. SEM micrographs of PG. (A) raw PG with tiny particles (< 20 µm) on the surface of larger particles. (B) tabular gypsum crystals related to the marked area in image A. (C) iron and sulfate-rich crystal and need-like Al-P-F-O complex. (D) elemental map of fluorine, relative to the region displayed in image C, (E) iron, (F) phosphorus, (G) calcium, (H) aluminum, (I) sulfur, (J) oxygen, (K) silicon, and (L) potassium.

The detailed F and P redistribution in the cementitious matrix is reported in Fig.4. CSH precipitation was found in the OCPB system in the form of a very fine matrix (Fig.4a and d). The EDS microanalysis highlights an enrichment in Al of the cementitious matrix (Fig.4c and f). This can be consistent with an aluminum-rich CSH composition or a mixture of CSH and ettringite. Moreover, the EPMA/WDS mapping (employed to avoid peak overlapping of the Kα emission line of F at 677 eV and the Lα line of Fe at 705 eV in EDS analysis) results highlight a very high stabilization efficiency for both F and P, which are homogeneously concentrated in this Ca, Al, and Si-rich matrix (Fig.4b and Fig.S5). The same behavior was found for P (Fig.4e and Fig.S6), which was evenly distributed in the Ca, Al, Si, and O-rich areas. Thus confirming that the two pollutants experienced the same fate. Besides, the WDS point analysis (Fig.S4 and

Table.S5) unveiled a homogeneous distribution of the two critical pollutants in the hydrated matrix with a medium concentration of 8.61 wt% and 0.23 wt% for F and P, respectively. It should be pointed out that, in addition, local areas with very high concentrations (Fig. 4b) up to 20.92 wt% for F (Fig.S4, spot A) were registered, thus confirming once more that such a fine-grained microcrystalline assemble plays a key role as adsorbents for fluorine and phosphorus and that their long term stability should be ensured for an effective material recycling.

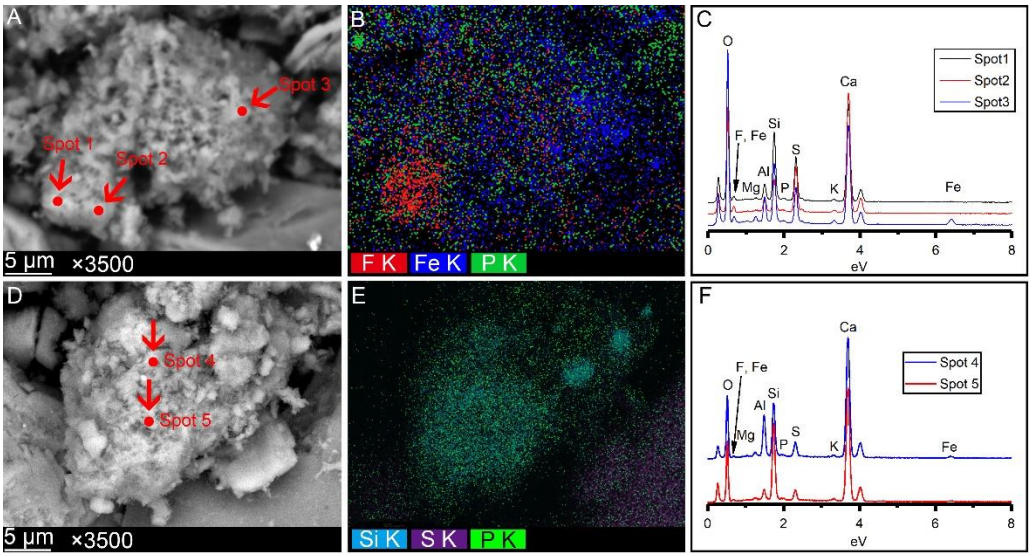

Figure.4. SEM and EMPA micrographs of OCPB. (A) EMPA image of CSH assemblage, (B) map of F, Fe, and P, based on WDS; (C) EDS spectra of points marked in the image (A); (D) SEM image of the cementitious matrix; (E) map of Si, S, and P, based on EDS; (F) EDS spectra of points marked in the image (D).

3.3. Retention of fluoride and phosphorus in PG and OCPB at various pH values

The pH-dependent leaching tests were performed to measure the neutralization capacity of the matrices and to quantify the impact of pH variation on the geochemical behavior of raw PG and stabilized OCPB. The acid and base neutralization capacity of PG and OCPB indicate the resistance to acid attack affecting matrix durability and thus leaching of contaminants. In general, immobilization scenario efficiency strongly depends on the ability of the cementitious matrix to maintain alkaline conditions (Giampaolo et al., 2002). As shown in Fig.5a and b, a significant increase in the alkalinity of the final eluate of OCPB, using deionized water as leachates, was noticed, with the pH value of PG and OCPB of 3.14 and 11.58, respectively. Noteworthy, a pH values plateau is found in OCPB samples at the pH range from 13 to 14, whereas in pH-range 9 to 13, a linear variation at increasing dosages of HCl is displayed, which is the range where hydration products (e.g., CSH gel, ettringite, and portlandite) exert their buffering capacity.

The fluoride and phosphorus leaching results are presented in Fig.5c and d, respectively. The current

Chinese industrial water guidelines (Tang et al., 2014; Wang et al., 2020), indicating fluoride and total phosphorus limit(20 and 0.3 mg/L, respectively), were used as the normative limit to be accomplished (dashed line marked in Fig. 5c and d) for the potential reuse of the material. The releasing values in excess of the limits, especially by one or more orders of magnitude, were considered potential environmental concerns. By comparing the leaching results of PG and OCPB in deionized water, a very high retention capacity was confirmed as the concentration of fluoride and phosphorus in the eluate decreased from 113.72 and 158.60 mg/L (PG at pH 3.14) to 11.95 and < 0.06 mg/L (OCPB at pH 11.58), revealing that the fluoride and phosphorus were well-retained by the cementitious matrix. These results highlight that, in neutral conditions, the OPC is an efficient material for PG in-situ remediation. Moreover, the experimental results unveiled a very high pH dependency on the stabilization efficiency of the two pollutants. The maximum concentration of leached fluoride occurs in strongly acidic conditions, while a significant decrease was found in neutral and alkaline conditions (pH 7-11). Nevertheless, such a pH increase proved to have an adverse effect on the solubility/stability of fluoride. Then a slight increase in F leaching was found under harsh alkaline conditions (pH 12-14). Similar pH-dependent leaching profiles were found and explained as an expression of the sorption of fluoride onto clay minerals that increases at acidic pH, whereas the mobilization takes place when the system is moved to alkaline conditions (Habuda-Stanić et al., 2014).

In the PG system, the decreased fluorine leaching in pH range from 6 to 11 was attributed to the formation of calcium fluoride (Rai et al., 2000; Kang et al., 2019) and/or precipitation of fluorite and mallardite (Bisone et al., 2017), even though these phases were not found in the studied assemblage. After the solidification/stabilization process, the best pH condition to ensure a F leaching below the law limit shifted to more alkaline conditions with the pH values in the range of 9 to 13. The above-mentioned pH range is suitable for CSH gel and ettringite stability, thus substantiating their involvement in the fluorine retention (Guan and Zhao, 2016, Tsunashima et al., 2012). Then a further increase in pH values (PG sample > 11 and OCPB sample > 13) will enhance the fluorine leachability in both scenarios. As said before, considering this pH range suitable for hydration products stability, the sorption process should still be active. Therefore, the deterioration of fluorine retention capacity may be mainly due to calcium complexation with hydroxyl to form calcium hydroxyl complex (CaOH) rather than calcium fluoride (Kang et al., 2019). The phosphorus release was only observed in acid conditions (Fig.5d), at pH values of PG sample <6.92 and OCPB sample < 2.97. In neutral to alkaline conditions, the P concentration in the leachate was below the detection limit (0.6mg/L). This reveals that, after the immobilization, P leaching accomplishes acceptable limits on a broad pH range (from neutral to acid). Even when the acid environment is unsuitable for the stability of hydration products, the phosphate species may react with other cations (primarily soluble Ca^{2+}) and then promote the formation of aqueous dissociated species as precursors of phosphate precipitation (Recillas et al., 2012).

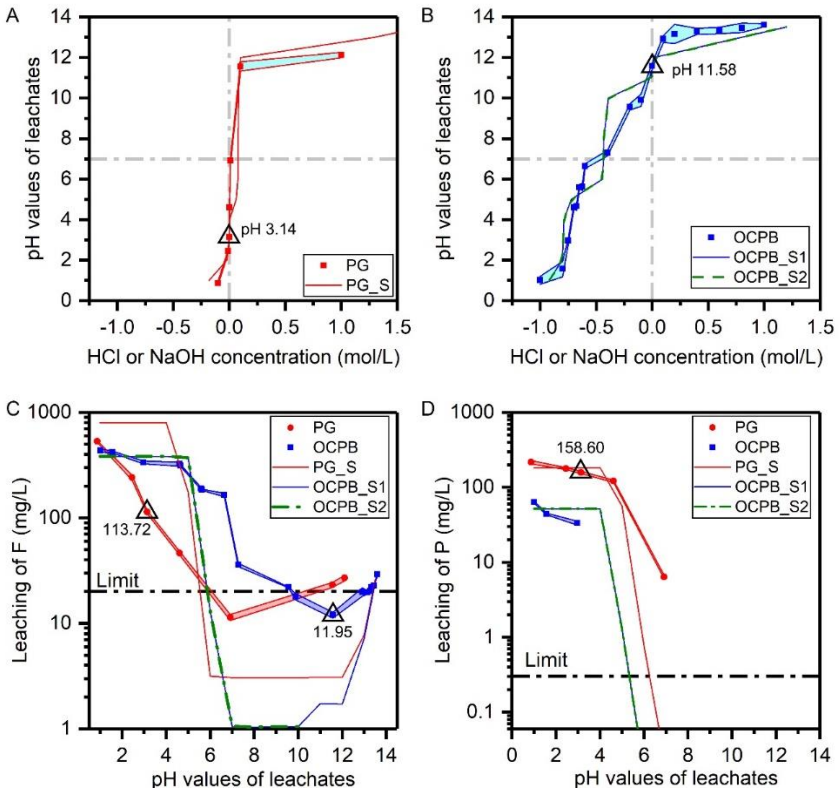

Figure.5. pH-dependent leaching results for sample PG and OCPB. Experimental and theoretical neutralization capacity of sample PG (A) and OCPB (B); Comparison between measured and calculated leachate concentrations of fluoride (C) and phosphorus (D). PG and OCPB refer to experimental data, whereas the abbreviation "S" represents the modeling data. The dotted lines marked in (c) and (d) represent the acceptable limit of phosphorus and fluoride in industrial water (0.3 and 20 mg/L, respectively). The missed experimental phosphorus leaching data in Fig.5d means leachate concentration is below the detection limit (0.06 mg/L). The triangle marked points mean leaching experiments using the deionized water as the leachate.

3.4. Model simulations and parameter optimization

The pH-dependent leaching results have shown that hydration products, clay minerals, and calcium phosphates may control the solubility of fluorine and phosphorus in neutral and alkaline pH regions. Although many hypotheses can be formulated from the abovementioned experimental results to explain the leaching behavior, they can hardly be confirmed. The PHREEQC geochemical simulations (Table.S6) are accordingly applied in this section to confirm and quantify the role of the recognized F/P bearing mineral phases. The comparison between simulations and experimental neutralizing capacity data (Fig.6a and b) demonstrate that the used model fits well in all the pH ranges, also for the description of the enhanced acid

resistance of the stabilized sample. All models describe the amphoteric character of F and P leaching (Fig.6c and d), but the quantitative match of F leaching in OCPB_S2 simulation is less satisfying between pH 10 and 13.5 because the upward trend found in the experiments at this range was not described.

According to the model, F is mainly present in acidic leachates (pH < 5) in the form of Al-F complexes (AlF_3, AlF_2^+, and AlF^{2+}). The formation of these complexes is due to the fact that the dissolved F ions, which have a high electronegativity and a small ionic size, have a strong affinity to Al^{3+} ions and form the Al-F species (Dubey et al., 2018). The relatively high Al concentrations could be attributed to the dissolution of aluminosilicate minerals (muscovite and feldspar) in PG, whereas in OCPB, it could be due to the hydration products ettringite and amorphous aluminum hydroxide. As shown in Fig.6, only gypsum and quartz are present in the residues at this pH range (pH < 5). With the increase in pH values, F begins to precipitate as calcium fluoride and calcium fluorophosphate at a pH of approximately 5 (Fig.6). Meanwhile, the decreased F release at this pH range also ascertained this observation (Fig.6). Calcium fluoride is a less soluble phase and thus limits F concentration in the leachate (Eary, 1999). Noteworthy previous researchers have confirmed that within the pH range of 5.5 to 7.0, calcium fluoride appears to be the main phase that controls the F solubility in soil (Street and Elwali, 1983; Elrashidi and Lindsay, 1985). Calcium fluorophosphate is a stable fluoride-containing phase that would theoretically form in combination with calcium fluoride at slightly acid and neural conditions (Elrashidi and Lindsay, 1985). As the pH values increased to alkaline levels (pH >10), different mechanisms were accordingly shown with the adsorption hypothesis. In PG and OCPB_S1 simulations, the increase of F concentration in the leachate between pH 11 and 13.5 is mainly attributed to the dissolution of calcium fluorophosphate. As displayed in Fig.6, calcium hydroxide phosphate is expected to form at this pH range. Therefore, the F is re-dissolved into the aqueous solutions with a concentration increase following the experimental patterns in Fig.6c. Zhu et al. (2009) ascertained the occurrence of this ion-exchange process between fluoride and hydroxyl ions on the surface of calcium fluorophosphate and calcium fluoride during their dissolution in the alkaline pH range (approximately 10). In OCPB_S2 simulations, with the adsorption hypothesis, the dissolved F was mainly adsorbed onto CSH matrix binding sites and no ion exchange between fluoride and hydroxyl ions took place. However, the quantitative match of F leaching in OCPB_S2 simulation is less satisfying at this range, which could be related to the overestimation of the reactive surface binding sites in the CSH matrix.

In comparison, the simulated leaching profiles of P adequately describe the pH-depend behavior. When the pH is below 5, H_3PO_4, $H_2PO_4^-4$, and $CaH_2PO_4^+$ are the main solubility-controlling forms present in leachate. Around the neutral pH, phosphate starts to precipitate as sparingly soluble calcium phosphates (hydroxyapatite and calcium fluorophosphate), which is in agreement with phosphorus retention mechanisms in wastewater (Froelich, 1988; Ready et al., 1999). Besides, Gerritse (1993) suggested that

increases in pH values and calcium and fluoride concentrations from solutions could eventually lead to increased incorporation of phosphate in sparingly soluble calcium phosphates. Phosphate is indeed well described over a large pH range by the solubility behavior of calcium (hydro or fluoro) phosphate forms (Fig.6).

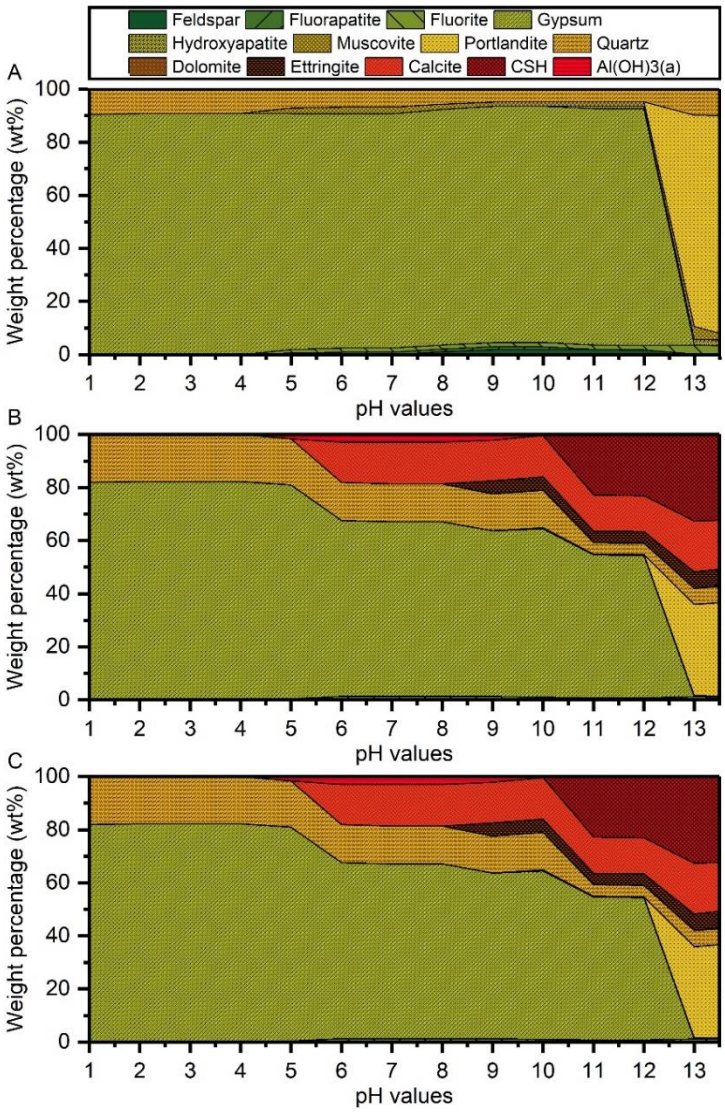

Figure.6. Predicted equilibrium concentrations evolution of mineral phases in residues. (A) PG simulation, (B) OCPB_S1 simulation, and (C) OCPB_S2 simulation.

In simulations, the leaching behavior of F and P under neutral and mildly alkaline conditions can be controlled by the precipitation of calcium fluoride, calcium fluorophosphate, and calcium hydroxide phosphate. To estimate the accuracy of the simulation results, three solid residues (after leaching at pH 1.0, 13.6, and in deionized water) were used to compare simulated and experimental mineral assemblages (Fig.7). The XRD spectra are shown in Fig.S7. Although the evidence of partial precipitation of F and P

was confirmed in models, mineralogic phases containing F and P were still not identified in the XRD patterns. It is to note that minor phases containing F and P are not detectable by XRD if their abundance is lower than the detection limit of the technique. When the pH value of the leachate is 1 (Fig.7a), experiment and simulation quantification results both demonstrate that only quartz and gypsum are present under these highly acidic conditions, thus providing further evidence that the incongruent dissolution of ettringite and amorphous aluminum in the acidic systems may feasibly be a source of aluminate for fluorine immobilization (Gomes et al., 2012). By simple interaction with deionized water, simulated mineral phases are in close agreement with the experimental XRD results after subtracting the cement phases (Fig.7b). Only dolomite, the minor phase (2.87 wt%) identified in XRD quantification, was not included in the simulation. Presumably, the dissolution of dolomite is limited by the reaction kinetics applied in the simulations. It is important to note that the solubility parameters used in the geochemical modeling may introduce some degree of error because mainly the data are based on single mineral equilibrium studies. Moreover, the model predicts the formation of a limited amount of fluorite (0.83 wt%) and hydroxyapatite (0.27%) in the OCPB system. The presence of these phases is not completely unexpected, as is already found by other authors (Bisone et al., 2017), but in this system, their amounts are near or below the detection limit of XRD. As the solution became more alkaline (Fig.7c), portlandite became the main calcium phase. Besides, in the experimental quantification results, precipitation thenardite (Na_2SO_4) was found but not observed in modeling. In OCPB_S2, fluorite is slightly under-saturated relative to the ordinary S1 simulation, and the dissolved fluorine is subsequently present on the CSH surface.

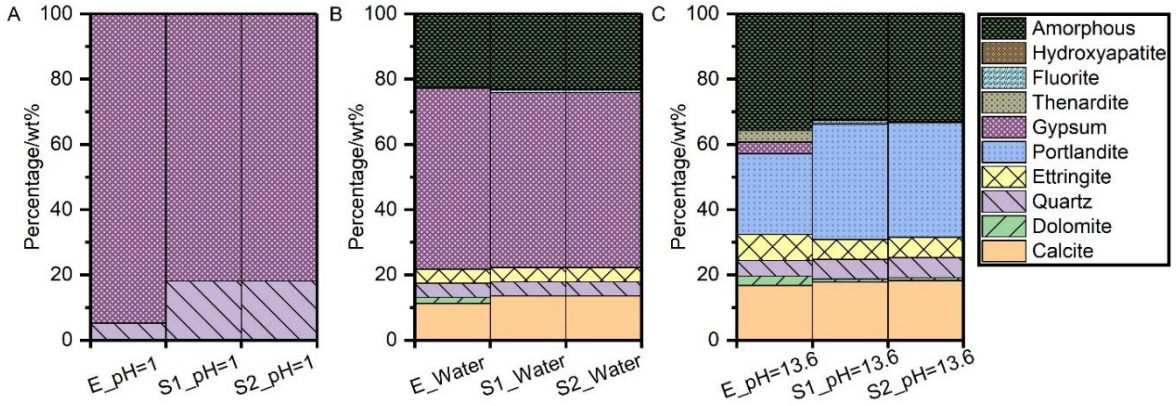

Figure.7. Mineral phases in residue assemblage from quantitative XRD calculation and OCPB modeling in the leachate at pH values of 1.00 (A), 11.58 (B), and 13.60 (C). (the abbreviation "E", "S1", and "S2" represent the experimental and simulation results based on OCPB_S1 and OCPB_S2, the values after the equal sign "=" means the final pH value of the leachates, and the "water" is the leaching experiment using the deionized water as the leachate).

Overall, despite the enhanced retention capacities for F and P of OCPB that were experimentally observed

and theoretically predicted, the environmental compatibility, for example, pH values of the groundwater, must be carefully considered when reusing these materials. If these immobilized materials are reused in an area suffering from acid precipitation (as shown in Fig.7a), they might consistently interact with the acidic groundwater. Then the alkaline components in the unstable OCPB mixtures could be exhausted, and the stabilized products may be a source of environmental risk.

4. Conclusion

This study explored the solidification/stabilization potential of OCPB for PG management and the associated immobilization mechanisms of F and P. Three simulations were performed to represent the F and P leaching behavior in original PG and immobilized OCPB samples. The agreement between experimental and simulated results suggests the geochemical modeling approach is helpful for F and P leaching predictions in a wide range of pH conditions. The main findings are as follows:

(1) PG is mainly composed of gypsum, bassanite, and anhydrite which were generated from the acidulation process and the following recrystallization process during stockpiling. The silicates were the remained gangue minerals in phosphate rock after acidulation. However, the source of the phosphorus-containing phase, scorzalite, needs further investigation. Significant correlations of Al, Si, P, and F fractions as poorly crystalline forms are found by elemental mapping.

(2) Although the newly formed crystalline phases containing fluorine and phosphorus are not observed in the XRD patterns, the SEM/EDS and EPMA/WDS confirmed an aluminum-rich CSH composition or a mixture of CSH and ettringite, which are potential adsorbing substrates for fluorine and phosphorus;

(3) The leaching behavior at different pH values revealed a significant reduction of contaminants released to the environment under neutral conditions. But the highly amphoteric F and P leaching behavior indicated that the optimal pH range for the contaminants retention is in the range of 10-13. Mineralogical evidence from simulations points out that calcium phosphate, fluorophosphate, and calcium fluoride are the forms likely to control pollutant release.

(4) Due to the wide variations in solid wastes and stabilized product characteristics, it is complicated to reveal the fate of these minor pollutant content through laboratory approaches. This research has set the reliable illustration for using geochemical modeling to provide reliable insight to understand the complex leaching behavior under changing conditions fundamentally. The continued work is ongoing to integrate the simulations into the widely different hazardous contaminants under a variety of conditions, which may open a cost-effective and less time-consuming pathway for the solid waste solidification/stabilization operation decision-making processes.

Acknowledgment

This research was funded by the Science and Technology innovation Program of Hunan Province (No. 2021RC3125), the National Natural Science Foundation of China（No.52104156, No. 52074351 and No. 52004330), a scholarship granted by the China Scholarship Council (No.CSC201906370062), and the PRIN project "Mineral reactivity, a key to understand large-scale processes: from rock-forming environments to solid waste recovering/lithification" n. 2017L83S77.

Author Contributions

Yikai Liu: data curation, methodology, software, visualization, writing—original draft

Qiusong Chen: funding acquisition, supervision, writing—original draft

Maria Chiara Dalconi: formal analysis and writing—original draft

Simone Molinari: formal analysis and writing—original draft

Luca Valentini: formal analysis and writing—original draft

Yunming Wang: funding acquisition and resources

Shiyuan Sun: resources and investigation

Peishen Wang: investigation

Gilberto Artioli: funding acquisition, supervision, and methodology.

All the authors discussed the data and agreed on their interpretations. All the co-authors contributed to the final polishing of the manuscript.

Reference

Adimalla, N., Marsetty, S.K., and Xu, P., 2020, Assessing groundwater quality and health risks of fluoride pollution in the Shasler Vagu (SV) watershed of Nalgonda, India: Human and Ecological Risk Assessment, doi:10.1080/10807039.2019.1594154.

Akin Altun, I., and Sert, Y., 2004, Utilization of weathered phosphogypsum as set retarder in Portland cement: Cement and Concrete Research, doi:10.1016/j.cemconres.2003.10.017.

Amrani, M., Taha, Y., Kchikach, A., Benzaazoua, M., and Hakkou, R., 2020, Phosphogypsum recycling: New horizons for a more sustainable road material application: Journal of Building Engineering, doi:10.1016/j.jobe.2020.101267.

Arocena, J.M., Rutherford, P.M., and Dudas, M.J., 1995, Heterogeneous distribution of trace elements and fluorine in phosphogypsum by-product: Science of the Total Environment, doi:10.1016/0048-9697(95)04446-8.

Behera, S.K., Mishra, D.P., Singh, P., Mishra, K., Mandal, S.K., Ghosh, C.N., Kumar, R., and Mandal, P.K., 2021, Utilization of mill tailings, fly ash and slag as mine paste backfill material: Review and future perspective: Construction and Building Materials, doi:10.1016/j.conbuildmat.2021.125120.

Bisone, S., Gautier, M., Chatain, V., and Blanc, D., 2017, Spatial distribution and leaching behavior of pollutants from phosphogypsum stocked in a gypstack: Geochemical characterization and modeling: Journal of Environmental Management, doi:10.1016/j.jenvman.2017.02.055.

Cai, R., He, Z., Tang, S., Wu, T., and Chen, E., 2018, The early hydration of metakaolin blended cements by non-contact impedance measurement: Cement and Concrete Composites, doi:10.1016/j.cemconcomp.2018.06.001.

Chen, Q., Zhang, Q., Fourie, A., and Xin, C., 2017, Utilization of phosphogypsum and phosphate tailings for cemented paste backfill: Journal of Environmental Management, v. 201, p. 19–27, doi:10.1016/j.jenvman.2017.06.027.

Chernysh, Y., Yakhnenko, O., Chubur, V., and Roubík, H., 2021, Phosphogypsum Recycling: A Review of Environmental Issues, Current Trends, and Prospects: Applied Sciences, doi:10.3390/app11041575.

Christensen, A.N., Jensen, T.R., and Hanson, J.C., 2004, Formation of ettringite, Ca(6)Al(2)(SO4) 3(OH)(12)·26H2O, AFt, and monosulfate, Ca(4)Al(2)O(6)(SO4)·14H 2O, AFm-14, in hydrothermal hydration of Portland cement and of calcium aluminum oxide - Calcium sulfate dihydrate mixtures studied by in situ synchrot: Journal of Solid State Chemistry, doi:10.1016/j.jssc.2003.12.030.

Chrysochoou, M., and Dermatas, D., 2006, Evaluation of ettringite and hydrocalumite formation for heavy

metal immobilization: Literature review and experimental study: Journal of Hazardous Materials, doi:10.1016/j.jhazmat.2005.11.008.

Contessi, S., Calgaro, L., Dalconi, M.C., Bonetto, A., Bellotto, M. Pietro, Ferrari, G., Marcomini, A., and Artioli, G., 2020, Stabilization of lead contaminated soil with traditional and alternative binders: Journal of Hazardous Materials, doi:10.1016/j.jhazmat.2019.120990.

Degirmenci, N., Okucu, A., and Turabi, A., 2007, Application of phosphogypsum in soil stabilization: Building and Environment, doi:10.1016/j.buildenv.2006.08.010.

Deng, J., Zhang, K., He, D., Zhao, H., Hakkou, R., and Benzaazoua, M., 2020, Occurrence of sesquioxide in a mid-low grade collophane-sedimentary apatite ore from guizhou, china: Minerals, doi:10.3390/min10111038.

Diaz Caselles, L., Roosz, C., Hot, J., Blotevogel, S., and Cyr, M., 2021, Immobilization of molybdenum by alternative cementitious binders and synthetic C-S-H: An experimental and numerical study: Science of The Total Environment, doi:10.1016/j.scitotenv.2021.148069.

Dubey, S., Agarwal, M., and Gupta, A.B., 2018, Experimental investigation of Al-F species formation and transformation during coagulation for fluoride removal using alum and PACl: Journal of Molecular Liquids, doi:10.1016/j.molliq.2018.06.080.

Eary, L.E., 1999, Geochemical and equilibrium trends in mine pit lakes: Applied Geochemistry, doi:10.1016/S0883-2927(99)00049-9.

Elrashidi, M.A., and Lindsay, W.L., 1985, Solubility Relationships of Fluorine Minerals in Soils: Soil Science Society of America Journal, doi:10.2136/sssaj1985.03615995004900050012x.

Ennaciri, Y., Bettach, M., Cherrat, A., and Zegzouti, A., 2016, Conversion of phosphogypsum to sodium sulfate and calcium carbonate in aqueous solution: Journal of Materials and Environmental Science,.

Ennaciri, Y., Zdah, I., El Alaoui-Belghiti, H., and Bettach, M., 2020, Characterization and purification of waste phosphogypsum to make it suitable for use in the plaster and the cement industry: Chemical Engineering Communications, doi:10.1080/00986445.2019.1599865.

Fox, I., and Malati, M.A., 1993, An investigation of phosphate adsorption by Clays and its relation to the problems of eutrophication of the river stour, Kent: Journal of Chemical Technology & Biotechnology, doi:10.1002/jctb.280570202.

Froelich, P.N., 1988, Kinetic control of dissolved phosphate in natural rivers and estuaries: A primer on the phosphate buffer mechanism: Limnology and Oceanography, doi:10.4319/lo.1988.33.4part2.0649.

Gerritse, R.G., 1993, Prediction of travel times of phosphate in soils at a disposal site for wastewater: Water Research, doi:10.1016/0043-1354(93)90084-U.

Giampaolo, C., Lo Mastro, S., Polettini, A., Pomi, R., and Sirini, P., 2002, Acid neutralisation capacity and hydration behaviour of incineration bottom ash-Portland cement mixtures: Cement and Concrete Research, doi:10.1016/S0008-8846(01)00760-8.

Gijbels, K., Nguyen, H., Kinnunen, P., Samyn, P., Schroeyers, W., Pontikes, Y., Schreurs, S., and Illikainen, M., 2020, Radiological and leaching assessment of an ettringite-based mortar from ladle slag and phosphogypsum: Cement and Concrete Research, doi:10.1016/j.cemconres.2019.105954.

Gomes, A.F.S., Lopez, D.L., and Ladeira, A.C.Q., 2012, Characterization and assessment of chemical modifications of metal-bearing sludges arising from unsuitable disposal: Journal of Hazardous Materials, doi:10.1016/j.jhazmat.2011.11.039.

Guan, W., and Zhao, X., 2016, Fluoride recovery using porous calcium silicate hydrates via spontaneous Ca2+ and OH- release: Separation and Purification Technology, doi:10.1016/j.seppur.2016.03.050.

Gutberlet, T., Hilbig, H., and Beddoe, R.E., 2015, Acid attack on hydrated cement - Effect of mineral acids on the degradation process: Cement and Concrete Research, doi:10.1016/j.cemconres.2015.03.011.

Habuda-Stanić, M., Ravančić, M., and Flanagan, A., 2014, A Review on Adsorption of Fluoride from Aqueous Solution: Materials, doi:10.3390/ma7096317.

Halim, C.E., Short, S.A., Scott, J.A., Amal, R., and Low, G., 2005, Modelling the leaching of Pb, Cd, As, and Cr from cementitious waste using PHREEQC: Journal of Hazardous Materials, v. 125, p. 45–61, doi:10.1016/j.jhazmat.2005.05.046.

Hentati, O., Abrantes, N., Caetano, A.L., Bouguerra, S., Gonçalves, F., Römbke, J., and Pereira, R., 2015, Phosphogypsum as a soil fertilizer: Ecotoxicity of amended soil and elutriates to bacteria, invertebrates, algae and plants: Journal of Hazardous Materials, doi:10.1016/j.jhazmat.2015.03.034.

Hewlett, P.C., 2003, Lea's Chemistry of Cement and Concrete:, doi:10.1016/B978-0-7506-6256-7.X5007-3.

Jiang, G., Wu, A., Wang, Y., and Lan, W., 2018, Low cost and high efficiency utilization of hemihydrate phosphogypsum: Used as binder to prepare filling material: Construction and Building Materials, v. 167, p. 263–270, doi:10.1016/j.conbuildmat.2018.02.022.

Jing, Z., Fan, X., Zhou, L., Fan, J., Zhang, Y., Pan, X., and Ishida, E.H., 2013, Hydrothermal solidification behavior of municipal solid waste incineration bottom ash without any additives: Waste Management, doi:10.1016/j.wasman.2013.01.038.

Kamei, T., Ahmed, A., Horai, H., and Ugai, K., 2015, A novel solidification technique for fluorine-contaminated bassanite using waste materials in ground improvement applications: Journal of Material Cycles and Waste Management, doi:10.1007/s10163-014-0251-0.

Kandil, A.-H.T., Cheira, M.F., Gado, H.S., Soliman, M.H., and Akl, H.M., 2017, Ammonium sulfate preparation from phosphogypsum waste: Journal of Radiation Research and Applied Sciences, doi:10.1016/j.jrras.2016.11.001.

Kang, J., Gou, X., Hu, Y., Sun, W., Liu, R., Gao, Z., and Guan, Q., 2019, Efficient utilisation of flue gas desulfurization gypsum as a potential material for fluoride removal: Science of the Total Environment, doi:10.1016/j.scitotenv.2018.08.416.

Li, X., Du, J., Gao, L., He, S., Gan, L., Sun, C., and Shi, Y., 2017a, Immobilization of phosphogypsum for cemented paste backfill and its environmental effect: Journal of Cleaner Production, v. 156, p. 137–146, doi:10.1016/j.jclepro.2017.04.046.

Li, X., Du, J., Gao, L., He, S., Gan, L., Sun, C., and Shi, Y., 2017b, Immobilization of phosphogypsum for cemented paste backfill and its environmental effect: Journal of Cleaner Production, doi:10.1016/j.jclepro.2017.04.046.

Li, J., Zhang, S., Wang, Q., Ni, W., Li, K., Fu, P., Hu, W., and Li, Z., 2020, Feasibility of using fly ash–slag-based binder for mine backfilling and its associated leaching risks: Journal of Hazardous Materials, doi:10.1016/j.jhazmat.2020.123191.

Li, X., Zhu, G.Y., Gong, X.K., Li, S.P., Xu, W., and Li, H.Q., 2019, Occurrence of the Impurities in Phosphorus Rock and the Research of Acidolysis Process: Guang Pu Xue Yu Guang Pu Fen Xi/Spectroscopy and Spectral Analysis, doi:10.3964/j.issn.1000-0593(2019)04-1288-06.

Lieberman, R.N. et al., 2020, The geochemical evolution of brines from phosphogypsum deposits in Huelva (SW Spain) and its environmental implications: Science of the Total Environment, doi:10.1016/j.scitotenv.2019.134444.

Mashifana, T.P., 2019, Chemical treatment of phosphogypsum and its potential application for building and construction, in Procedia Manufacturing, doi:10.1016/j.promfg.2019.06.007.

Melki, S., and Gueddari, M., 2018, Impact Assessment of Phosphogypsum Leachate on Groundwater of Sfax-Agareb (Southeast of Tunisia): Using Geochemical and Isotopic Investigation: Journal of Chemistry, doi:10.1155/2018/2721752.

Molinari, S. et al., 2021, Environmental implications of one-century COPRs evolution in a single industrial site: From leaching impact to sustainable remediation of CrVI polluted groundwater: Chemosphere,

v. 283, p. 131211, doi:10.1016/J.CHEMOSPHERE.2021.131211.

Park, J.Y., Byun, H.J., Choi, W.H., and Kang, W.H., 2008, Cement paste column for simultaneous removal of fluoride, phosphate, and nitrate in acidic wastewater: Chemosphere, doi:10.1016/j.chemosphere.2007.09.012.

Parkhurst, D.L., and Appelo, C.A.J., 2013, Description of Input and Examples for PHREEQC Version 3 — A Computer Program for Speciation , Batch-Reaction , One-Dimensional Transport , and Inverse Geochemical Calculations.: U.S. Geological Survey Techniques and Methods, book 6, chapter A43,.

Pérez-López, R., Nieto, J.M., López-Coto, I., Aguado, J.L., Bolívar, J.P., and Santisteban, M., 2010, Dynamics of contaminants in phosphogypsum of the fertilizer industry of Huelva (SW Spain): From phosphate rock ore to the environment: Applied Geochemistry, doi:10.1016/j.apgeochem.2010.02.003.

Priyantha, N., and Perera, S., 2000, Removal of sulfate, phosphate and colored substances in wastewater effluents using feldspar: Water Resources Management, doi:10.1023/A:1011171330097.

Rai, K., Agarwal, M., Dass, S., and Shrivastav, R., 2000, Fluoride: Diffusive mobility in soil and some remedial measures to control its plant uptake: Current Science,.

Rashad, A.M., 2017, Phosphogypsum as a construction material: Journal of Cleaner Production, v. 166, p. 732–743, doi:10.1016/j.jclepro.2017.08.049.

Ready, K.R., Kadlec, R.H., Flaig, E., and Gale, P.M., 1999, Phosphorus retention in streams and wetlands: A review: Critical Reviews in Environmental Science and Technology, doi:10.1080/10643389991259182.

Recillas, S., Rodríguez-Lugo, V., Montero, M.L., Viquez-Cano, S., Hernandez, L., and Castaño, V.M., 2012, Studies on the precipitation behavior of calcium phosphate solutions: Journal of Ceramic Processing Research,.

Rentería-Villalobos, M., Vioque, I., Mantero, J., and Manjón, G., 2010, Radiological, chemical and morphological characterizations of phosphate rock and phosphogypsum from phosphoric acid factories in SW Spain: Journal of Hazardous Materials, doi:10.1016/j.jhazmat.2010.04.116.

Rock, N.M.S., 1987, The nature and origin of lamprophyres: An overview: Geological Society Special Publication, doi:10.1144/GSL.SP.1987.030.01.09.

Rutherford, P.M., Dudas, M.J., and Arocena, J.M., 1995, Trace elements and fluoride in phosphogypsum leachates: Environmental Technology (United Kingdom), doi:10.1080/09593331608616276.

Rutherford, P.M., Dudas, M.J., and Samek, R.A., 1994, Environmental impacts of phosphogypsum: Science

of the Total Environment, The, doi:10.1016/0048-9697(94)90002-7.

Shi, Y., Cheng, L., Tao, M., Tong, S. Sen, Yao, X., and Liu, Y., 2021, Using modified quartz sand for phosphate pollution control in cemented phosphogypsum (PG) backfill: Journal of Cleaner Production, doi:10.1016/j.jclepro.2020.124652.

Solpuker, U., Sheets, J., Kim, Y., and Schwartz, F.W., 2014, Leaching potential of pervious concrete and immobilization of Cu, Pb and Zn using pervious concrete: Journal of Contaminant Hydrology, doi:10.1016/j.jconhyd.2014.03.002.

Street, J.J., and Elwali, A.M.O., 1983, Fluorite Solubility in Limed Acid Sandy Soils: Soil Science Society of America Journal, doi:10.2136/sssaj1983.03615995004700030017x.

Tan, H., Zou, F., Liu, M., Ma, B., Guo, Y., and Jian, S., 2017, Effect of the Adsorbing Behavior of Phosphate Retarders on Hydration of Cement Paste: Journal of Materials in Civil Engineering, doi:10.1061/(asce)mt.1943-5533.0001929.

Tang, X., Wu, M., Dai, X., and Chai, P., 2014, Phosphorus storage dynamics and adsorption characteristics for sediment from a drinking water source reservoir and its relation with sediment compositions: Ecological Engineering, v. 64, p. 276–284, doi:10.1016/j.ecoleng.2014.01.005.

Tong, Y. et al., 2017, Decline in Chinese lake phosphorus concentration accompanied by shift in sources since 2006: Nature Geoscience, v. 10, p. 507–511, doi:10.1038/ngeo2967.

Wang, M. et al., 2020, Thyroid function, intelligence, and low-moderate fluoride exposure among Chinese school-age children: Environment International, v. 134, doi:10.1016/j.envint.2019.105229.

Wei, J., Gu, Y., Lv, H., and Wu, X., 2021, A zero-emission method for recycling phosphogypsum using Na2SO4 electrolysis: Preliminary study: Separation and Purification Technology, doi:10.1016/j.seppur.2020.118168.

Wu, R.J., and Liu, J.C., 2018, Removal of Phosphate Using Ettringite Synthesized from Industrial By-products: Water, Air, and Soil Pollution, doi:10.1007/s11270-018-3828-8.

Xu, W., Dai, J.G., Ding, Z., and Wang, Y., 2017, Polyphosphate-modified calcium aluminate cement under normal and elevated temperatures: Phase evolution, microstructure, and mechanical properties: Ceramics International, doi:10.1016/j.ceramint.2017.08.102.

Xue, X., Ke, Y., Kang, Q., Zhang, Q., Xiao, C., He, F., and Yu, Q., 2019, Cost-Effective Treatment of Hemihydrate Phosphogypsum and Phosphorous Slag as Cemented Paste Backfill Material for Underground Mine: Advances in Materials Science and Engineering, v. 2019, doi:10.1155/2019/9087538.

Yang, J., Ma, L., Liu, H., Guo, Z., Dai, Q., Zhang, W., and Bounkhong, K., 2020, Chemical behavior of fluorine and phosphorus in chemical looping gasification using phosphogypsum as an oxygen carrier: Chemosphere, doi:10.1016/j.chemosphere.2020.125979.

Yoshida, S., Elakneswaran, Y., and Nawa, T., 2021, Electrostatic properties of C–S–H and C-A-S-H for predicting calcium and chloride adsorption: Cement and Concrete Composites, doi:10.1016/j.cemconcomp.2021.104109.

Zeng, L.L., Bian, X., Zhao, L., Wang, Y.J., and Hong, Z.S., 2021, Effect of phosphogypsum on physiochemical and mechanical behaviour of cement stabilized dredged soil from Fuzhou, China: Geomechanics for Energy and the Environment, doi:10.1016/j.gete.2020.100195.

Zhou, S., Li, X., Zhou, Y., Min, C., and Shi, Y., 2020, Effect of phosphorus on the properties of phosphogypsum-based cemented backfill: Journal of Hazardous Materials, doi:10.1016/j.jhazmat.2020.122993.

Zhu, Y., Zhang, X., Chen, Y., Xie, Q., Lan, J., Qian, M., and He, N., 2009, A comparative study on the dissolution and solubility of hydroxylapatite and fluorapatite at 25 °C and 45 °C: Chemical Geology, doi:10.1016/j.chemgeo.2009.07.014.

Supporting information for Chapter 4

Retention of phosphorus and fluorine in phosphogypsum for cemented paste backfill: Experimental and numerical simulation studies

Yikai Liu[1]; Qiusong Chen[2, 3]; Maria Chiara Dalconi[1]; Simone Molinari[1]; Luca Valentini[1]; Yunmin Wang[2,3]; Shiyuan Sun[3]; Peishen Wang[3]; Gilberto Artioli[1]

[1] *Department of Geosciences and CIRCe Centre, University of Padua, via G. Gradenigo 6, 35129, Padua, Italy*

[2] *Sinosteel Maanshan General Institute of Mining Research Co., Ltd., Maanshan, 24300, China;*

[3] *School of Resources and Safety Engineering, Central South University, Lushan South Road 932, 410083, Hunan, China*

Table.S1. XRD instrument settings.

Labels	Parameters
Equipment	Bruker D8 ADVANCE
Radiation source	Copper, Ni filtered
Detector	LYNXEYE XE-T
Geometry	Bragg-Brentano
Soller Slits	2.5
Divergence Slit	0.20
Antiair scatter degree (Å)	2.24
Goniometer_radius	280 mm
2θ range	4 ~ 80 °
Step size	0.02 °
Time per step	28.8 s

Table.S2. Component contents of PC and PG.

Species	PG (wt%)	PC (wt%)
F	0.80	-
Na_2O	0.08	0.14
MgO	0.08	2.23
Al_2O_3	0.70	6.19
SiO_2	5.28	21.74
P_2O_5	1.07	0.16
SO_3	53.69	1.92
Cl	-	0.04
K_2O	0.26	1.06
CaO	37.07	61.41
TiO_2	0.10	0.39
Cr_2O_3	-	0.05
MnO	-	0.33
Fe_2O_3	0.63	3.20
CuO	0.01	0.01
ZnO	-	0.03
SrO	0.05	0.03
ZrO_2	-	0.01
BaO	0.16	0.11
Total	99.98	99.05
Loss	0.02	0.95

Table.S3 Possible assignments of PG

Wavenumber (cm^{-1})	Assignments
466	Bending vibrations δ_{as} of (Si–F) and/or (O–P)
602	v_4 vibration of SO_4^{2-}
670	v_4 vibration of SO_4^{2-}
777	bending vibration of Si–O
797	bending vibration of Si–O
837	v HPO_4^{2-}
1115	v_3 and v_1 vibration of SO_4^{2-}
1142	v_3 and v_1 vibration of SO_4^{2-}
1620.90	H–O–H bending mode
1685.79	H–O–H bending mode
2116.03	stretching of SO_4^{2-}
2238.62	stretching of SO_4^{2-}
3244.01	stretching vibrations of H_2O
3405.32	stretching vibrations of H_2O
3491.08	stretching vibrations of H_2O
3546.74	stretching vibrations of H_2O

Table.S4 Possible assignments of 28 days cured PC and OCPB.

PC	assignments	OCPB	assignments
3643.1	-OH stretching vibrations		
3516.5	stretching vibrations of H_2O		
3438.5	stretching vibrations of H_2O		
		3408.9	stretching vibrations of H_2O
		2926.4	stretching vibrations of H_2O
		2855.1	overtone bands CO_3
2517.2	Asymmetric stretching of CO_3	2514.6	Asymmetric stretching of CO_3
		2239.9	the tetrahedral sulfate anion
		2116.1	the tetrahedral sulfate anion
1791.1	$CaCO_3$	1795.2	$CaCO_3$
		1685.6	H2O bend
1630.2	bending modes of adsorbed water molecules	1621.3	bending modes of adsorbed water molecules
1427.4	Asymmetric stretching of CO_3	1420.9	Asymmetric stretching of CO_3
		1138.9	v_3 vibration of SO_4
		1113.9	v_3 vibration of SO_4
995.4	Si-O stretching vibration		
875.3	v_3 vibration of CO_3	874.3	v_3 vibration of CO_3
		798.0	bending Si–O vibration
		778.2	bending Si–O vibration
712.8	v_3 vibration of CO_3	712.2	v_3 vibration of CO_3
		670.4	v_4 vibration of SO_4
		601.9	v_4 vibration of SO_4
519.9	bending Si–O vibration	519.7	bending Si–O vibration
485.9			
		471.3	v_2 vibration of SO_4

Table.S5. Semi-quantification of the F and P weight percentage of points marked in Fig.4a and Fig.S4.

	WDS			EDS	
Points	F (wt%)	P (wt%)	Points	F (wt%)	P (wt%)
Spot A	20.92	0.13	-	-	-
Spot B	5.46	0.19	Spot 1	3.70	0.21
Spot C	17.89	0.16	Spot 2	1.96	0.00
Spot D	3.67	0.34	Spot 3	2.42	0.11
Spot E	4.79	0.29	-	-	-
Spot F	5.36	0.22	-	-	-
Spot G	2.19	0.29	-	-	-
Average	8.61	0.23	Average	2.69	0.11

Table.S6. Modeling input of PHREEQC: Reactions, equilibrium constant, and initial content (mol/100g) of the mineral assemblages.

Mineral phases	Chemical formula	Dissolution reaction	log *K*	Input1[a]	Input2 [b]
Gypsum	$CaSO_4{\cdot}2H_2O$	$CaSO_4{\cdot}2H_2O \leftrightarrows Ca^{2+} + SO_4^{2-} + 2H_2O$	-4.58	0.48461	0.31314
Bassanite	$CaSO_4{\cdot}0.5H_2O$	$CaSO_4{\cdot}0.5H_2O \leftrightarrows Ca^{2+} + SO_4^{2-} + 0.5H_2O$	-3.92	0.04621	0
Anhydrite	$CaSO_4$	$CaSO_4 \leftrightarrows Ca^{2+} + SO_4^{2-}$	-4.36	0.01269	0
Quartz	SiO_2	Precipitate_only	-	0.03359	0.06876
Feldspar	$KAlSi_3O_8$	$KAlSi_3O_8 + 4H^+ + 4H_2O \leftrightarrows Al^{3+} + 3H_4SiO_4 + K^+$	-0.28	0.00730	-
Muscovite	$KAl_3Si_3O_{10}(OH)_2$	$KAl_3Si_3O_{10}(OH)_2 + 10H^+ \leftrightarrows K^+ + 3Al^{3+} + 3H_4SiO_4$	12.70	0.00383	-
Calcite	$CaCO_3$	$CaCO_3 \leftrightarrows Ca^{2+} + CO_3^{2-}$	-8.48	- [c]	0.10938
Dolomite	$CaMg(CO_3)_2$	$CaMg(CO_3)_2 \leftrightarrows Ca^{2+} + Mg^{2+} + CO_3^{2-}$	-17.09	-	0.01008
Whitlockite	$Ca_3(PO_4)_2$	$Ca_3(PO_4)_2 + 2H^+ \leftrightarrows 2HPO_4^{2-} + 3Ca^{2+}$	-4.23	0 [d]	0.00085
Brushite	$CaHPO_4{\cdot}2H_2O$	$CaHPO_4{\cdot}2H_2O \leftrightarrows Ca^{2+} + HPO_4^{2-} + 2H_2O$	6.55	0	0
Fluorite	CaF_2	$CaF_2 \leftrightarrows Ca^{2+} + 2F^-$	-10.60	0	0.01021
Strengite	$FePO_4{\cdot}2H_2O$	$FePO_4{\cdot}2H_2O + H^+ \leftrightarrows Fe^{3+} + HPO_4^{2-} + 2H_2O$	-11.34	0	0
Vivianite	$Fe_3(PO_4)_2{\cdot}8H_2O$	$Fe_3(PO_4)_2{\cdot}8H_2O \leftrightarrows 3\ Fe^{2+} + 2PO_4^{3-} + 8H_2O$	-36.00	0	0
Hydroxyapatite	$Ca_5(PO_4)_3OH$	$Ca_5(PO_4)_3OH + 4H^+ \leftrightarrows H_2O + 3HPO_4^{2-} + 5Ca^{2+}$	-3.42	0	0.00265
Fluorapatite	$Ca_5(PO_4)_3F$	Ca5(PO4)3F + 3H+ ⇆ 5Ca+2 + 3HPO4-2 + F-	-17.60	0	-
Ettringite	$Ca_6Al_2(SO_4)_3(OH)_{12}{\cdot}26H_2O$	$Ca_6Al_2(SO_4)_3(OH)_{12}{\cdot}26H_2O + 12H^+ \leftrightarrows 2Al^{3+} + 3SO_4^{2-} + 6Ca^{2+} + 38H_2O$	56.7	-	0.00329
Portlandite	$Ca(OH)_2$	$Ca(OH)_2 \leftrightarrows Ca^{2+} + 2OH^-$	-5.3	0	0.01720
C1.5-S-H (Amorphous)	Ca3.0Si2O7.9783H1.9566:2.2848H2O	Ca3.0Si2O7.9783H1.9566:2.2848H2O + 6.0 H+ = 3.0 Ca+2 + 2 H4SiO4 + 2.2631 H2O	51.45	-	0.06336
$Fe(OH)_3$ (Amorphous)	$Fe(OH)_3$	$Fe(OH)_3 + 3H^+ \leftrightarrows Fe^{3+} + 3H_2O$	4.89	0	0
$Al(OH)_3$ (Amorphous)	$Al(OH)_3$	$Al(OH)_3 + 3H^+ \leftrightarrows Al^{3+} + 3H_2O$	10.80	0	0.02510
Fluoride acid	HF	-	-	0.04211	0
Phosphate acid	H_3PO_4	-	-	0.00589	0
Sulfate acid	H_2SO_4	-	-	0.01078	0

Notes: The "0" in the initial input table means that the phase is absent in the original assemblage, whereas the abbreviation "-" indicates the phases are not considered in the system.

[a] Input mineral composition of PG modeling.

[b] Input mineral composition of OCPB modeling.

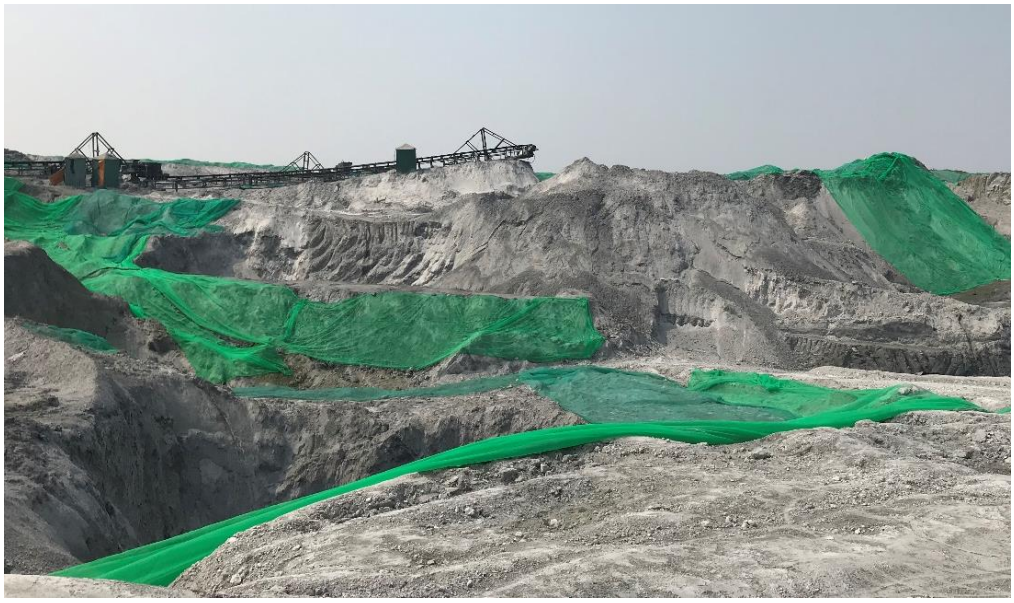

Figure.S1. Phosphogypsum disposal sites and sampling area

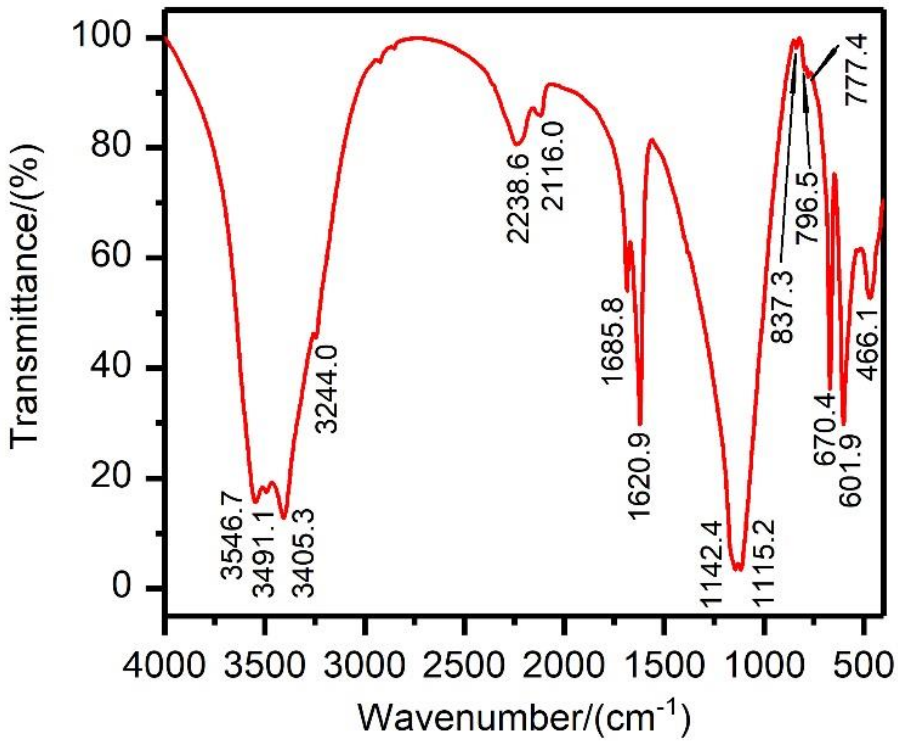

Figure.S2. FTIR spectra of PG sample.

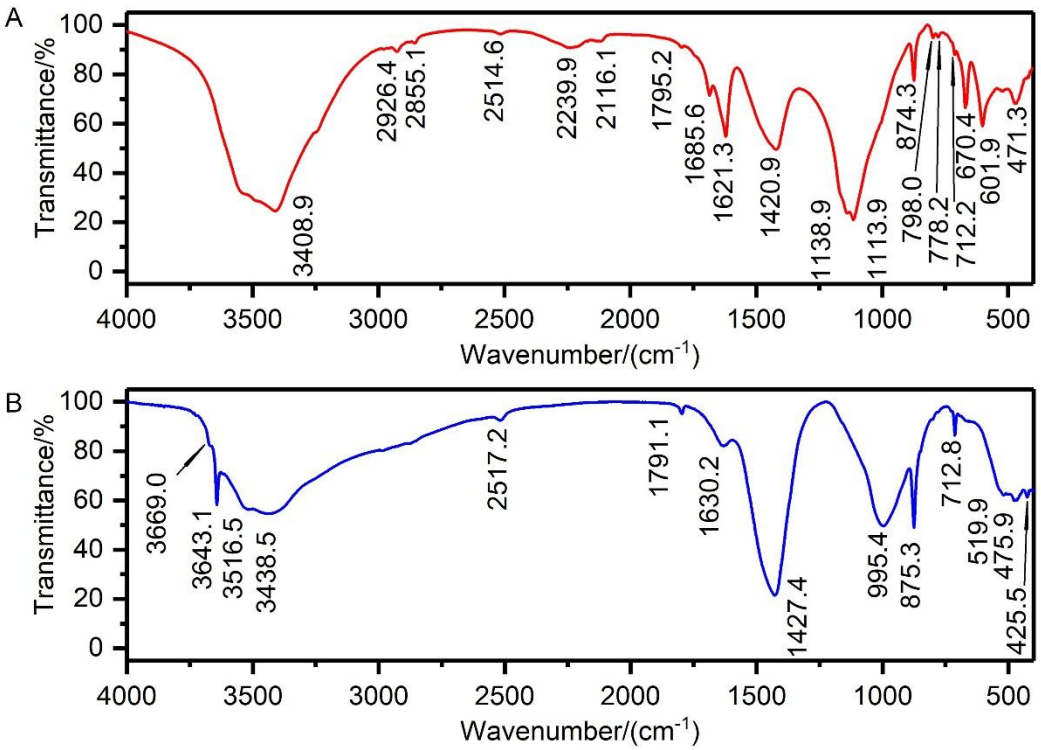

Figure.S3. FT-IR spectra of 28 days cured OCPB (a) and PC (b).

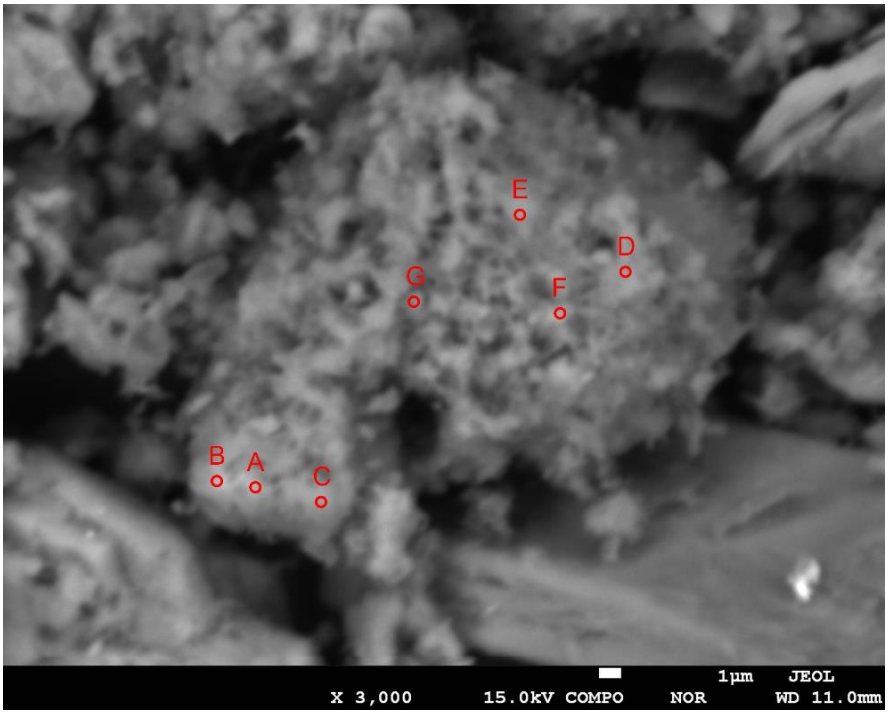

Figure.S4 WDS point analysis of the amorphous matrix presented in Fig.4a

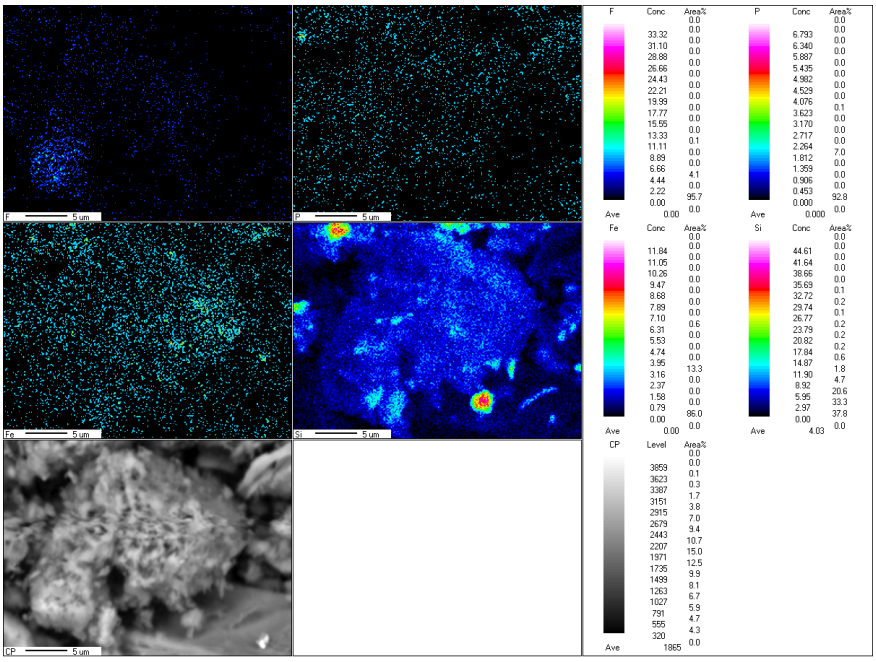

Figure.S5. Elemental mapping of OCPB assemblage based on EMPA/WDS, scan area relative to Fig.4a.

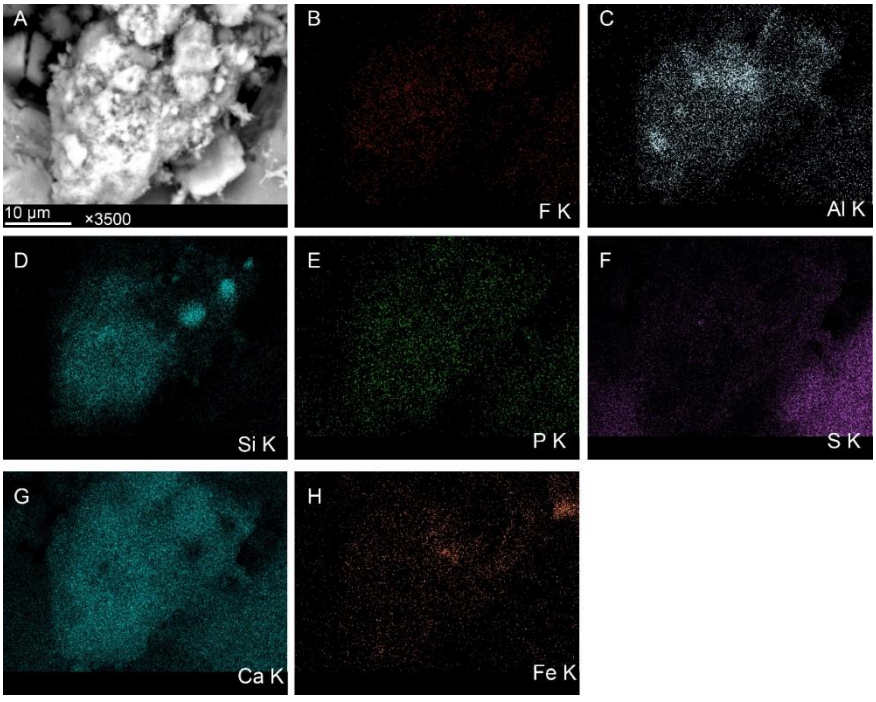

Figure.S6. Elemental mapping of OCPB assemblage based on SEM/EDS, scan area relative to Fig.4d.

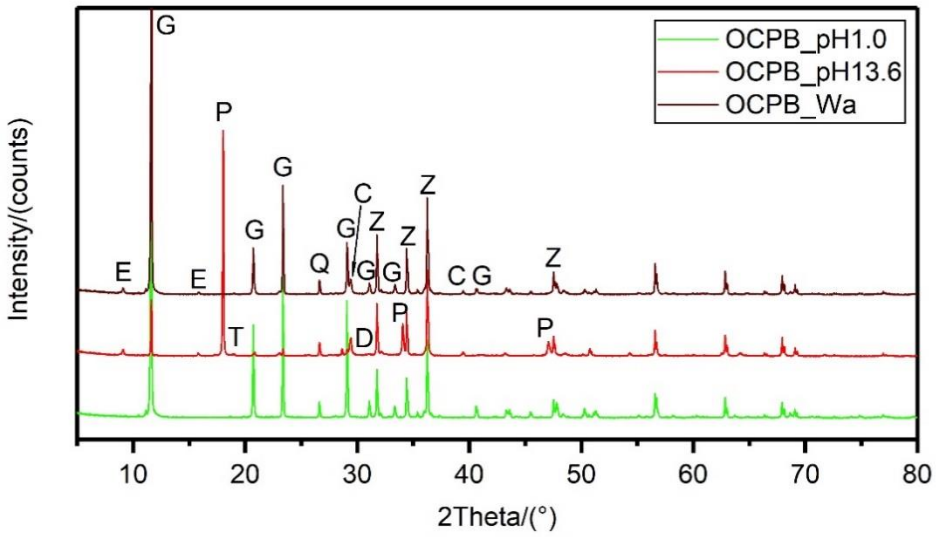

Figure.S7. XRD patterns of the OCPB residues after leaching. (C: Calcite; D: Dolomite; E: Ettringite; G: Gypsum; P: Portlandite; T: Thenardite; Z: Zincite)

Chapter 5

Enhancing the sustainable immobilization of phosphogypsum by cemented paste backfill with the activation of γ-Al_2O_3

Yikai Liu[1]; Qiusong Chen[2, 3]; Maria Chiara Dalconi[1]; Simone Molinari[1]; Luca Valentini[1]; Yunmin Wang[2,3]; Shiyuan Sun[3]; Peishen Wang[3]; Gilberto Artioli[1]

[1] *Department of Geosciences and CIRCe Centre, University of Padua, via G. Gradenigo 6, 35129, Padua, Italy*

[2] *Sinosteel Maanshan General Institute of Mining Research Co., Ltd., Maanshan, 24300, China;*

[3] *School of Resources and Safety Engineering, Central South University, Lushan South Road 932, 410083, Hunan, China*

Graphical abstract

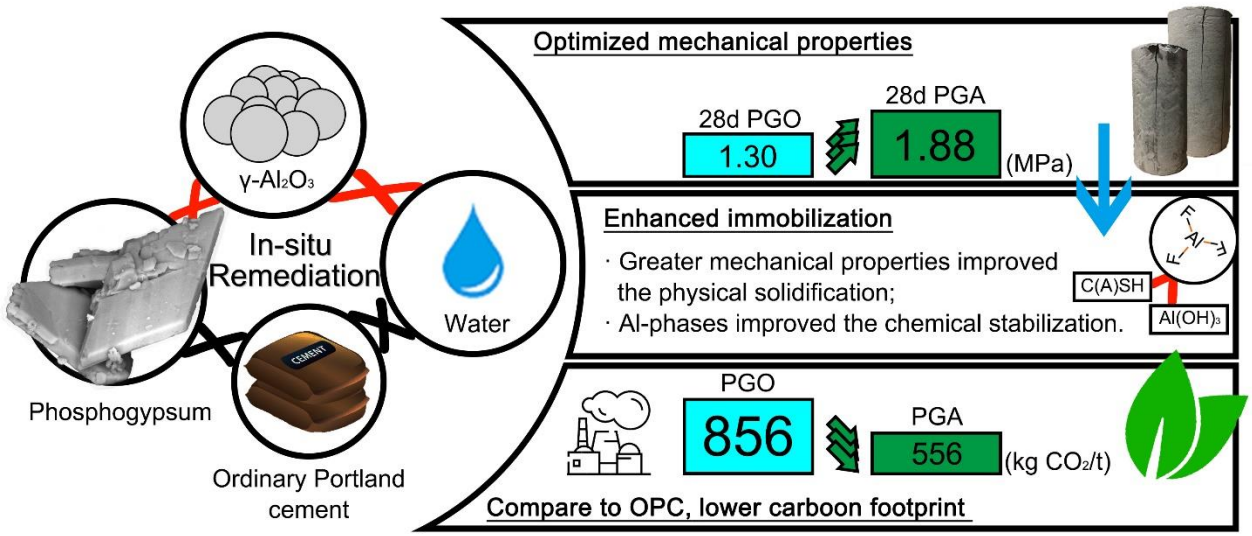

This manuscript is a published paper in Construction and Building Materials, Volume 347, 128624

Abstract

The in-situ solidification/stabilization of phosphogypsum (PG) has been deemed to be an efficient technology for large-scale stockpiled waste remediation. But there is still great uncertainty and controversy concerning fluorine and phosphorus transformation. Further, with a great concern for the high carbon footprint of the typical Portland cement binder, developing a low-carbon binder is of increasing importance for sustainable development. Herein, γ-Al_2O_3, an alternative with lower CO_2 emissions and energy consumption, was preliminarily explored in PG remediation. Results showed that γ-Al_2O_3 promoted ettringite and amorphous precipitation. The SEM/EDS evidenced the role of aluminum-containing assemblages in pollutant retention. The pH-dependent leaching tests illustrated that the addition of γ-Al_2O_3 increases the fluorine retention capacity, but it is less dominant in phosphorus and sulfate immobilization. The modeling approach verified Al-F, Ca-F, and Ca-P phases as the primary phases for pollutant retention. The deviation in experimental and modeling leaching results indicates that the physical encapsulation cannot be ignored, which is evidenced by the higher mechanical strength that γ-Al_2O_3 modified mixtures achieved, presenting mechanically stable assemblages for engineering application and pollutants retention. This study proved that the utilization of γ-Al_2O_3 can expand the scalable application of PG, both in view of low-carbon strategy and high-performance solidification/stabilization.

Keywords

Phosphogypsum, solidification/stabilization, cemented paste backfill, aluminum oxide, solid waste management

1. Introduction

Phosphogypsum (PG) is one of the most pressing environmental burdens associated with phosphorus fertilizer and phosphoric acid production. In China, it was estimated that approximately 250 million tons of PG were produced annually, with more than 55 million tonnes of growth rates each year (Qiu et al., 2020). Most of the generated PG has been dumped in the ocean and deposited in waste piles near the phosphoric acid factory and/or the mines where the phosphate ores are extracted without any treatment (Silva et al., 2022). The PG stacks are exposed to weathering with aeolian and fluvial processes, and the pollutants within PG are accordingly dispersed into the environment, contaminating groundwater systems and threatening human health (Bisone et al., 2017). Therefore, effective treatments of PG are essential to control its potential negative impacts. Several scholars have implemented recycling initiatives to ensure that PG can be utilized as primarily used resources in construction (Calderón-Morales et al., 2021), aggregates in cemented paste backfill (CPB) materials (Li et al., 2017; Zhou et al., 2020a), off-site agriculture amendments to saline soil (Smaoui-Jardak et al., 2017), ex-situ sulfate resources for sulfuric acid production

(Chernysh et al., 2021). Because of its high abatement capacity, practical engineering feasibility, and profitable economic viability (Saedi et al., 2020), CPB is considered one of the prevalent and robust techniques for PG in-situ treatment (Chen et al., 2018; Shi et al., 2021). Nevertheless, CPB may pose various risks if not managed properly. As the secondary pillars to ensure the stability of the underground excavations, an efficient CPB should have both adequate mechanical permeance (Belem et al., 2000) and sufficient pollutants immobilization capacity (Qi and Fourie, 2019).

However, studies stated that the presence of PG recycled materials could deteriorate the hydraulic stability, long-term durability, and mechanical properties of the CPB materials (Chen et al., 2017; Qi and Fourie, 2019). Especially from a geotechnical point of view, numerous studies have reported that due to weak hydraulic properties, the increase of PG percentage due to the weak hydraulic property would significantly decrease the uniaxial compressive strength of CPB samples (Li et al., 2017; Meskini et al., 2021). Although a simple increase of OPC proportion can optimize the physical properties and the retention capacity, the subsequent greenhouse gas emissions raising should be of grave concern. Another difficulty of PG valorization comes from the redistribution of impurities. Because of the complexity of underground structures (e.g., the long-term exposure to percolating water/groundwater and the deteriorated mechanical stability due to the processed mining operation), as the CPB is pumped into goaf, the hazardous substances may leach out and contaminate groundwater systems and then fauna and flora despite already being immobilized by binders (Fall et al., 2007; Liu et al., 2021).

Therefore, in order to be utilized massively, efficient additives are needed to optimize the conventional process for PG recycling. Previous work has confirmed that silica fume (Gu et al., 2020) and ground granulated blast furnace slag (Min et al., 2021) are promising additive agents for improving mechanical performance. In addition to the physical properties, modified quartz sand displayed an excellent phosphorus immobilization capacity due to its large volume of pores, which favors the adsorption of phosphate (Shi et al., 2021). However, this study did not consider the fluorine immobilization performance and the associated retention mechanisms. MgO and NaOH were also incorporated in the electrolytic manganese residue-PG-ordinary Portland cement (OPC) mixtures to solidify/stabilize fluorine and phosphate synergistically (Shu et al., 2019). Despite the fact that the leaching of fluorine and phosphate decreases by the above additions, the retention of pollutants is still not satisfactory, with the concentration of leached fluorine and phosphate being unqualified for the drinking water limits (10 and 0.5 mg/L, respectively, according to Chinese standard GB 8978-1996). Moreover, although sulfate is a common contaminant in industrial wastewaters, it can cause the corrosion of steel and the deterioration of concrete mechanical properties (Chen et al., 2020; Amine Laadila et al., 2021) is barely mentioned in the PG management research. Therefore, exploring a facile additive agent to efficiently disperse fluorine, phosphorus, and sulfate pollutants on a cost-effective

and chemically stable substrate is vital for promoting practical in-situ PG remediation. Aluminum was presumably reported to facilitate the pollutants' retention, but its role has not been explicitly determined (Feng et al., 2022). In this work, we suggest the use of a more environmentally friendly and lower carbon footprint agent, γ-Al_2O_3, in PG-CPB sample preparation, which can react with excess sulfate and promote binder hydration (Zhou et al., 2019). In particular, aluminum oxide has excellent adsorption capacity for both fluorine and phosphorus due to its large specific surface and high mass transfer efficiency (Moharami and Jalali, 2014; Hafshejani et al., 2017). Further compared with the α-Al_2O_3, the γ polymorph has a lower surface energy and higher reactivity, which may have great potential to promote the CPB hydration process and boost pollutants retention (Valero et al., 2006; Yang et al., 2020).

This study attempts to explore the feasibility of γ-Al_2O_3 in PG in-situ management. Herein, in order to examine the possible retention mechanisms, CPB samples, both in the presence and in the absence of fluorine and phosphorus, are prepared as comparative studies. X-ray powder diffraction (XRD), X-ray fluorescence spectroscopy (XRF), Fourier-transform infrared spectroscopy (FT-IR), and scanning electron microscopy/energy-dispersive X-ray spectroscopy (SEM/EDS) are applied to investigate the phase transformation and microstructural evolution and to understand the role of reactions occurring in cementitious systems in relation to fluorine and phosphorus fixation. Lastly, the fluorine, phosphorus, and sulfate retention capacity is tested by pH-dependent leaching tests. This work benefits extending the PG in-situ remediation with the direct use of the γ-Al_2O_3 additive. This technology may make positive contributions towards achieving a circular economy and industrial decarbonization towards net-zero emissions. Furthermore, the geochemical modeling applied in this work should allow for providing more comprehensive insights to extrapolate the new binders in solid waste management systems.

2. Materials and methods

2.1 PG sampling and CPB mixtures preparation

The PG used in the experiment was sampled from a stockpile site of a phosphorus fertilizer manufacturing plant. All the chemical reagents are analytical grade (γ-Al2O3 is from Guangzhou nano chemical technology co., Ltd, NaF is from Xilong Scientific co., Ltd, P_2O_5 is manufactured by Tianjin Fuchen chemical reagent factory, gypsum and quartz are provided by Tianjin Kermal Chemical Reagent Co., Ltd). The mixture designs of CPB samples are given in Table 1. 10 wt% of γ-Al_2O_3 was employed to replace the OPC. The water-to-binder ratio was kept at 1.5. The control groups, mixtures with or without phosphorus pentaoxide and sodium fluoride, were prepared to determine the individual influence of phosphorus and fluorine on the evolution of the mineralogical phases. The blends were homogeneously mixed and poured into plastic cylinders (5 cm in diameter and 10 cm in height). After 3 days of hardening, all the samples were demoulded and sealed with plastic membranes before subsequent characterization tests.

Table.1 Mix proportions of CPB mixtures (wt.%).

	PG	P_2O_5	NaF	Gypsum	Quartz	OPC	γ-Al_2O_3	Water
PGO	28.6	-	-	-	-	28.6	-	42.8
PGA	28.6	-	-	-	-	18.6	10.0	42.8
PO	-	0.6	-	25.7	2.3	28.6	-	42.8
PA	-	0.6	-	25.7	2.3	18.6	10.0	42.8
FO	-	-	0.3	26	2.3	28.6	-	42.8
FA	-	-	0.3	26	2.3	18.6	10.0	42.8
PFO	-	0.6	0.3	25.4	2.3	28.6	-	42.8
PFA	-	0.6	0.3	25.4	2.3	18.6	10.0	42.8

Note: PGO and PGA represent the PG sample immobilized by OPC or mixed binder (OPC+ γ-Al_2O_3); PO and PA mean the manually prepared aggregates only with P_2O_5, quartz, and gypsum then mixed with OPC or mixed binder; FO and FA are the manually prepared aggregates with NaF, quartz, and gypsum then mixed with OPC or mixed binder; PFO and PFA indicate the manually prepared aggregates with P_2O_5, NaF, quartz, and gypsum then mixed with the OPC or mixed binder.

2.2. Mineralogical and microstructural characterization

All the samples were preliminarily crushed and sieved with an 80 μm mesh, then dried at 55 ± 5℃. An automated diffractometer (D8 Advance, Bruker Co. Ltd, Germany) in Bragg-Brentano configuration with a copper radiation source (at 40 kV and 40 mA) was used to record the XRD patterns. Angles from 5° to 80° 2θ were scanned with a step size of 0.02°. Zincite (ZnO, ACS Reagent) was used as an internal standard to quantify the amorphous content. Jade 6.5. and Profex (Doebelin and Kleeberg, 2015) were applied for the qualitative and quantitative phase analysis of XRD patterns. The bulk elemental composition of the raw materials was determined with wavelength dispersive XRF spectrometry (AXS S4 Pioneer, Bruker Co. Ltd, Germany). FTIR spectra in the range of 400 to 4000 cm^{-1} were obtained by a spectrometer (Nicolet iS50, Thermo Fisher, Madison, USA), preparing specimens with a sample to KBr powder ratio of 1/100. Microstructural investigation on polished and carbon-coated PGO and PGA samples was performed using SEM (Mira 4, Tescan, Czech Republic) equipped with an EDS spectrometer.

2.3. Mechanical properties

The uniaxial compressive strength tests were performed on the PGO and PGA specimens with an electromechanical compression testing machine (CDT1305, MTS Systems Co., Ltd). The equipment has a maximum loading capacity of 300 kN with a 0.6 kN of contact pressure. The loading rate was kept at 0.1 mm/min. All data regarding the test were monitored and collected using the computer software PowerTest (Model V3.0).

2.4. pH-dependent leaching tests

The immobilization efficiency of pollutants was tested according to the standard for leaching toxicity of solid wastes (GB/5086.1; 1997, Jing et al., 2013). The acid attack was carried out in the presence of a predetermined amount of nitric acid (1 N HNO_3) as the eluent at a liquid-solid ratio (L/S) of 10. Before the leaching procedure, the PGO and PGA were preliminary broken into particles less than 5 mm in diameter. After being immersed for 18 h using a rotary shaker at 30±2 rpm, the leachates were filtered through 0.45 μm filter paper. The fluoride, phosphorus, and sulfate concentration in the eluates were quantified according to the specific standards: fluoride - Determination of fluoride: ion-selective electrode method, GB/7484-87, 1987; phosphorus - Inductively Coupled Plasma atomic emission spectrometry, HJ/776, 2015; sulfate - Determination of sulfate: barium chromate spectrophotometry, HJ/T 342, 2007.

2.5. Modeling Approach

The modeling of the aqueous-solid partitioning and the mineralogical species equilibrium was accomplished using the U.S. Geological Survey (USGS) program Phreeqc Interactive 3.0.6 (Parkhurst and Appelo, 2013). Minerals controlling the solubility of constituents were selected from the MINTEQ (Gustafsson, 2011), Cemdata18 (Lothenbach et al., 2019), Phreeqc database (Appelo et al., 2014), and Lawrence Livermore National Laboratory (LLNL) thermodynamic databases at 25 °C. The initial assemblage used in the simulation was based on the XRD and XRF characterization. A basic assumption for the geochemical speciation modeling is that the dissolution, precipitation, and adsorption reactions of all constituents reach equilibrium. The details of the initial phase assemblages are summarized in Table.S3.

2.6. Operating costs and CO_2 emission

The total CO_2 emissions for recycling PG with different scenarios were analyzed from a “cradle-to-gate” perspective according to the assumed equipment performance standards. Fig.S1 displays the system energy boundary of the PGO and PGA sample preparation process. The CO_2 emission of OPC production and water supply system was conventionally given as 852 kg CO_2/t (Ravikumar et al., 2021) and 2.50 kg CO_2/m^3 (Chang et al., 2012). The average disposal cost expense for hazardous solid waste in China was estimated as 2015 CNY/t (Zhu and Jin, 2021). Considering that there were no existing inventories with respect to the γ-Al_2O_3 as aforementioned, the key data were obtained from previous literature. To note, the carbon footprint of the kaolin and limestone mining process was not considered. Meanwhile, the transportation distance for OPC, PG, and γ-Al_2O_3 to the in-situ remediation factory was assumed negligible in the analysis. The major unit operations in the γ-Al_2O_3 processing include raw materials acquisition, physical grinding, oxy-fired calcination, and drying process (Hosseini et al., 2011; Sousa and Bogas, 2021) (Fig.S1b). The energy consumption and CO_2 emission for each unit were determined by the electricity generated for acquiring 1 tonne of γ-Al2O3 (Vizcaíno-Andrés et al., 2015; Cao et al., 2021). The CO_2 emission of the grid and renewable electricity used is estimated as 0.540 and 0.025 CO_2/kWh (Renforth et al., 2013;

McQueen et al., 2020). And the ratio of the electricity from different energy sources is anticipated as 2.33 (Grid electricity to renewable electricity) (Yao and Zang, 2021). Additionally, the calcination efficiency of kaolinite and total mass loss in γ-Al_2O_3 production processes were assumed as 85 and 90%, respectively. Parameters for product benefit, disposal fee saving, CO_2 emission, carbon tax/credit, and associated energy demand are outlined in Table.S5.

3. Results

3.1. XRD and FTIR characterization of mixtures

Fig.1a shows the XRD patterns of specimens after 28 days of curing time. In all the patterns, gypsum occurs as the major crystalline phase (e.g., PGO 35 wt.% and PGA 18 wt%), with the most intense diffraction peak observed at 11.6° 2θ, as well as 20.7° and 23.3° 2θ. As expected from cement chemistry, typical hydration products ettringite and portlandite are detected. The presence of calcite could be related to the carbonation of hydration products in contact with the atmosphere (Šavija and Luković, 2016). Muscovite, originating from the raw PG, has only been identified in the PGA and PGO patterns.

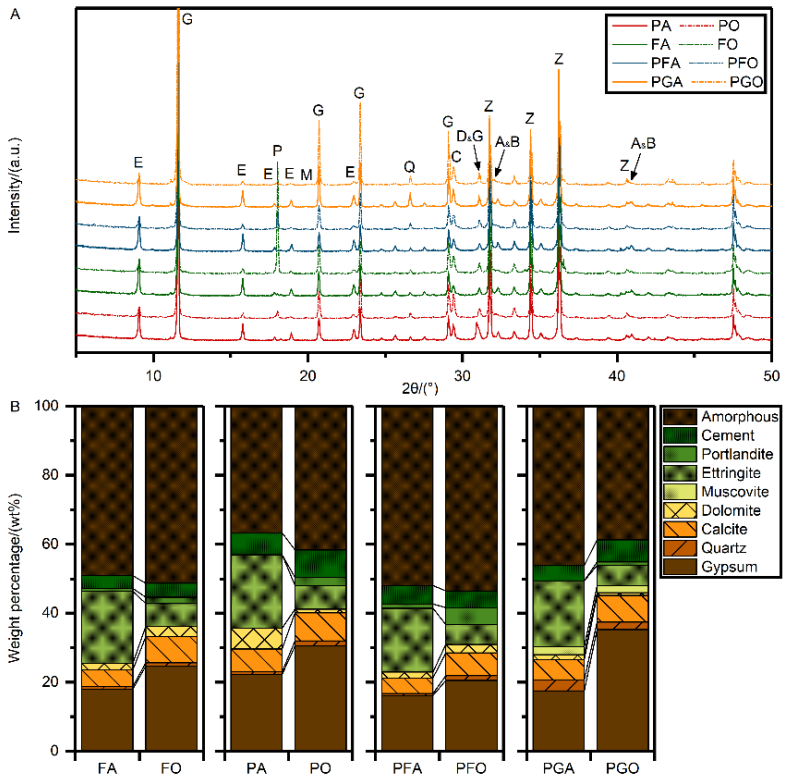

Figure.1. XRD analyses of CPB samples. (a) XRD patterns of the 28 days cured samples and (b) quantitative mineralogical composition obtained by the Rietveld method. A: Alite; B: Belite, C: Calcite, D: Dolomite, E: Ettringite, G: Gypsum, M: muscovite; P: Portlandite, Q: Quartz, Z: Zincite.

The addition of γ-Al_2O_3 does not lead to the formation of additional crystalline phases. Based on Rietveld's quantitative phase analysis, after subtracting the known content of ZnO used as the internal standard, the mineralogical quantification results are summarized in Fig.1b. All tested samples are characterized by high amorphous content, in particular, 51%, 42%, 54%, and 39% are observed in FO, PO, PFO, and PGO specimens, respectively. While in the group of samples with γ-Al_2O_3 activation, FA, PA, and PFA, the amorphous content was kept at percentages of 49%, 37%, and 52%. However, the amorphous content increases to 46% in the PGA sample.

To further evaluate the pollutants retention mechanisms in the presence of γ-Al_2O_3, FT-IR spectra (from wavenumber 400 to 1600 cm^{-1}) and the corresponding assignments are presented in Fig.2 and Table.S2. The detected vibrational frequencies are in good agreement with crystalline phases obtained from the XRD measurements and generally give an indication of sulfate, carbonate, silicate, and hydroxide phases. The features at 460, 602, 670, 1115, 1137, and 1425 cm^{-1} can be attributed to the bending and stretching vibration of SO_4^{2-} (Ölmez and Yilmaz, 1988; Trezza and Lavat, 2001). The sharp bands at 712 and 874 cm^{-1} and the broadband at 1430-1480 cm^{-1} correspond to the bending vibration of CO_3^{2-} and stretching vibration of C–O (Wang et al., 2019a) ascertained the carbonation reactions. The broad bands around 516 cm^{-1} present in FO, PO, and PGO samples were due to the out-of-plane skeletal vibration of the Si-O bond (Wang et al., 2019a).

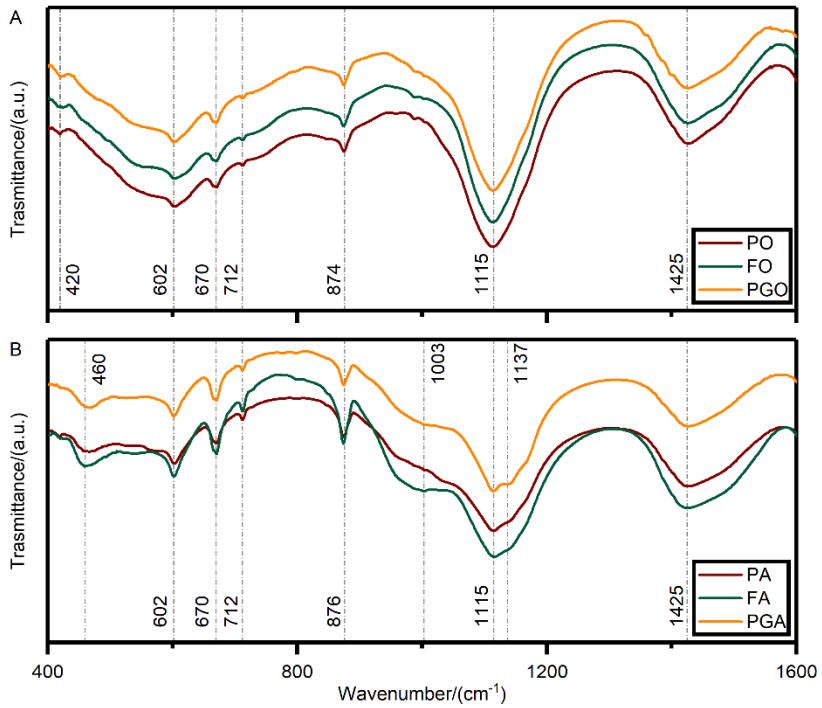

Figure.2. FT-IR patterns of CPB samples. (a) Spectra of unaccelerated samples PO, FO, and PGO; (b) spectra of accelerated samples, PA, FA, and PGA.

The broad peak ranging from 900 to 1000 cm^{-1} in PA, FA, and PFA samples could be assigned to the multiple T–O bonds vibrations (where T is Si or Al). As it is possible to observe two different modes here (i) a deepening of the transmittance associated with the C-S-H gel, the position of which remains fairly constant, and (ii) a broadening of the absorbance associated with the C-A-S-H gel (Garcia-Lodeiro et al., 2011; Kapeluszna et al., 2017). Noteworthy, the unhydrated cement components (Alite and Belite) were also confirmed that contribute to the vibration at this range (Hughes et al., 1995; Higl et al., 2021). Although the hydration process accompanies the dissolution of Alite and Belite, their characteristic band (approximately at 920 cm^{-1}) still overlaps with C-(A)-S-H bands making it hard to distinguish the transmittance contribution from different components. Further, a shoulder peak was observed in the region from 1450 to 1500 cm^{-1}, which could be related to the vibrations of $Ca(OH)_2$ (approximately at 1460 cm^{-1}) and the significant output of amorphous C-S-H gel. Thus, FTIR spectra analysis further shows that the dominant components in the samples were mainly gypsum and carbonates.

3.2. Microstructural observations

To explore the influence of γ-Al_2O_3 on the microstructural features and pollutants distribution, samples were analyzed by SEM/EDS. The microstructural observation (Fig.3a and Fig.S3) evidence that the internal microstructure of PGO was mainly composed of a homogenous gel matrix, short ettringite prisms, and tabular gypsum crystals, accompanied by several unhydrated cement particles (see in Fig.S3a and b). Similarly, a homogeneous distribution (Fig.3e, S4, and S5) is observed in the analyzed area of PGA samples. By contrast, needle-like ettringite crystals (around 5 μm in length) are present in the transition zones along with the cement particles and amorphous matrix (see Fig.S4c and d). These results are consistent with the XRD and FTIR characterization. Further, the elemental mapping (Fig.3a–d) and EDS spot analysis (Fig.3l) suggested that the concentration of F and P are correlated to the Ca and Si ones, which are the typical elements originating from the OPC constituents. Meanwhile, Al is mainly concentrated, together with the Ca, on unhydrated cement particles (see Fig.S3). A similar homogeneous distribution of F and P, with a preferable enrichment at Ca and Si concertation areas, is observed in PGA samples (see Fig.3e–h and Fig.S4). This preference suggests that the chemical fixation from the binder component plays a role in the pollutants immobilization, where the high concentration of F and P was observed on the rim of the unreacted cement particles, representing the area undergoing hydration reactions. Whereas the fine distribution of Al is massively observed in the matrix (Fig.3e and g), indicating that apart from ettringite precipitation, the homogeneously dispersing of γ-Al_2O_3 also offers important incorporation feasibility. Further, calcium-phosphate-fluorine complexes (CPF, Fig.3i–k and Fig.S5) are occasionally found, which is not observed in PGO samples. Herein, we hypothesize that, based on the SEM/EDS images, the generation of calcium-silicate-fluorine/phosphate precipitates could be the principal removal mechanism.

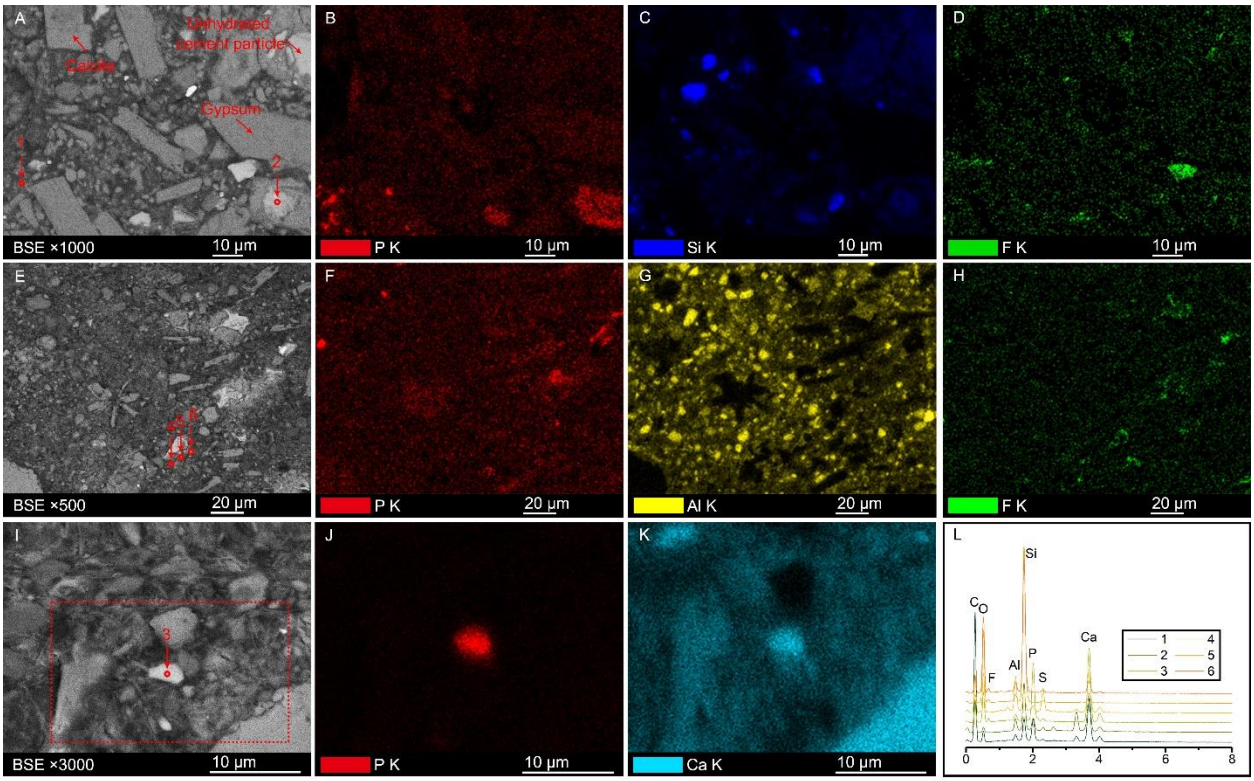

Figure.3. BSE/SEM images, elemental mapping, and EDS spot analyses of PGO and PGA samples with 28 days of curing. (a) BSE graph of PGO samples with the mapping of P, Si, and F (b-d); (e) internal microstructure of PGA sample with elemental mapping of P, Al, and F (f-h); (i) occasionally found CPF with the mapping of P (j) and Ca (k) correlated the red dash line marked area in image i; (l) EDS spectrum correspondent to the red point marked in previous images.

3.3. Examination of the mechanical properties

The compressive strength of CPB samples is reported in Fig.4a, and the calculated relative changes are shown in Fig.4b. Overall, the addition of γ-Al_2O_3 does not have a positive impact on the early age mechanical performance. The strength values of the tested FA, PA, and PGA specimens (7 days) are reduced to 0.3, 0.4, and 0.3 MPa, respectively, with only a slight increase which is observed in PFA (see Fig.4b).

At 28 days, the γ-Al_2O_3 exhibited a positive influence on the strength development, with the compressive strength increased by a maximum of 0.6 MPa at PGA samples. Interestingly, the FO and PO samples attain 1.1 and 0.9 MPa at 7 days, whereas they have no strength development later. Similar findings are also reported in previous studies (Singh, 2003; Zhou et al., 2020a).

3.4. pH-dependent leaching tests: fluoride, phosphorus, and sulfate releasing

The fluoride, phosphate, and sulfate pH-dependent leaching results from raw PG (Liu et al., 2022), PGO, and PGA specimens are shown in Fig.5, 6, and S6, respectively. Overall, such elements are generally well

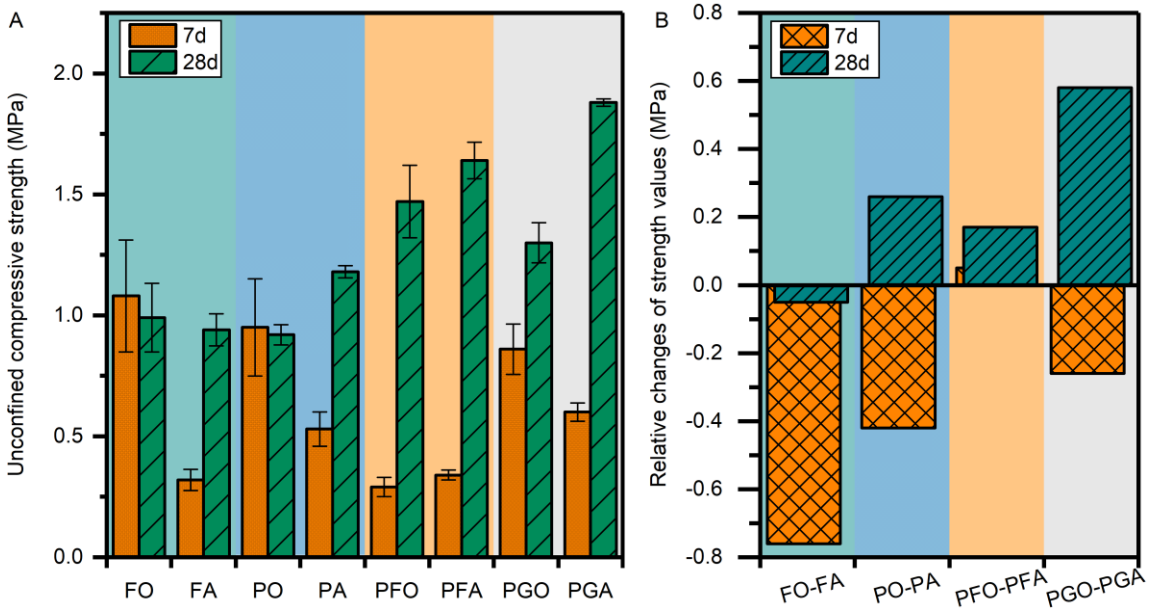

Figure.4. Mechanical properties of CPB samples. (a) the tested unconfined compressive strength values of 7 and 28 days hardened CPB samples and (b) the relative changes of strength values with the influence of Al_2O_3.

immobilized in the intact hardened paste at the near-neutral pH ranges, indicating that PGO and PGA scenarios both represent effective remediation at pH values of approximately 5 to 10. In this pH range, the fluoride leaching (limit 10 mg/L) of PGO and PGA samples varies from 0.07 to 0.45 mg/L and from 0.06 to 0.21 mg/L. Meanwhile, the phosphate releasing (limit 0.5 mg/L) of PGO and PGA samples are from 0.22 to 0.46 mg/L and 0.09 and 0.37 mg/L. But the leached amounts for fluoride and phosphate in PGO and PGA samples are both at their maxima in the extreme acidic region. Additionally, the results also demonstrate that the presence of γ-Al_2O_3 induced an improvement in fluoride retention. When the pH values of PGO and PGA leachates are at 1.07 and 2.05, respectively, the fluoride concentration decreases from 24.08 to 0.99 mg/L. Further, as shown in Fig.5, fluoride leaching exhibits a strong amphoteric characteristic. The fluoride concentration of PGO and PGA leachates increased to 0.48 and 0.23 mg/L at pH values of 12.61 and 12.26, respectively. Thus the concentration increase in strongly alkaline conditions indicates the decomposition and/or precipitation of the phases controlling fluoride solubility. To note, although the insight from the pH-dependent leaching tests is unable to furnish direct proof of mineralogical facts, it provides a reference for accessing the possible mechanisms in the following simulations. On the contrary, high pH values have a negligible effect on phosphate immobilization (see Fig.6), and both matrices (PGO and PGA) exhibit a similar trend in phosphate release. In PGO samples, 4.99 mg/L of phosphate was leached out at pH values of 2.05, whereas in PGA samples, it was 1.43 mg/L (pH 1.07). Then, the concentration of phosphate decreased with the pH values. Furthermore, the pH values poorly influence

sulfate releasing, with the sulfate concentrations remaining relatively constant (around 4.00 g/L, R1 and R2 in Fig.S6) within the studied range. Therefore, this observation suggests that despite the sulfate being partially stabilized as ettringite in samples with the incorporation of γ-Al_2O_3, we predictably ascribed that massively remaining gypsum in both PGO and PGA mixtures dominates the equilibrium of sulfate. The slight increase of sulfate release observed at stage 3 (R3 in Fig.6) evidenced the role of gypsum. In fact, according to thermodynamic modeling at pH >12, gypsum is no longer stable and portlandite is formed instead. Furthermore, there are no explicit restrictions for sulfate concentration in Chinese water quality standards nowadays. But in the E.U. region and from the WHO guidance, the limitation is set as 0.25 g/L (Akoteyon et al., 2011). Hence the retention of sulfate should be carefully investigated in the following works.

3.5. Leaching simulation results and the evolution of fluoride- and phosphorus-containing phases

In order to characterize the possible retention mechanisms of pollutant-containing phases at various pH conditions, the geochemical leaching model is applied here as an aid tool to reveal the mineralogical evidence involved in this process. The model parameters for the initial phase assemblages are estimated from the previous characterization and reported in Table.S3. The model assumes a chemical equilibrium between the solid assemblages and the leachates. The clinker phases (C_2S, C_3S, C_3A, and C_4AF) were not considered in this system because of the absence of available thermodynamic data. Since the typical gangue minerals, quartz and muscovite, have already experienced harsh acidic procedures during the acidification of phosphorus rock, they were assumed not to participate in the dissolution and precipitation reactions (El Zrelli et al., 2018). In addition, the stabilized phosphorus and fluoride in PGO samples were assumed in the form of calcium phosphate ($Ca_3(PO_4)_2$) and fluorite (CaF_2). Considering the CPF found in PGA samples (Fig.3i), two retention hypotheses, CPF and $Ca_3(PO_4)_2$, are successively simulated. Besides, based on the fine matrix that is observed in Fig. 4 that is reasonably ascribed to C-A-S-H and the complementary thermodynamic GEMS modeling (Kulik et al., 2013), the amorphous content quantified in PGA samples by XRD analysis is classified into C-A-S-H and amorphous aluminum hydroxide ($Al(OH)_3$). Whereas, in PGO samples, the amorphous content was assumed to only consist of C-S-H. The simulated leaching behavior of F and P under different pH conditions are plotted in Fig.5 and 6.

Thus, overall, the proposed mineral set is deemed reasonable for describing the leaching profiles of F and P. In Fig.5, the results illustrate that the concentration of F is mainly controlled by the Al-F complexes (AlF_3, AlF_2^+, and AlF^{2+}) and hydrofluoric acid at lower pH values. When the alkalinity of the solution increased to the neutral pH range (approximately at 5), calcium fluoride ions and fluorine ions were the dominant species in the solution, and solid phases containing fluorine and calcium started precipitating, thus controlling the F retention. The literature suggests that fluorite and fluorapatite are less soluble fluoride-

containing phases that would theoretically form under neutral conditions (Street and Elwali, 1983; Elrashidi and Lindsay, 1985; El Zrelli et al., 2018). Whereas F concentration increase at strong base conditions (pH > 11) could be attributed to the precipitation of portlandite, the exceeded consumption of active (or free) calcium strongly influenced the precipitation/dissolution of fluorite. The marked shift in sulfate releasing at strong base conditions further evidenced this hypothesis (R3 in Fig.S6). The evolution of P-containing phases (Fig.6) implied that the aluminum addition has a more negligible effect on phosphorus retention, while calcium plays the dominant role. At acid conditions (pH < 5), phosphorus mainly consists of HPO_4 (PO_4^{3-}, HPO_4^{2-}, $H_2PO_4^-$, and H_3PO_4) and $CaPO_4$ ($CaPO_4^-$, $CaHPO_4$, and $CaH_2PO_4^+$) species. As leachate pH increases, calcium fluorophosphate is theoretically expected to precipitate, thereby contributing to P immobilization (Froelich, 1988; Wu et al., 2022a). Additionally, it is worthy to note that in both samples, the cumulative leached amounts of F and P were overestimated. The main reason contributing to the differences is hypothesized to be the presence of physical protection. In the view of magnitude order, the simulations are closer to the PG leaching profiles, representing the total amount of F and P that can be leached out in the CPB matrix. It again suggests that, despite the pH values being unsuitable for the hydration products, the physical solidification still plays a significant role in the reduction of F and P release, although the mechanism still needs to be uncovered.

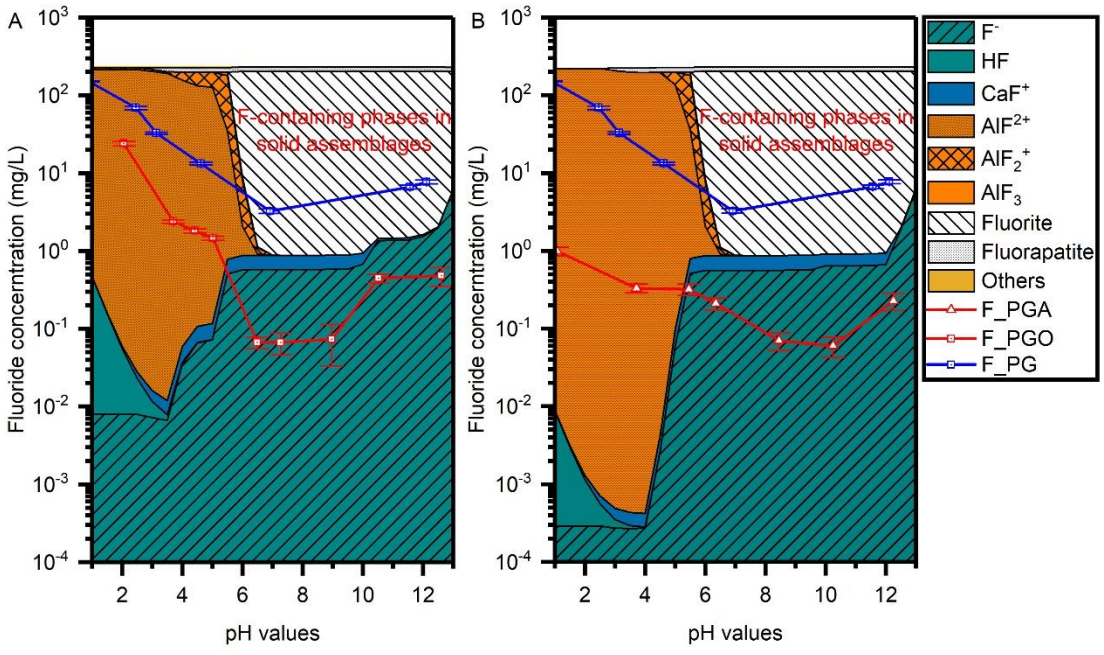

Figure.5. Fluorine leaching results from pH-dependent leaching tests and the simulated fluorine-containing phases distribution. (a) PGO samples and (b) PGA samples. The others represent the trace fluorine-containing phases (e.g., MgF^+, NaF, and SiF_6^{2-}). F_PGA, F_PGO, and F_PG mean the fluorine concentration in the leachate of PGA, PGO, and PG, respectively. The area with orange,

green, and blue marks means the fluorides in the solutions, whereas white marks indicate the fluorides present in the solid assemblages.

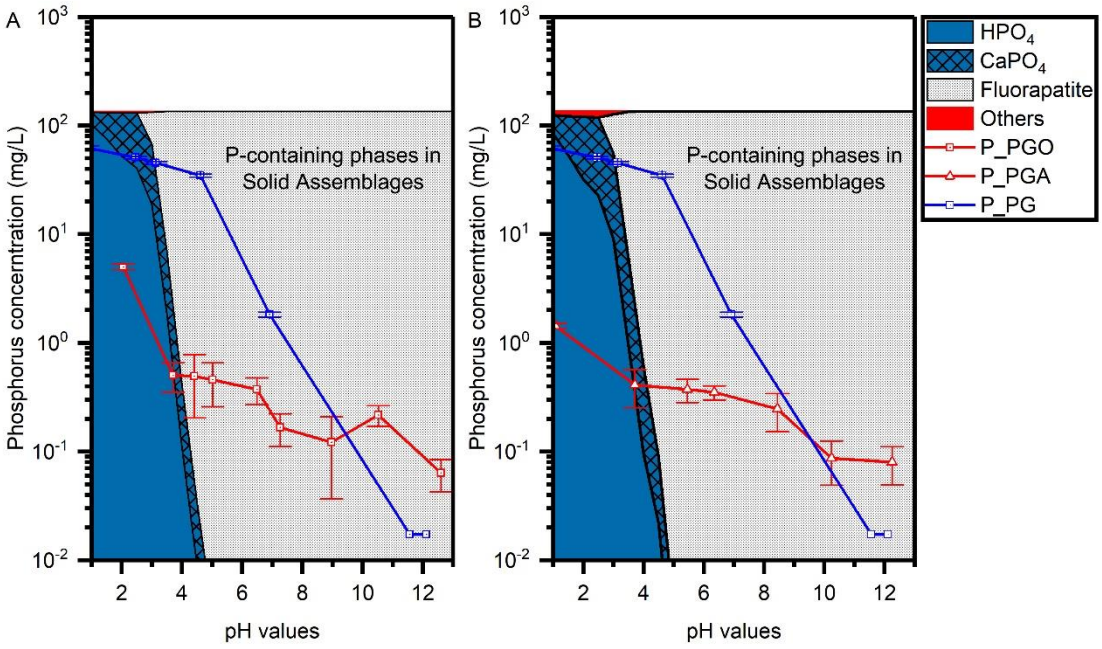

Figure.6. Phosphorus leaching results from pH-dependent leaching tests and the simulated fluorine-containing phases distribution. (a) PGO samples and (b) PGA samples. The others represent the trace fluorine-containing phases (e.g., $MgPO_4^-$, $NaHPO_4^-$, and $KHPO_4^-$), "HPO_4" is the accumulation of PO_4^{3-}, HPO_4^{2-}, $H_2PO_4^-$, and H_3PO_4, "$CaPO_4$" is the accumulation of $CaPO_4^-$, $CaHPO_4$, and $CaH_2PO_4^+$. The abbreviation P_PGA, P_PGO, and P_PG mean the phosphorus concentration in the leachate of PGA, PGO, and PG, respectively. The area with red and blue marks means the phosphates in the solutions, whereas white marks indicate the phosphates in the solid assemblages.

4. Discussion

4.1. Efficacy of γ-Al_2O_3 activation on hydration products formation and physical consequences

The direct correlation between the mineralogical phases and the consequential mechanical properties is not always evident (de Figueirêdo et al., 2020). Herein, the FO samples, with the dependent presence of F, demonstrated a persistent mechanical performance at 7 and 28 days (Fig.4) and a higher portlandite content retained after 28 days (Fig.1). This result is in good agreement with the strength and mineralogical phases evolution proposed in Krivenko et al.'s work (2019), which could be attributed to the accelerating effects of fluorine on the very early age hydration. As reported, incorporating fluoride can promote the consumption of calcium ions and accelerate the setting of Portland cement by promoting the dissolution and hydration of C_3S and C_3A at early ages (Wang et al., 2021). But the dissolved fluoride would form an

impermeable membrane covering the calcium silicate grains and retard further hydration (Krivenko et al., 2019). Therefore, no significant mechanical increment was observed in the FO samples at later ages. Moreover, from Fig.3d and Fig.S2, the homogeneous distribution of F in the Ca and Si matrix reinforces the idea that F works as an accelerator in promoting the hydration of calcium silicate. A similar observation was also reported as the fine fluorine-silicate oxide particles would generate by reactions between calcium silicate and fluoride ions (Matsuzawa et al., 2017). Interestingly, a similar hypothesis for the phosphorus retarding mechanisms, same as the formed fluorine coating film, is proposed in these studies. However, other investigations and consequent mechanisms were given as the retard primarily focuses on the first 24 hours (Boughanmi et al., 2018; Wu et al., 2022b). The presence of P in the amorphous matrix (Fig.3b) further supported the previous observations (Tan et al., 2017; Zhou et al., 2020a; Shi et al., 2021) as the retention is mainly controlled by P, Ca, and Si co-precipitation. Noteworthy, the mechanical weakening effects were also not found in the later ages compressive strength values (3 to 28 days) of the various phosphorus-containing samples prepared in the given works. The approximately identical mechanical properties of PO samples at 7 and 28 days (Fig.4) also ascertain this hypothesis. Previous works assumed that calcium phosphate (amorphous and/or crystalline precipitate) might produce and retard cement hydration (Zhang et al., 2022). However, due to the variability in mineralogy and reactivity in cementitious phases of such phosphate-binder systems, no clear and recognized conclusion was ever drawn that reveals the interaction in complex processes. Although mechanical deterioration was found in PGO samples at early ages, the 28 days strength developed significantly, which is in accordance with previous observations (Guo et al., 2012; Cao et al., 2022). This behavior can be explained by the theory of tight packing of grown crystals, but further independent examination is required to reveal the associated mechanisms.

With γ-Al_2O_3, the previous characterization evidenced the promotion of ettringite crystallization (Fig.1) and the incorporation of Al into hydration products (e.g., C-A-S-H or $Al(OH)_3$ complexes) (Fig.2), indicating that the agent has little effect on the types of crystalline hydration products but mainly on the phases' weight percentages of phases. Additionally, the promoted ettringite formation and gypsum consumption in samples containing γ-Al_2O_3 suggest that alumina addition improves sulfate retention by fixing sulfate ions in ettringite that is less soluble than gypsum. These findings can be attributed to the supersaturation of the Al^{3+} and SO_4^{2-} ions in the pore solution. Consequently, the ongoing ettringite crystallization and the high consumption of Ca^{2+} and OH^- decreased effective saturation indices for portlandite (Quennoz and Scrivener, 2013). Therefore, the portlandite is totally dissolved and works as a calcium source for ettringite formation, leading to a reduced portlandite weight percentage. As seen in Fig.1, the portlandite content is significantly lower in all specimens prepared with γ-Al_2O_3 than with respect to specimens prepared without alumina. To note, although more ettringite formation is confirmed, the 7 days mechanical properties of all the samples with γ-Al_2O_3 are still far away from satisfactory. But with the continuous hydration, the samples

demonstrated an apparent potentiality for achieving greater mechanical properties at 28 days of curing. Some authors argued that the improvement of mechanical properties could derive from the formation and accumulation of excessive amounts of the more dense structure of hydrated products (e.g., C-(A)-S-H and CAH), which tends to increase the gel/space ratio as well as bulk density (Nazari and Riahi, 2011; Heikal et al., 2015). Therefore, in the presence of γ-Al_2O_3, although more significant ettringite formation is observed, it is less likely to promote early strength enhancement. But the dissolved Al ions in the solution may positively correlate with strength and structure optimization at later ages.

4.2. The solidification/stabilization of fluorine and phosphorus with γ-Al_2O_3 activation

Since the release of pollutants in high concentration for the solidified assemblages, especially under acid conditions, is still concerned, both solidified/stabilized systems have the potential for suffering performance loss or failure (Li et al., 2017). Moreover, the effect of pollutants within PG on the mineralogy and the reactivity of industrial binders is much more complex than what can be expected from laboratory trials. Herein, morphological and mineralogical tests were carried out to assess the main retention mechanisms. As shown in the combined experimental and modeling inspection (Fig.3, S3, and S4), the dominant controlling phases of P and F are positively correlated to Ca and Si, which are the typical elements of the OPC main components. It is believed that this correlation, which is also reported in previous studies, is the result of the interplay of multiple mechanisms, such as the formation of calcium fluorine/phosphate precipitates (Recillas et al., 2012; Kang et al., 2019), adsorption and ion exchange of ettringite (Wei et al., 2021), and adsorption and physical encapsulation on C-S-H (Shi et al., 2021). Further, the Al is found to be highly correlated with pollutants immobilization (Fig.3g). The retention is presumably in the way of adsorption of the amorphous phase C-A-S-H and/or coexisting of aluminum hydroxyfluoride products (Lisbona et al., 2013; Yang et al., 2020), of which the anions can replace OH^- to maintain the charge balance or electroneutrality of the system. To ensure that the stabilized products can effectively retain pollutants in acidic conditions, the fluorine and phosphorus concentration in the leachate of PGO and PGA was determined after leaching tests at pH < 4 and geochemical modeling was carried out based on the abovementioned experimental conditions. In general, compared to raw PG leaching, the fluorine and phosphorus retention is drastically strengthened in stabilized systems both using OPC (PGO) and OPC with γ-Al_2O_3 (PGA) (Fig.5 and 6).

To note, the PGA samples deliver remarkable fluorine retention efficiency resulting in fluoride concentration in the leachate 1.0 mg/L (pH 1.07) compared to PGO and PG samples, with 24.1 mg/L, pH 2.05 and 125.0 mg/L, pH 1.01, respectively. The chemical protection mechanism underlying the promoted performance is interpreted on the base of geochemical modeling data. It is revealed that, in the individual aspect of thermodynamic equilibrium, γ-Al_2O_3 would not modify the possible retention phases at neutral

and alkaline pH conditions, which is ascribed to the precipitation of calcium fluoride/phosphate (fluorite and fluorapatite). This emphasizes that the calcium-phosphate-fluoride complexes presented in Fig.3i could be a possible coexisting phase in PG-binder systems, whether they originated from PG or formed after the mixing. In addition, greater fluoride retention in the PGA samples at acid conditions (pH < 5) is experimentally observed, which is theoretically attributed to the formation of the aluminum fluoride complexes (see the simulations presented in Fig.5). This highlights the importance of aluminum in controlling fluorine leaching. Recent works have reasonably assumed that the existence of secondary precipitation phases (insoluble AlF complex) plays an important role in driving fluorine leaching (Stone et al., 2016; Zhou et al., 2020b). In comparison, phosphate leaching could be dominated by the crystallization and dissolution of calcium phosphate precipitates (fluorapatite), as the estimated high formation of phosphate precipitates (Fig.6) rationalizes the low leaching efficiency. Noteworthy, apart from the formation of complexes, the deviation between the experimental and theoretical results also could be partly explained by physical protection. The hydration products can not only provide the strength of solidified matrices but also can stabilize pollutants through physical encapsulation and adsorption (Baur and Johnson, 2003; Halim et al., 2005). Especially for the phosphate leaching, although the simulations reveal that the aluminum is less relevant to the phosphate phase formation, a drop of phosphate release was observed. Therefore, the strengthened performance in pollutants retention performance of PGA samples could also take advantage of their stronger mechanical properties, which contribute to greater physical protection. Furthermore, despite not being observed in the characterization experiments, the possible presence of $Al(OH)_3$ in the PGA systems may benefit fluoride retention by means of Al-F complexation and adsorption (Gong et al., 2012). In short, the findings here demonstrate that the addition of γ-Al_2O_3 enhances both chemical fixation and physical encapsulation, resulting in the drop in fluoride and phosphate leaching.

4.3. The feasibility of γ-Al_2O_3 application: CO_2 neutrality and cost analysis

The assumed carbon footprint of PGO and PGA samples shows that the γ-Al_2O_3 incorporation reduced the CO_2 emission by 35%. The investigation demonstrates that the majority of CO_2 emissions of CPB are related to OPC production (direct emissions due to the calcination of limestone and indirect emissions because of the electricity used for heating and grinding) (Cao et al., 2021; Ravikumar et al., 2021). In comparison, the key constituent in γ-Al_2O_3 production is kaolin (main constituent in kaolin is kaolinite mineral: $Al_2O_3 \cdot 2SiO_2 \cdot 2H_2O$) (Hosseini et al., 2011). The calcination of it would not lead to direct CO_2 emission, which amounts to approximately 60% for OPC production. Further, it is evident that the highest calcination temperature of kaolinite (900 °C) is much lower than that of OPC (1450 °C), indicating a lower energy consumption. Therefore, a greater percentage of renewable energies can be used to reach this relatively low calcination temperature (Cao et al., 2021) since the ratio of ordinary grid electricity to

renewable electricity used in this work is 2.33. Hence, additional CO_2 profits would generate with the application of cleaner energy. The total costs of CPB samples were calculated based on the local market price of the introduced agents, and the PG stock expenses were assumed based on the regular landfill disposal fee and hazardous solid waste tax. Nevertheless, we realize that γ-Al_2O_3 incorporation inevitably increased the total expense due to its high cost (Table.2), but the treatment of PGA samples is still more profitable than the PG stock. More importantly, compared to the carbon price of 0.455 CNY/t in E.U. (Chen et al., 2022b), the price in P.R.C (0.100 CNY/t) still has a tremendous upward movement in the coming years (Wang et al., 2019b; Chen et al., 2022a). To note, based on the Paris agreement (World Bank., 2021), the carbon price would rise further to achieve the 1.5 °C goals. Meanwhile, aside from the existing industrial-scale γ-Al_2O_3 production initiatives, scholars (Osman et al., 2017) attempted to synthesize γ-Al_2O_3 from the aluminum foil waste, which would benefit its profitable price. But additional calculations would need to be performed to investigate the economic feasibility and carbon neutrality implementation using the alternatives.

Table.2. Assumed cost and carbon footprint associated with PGO and PGA samples preparation.

Samples	PGO	PGA	PG stock
CO_2 Emission (kg CO_2/t)	855.74	555.74	-
Preparation cost[1] (CNY/t)[2]	526.15	1044.15	2015.00
CO_2 tax (CNY/t)	85.57/389.36[3]	69.45/315.98	-
Total expense (CNY/t)	611.72/915.51	1113.60/1360.13	2015.00

Note: [1] The preparation cost is based on the mix proportion presented in Table.1; [2] CNY/t represents the cost for recycling 1 tonne of PG; [3] A/B means the CO_2 tax from the P.R.C. standard (A, 0.100 CNY/kg CO_2) and the E.U. standard (B, 0.455 CNY/kg CO_2).

5. Conclusions

In the present study, γ-Al_2O_3 was explored as an innovative potential agent for the in-situ remediation of PG using the CPB technique. Overall results demonstrated that the incorporation of **γ-Al_2O_3** promoted the ettringite precipitation and induced aluminum-containing amorphous phase formation. In the view of the engineering application, the compressive strength of PGA achieved 1.9 MPa, fulfilling the strength requirement of the CPB mixtures. Evidence from elemental mapping implies that most of the F and P retention is related to the precipitation of Ca-Si-containing phases. Although the leaching tests demonstrate that the solubility of precipitated F and P components is very pH-dependent, the PGA samples exhibit promising F and P immobilization results within the studied pH range. The geochemical modeling provides qualitative support for determining the role of hardly detectable F- and P-containing phases and describing the amphoteric leaching profiles. The deviation between the experimental measurements and simulation results indicates that the physical incapsulation/solidification has a role in governing the retention behavior in addition to the individual impact of chemical precipitation/stabilization. The assumed carbon footprint

confirmed that for recycling 1 tonne of PG, the use of γ-Al_2O_3 to partially replace cement could significantly reduce the total CO_2 emissions by approximately 35%. Therefore, the utilization of the proposed novel binding system is potentially viable to offer a practical, carbon-neutral, and profitable application for sustainable recycling of PG waste, especially with the concern for implementing additional carbon neutrality policies to limit global warming. In future works, the exploration of inexpensive and low-carbon alternative Al source agents could be further investigated. Meanwhile, the emphasis on the durability of immobilized products should be precisely validated before large-scale applications.

Acknowledgments

This study was conducted with financial support from the PRIN project “Mineral reactivity, a key to understand large-scale processes: from rock-forming environments to solid waste recovering/lithification” (No.2017L83S77) and a scholarship granted by the China Scholarship Council (No.CSC201906370062).

Author contributions

Yikai Liu: data curation, methodology, software, visualization, writing—original draft

Qiusong Chen: funding acquisition, supervision, writing—original draft

Maria Chiara Dalconi: formal analysis and writing—original draft

Simone Molinari: formal analysis and writing—original draft

Luca Valentini: formal analysis and writing—original draft

Yunming Wang: funding acquisition and resources

Shiyuan Sun: resources and investigation

Peishen Wang: investigation

Gilberto Artioli: funding acquisition, supervision, and methodology.

All the authors discussed the data and agreed on their interpretations. All the co-authors contributed to the final polishing of the manuscript.

Reference

Akoteyon, I., Omotayo, A., Soladoye, O., Akoteyon, I.S., Omotayo, A.O., and Olaoye, H.O., 2011, Determination of water quality index and suitability of Urban River for municipal water supply in Lagos-Nigeria Effects of Wage Labour on Rural Poverty View project Assessment of the quality and sustainability of groundwater in Lagos View project Determination of Water Quality Index and Suitability of Urban River for Municipal Water Supply in Lagos-Nigeria: European Journal of Scientific Research, v. 54, p. 263–271, http://www.eurojournals.com/ejsr.htm (accessed April 2022).

Amine Laadila, M., LeBihan, Y., Caron, R.F., and Vaneeckhaute, C., 2021, Construction, renovation and demolition (CRD) wastes contaminated by gypsum residues: Characterization, treatment and valorization: Waste Management, doi:10.1016/j.wasman.2020.11.031.

Appelo, C.A.J., Parkhurst, D.L., and Post, V.E.A., 2014, Equations for calculating hydrogeochemical reactions of minerals and gases such as CO2 at high pressures and temperatures: Geochimica et Cosmochimica Acta, v. 125, p. 49–67, doi:10.1016/J.GCA.2013.10.003.

Bank., W., 2021, State and Trends of Carbon Pricing 2021.:, https://openknowledge.worldbank.org/handle/10986/35620.

Baur, I., and Johnson, C.A., 2003, Sorption of selenite and selenate to cement minerals: Environmental Science and Technology, v. 37, p. 3442–3447, doi:10.1021/es020148d.

Belem, T., Benzaazoua, M., and Bussière, B., 2000, Mechanical behaviour of cemented paste backfill: Proceedings of 53rd Candadian Geotechnical Conference,.

Bisone, S., Gautier, M., Chatain, V., and Blanc, D., 2017, Spatial distribution and leaching behavior of pollutants from phosphogypsum stocked in a gypstack: Geochemical characterization and modeling: Journal of Environmental Management, doi:10.1016/j.jenvman.2017.02.055.

Boughanmi, S., Labidi, I., Megriche, A., Tiss, H., and Nonat, A., 2018, Does phosphorus affect the industrial Portland cement reactivity? Construction and Building Materials, v. 188, p. 599–606, doi:10.1016/j.conbuildmat.2018.08.060.

Calderón-Morales, B.R.S., García-Martínez, A., Pineda, P., and García-Tenório, R., 2021, Valorization of phosphogypsum in cement-based materials: Limits and potential in eco-efficient construction: Journal of Building Engineering, doi:10.1016/j.jobe.2021.102506.

Cao, Y., Wang, Y., Zhang, Z., Ma, Y., and Wang, H., 2021, Recent progress of utilization of activated kaolinitic clay in cementitious construction materials: Composites Part B: Engineering, v. 211, p. 108636, doi:10.1016/j.compositesb.2021.108636.

Cao, W., Yi, W., Peng, J., Li, G., and Yin, S., 2022, Preparation of anhydrite from phosphogypsum: Influence of phosphorus and fluorine impurities on the performances: Construction and Building Materials, v. 318, p. 126021, doi:10.1016/j.conbuildmat.2021.126021.

Chang, N. Bin, Qi, C., and Yang, Y.J., 2012, Optimal expansion of a drinking water infrastructure system with respect to carbon footprint, cost-effectiveness and water demand: Journal of Environmental Management, v. 110, p. 194–206, doi:10.1016/j.jenvman.2012.06.004.

Chen, L., Wang, L., Zhang, Y., Ruan, S., Mechtcherine, V., and Tsang, D.C.W., 2022a, Roles of biochar in cement-based stabilization/solidification of municipal solid waste incineration fly ash: Chemical Engineering Journal, v. 430, p. 132972, doi:10.1016/J.CEJ.2021.132972.

Chen, Q., Zhang, Q., Fourie, A., and Xin, C., 2017, Utilization of phosphogypsum and phosphate tailings for cemented paste backfill: Journal of Environmental Management, v. 201, p. 19–27, doi:10.1016/j.jenvman.2017.06.027.

Chen, Q., Zhang, Q., Qi, C., Fourie, A., and Xiao, C., 2018, Recycling phosphogypsum and construction demolition waste for cemented paste backfill and its environmental impact: Journal of Cleaner Production, v. 186, p. 418–429, doi:10.1016/j.jclepro.2018.03.131.

Chen, L., Zhang, Y., Wang, L., Ruan, S., Chen, J., Li, H., Yang, J., Mechtcherine, V., and Tsang, D.C.W., 2022b, Biochar-augmented carbon-negative concrete: Chemical Engineering Journal, v. 431, p. 133946, doi:10.1016/j.cej.2021.133946.

Chen, X., Zheng, L., Dong, X., Jiang, C., and Wei, X., 2020, Sources and mixing of sulfate contamination in the water environment of a typical coal mining city, China: evidence from stable isotope characteristics: Environmental Geochemistry and Health, doi:10.1007/s10653-020-00525-2.

Chernysh, Y., Yakhnenko, O., Chubur, V., and Roubík, H., 2021, Phosphogypsum recycling: A review of environmental issues, current trends, and prospects: Applied Sciences (Switzerland), doi:10.3390/app11041575.

Doebelin, N., and Kleeberg, R., 2015, Profex: a graphical user interface for the Rietveld refinement program BGMN: urn:issn:1600-5767, v. 48, p. 1573–1580, doi:10.1107/S1600576715014685.

Elrashidi, M.A., and Lindsay, W.L., 1985, Solubility Relationships of Fluorine Minerals in Soils: Soil Science Society of America Journal, doi:10.2136/sssaj1985.03615995004900050012x.

Fall, M., Belem, T., Samb, S., and Benzaazoua, M., 2007, Experimental characterization of the stress-strain behaviour of cemented paste backfill in compression: Journal of Materials Science, doi:10.1007/s10853-006-0403-2.

Feng, H., Zhu, P., Guo, A., Cheng, Z., Zhao, X., and Gao, D., 2022, Assessment of the mechanical properties and water stability of nano-Al2O3 modified high ductility magnesium potassium phosphate cement-based composites: Materials Today Communications, v. 30, p. 103179, doi:10.1016/J.MTCOMM.2022.103179.

de Figueirêdo, J.M.R., da Costa, F.P., Fernandes, J.V., Rodrigues, A.M., Neves, G. de A., Menezes, R.R., and Santana, L.N. de L., 2020, Development of Scheelite Tailings-Based Ceramic Formulations with the Potential to Manufacture Porcelain Tiles, Semi-Stoneware and Stoneware: Materials 2020, Vol. 13, Page 5122, v. 13, p. 5122, doi:10.3390/MA13225122.

Froelich, P.N., 1988, Kinetic control of dissolved phosphate in natural rivers and estuaries: A primer on the phosphate buffer mechanism: Limnology and Oceanography, doi:10.4319/lo.1988.33.4part2.0649.

Garcia-Lodeiro, I., Palomo, A., Fernández-Jiménez, A., and MacPhee, D.E., 2011, Compatibility studies between N-A-S-H and C-A-S-H gels. Study in the ternary diagram Na2O-CaO-Al2O3-SiO 2-H2O: Cement and Concrete Research, v. 41, p. 923–931, doi:10.1016/j.cemconres.2011.05.006.

Gong, W.X., Qu, J.H., Liu, R.P., and Lan, H.C., 2012, Effect of aluminum fluoride complexation on fluoride removal by coagulation: Colloids and Surfaces A: Physicochemical and Engineering Aspects, v. 395, p. 88–93, doi:10.1016/J.COLSURFA.2011.12.010.

Gu, K., Chen, B., and Pan, Y., 2020, Utilization of untreated-phosphogypsum as filling and binding material in preparing grouting materials: Construction and Building Materials, doi:10.1016/j.conbuildmat.2020.120749.

Guo, C., Zhu, J., Zhou, W., Sun, Z., and Chen, W., 2012, Effect of phosphorus and fluorine on hydration process of tricalcium silicate and tricalcium aluminate: Journal Wuhan University of Technology, Materials Science Edition, v. 27, p. 333–336, doi:10.1007/s11595-012-0462-y.

Gustafsson, J.P., 2011, Visual MINTEQ 3.1 user guide: Department of Land and Water Recources, Stockholm, Sweden, p. 1–73.

Hafshejani, L.D., Tangsir, S., Daneshvar, E., Maljanen, M., Lähde, A., Jokiniemi, J., Naushad, M., and Bhatnagar, A., 2017, Optimization of fluoride removal from aqueous solution by Al2O3 nanoparticles: Journal of Molecular Liquids, doi:10.1016/j.molliq.2017.04.104.

Halim, C.E., Short, S.A., Scott, J.A., Amal, R., and Low, G., 2005, Modelling the leaching of Pb, Cd, As, and Cr from cementitious waste using PHREEQC: Journal of Hazardous Materials, v. 125, p. 45–61, doi:10.1016/j.jhazmat.2005.05.046.

Heikal, M., Ismail, M.N., and Ibrahim, N.S., 2015, Physico-mechanical, microstructure characteristics and

fire resistance of cement pastes containing Al2O3 nano-particles: Construction and Building Materials, v. 91, p. 232–242, doi:10.1016/j.conbuildmat.2015.05.036.

Higl, J., Hinder, D., Rathgeber, C., Ramming, B., and Lindén, M., 2021, Detailed in situ ATR-FTIR spectroscopy study of the early stages of C-S-H formation during hydration of monoclinic C3S: Cement and Concrete Research, v. 142, p. 106367, doi:10.1016/J.CEMCONRES.2021.106367.

Hosseini, S.A., Niaei, A., and Salari, D., 2011, Production of γ-Al2O3 from Kaolin: Open Journal of Physical Chemistry, v. 01, p. 23–27, doi:10.4236/ojpc.2011.12004.

Hughes, T.L., Methven, C.M., Jones, T.G.J., Pelham, S.E., Fletcher, P., and Hall, C., 1995, Determining cement composition by Fourier transform infrared spectroscopy: Advanced Cement Based Materials, v. 2, p. 91–104, doi:10.1016/1065-7355(94)00031-X.

Jing, Z., Fan, X., Zhou, L., Fan, J., Zhang, Y., Pan, X., and Ishida, E.H., 2013, Hydrothermal solidification behavior of municipal solid waste incineration bottom ash without any additives: Waste Management, doi:10.1016/j.wasman.2013.01.038.

Kang, J., Gou, X., Hu, Y., Sun, W., Liu, R., Gao, Z., and Guan, Q., 2019, Efficient utilisation of flue gas desulfurization gypsum as a potential material for fluoride removal: Science of the Total Environment, doi:10.1016/j.scitotenv.2018.08.416.

Kapeluszna, E., Kotwica, Ł., Różycka, A., and Gołek, Ł., 2017, Incorporation of Al in C-A-S-H gels with various Ca/Si and Al/Si ratio: Microstructural and structural characteristics with DTA/TG, XRD, FTIR and TEM analysis: Construction and Building Materials, v. 155, p. 643–653, doi:10.1016/j.conbuildmat.2017.08.091.

Krivenko, P., Vaičiukynienė, D., Kantautas, A., Vaitkevičius, V., and Šerelis, E., 2019, Effect of AlF3 production waste on the processes of hydration and hardening of the alkali-activated Portland cement with sodium silicate hydrate: Journal of Thermal Analysis and Calorimetry, v. 138, p. 879–887, doi:10.1007/s10973-019-08086-y.

Kulik, D.A., Wagner, T., Dmytrieva, S. V., Kosakowski, G., Hingerl, F.F., Chudnenko, K. V., and Berner, U.R., 2013, GEM-Selektor geochemical modeling package: Revised algorithm and GEMS3K numerical kernel for coupled simulation codes: Computational Geosciences, doi:10.1007/s10596-012-9310-6.

Li, X., Du, J., Gao, L., He, S., Gan, L., Sun, C., and Shi, Y., 2017, Immobilization of phosphogypsum for cemented paste backfill and its environmental effect: Journal of Cleaner Production, v. 156, p. 137–146, doi:10.1016/j.jclepro.2017.04.046.

Lisbona, D.F., Somerfield, C., and Steel, K.M., 2013, Leaching of spent pot-lining with aluminium nitrate and nitric acid: Effect of reaction conditions and thermodynamic modelling of solution speciation: Hydrometallurgy, v. 134–135, p. 132–143, doi:10.1016/j.hydromet.2013.02.011.

Liu, Y., Chen, Q., Dalconi, M.C., Molinari, S., Valentini, L., Wang, Y., Sun, S., Wang, P., and Artioli, G., 2022, Retention of phosphorus and fluorine in phosphogypsum for cemented paste backfill: Experimental and numerical simulation studies: Environmental Research, p. 113775, doi:10.1016/J.ENVRES.2022.113775.

Liu, H., Zhang, J., Li, B., Zhou, N., Li, D., Zhang, L., and Xiao, X., 2021, Long term leaching behavior of arsenic from cemented paste backfill made of construction and demolition waste: Experimental and numerical simulation studies: Journal of Hazardous Materials, doi:10.1016/j.jhazmat.2021.125813.

Lothenbach, B., Kulik, D.A., Matschei, T., Balonis, M., Baquerizo, L., Dilnesa, B., Miron, G.D., and Myers, R.J., 2019, Cemdata18: A chemical thermodynamic database for hydrated Portland cements and alkali-activated materials: Cement and Concrete Research, doi:10.1016/j.cemconres.2018.04.018.

Matsuzawa, K., Atarashi, D., Miyauchi, M., and Sakai, E., 2017, Interactions between fluoride ions and cement paste containing superplasticizer: Cement and Concrete Research, v. 91, p. 33–38, doi:10.1016/j.cemconres.2016.10.006.

McQueen, N., Kelemen, P., Dipple, G., Renforth, P., and Wilcox, J., 2020, Ambient weathering of magnesium oxide for CO2 removal from air: Nature Communications, v. 11, p. 1–10, doi:10.1038/s41467-020-16510-3.

Meskini, S., Samdi, A., Ejjaouani, H., and Remmal, T., 2021, Valorization of phosphogypsum as a road material: Stabilizing effect of fly ash and lime additives on strength and durability: Journal of Cleaner Production, doi:10.1016/j.jclepro.2021.129161.

Min, C., Shi, Y., and Liu, Z., 2021, Properties of cemented phosphogypsum (PG) backfill in case of partially substitution of composite Portland cement by ground granulated blast furnace slag: Construction and Building Materials, doi:10.1016/j.conbuildmat.2021.124786.

Moharami, S., and Jalali, M., 2014, Effect of TiO2, Al2O3, and Fe3O4 nanoparticles on phosphorus removal from aqueous solution: Environmental Progress and Sustainable Energy, doi:10.1002/ep.11917.

Nazari, A., and Riahi, S., 2011, Improvement compressive strength of concrete in different curing media by Al2O3 nanoparticles: Materials Science and Engineering A, v. 528, p. 1183–1191, doi:10.1016/j.msea.2010.09.098.

Ölmez, H., and Yilmaz, V.T., 1988, Infrared study on the refinement of phosphogypsum for cements: Cement and Concrete Research, doi:10.1016/0008-8846(88)90079-8.

Osman, A.I., Abu-Dahrieh, J.K., McLaren, M., Laffir, F., Nockemann, P., and Rooney, D., 2017, A Facile Green Synthetic Route for the Preparation of Highly Active γ-Al2O3 from Aluminum Foil Waste: Scientific Reports, v. 7, p. 1–11, doi:10.1038/s41598-017-03839-x.

Parkhurst, D.L., and Appelo, C.A.J., 2013, Description of Input and Examples for PHREEQC Version 3 — A Computer Program for Speciation , Batch-Reaction , One-Dimensional Transport , and Inverse Geochemical Calculations.: U.S. Geological Survey Techniques and Methods, book 6, chapter A43,.

Qi, C., and Fourie, A., 2019, Cemented paste backfill for mineral tailings management: Review and future perspectives: Minerals Engineering, doi:10.1016/j.mineng.2019.106025.

Qiu, J., Guo, Z., Yang, L., Jiang, H., and Zhao, Y., 2020, Effect of tailings fineness on flow, strength, ultrasonic and microstructure characteristics of cemented paste backfill: Construction and Building Materials, v. 263, p. 120645, doi:10.1016/j.conbuildmat.2020.120645.

Quennoz, A., and Scrivener, K.L., 2013, Interactions between alite and C3A-gypsum hydrations in model cements: Cement and Concrete Research, v. 44, p. 46–54, doi:10.1016/j.cemconres.2012.10.018.

Ravikumar, D., Zhang, D., Keoleian, G., Miller, S., Sick, V., and Li, V., 2021, Carbon dioxide utilization in concrete curing or mixing might not produce a net climate benefit: Nature Communications, v. 12, p. 1–13, doi:10.1038/s41467-021-21148-w.

Recillas, S., Rodríguez-Lugo, V., Montero, M.L., Viquez-Cano, S., Hernandez, L., and Castaño, V.M., 2012, Studies on the precipitation behavior of calcium phosphate solutions: Journal of Ceramic Processing Research,.

Renforth, P., Jenkins, B.G., and Kruger, T., 2013, Engineering challenges of ocean liming: Energy, v. 60, p. 442–452, doi:10.1016/j.energy.2013.08.006.

Saedi, A., Jamshidi-Zanjani, A., and Darban, A.K., 2020, A review on different methods of activating tailings to improve their cementitious property as cemented paste and reusability: Journal of Environmental Management, v. 270, p. 110881, doi:10.1016/j.jenvman.2020.110881.

Šavija, B., and Luković, M., 2016, Carbonation of cement paste: Understanding, challenges, and opportunities: Construction and Building Materials, doi:10.1016/j.conbuildmat.2016.04.138.

Shi, Y., Cheng, L., Tao, M., Tong, S. Sen, Yao, X., and Liu, Y., 2021, Using modified quartz sand for phosphate pollution control in cemented phosphogypsum (PG) backfill: Journal of Cleaner Production, doi:10.1016/j.jclepro.2020.124652.

Shu, J., Chen, M., Wu, H., Li, B., Wang, B., Li, B., Liu, R., and Liu, Z., 2019, An innovative method for synergistic stabilization/solidification of Mn2+, NH4+-N, PO43− and F− in electrolytic manganese residue and phosphogypsum: Journal of Hazardous Materials, doi:10.1016/j.jhazmat.2019.05.017.

Silva, L.F.O., Oliveira, M.L.S., Crissien, T.J., Santosh, M., Bolivar, J., Shao, L., Dotto, G.L., Gasparotto, J., and Schindler, M., 2022, A review on the environmental impact of phosphogypsum and potential health impacts through the release of nanoparticles: Chemosphere, doi:10.1016/j.chemosphere.2021.131513.

Singh, M., 2003, Effect of phosphatic and fluoride impurities of phosphogypsum on the properties of selenite plaster: Cement and Concrete Research, doi:10.1016/S0008-8846(03)00068-1.

Smaoui-Jardak, M., Kriaa, W., Maalej, M., Zouari, M., Kamoun, L., Trabelsi, W., Ben Abdallah, F., and Elloumi, N., 2017, Effect of the phosphogypsum amendment of saline and agricultural soils on growth, productivity and antioxidant enzyme activities of tomato (Solanum lycopersicum L.): Ecotoxicology, doi:10.1007/s10646-017-1836-x.

Sousa, V., and Bogas, J.A., 2021, Comparison of energy consumption and carbon emissions from clinker and recycled cement production: Journal of Cleaner Production, v. 306, doi:10.1016/j.jclepro.2021.127277.

Stone, K., Bandara, A.M.T.S., Senanayake, G., and Jayasekera, S., 2016, Processing of rare earth phosphate concentrates: A comparative study of pre-leaching with perchloric, hydrochloric, nitric and phosphoric acids and deportment of minor/major elements: Hydrometallurgy, v. 163, p. 137–147, doi:10.1016/j.hydromet.2016.03.014.

Street, J.J., and Elwali, A.M.O., 1983, Fluorite Solubility in Limed Acid Sandy Soils: Soil Science Society of America Journal, doi:10.2136/sssaj1983.03615995004700030017x.

Tan, H., Zou, F., Liu, M., Ma, B., Guo, Y., and Jian, S., 2017, Effect of the Adsorbing Behavior of Phosphate Retarders on Hydration of Cement Paste: Journal of Materials in Civil Engineering, doi:10.1061/(asce)mt.1943-5533.0001929.

Trezza, M.A., and Lavat, A.E., 2001, Analysis of the system 3CaO·Al2O3-CaSO4· 2H2O-CaCO3-H2O by FT-IR spectroscopy: Cement and Concrete Research, v. 31, p. 869–872, doi:10.1016/S0008-8846(01)00502-6.

Valero, M.C., Raybaud, P., and Sautet, P., 2006, Influence of the hydroxylation of γ-Al2O3 surfaces on the stability and diffusion of single Pd atoms: A DFT study: Journal of Physical Chemistry B, doi:10.1021/jp0554240.

Vizcaíno-Andrés, L.M., Sánchez-Berriel, S., Damas-Carrera, S., Pérez-Hernández, A., Scrivener, K.L., and Martirena-Hernández, J.F., 2015, Industrial trial to produce a low clinker, low carbon cement: Materiales de Construccion, v. 65, p. e045, doi:10.3989/mc.2015.00614.

Wang, X., Ni, W., Li, J., Zhang, S., Hitch, M., and Pascual, R., 2019a, Carbonation of steel slag and gypsum for building materials and associated reaction mechanisms: Cement and Concrete Research, v. 125, p. 105893, doi:10.1016/j.cemconres.2019.105893.

Wang, Y., Shi, C., Ma, Y., Xiao, Y., and Liu, Y., 2021, Accelerators for shotcrete – Chemical composition and their effects on hydration, microstructure and properties of cement-based materials: Construction and Building Materials, v. 281, p. 122557, doi:10.1016/j.conbuildmat.2021.122557.

Wang, C., Zhang, L., Zhou, P., Chang, Y., Zhou, D., Pang, M., and Yin, H., 2019b, Assessing the environmental externalities for biomass- and coal-fired electricity generation in China: A supply chain perspective: Journal of Environmental Management, v. 246, p. 758–767, doi:10.1016/j.jenvman.2019.06.047.

Wei, J., Gu, Y., Lv, H., and Wu, X., 2021, A zero-emission method for recycling phosphogypsum using Na2SO4 electrolysis: Preliminary study: Separation and Purification Technology, doi:10.1016/j.seppur.2020.118168.

Wu, F., Liu, S., Qu, G., Chen, B., Zhao, C., Liu, L., Li, J., and Ren, Y., 2022a, Highly targeted solidification behavior of hazardous components in phosphogypsum: Chemical Engineering Journal Advances, v. 9, p. 100227, doi:10.1016/J.CEJA.2021.100227.

Wu, S., Yao, X., Yao, Y., Ren, C., Wu, C., Zhang, C., and Wang, W., 2022b, Recycling phosphogypsum as the sole calcium oxide source in calcium sulfoaluminate cement production and solidification of phosphorus: Science of The Total Environment, v. 808, p. 152118, doi:10.1016/j.scitotenv.2021.152118.

Yang, Z., Sui, S., Wang, L., Feng, T., Gao, Y., Mu, S., Tang, L., and Jiang, J., 2020, Improving the chloride binding capacity of cement paste by adding nano-Al2O3: The cases of blended cement pastes: Construction and Building Materials, doi:10.1016/j.conbuildmat.2019.117219.

Yao, H., and Zang, C., 2021, The spatiotemporal characteristics of electrical energy supply-demand and the green economy outlook of Guangdong Province, China: Energy, v. 214, p. 118891, doi:10.1016/j.energy.2020.118891.

Zhang, T., Ma, B., Tan, H., Qi, H., and Shi, T., 2022, Effect of sodium carbonate and sodium phosphate on hydration of cement paste: Journal of Building Engineering, v. 45, p. 103577,

doi:10.1016/J.JOBE.2021.103577.

Zhou, S., Li, X., Zhou, Y., Min, C., and Shi, Y., 2020a, Effect of phosphorus on the properties of phosphogypsum-based cemented backfill: Journal of Hazardous Materials, doi:10.1016/j.jhazmat.2020.122993.

Zhou, J., Zhao, J., Yang, F., Wang, T., Du, F., Qin, Y., Ma, J., Wu, Z., and Wang, C., 2020b, Leaching kinetics of potassium and aluminum from phosphorus-potassium associated ore in HCl-CaF2 system: Separation and Purification Technology, v. 253, p. 117528, doi:10.1016/j.seppur.2020.117528.

Zhou, J., Zheng, K., Liu, Z., and He, F., 2019, Chemical effect of nano-alumina on early-age hydration of Portland cement: Cement and Concrete Research, doi:10.1016/j.cemconres.2018.11.007.

Zhu, X., and Jin, Q., 2021, Comparison of Three Emerging Dross Recovery Processes in China's Aluminum Industry from the Perspective of Life Cycle Assessment: ACS Sustainable Chemistry and Engineering, v. 9, p. 6776–6787, doi:10.1021/acssuschemeng.1c00960.

El Zrelli, R. et al., 2018, Characterization of phosphate rock and phosphogypsum from Gabes phosphate fertilizer factories (SE Tunisia): high mining potential and implications for environmental protection: Environmental Science and Pollution Research, v. 25, p. 14690–14702, doi:10.1007/s11356-018-1648-4.

Supporting information for Chapter 5

Enhancing the sustainable immobilization of phosphogypsum by cemented paste backfill with the activation of γ-Al_2O_3

Yikai Liu[1]; Qiusong Chen[2, 3]; Maria Chiara Dalconi[1]; Simone Molinari[1]; Luca Valentini[1]; Yunmin Wang[2,3]; Shiyuan Sun[3]; Peishen Wang[3]; Gilberto Artioli[1]

[1] *Department of Geosciences and CIRCe Centre, University of Padua, via G. Gradenigo 6, 35129, Padua, Italy*

[2] *Sinosteel Maanshan General Institute of Mining Research Co., Ltd., Maanshan, 24300, China;*

[3] *School of Resources and Safety Engineering, Central South University, Lushan South Road 932, 410083, Hunan, China*

Table.S1. XRD instruments settings

Labels	**Parameters**
Equipment	Bruker D8 ADVANCE
Radiation source	Copper, Ni filtered
Detector and geometry	LYNXEYE XE-T, Bragg-Brentano
Soller Slits and divergence Slit	2.5 and 0.20
Antiair scatter degree (Å)	2.24
Goniometer_radius	280 mm
2θ range	4 ~ 80 °
Step size	0.02 °
Time per step	28.8 s

Table.S2. Possible assignments of FTIR spectra

Wavenumber/(cm^{-1})	Possible assignments
420	bending vibration of CO_3
460	bending vibration of CO_3
602	vibration of SO_4
670	vibration of SO_4
712	vibration of CO_3
874/876	symmetric stretching vibration of C–O
1003	bending vibration of CO_3
1115	bending vibration of CO_3
1137	vibration of SO_4
1425	Asymmetric stretching of CO_3

Table.S3. Modeling parameters

Elements	Minerals	Equilibrium equitions	Log k	Initial PGO (mol/100g)[a]	Initial PGA (mol/100g)
Ca	Gypsum	$CaSO_4 \cdot 2H_2O = Ca^{2+} + SO_4^{2-} + 2H_2O$	-4.6 (1)	0.2166	0.1054
	Bassanite	$CaSO_4 \cdot 0.5H_2O = Ca^{2+} + SO_4^{2-} + 0.5H_2O$	-3.9 (1)	0.0000	0.0000
	Anhydrite	$CaSO_4 = Ca^{2+} + SO_4^{2-}$	-4.4 (1)	0.0000	0.0000
	Portlandite	$Ca(OH)_2 + 2H^+ = Ca^{2+} + 2H_2O$	22.7 (1)	0.0143	0.0000
	Calcite	$CaCO_3 = CO_3^{2-} + Ca^{2+}$	-8.5 (2)	0.0822	0.0601
	Fluorapatite	$Ca_5(PO_4)_3F + 3\ H^+ = 5\ Ca^{2+} + 3\ HPO_4^{2-} + F^-$	-25.0 (1)	0.0000	0.0000
	Hydroxyapatite	$Ca_5(PO_4)_3OH + 4H^+ = H_2O + 3\ HPO_4^{2-} + 5\ Ca^{2+}$	-3.4 (4)	0.0000	0.0000
	Whitlockite	$Ca_3(PO_4)_2 + 2H^+ = 2HPO_4^{2-} + 3\ Ca^{2+}$	-4.2 (4)	0.0022	0.0022
	Brushite	$CaHPO_4 \cdot 2H_2O = Ca^{2+} + HPO_4^{2-} + 2H_2O$	-6.6 (1)	0.0000	0.0000
	Dolomite	$CaMg(CO_3)_2 = Ca^{2+} + Mg^{2+} + CO_3^{2-}$	-17.1 (4)	0.0046	0.0084
	Fluorite	$CaF_2 = Ca^{2+} + 2\ F^-$	-10.6 (4)	0.0030	0.0060
	C-S-H	Ca2.0Si2O6.6436H1.2872:1.7542H2O + 4.0 H+ = 2.0 Ca+2 + 2 H4SiO4 + 0.3978 H2O	29.5 (3)	0.1545	0.0000
	C-A-S-H	(CaO)(Al2O3)0.15625(SiO2)1.1875:1.65625H2O + 2.9375 H+ = 0.3125 Al+3 + Ca+2 + 0.75 H2O + 1.1875 H4SiO4	16.6 (3)	0.0000	0.0944
	Ettringite	$Ca_6Al_2(SO_4)_3(OH)_{12} \cdot 26H_2O + 12H^+ = 2Al^{3+} + 3SO_4^{2-} + 6Ca^{2+} + 38H_2O$	56.7 (3)	0.0050	0.0158
				0.0000	0.0000
Others	Quartz	$SiO_2 + 2\ H_2O = H_4SiO_4$	-4.0 (4)	0.0388	0.0552
	MagnesiumF	$MgF_2 = Mg^{2+} + 2\ F^-$	-8.1 (4)	0.0000	0.0000
	SodiumF	$NaF = Na^+ + F^-$	-0.02 (4)	0.0000	0.0000
	Muscovite	$KAl_3Si_3O_{10}(OH)_2 + 10H^+ = K^+ + 3Al^{3+} + 3H_4SiO_4$	12.70 (4)	0.0054	0.0059
	Thenardite	$Na_2SO_4 = SO_4^{2-} + 2\ Na^+$	-0.3 (4)	0.0000	0.0000
	Aluminafluoride	$AlF_3 = Al^{3+} + 3F^-$	-17.2 (4)	0.0000	0.0000
	$Fe(OH)_3$ (Amorphous)	$Fe(OH)_3 + 3H^+ = Fe^{3+} + 3H_2O$	4.89 (4)	0.0000	0.0000
	$Al(OH)_3$ (Amorphous)	$Al(OH)_3 + 3H^+ = Al^{3+} + 3H_2O$	10.80 (4)	0.0000	0.4046

Notes: [a] The mole concentration of the minerals for 100 grams of the soil;
[b] The maximum mole content of the phase that can dissolve in the solution;
[c] This phase is assumed to be stable in the simulation.
[d] The source of the thermodynamic database (1) indicates LLNL, (2) represents MINTEQ, (3) means CEMDATA18, and (4) is PHREEQC.

Table.S4. Normalized oxide weight percentage of PG and OPC samples.

Species	PG (wt%)	OPC (wt%)
F	0.81	0.00
MgO	0.00	2.31
Al_2O_3	0.71	5.23
SiO_2	5.32	22.72
P_2O_5	1.08	0.00
SO_3	54.10	3.88
K_2O	0.00	0.82
CaO	37.35	60.91
Fe_2O_3	0.63	4.12

Table.S5. Assumptions and parameters used for the carbon footprint of PGO and PGA production

Assumption	Units	Value	Comments
Kaolin calcination			
Calcination tempreature	[℃]	800	Ref. Hosseini et al., 2011
Calcination time	[h]	2	Ref. Hosseini et al., 2011
Decomposition temperature	[℃]	900	Ref. Hosseini et al., 2011
Decomposition time	[h]	2	Ref. Hosseini et al., 2011
Drying temperature	[℃]	70	Ref. Hosseini et al., 2011
Total drying time	[h]	28	Ref. Hosseini et al., 2011
Calcination efficiency	[%]	85	Assumed
Mass loss in processes	[%]	90	Assumed
Calcination and decomposition energy demand	[kWh/t]	759.44	Ref. Cao et al., 2021
Grinding			
Grinding equipment	[kg CO_2/t]	34.60	Ref. Vizcaíno-Andrés et al., 2015
Energy costs and emissions			
Grid electricity	[CNY/kWh]	0.49	Ref. Niu et al., 2017
Grid electricity CO_2 emission	[kg CO_2/kWh]	0.540	Ref. Renforth et al., 2013
Renewable electricity	[CNY/kWh]	0.43	Ref. McQueen et al., 2020
Renewable electricity CO_2 emission	[kg CO_2/kWh]	0.025	Ref. McQueen et al., 2020
Percentage of the grid and renewable electricity	[%]	70/30	Ref. Yao and Zang, 2021
Solid waste disposal expense			
Average disposing costs (e.g., dump construction, transportation)	[CNY/t]	2000.00	Ref. Zhu and Jin, 2021
Stock fee	[CNY/t]	15.00	The hazardous solid waste stock fee, based on Regulation on the Implementation of the Environmental Protection Tax Law of the People's Republic of China.
OPC preparation			
OPC	[CNY/t]	520.00	Assumed average price of OPC in China in 2021
OPC production CO_2 emission	[kg CO_2/t]	852.00	Ref. Ravikumar et al., 2021
OPC Energy demand	[kWh/t]	1311.11	Ref. Cao et al., 2021
Water preparation			
Water	[CNY/m^3]	4.10	The price of industrial and commercial water in Beijing, PRC
Water supply CO_2 emission	[kg CO_2/m^3]	2.50	Ref. Chang et al., 2012
CO_2 emission tax			
P.R.C.	[CNY/kg]	0.100	Ref. (Wang et al., 2019c)
U.S.	[$/t]	50	Approximately equal to 0.325 CNY/kg
E.U.	[€/t]	70	Approximately equal to 0.455 CNY/kg

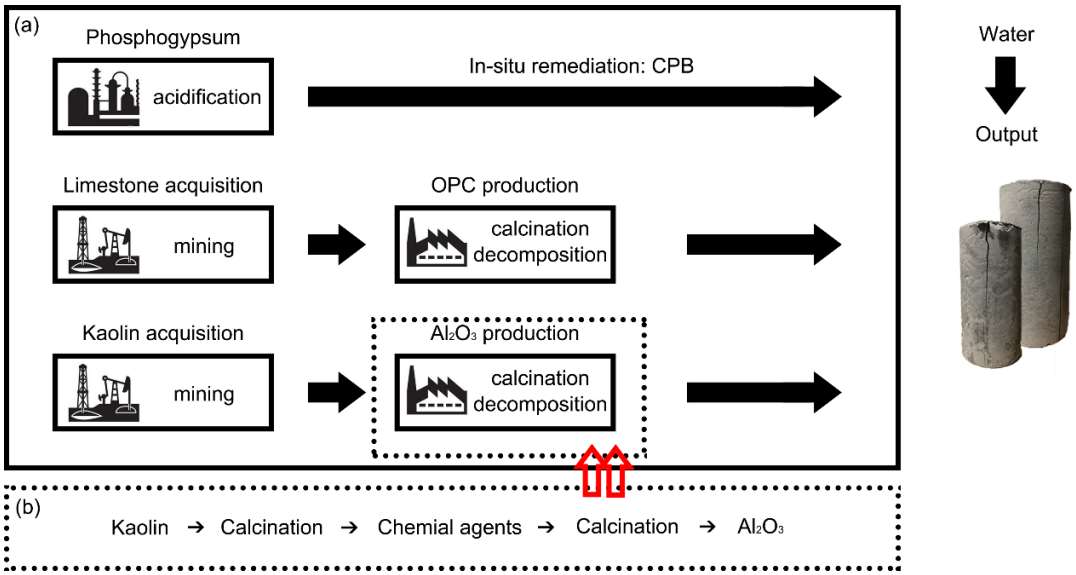

Figure.S1. The system boundary of PGO and PGA preparation.

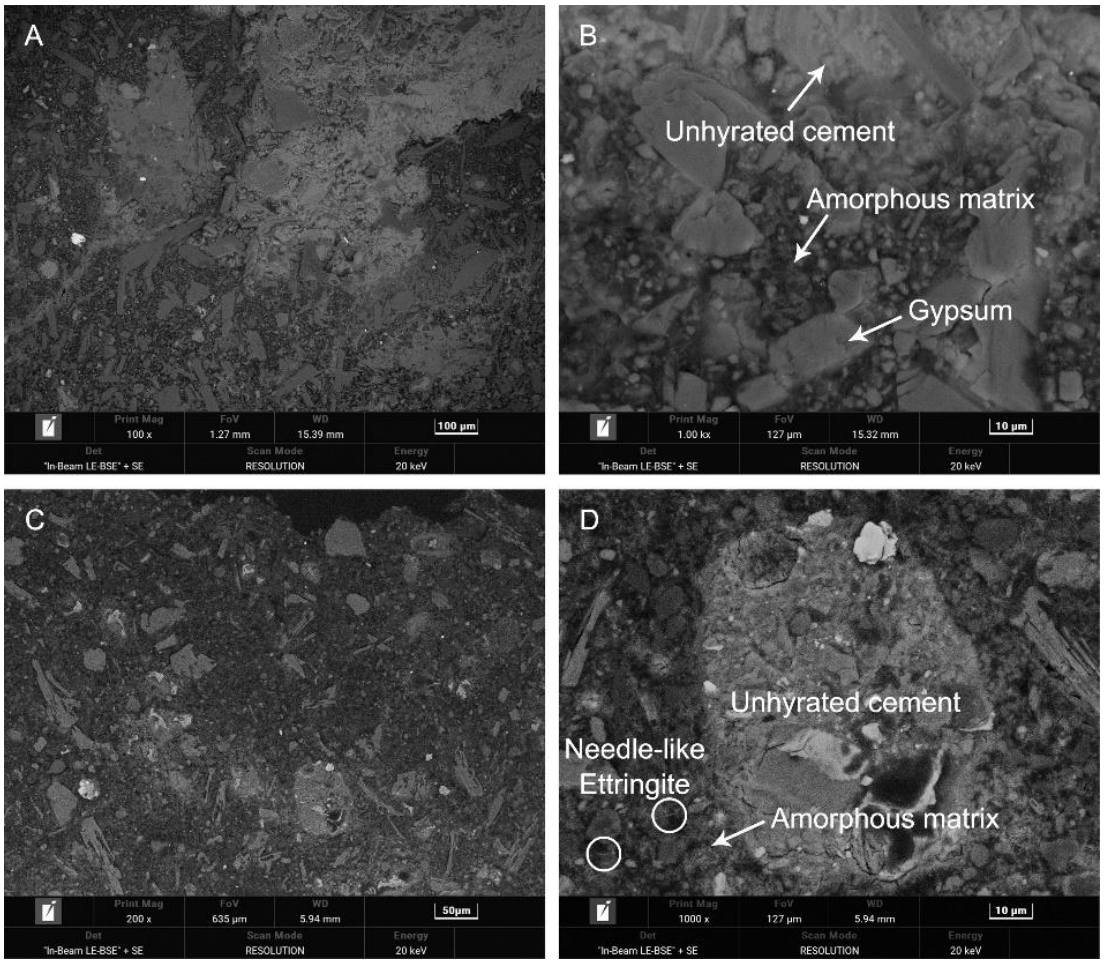

Figure.S2. SEM iamges of the PGO (a and b) and PGA (c and d) samples.

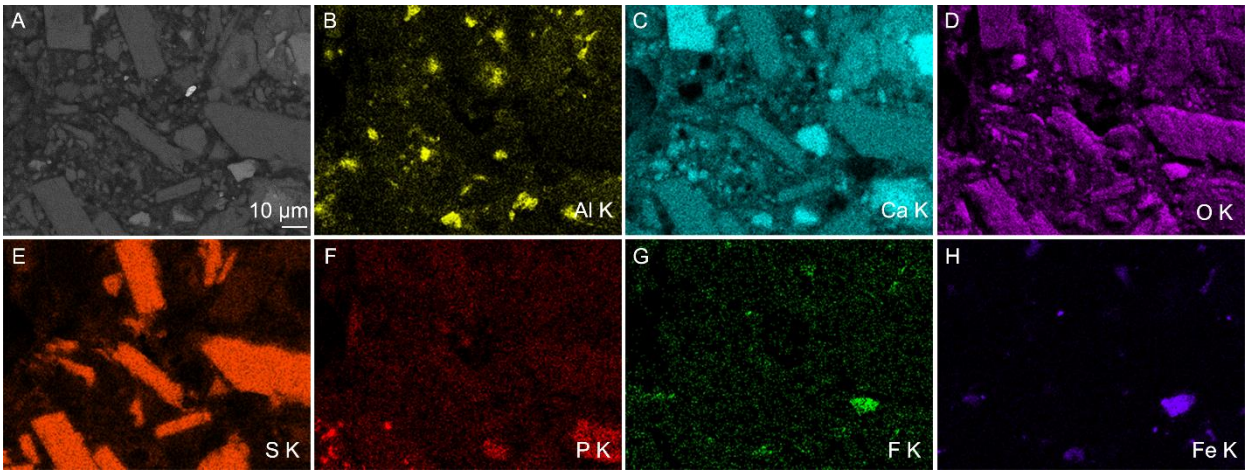

Figure.S3. Elemental mapping of the PGO samples correlated to Fig.3A.

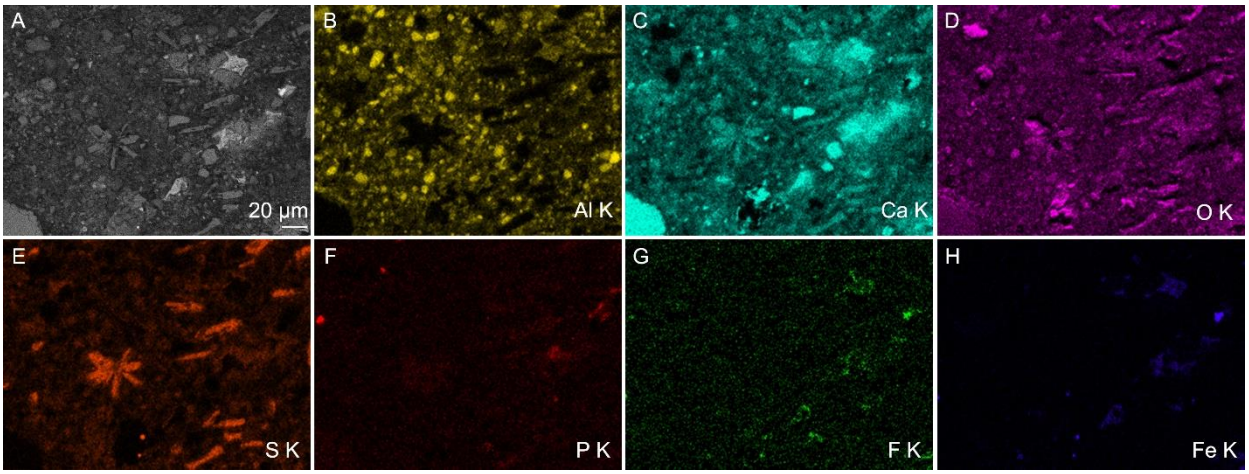

Figure.S4. Elemental mapping of the PGA samples correlated to Fig.3E.

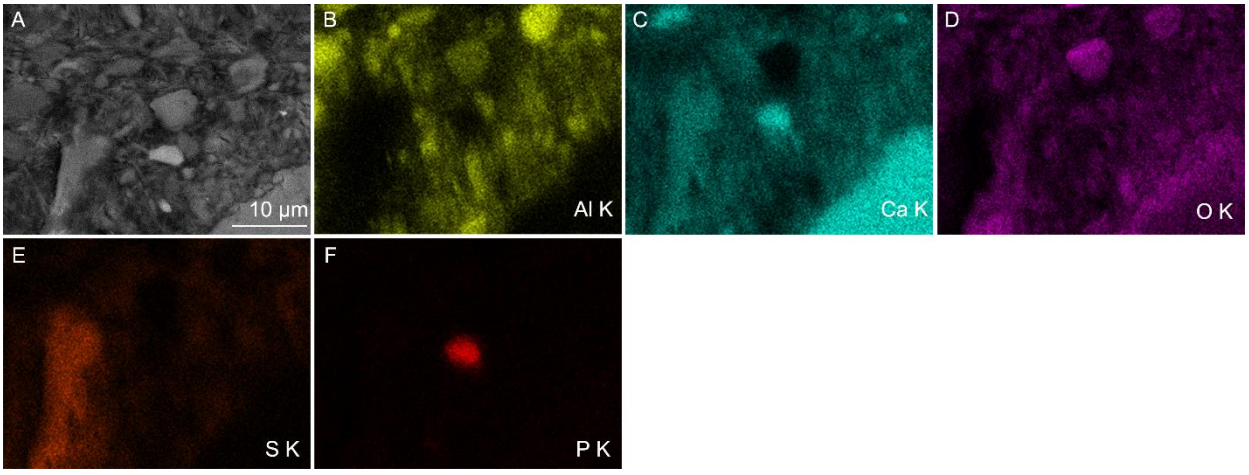

Figure.S5. Elemental mapping of the PGA samples correlated to Fig.3I.

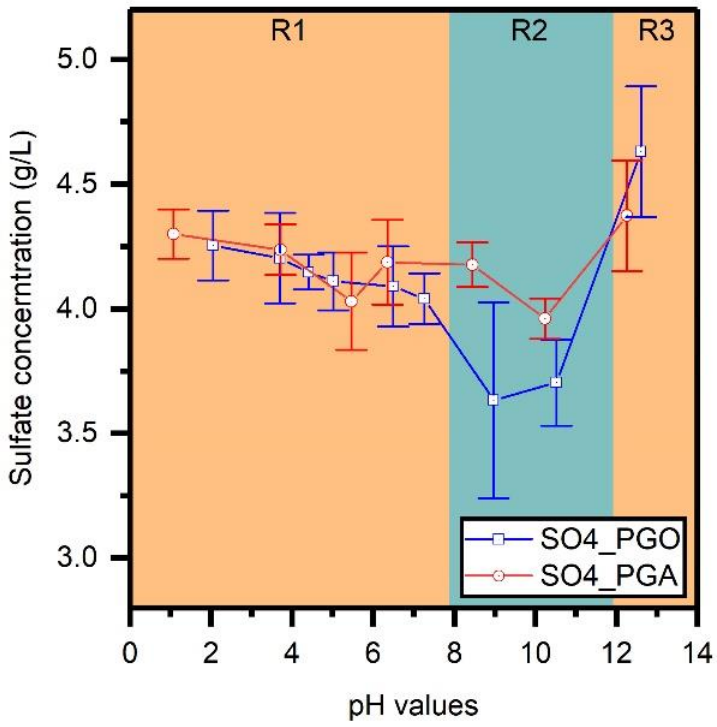

Figure.S6. Sulfate leaching results from pH-dependent leaching tests. R1 means the region where sulfate releasing is dominated by gypsum, R2 is the pH range for the ettringite to start to precipitate, and R3 represents the area suitable for saturation of portlandite.

Chapter 6

The sponge effect of phosphogypsum-based cemented paste backfill in the atmospheric carbon capture: roles of fluorides, phosphates, and alkalinity

Yikai Liu[1]; Qiusong Chen[2, 3]; Maria Chiara Dalconi[1]; Simone Molinari[1]; Luca Valentini[1]; Yunmin Wang[2,3]; Shiyuan Sun[3]; Peishen Wang[3]; Gilberto Artioli[1]

[1] *Department of Geosciences and CIRCe Centre, University of Padua, via G. Gradenigo 6, 35129, Padua, Italy*

[2] *Sinosteel Maanshan General Institute of Mining Research Co., Ltd., Maanshan, 24300, China;*

[3] *School of Resources and Safety Engineering, Central South University, Lushan South Road 932, 410083, Hunan, China*

Graphical abstract

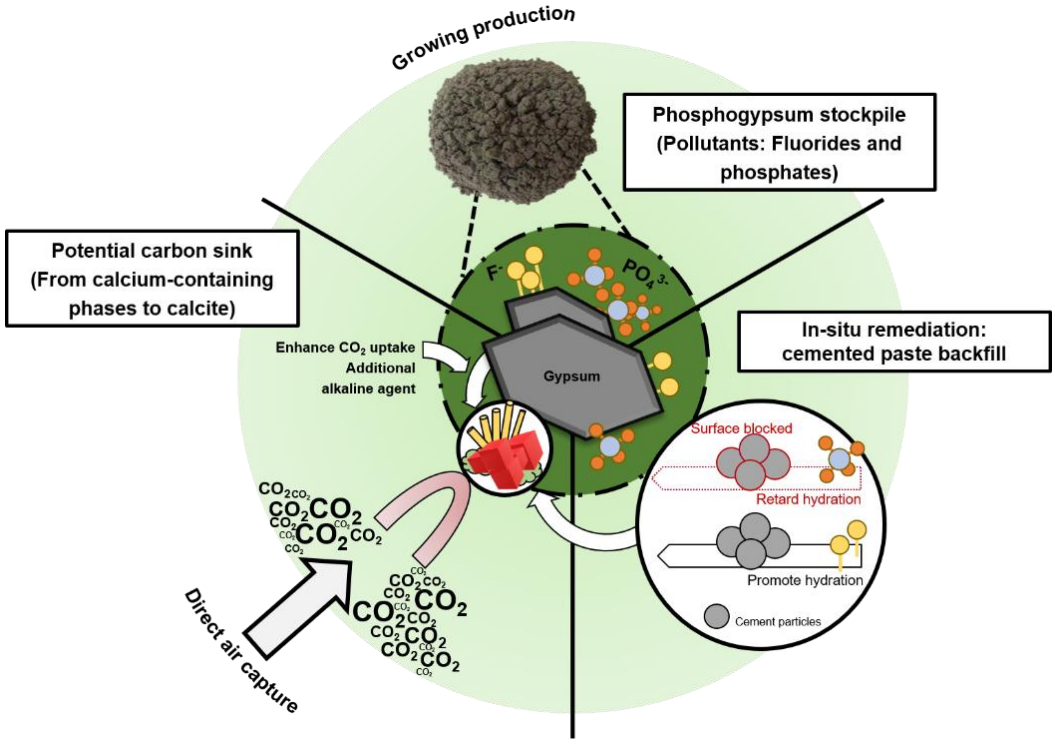

This manuscript is in preparation

Abstract

The use of cement for solid waste solidification/stabilization is under scrutiny due to its substantial emission of greenhouse gases. However, the dual role of hydration products and calcium-rich minerals may serve as a CO_2 sink and promisingly reabsorb a great content of atmospheric CO_2, which is hitherto unexplored. In this study, we detail the inherent potential sponge effect of phosphogypsum (PG) based cemented paste backfill (PCPB), finding that the PCPB application may produce 16.7 Mt/year of CO_2 in China, whereas a reduction of 5.76 Mt/year could promisingly reach up when considering the future reabsorption. The phosphate impurities within the PG demonstrate an adverse effect on the CO_2 uptake, which inhibits the precipitation of hydration products and inversely favors the formation of calcium-phosphate species that retard the dissolution of cement particles. By contrast, the fluorides imply an acceleration of the hydration reactions and accordingly hasten the carbonation process. Further, geochemical modeling suggests that maintaining a basic pH condition of the system is another significant factor in promoting the CO_2 capture capacity, of which a 35% increase in CO_2 uptake can be acquired with a continuous low concentration NaOH supply, but this enhancement will require the widespread deployment of future validation. The overall work sheds light on the PCPB application having a scalable potential to be an efficient pathway for in-situ remediating PG from the perspectives of CO_2 balance, environmental requirements, and technological feasibility.

Keywords

Phosphogypsum; Cemented paste backfills; Solidification/stabilization; Decarbonization; Solid waste management

1. Introduction

Phosphogypsum (PG) is a typical by-product generated from acid digestion of phosphorus fertilizer production, which is generally enriched in phosphates and fluoride pollutants (Holanda et al., 2017; Tsioka and Voudrias, 2020). Statistics show that about 300 million tonnes of PG are produced annually worldwide (Chen et al., 2017). However, over 85% of the PG output is haphazardly abandoned at various industrial sites or landfills without any treatment (Silva et al., 2022). The relatively weak stability of PG in ambient conditions would allow the concentrated pollutants to be massively rereleased into the environment, posing severely secondary pollution to the environment and humans (Lütke et al., 2020). Therefore, efficient and profitable immobilization technologies must be developed and strategically displayed to manage this waste. Regardless of many in-situ and ex-situ trials that have been carried out to address these hard-to-abate industrial by-products, the in-situ cemented paste backfill (CPB) technology remains an attractive application due to its advantages, such as practicable procedures, profitability, minimized potential

secondary pollutants from the transportation, large daily processing capacity, and reduced toxicity of the final mixtures (Li et al., 2017; Chen et al., 2018). This well-established disposal technique is based on the use of hydraulic binders (mainly ordinary Portland cement, PC), together with water, to solidify and stabilize the waste (Belem et al., 2000). Researchers investigated the PG-based CPB (PCPB) mixtures with respect to the microscopic and macroscopic properties, such as hydration products (Li et al., 2019a; Shi et al., 2021), microstructure (Zhou et al., 2020), mechanical properties (Chen et al., 2018; Maierdan et al., 2021), acoustic emission signals (Liu et al., 2021a), and durability (Meskini et al., 2021). However, the great environmental impact of PC production has positioned the PCPB strategy as one of the largest energy consumers and CO_2 emitters, which has become a significant constraint for its practical application (Saedi et al., 2020; Zhao et al., 2021). To overcome the drawbacks of over-reliance on PC, scientific evidence highlights the capability of multiple lower-carbon footprint additives agents in substituting cement production, for example, modified quartz sand (Shi et al., 2021), fly ash (Meskini et al., 2021), and lime (Zhao et al., 2022). These improvements are accepted as a promising strategy to improve the properties and reduce greenhouse gas emissions of PCPB mixtures if implemented in a field application in the next few decades. But before fully or extensively replacing PC proportions, the abovementioned approaches can be limited by technical shortcomings, such as the uncompetitive cost of the alternative materials, the possibility of deteriorated physical stabilization, and the uncertainties in long-term performance (Miller et al., 2021). Therefore, considering the unique properties and simplicity of PC application (Hossain et al., 2020; Wang et al., 2021), to date, a minimum but appreciable PC content is still required for the PCPB mixtures design, indicating that PC-free formulations are still challenging and the demand for PC will continue to increase (Habert et al., 2020).

Conversely, aside from the substantial greenhouse gas emissions from the PC calcination process, cement-related materials are significant CO_2 sinks due to their ability to react with atmospheric CO_2 (McQueen et al., 2020; Habert et al., 2020). This sponge effect mainly benefits from the carbonation of the calcium-containing phases, such as portlandite and calcium silicate hydrates (Morandeau et al., 2014; Mascarin et al., 2022). As a spontaneous process, the carbonation of cementitious materials occurs when the sample is exposed to the atmosphere (Steiner et al., 2020). Noteworthy, the primary component of PG is gypsum (approximately 90 wt%) (Zhao et al., 2015; Chen et al., 2017), which can provide additional calcium for carbonation. Considering the massive stockpile of PG, such a practicable and well-constructed solid waste in-situ remediation procedure (PCPB) has great potential to capture a huge amount of CO_2 in the direct carbonation process. Therefore, a better understanding of the mitigation potential of the sponge effect is required, which has been missing in previous work (Edraki et al., 2014; Li et al., 2019b; Zhou et al., 2020). Furthermore, it has been widely reported that the formation of hydration products (portlandite, ettringite, and C-S-H gel), which are the primary feedstock of carbonation, starts a few minutes after being mixed

with water (Zhou et al., 2019; Liu et al., 2019a). However, the impurities within the PG can inhibit the formation of hydration products, with several hypotheses and assumptions have been proposed that the phosphates and fluorides, the main pollutants in PG, may adversely affect the hydration kinetics at early age, which may impact the final conversion efficiency of Ca species (Li et al., 2017; Chen et al., 2018; Zhou et al., 2020). These adverse effects are postulated mainly based on the observations of the deteriorated mechanical properties or the extended setting time, where little attention has been paid to deeply understanding the early-age hydration reactions as well as the evolution of the solid/aqueous phases. Especially, the dissolution of soluble fluorides and phosphates coincides with the development of early age hydration (Rashad, 2017; Xu et al., 2019). Therefore, the possible role of fluorides and phosphates in affecting the kinetics of the carbonation process needs to be investigated.

In this paper, an in-depth characterization of the sponge effect of PCPB in future CO_2 emissions mitigation is carried out to address the research gaps in solid waste net-zero emission and sustainable management. Our approach builds on the investigation of early age hydration progression in order to scrutinize the effect of rapidly dissolved pollutants (phosphates and fluorides) in carbonation. Additionally, comparison experiments on the individual effect of phosphates and fluorides were undertaken. Moreover, geochemical modeling approaches were applied to elucidate underlying mechanisms involving mineral dissolution and precipitation. Accordingly, the species distribution of phosphates/fluorides/clinker phases with the influence of the CO_2 concentration and alkaline agent supply was conducted. An end-to-life CO_2 emission and storage model of PCPB applications was developed to elucidate the CO_2 balance within China's PG recycling cycle, which has been missing in previous work. Overall, this study attempted to fill the gap in the literature on reusing industrial waste in CPB technology by providing credible evidence from the carbon perspective.

2. Material and methods

2.1. Samples preparation

The PG (Fig.S1) was collected from a by-product stockpile site devoted to a phosphorus fertilizer manufacturing plant. CEM I 42.5 PC (compliant with GB 175-2007) was used in the mixture preparation procedure. All the chemical reagents (γ-Al_2O_3, NaF, P_2O_5, gypsum, and quartz) were of analytical grade (see the details given in Table.S1). Four mixtures (Table.1) were prepared to study the effects of phosphates and fluorides on the early age hydration and carbon capture capacity. They are PCPB (mixture prepared by blending PC, γ-Al_2O_3, and PG), MF (mixture prepared by blending PC, γ-Al_2O_3, NaF, gypsum, and quartz), MP (mixture prepared by blending PC, γ-Al_2O_3, P_2O_5, gypsum, and quartz), and binder (comparison group only with PC, γ-Al_2O_3, gypsum, and quartz). Although increasing the PC content can enhance the immobilization efficiency of CPB mixtures, this research aimed to use as much PG as possible to provide

maximum benefit for circular economy and carbonization strategies. Hence, the PG to binder ratio was set as 2 to 1. The agents were homogeneously mixed for 5 mins and cast into a mold (approximately 100 mm in diameter and 5 mm in height). After 15, 60, 180, 360, 720, 1440, and 4320 minutes since the first contact of solid agents and water, the entire sample holder and the mixture are immersed in liquid nitrogen to stop the hydration, reaching −190 °C in approximately 10 s. Subsequently, the frozen mixtures were grounded and sieved to 63 μm. Before the following characterization experiments, the specimens were still kept in a frozen and vacuum state to avoid the influence of further hydration in phase composition (Zhang and Scherer, 2011; Salvador et al., 2016).

Table.1. Proportions of the mixtures (wt%)

Label	PG	P_2O_5	NaF	Gypsum	Quartz	OPC	γ-Al_2O_3	Water
PCPB	42.9	/	/	/	/	21.4	4.3	31.4
MP	/	2.2	/	37.5	3.2	21.4	4.3	31.4
MF	/	/	2.2	37.5	3.2	21.4	4.3	31.4
MB	/	/	/	42.9	/	21.4	4.3	31.4

2.2. Characterization techniques

The mineralogical compositions of the prepared mixtures was obtained by XRD characterization using a D8 advance diffractometer (Bruker Co. Ltd, Germany) with Cu Kα radiation, operated at the scanning region range from 5° to 80° 2θ, with a step size of 0.02°. Zincite (ZnO, ACS Reagent) was homogeneously mixed with the sample powders as the internal standard. The FTIR tests were conducted by a Nicolet iS50 spectrometer (Thermo Fisher, USA) at the frequency range of 400–4000 cm^{-1}. The KBr powder to sample ratio was kept at 100. The decomposition process of phases at elevated temperatures was deduced from TG/DTG by using a simultaneous thermal analyzer (STA 449F3 Jupiter, Netzsch, Germany). The samples were heated from room temperature to 1050 °C at a 15 °C/min rate in a nitrogen atmosphere.

2.3. Carbon capture and storage

The CO_2 emission for the PCPB mixture preparation is mainly related to the OPC production, γ-Al_2O_3 production, and water supply (Fig.S2), which is conventionally given as 852 kg CO_2/t, 390.7 kg CO_2/t, and 2.50 kg CO_2/m^3, respectively. The emission sources of the binder mainly come from the direct CO_2 emission related to the resources, grinding process, drying procedures, calcination, and the electricity used for the aforementioned procedures. The CO2 emission related to binder transportation activities is not considered. The CO_2 emission attributed to the water supply is roughly based on the pipe construction, electricity-related CO_2 emission, and water recycling phases. The detailed calculation can be found in previous literature (Chang et al., 2012; Liu et al., 2022). The potential captured CO_2 is based on the quantification results of

calcite from experiments and geochemical modeling (Cao et al., 2020). The analysis of the Chinese PG stock cycle begins with an estimation of PG production in the next 15 years (Cui et al., 2022), and the overall rate of PG devoted to the PCPB application is based on statistical data in 2019 (Ye, 2020). Note that the overall recycling rate is estimated as a slowly-growing process (Cui et al., 2022). Therefore, the nationwide PG weight used in the PCPB application is calculated assuming that the rate keeps constant as the statistics in 2019 (14%).

2.4. Geochemical modeling

The geochemical model was constructed using the PHREEQC v3 program (Parkhurst and Appelo, 2013) with the thermodynamic databases from PHREEQC (Appelo et al., 2014) and CEMDATA 18 (Lothenbach et al., 2019). The calculations were performed at 25 ℃ and at the pressure of 1 bar. The simulation of the binder hydration was determined based on the methodology proposed by previous literature (Lothenbach et al., 2008a, 2008b; Holmes et al., 2022). Noteworthy, we are convinced that the presence of phosphorus and fluoride have adverse/promoting impacts on the rate of clinker phase dissolution and hydration reactions (Singh, 2003; Matsuzawa et al., 2017; Saadaoui et al., 2017). However, it has not been accounted for in the model proposed in this work because no reliable thermodynamic data or numerical methods exist to describe this behavior. To reveal the role of fluorides and phosphates at different ages, the hydration degree used in the simulation was selected at 5%, 20%, and 50%, respectively. The calculations enable predicting the progressive modification of the phase assemblage as a consequence of the increasing concentration of fluorides and phosphates (from 0 to 0.05 mol/100 g PCPB). Further, to simulate the effect of the CO_2 content, as well as the additional alkaline agent, on the carbonation of the PCPB mixtures, the mineralogical assemblages from the XRD quantification were used as the initial input of the simulation with constant CO_2 flux input (1 mol/100 g PCPB mixture in total divided by 100 steps at 1.0 atm and 20 ℃). The gas phase volume is fixed as 1L. Simultaneously, NaOH was added to the system with a 1/20 ratio to the CO_2 input. In addition, it was assumed that there was no more hydration reaction and cement clinkers fraction kept stable.

3. Results

3.1. XRD analysis

Fig.1a shows the XRD patterns of the PCPB mixtures after air curing with ages ranging from 15 to 4320 minutes (3 days). Ettringite and portlandite are the crystalline reaction products detected in all the patterns, along with the trace of unhydrated cement phases alite and belite. The characteristic peaks of γ-Al_2O_3 were not found, possibly due to its rapid dissolution and formation of hydroxides (Yang et al., 2020). The carbonation product, calcite, was observed since the hydration time was over 60 mins. The weight

percentage of each crystalline phase was quantified using the Rietveld's method (Fig.1c). After subtracting the mixed internal standard content, the amorphous fraction was accordingly quantified at approximately 32.5 wt% at 15 mins and decreased to 14.8 wt% at 360 mins. With the curing time, the amorphous fraction increased to 32.6 wt% at 4320 mins. The presence of amorphous may mainly be related to $Al(OH)_3$ and C-(A)-S-H precipitation (Yang et al., 2020; Gu and Chen, 2020), as well as pore water. The continuously decreasing OPC content (sum fractions of alite and belite, from 10.8 wt% at 15 mins to 6.6 wt% at 4320 mins) suggests that the reaction process proceeds with more clinker phases dissolved and more hydration products formed. The progress of ettringite and portlandite precipitation displayed a constant increase up to 360 mins, with the maximum contents detected of 8.4 and 8.8 wt%, respectively. Then the ettringite content is approximately not changing up to 4320 mins, whereas the portlandite shows a significant decrease during this period (from 8.8 wt% to undetectable). Instead, calcite is starting to precipitate massively (from 1.5 to 4.8 wt%).

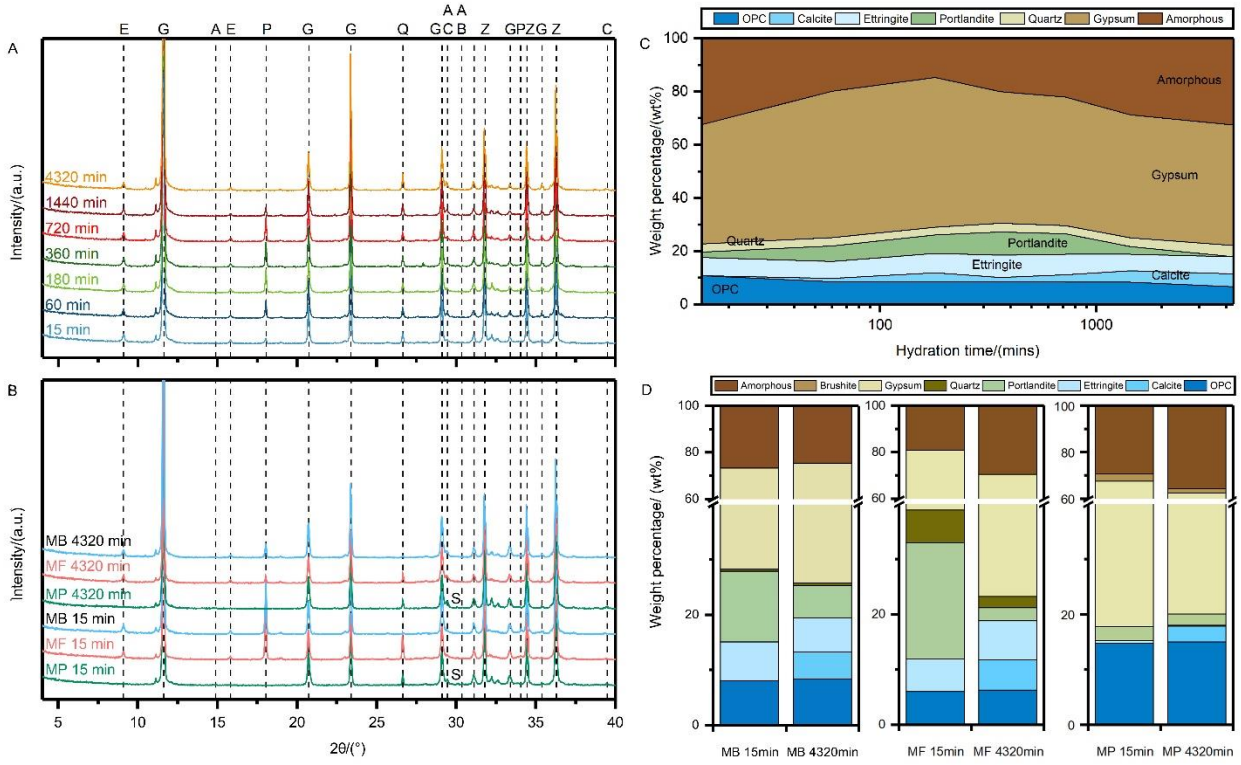

Figure.1. XRD patterns and the correlated quantification results of PCPB mixtures (a and b) and manually prepared mixtures (c and d). A: alite, B: belite, C: Calcite, E: Ettringite, G: Gypsum, P: Portlandite, Q: Quartz, S: Brushite, Z: zincite. OPC is the accumulated weight percentages of alite and belite.

To better understand the roles of fluorides and phosphates on the phases forming during the process, the XRD characterization of the control groups (MF and MP samples) was carried out and the results are shown in Fig.1b and d. In the early reaction period (15 mins), MF and MP display an appreciable difference in the characterized phases. In the MF sample, a significant portlandite content (21.1 wt%) is observed, with only 6.0 wt% of OPC phases present in the mixture, suggesting an increased clinker phase consumption at the early ages. On the contrary, diffraction peaks of portlandite disappeared in the MP system, and brushite was found as the newly observed Ca-bearing phase. Further, the dissolution of cement phases and the formation of ettringite in the MP mixture were somewhat delayed, with approximately 14.7 wt% of OPC and 0.5 wt% of ettringite being determined. At 4320 mins, no major changes in OPC, ettringite, and portlandite amount in MP samples are detected, in turn, the amount of portlandite in MF samples significantly decreased to 2.4 wt%. In addition, calcite is quantified as 5.5 and 2.8 wt% in MF and MP samples, respectively.

3.2. FTIR analysis

FTIR was performed to further investigate the change of functional groups in reaction compounds. The spectra of the mixtures at the different hydration stages are shown in Fig.2, while the associated possible vibration assignments are reported in Table.S6. The peaks that appeared in the high-frequency zones (3520, 3400, 1682, and 1621 cm^{-1}) are the typical hydroxides-corrected vibrations due to the stretching vibration of the O–H group in H_2O and H–O–H bending vibration, which might be associated to crystalline-bound water in C-(A)-S-H, gypsum, ettringite, and portlandite (Zarzuela et al., 2020; Padilla-Encinas et al., 2022). The presence of the sulfate group was inferred by the bands at 599, 668, and 1109 cm^{-1} (Anbalagan et al., 2009; Scholtzová et al., 2015). However, the overlapping in sulfate peaks typical of ettringite and gypsum makes it difficult to distinguish between these two minerals based on these peaks alone. But the signal observed at 988 cm^{-1} could be the distinct peak for the ettringite that correlated to the Al–O–H bonding mode (Scholtzová et al., 2015). Especially in the MP pattern (Fig.2b), the intensity of this band is the lowest, which ascertained the XRD quantification results (Fig.1d) that MP has limited ettringite precipitation. The shoulder at 510 cm^{-1} is typical of Si–O bondings (Wang et al., 2020). However, this could also be assigned to the Al-O stretching vibrations (Gijbels et al., 2019). Considering the given low intensity and overlapping in these bands, they cannot be readily attributed. Besides, the broad peak along the region from 420 to 450 cm^{-1} may be due to the $Al(OH)_3$ precipitation (Gijbels et al., 2019). The intensity of this absorption band is substantially lower in the mixtures over time, evidencing that the $Al(OH)_3$ is consumed by the reaction. Noteworthy, in MP mixtures (Fig.2b), a band at around 919 cm^{-1} was observed, which could be associated with the P–OH stretching mode of HPO_4 groups (Mandel and Tas, 2010), thereby confirming the brushite precipitation. In addition to the foregoing signals, the bands at 873, 1004, and 1417 cm^{-1} are indicative of

the C–O modes, of which the intensity slightly increased with the curing time (Fig.2a), demonstrating the substantial formation of calcite. In turn, it is also worth mentioning that the absence of these C–O bands in MP mixtures suggests that carbonates are not forming, verifying the XRD analysis above.

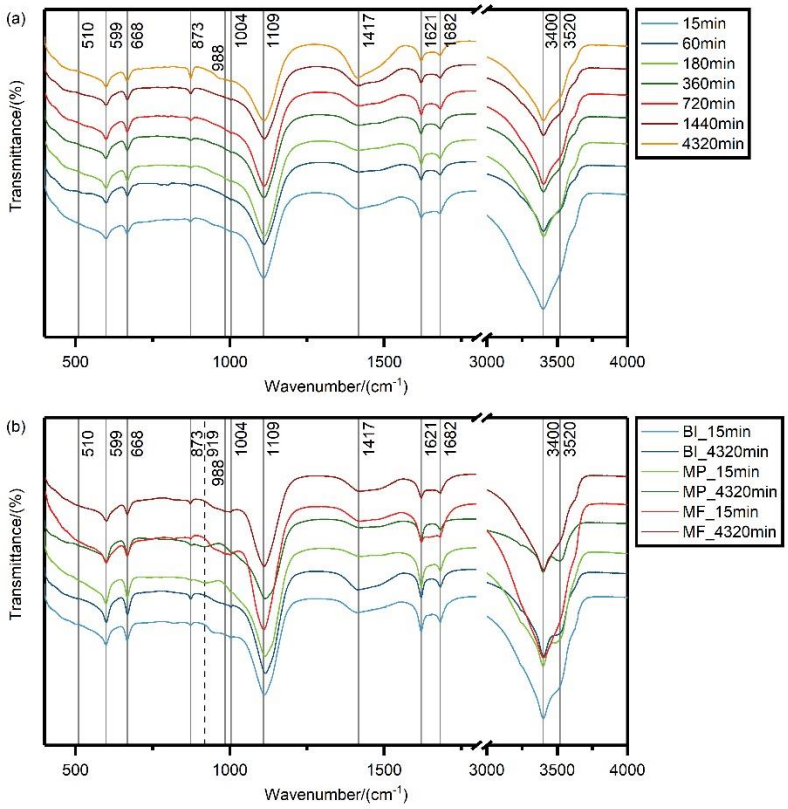

Figure.2. FT-IR spectra of cured samples. (a) patterns of PCPB samples and (b) patterns of control groups.

3.3. TG/DTG-DSC analysis

A more detailed characterization of the phase evolution in the mixtures was performed by thermogravimetric analysis. Based on the TGA curves presented in Fig.3a and d, all the tested samples demonstrate a similar profile where three regions characterize the total mass loss: (1) 60–200 °C, related to the loss of free water and weakly bound water in ettringite, gypsum, and C-(A)-S-H gel; (2) 400–500 °C, related to portlandite decomposition; and (3) 650–750 °C, related to calcite decomposition. The detailed derivative thermogravimetric (DTG) curves (Fig.2b and e) indicate more specific differences within these similar profiles. In the 60–200 °C region, two shoulders were found to have formed before and after the temperature reached 150 °C. From the DTG peak around 120 °C, the presence of ettringite and amorphous C–(A)–S–H can be confirmed (Barzgar et al., 2021). The absence of this peak in the MP sample, characterized by a broad shoulder, is related to the contribution of gypsum, which formed bassanite at this

temperature. Herein, the combined decomposition of ettringite (Winnefeld and Lothenbach, 2010), partial dehydration of gypsum (Jiménez and Prieto, 2015), and release of water molecules that are confined in the interlayer region of C–(A)–S–H (Barzgar et al., 2021) could explain the DTG behavior. The largest DTG peak occurring at 170 °C indicates the complete dehydration of gypsum, with anhydrite formed as the final product (Secco et al., 2015; Jiménez and Prieto, 2015). Thereafter, the mass loss presented at 430 °C corresponds to the decomposition of portlandite. As identified by the XRD analysis, in the DTG curves, the portlandite correlated peak intensity decreased with the curing time (Fig.3b) and P_2O_5 presence (Fig.3e). In turn, the intensity of the endothermic peak related to the decomposition of calcite which occurs around 780 °C increased remarkably suggesting that the reaction is proceeding continuously.

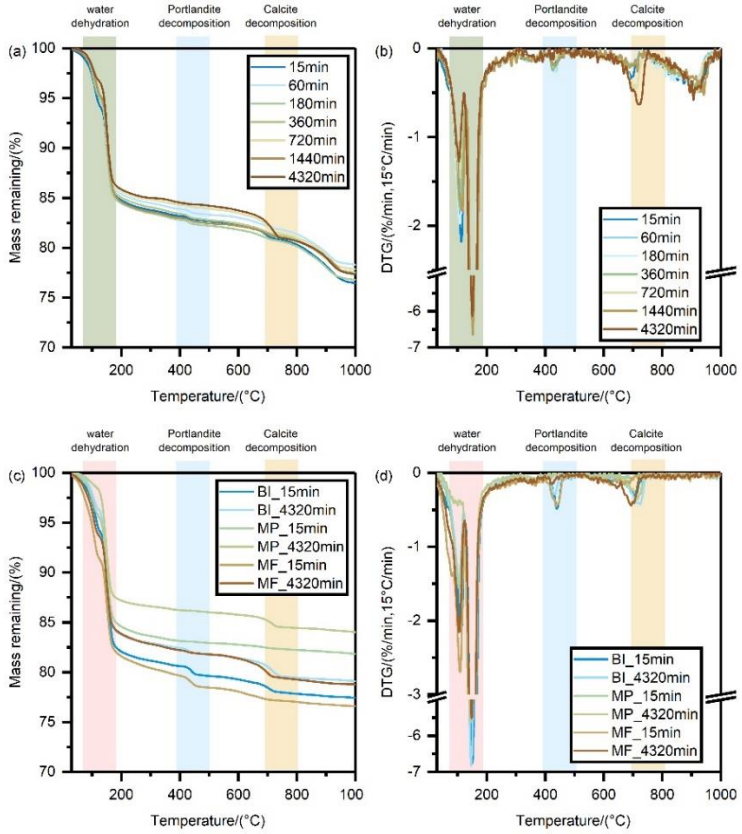

Figure.3. The TG/DTG curves of mixtures. (a) TG curves for PCPB from 15 to 4320 mins, (b) DTG patterns for PCPB mixtures from 15 to 4320 mins, (c) TG curves for control groups, and (d) DTG patterns for TG curves for control groups.

3.4. Geochemical model results

Geochemical modeling was carried out to investigate the impacts of fluorides and phosphates on the thermodynamic stability of hydration product assemblages. The results presented in Fig.4 and 5 reveal the influence of NaF and H_3PO_4 concentrations on hydration product precipitation, considering the hydration

degrees of 5%, 20%, and 80%, respectively. In the analysis with NaF (Fig.4a, b, and c), fluorite is the only F-bearing solid phase identified. The saturation index of NaF and AlF_3 are below -1 (Fig.S4), representing they are prone to dissolve completely under the given conditions (Parkhurst and Appelo, 2013). The Na in the system is primarily present in the solution as ions and pairs, whereas the Al is preserved as amorphous $Al(OH)_3$ and ettringite. The portlandite weight percentage is only minorly affected by the NaF input, remaining at approximately 2.6 wt%. Conversely, the increasing addition of NaF content lowered the gypsum concentration (e.g., at 5% hydration degree, from 38.2 to 34.0 wt%), which indicates that the partially dissolved gypsum could be the Ca source of fluorite precipitation. This gypsum dissolution is consistent with the XRD results (Fig.1d), as the quantified gypsum content of the MF mixture is lower than the fraction quantified in MP and MP samples, equating to roughly 3.0 and 7.9 wt% of difference, respectively.

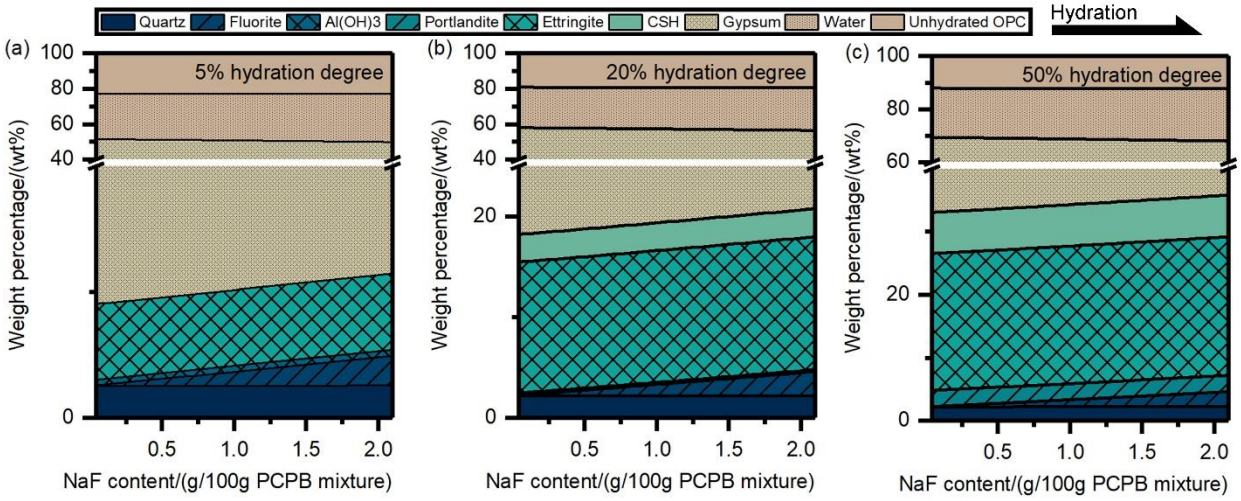

Figure.4. PCPB phases assemblages evolution with the NaF content at the hydration degree of 5% (a), 20% (b), and 50% (c).

Regarding the impact of phosphates, the phase diagrams display an obvious inhibiting influence on the precipitation of hydration products (CSH, portlandite, and ettringite). Especially at the early hydration (5%, Fig.5a), the hydration products are all thermodynamically unstable when 0.8g of H_3PO_4 is added to the system. But this effect is progressively alleviated with continuous hydration, which confirms observations from the literature (Holanda et al., 2017). From Fig.5c, it is evident that although the fraction of ettringite, portlandite, and C–S–H decreased with the phosphates content, these hydration products are retained with a total amount of 17.2 wt% at the maximum input. Noteworthy, the portlandite is more sensitive to the phosphates as its weight percentage (Fig.5) and saturation index (Fig.S5) illustrate a sharp drop since the PCPB mixture gets the contact of H_3PO_4, which is assumed because of the buffering effect (Ren et al., 2022). The phosphorus present in the system mainly exists in the form of hydroxyapatite. Instead, the

saturation indices of brushite and whitlockite are all below -1 (Fig.S5). However, hydroxyapatite tends to dissolve partially with the increase in phosphorus content, and its saturation index is still approximately 0. Subsequently, the dissolved phosphorus converts into the forms of H_3PO_4 and $H_2PO_4^-$, and HPO_4^{2-}.

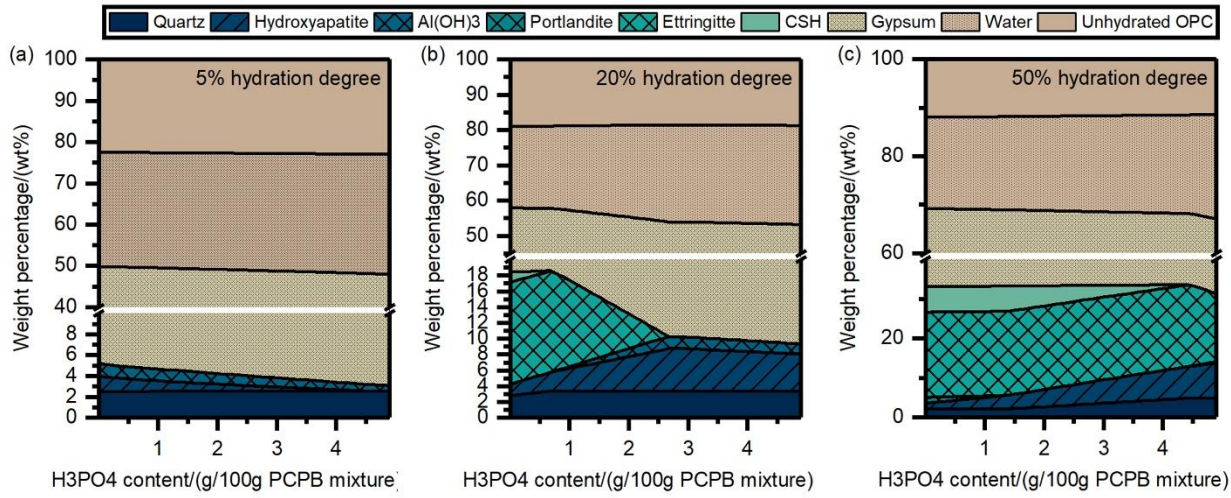

Figure.5. PCPB phases assemblages evolution with the H_3PO_4 content at the hydration degree of 5% (a), 20% (b), and 50% (c).

The evolution of weight percentages and saturation indices of phase assemblages with the captured CO_2 weight content is given in Fig.6. In agreement with the experimental observations mentioned above, portlandite is the main component that is able to react with the atmospheric CO_2 in the form of calcite. During this period (portlandite carbonation), although the amount of calcite keeps increasing at the expense of portlandite, the overall pH of the system remains stable, which revalidates the buffering effect of portlandite. When the portlandite is all depleted with 20.3 g CO_2 being absorbed, the carbonation reaction enters into the second stage in which the pH decreases and dissolution of C–S–H and ettringite starts, respectively. Experimental data also confirm the concurrent carbonation of C–S–H and ettringite that it can occur under ambient conditions within a time span of hours (Steiner et al., 2020; Xie et al., 2022). Although a deep and complete conversion is usually limited by many factors (McQueen et al., 2020), for instance, relative humidity, water vapor partial pressure, and CO_2 concentration, the geochemical model proposed here provides reliable quantitative predictions for the potential CO_2 capture capacity of PCPB mixtures. After the complete transformation of C–S–H and ettringite (31.7 g of CO_2 being captured), fluorite is here assumed as the predominant component for carbon retention. In the third period, due to the progressively decreased pH values, the fluorite is no more thermodynamically stable, then the dissolved Ca ions are partially converted to calcite. It is estimated that approximately 3.5 g of CO_2 can be collected when the fluorite is completely decomposed

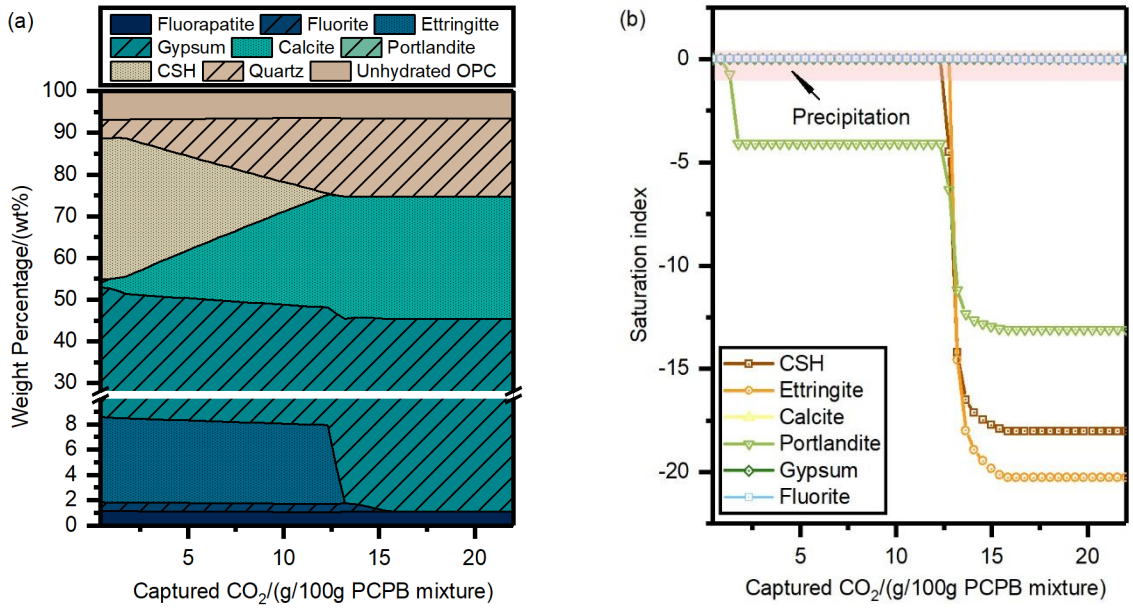

Figure.6. Carbon capture capacity of PCPB mixture with the influence of CO_2 input. (a) Phase assemblages evolution and (b) solubility of the primary Ca-bearing phases.

4. Discussion

4.1. Reconstruction of the early age hydration systems: the influence of fluorides and phosphates

The results obtained in this work, as well as previous observations, highlight that fluorides and phosphates have a significant influence, both favorable and unfavorable, on the early age hydration of PCPB mixtures which implies a superior limitation for carbonation (Zhou et al., 2020; Wang et al., 2022). In general, the hydration process is fundamentally a dissolution–precipitation process that can be affected by (1) the dissolution kinetics of anhydrous phases, (2) the nucleation rates of hydrates, and (3) the calcium-aluminate-silicate-sulfate balance in the solution (Scrivener and Nonat, 2011; Marchon and Flatt, 2016). However, the exact impact of fluorides and phosphates within the PG is questioned in the literature (Jiang et al., 2022). To explore the possible mechanisms, starting with the manually prepared mixtures may be the "silver bullet" that can provide technical clarity. The results of MF mixtures suggest the acceleration of the early age hydration when fluoride is added to the mixture. This promotion may be attributed to the formation of the calcium-fluoride complex (Fig.4), which contributes to the calcium ion consumption and inversely increases the dissolution of clinker phases (e.g., alite and belite) (Yang and He, 2021; Wang et al., 2022). Although this accelerated dissolution was not directly caught by the experiments, the abundant portlandite and ettringite precipitation in the MF mixtures (Fig.1d) may partly support the hypothesis. Additionally, the geochemical modeling suggests that, even at the early hydration (5%, Fig.4a), the dissolved fluorine remains in the system as a quite stable fluorite compound, whereas it synchronously remains as fluorite and fluorapatite when the phosphates are present in the system (Fig.6). Further, the increasing content of sodium

fluoride does not cause perturbation to the delicate balance of dissolution–precipitation of hydration products. As demonstrated in Fig.4, the gypsum-fluorite weight percentage transformation at high fluorine contents suggests that the Ca source for the fluorite precipitation can also originate from gypsum instead of the dissolution of hydration products. This is due to high pH conditions maintained in the mixture systems, which leads the fluorite to cross the saturation limit and attain a more saturated condition (Dehbandi et al., 2017). At the same time, under alkaline conditions, the hydroxide pairs from the dissolved clinker phases were enriched without disturbing the availability of main hydration products, with the SI of ettringite, C–S–H, and portlandite kept approximately at 0 (Fig.S4). Hence, it can be supposed that the Ca sources devoted to the equilibrium of fluorite are driven by the gypsum dissolution, which is a high solubility mineral, rather than the soluble calcium from C_2S and C_3S. However, more work needs to be done to confirm this implication.

In contrast to the fluoride impact, the addition of phosphates produced a mostly retarding effect on early hydration. It was claimed that the dissolved phosphates tend to precipitate in the form of calcium-phosphate complexes following earlier hydration and protectively coating the anhydrous cement particles (Bénard et al., 2005; Huang et al., 2017). The XRD data acquired in this work (Fig.1d) also implies that the potential mechanism, the coating effect, greatly inhibits the OPC hydration in MP mixtures. Noteworthy, as observed in the geochemical modeling and experimental observations reported in Bénard et al.'s (2005) work, hydroxyapatite is a highly-possible mineral phase that may precipitate and block the surface of the anhydrous clinkers. The XRD data reported in this work indicate that brushite is the only detected crystalline phosphate-bearing mineral that contributes to the retardation effect. Indeed, poorly crystalline hydroxyapatite is not detectable by XRD data if present in quantity below the detection limit of the technique. Hence it is hard to be found in the XRD. Meanwhile, previous reports (Liu et al., 2020b) suggest that the hydroxyapatite transformation from poorly to highly crystalline phase under normal ambient conditions requires a long time. Further, although hydroxyapatite is considered a stable mineral with low solubility, calcium hydrogen phosphate species have been rapidly formed during hydroxyapatite dissolution in simple aqueous solutions (Boudia et al., 2018). Nevertheless, the exact form of the proposed calcium-phosphates species still needs to be elucidated. We believe that future investigation on the kinetics of brushite-hydroxyapatite transformation may explain the solution undersaturation in geochemical simulation and the poorly crystalline structure with respect to hydroxyapatite. Subsequently, as a consequence of the inhibition of clinker phase dissolution, the lack of soluble calcium, aluminate, and hydroxide in the solution further retard the formation of hydrates. This was also evidenced in the case of MP mixtures, where crystalline hydration products did not appear in the system, either from experiments or simulations. Concurrently, the dissolved H_3PO_4 can consume the hydroxides ions provided by the clinker phases and

lower the pH values of the systems, consequently, the precipitation of portlandite, ettringite, and CSH is delayed (Huang et al., 2017).

In the real case of PCPB mixtures, by comparing the PCPB mixtures and control groups (PCPB and BI in Fig.1), the retardation effect is also evident because of the lower amount of available portlandite and greater content of anhydrous OPC. The former could be associated with the buffering effect to maintain the basic conditions because the majority of the PCPB mixture is composed of the acid PG (Zhou et al., 2020) and the latter is possible due to the coating effect of phosphates that retarded the dissolution of clinker contents. Meanwhile, the amorphous fraction of PCPB mixtures at early ages (Fig.1b) indicates the possibility of amorphous $Al(OH)_3$ precipitation, which means the solution pH at this period may be close to the neutral conditions that are unsuitable for its dissolution (Lydersen et al., 1991). Along with the successive dissolution behavior, the pH values of the solution increase significantly, which facilitates the dissolution of $Al(OH)_3$, with the intensity of Al–O–H shoulder vibration peak ranging from 420 to 450 cm^{-1} obviously decreased (Fig.2a). Further, the increased OH^-, Ca^{2+}, and Al^{3+} concentration, in conjunction with the sulfates originates from PG, leads to the hydration products formation (Radwan and Heikal, 2005), which is supported by the XRD results with more ettringite being quantified (Fig.1b). Simultaneously, it is clear that carbonation starts at this stage, as the XRD pattern clearly evidences the presence of calcite. After that, the Ca^{2+} ions continuously released react with the SiO_4^{4-} ions to form large amounts of gel products. The XRD quantification results of amorphous fraction from 14.8wt% at 180 min to 32.6 wt% at 4320 min are ascribed to the C–(A)–S–H formation.

It can thus be concluded that despite fluorides can accelerate early hydration and further promote the carbonation process, the retarding effect of phosphates and acid pH values of PG dominate the roles of the seesaw battle. Notwithstanding, there is a wide variety of impurities within the PG due to the applied acidification procedures in different factories and the weathering process in the stockpile sites (Silva et al., 2022) (e.g., the minerals of phosphates and fluorides, the pH values of the PG samples, and the gangue minerals presented). Therefore, the candidate mechanisms mentioned above may substantially be slightly altered when the introduced PG is from different origins. It is clear that pretreatment applications have a great potential to efficiently improve the hydration process and CO_2 uptake by unlocking the anhydrous clinker phases from the coating effect and refraining the portlandite from the CO_2 capture agent to pH buffers.

4.2. Implications for the carbon storage potential

The basis of the effective climate change mitigation programs is to reduce atmospheric CO_2 emissions to achieve net zero emissions and avoid more than a 2 °C increase in global average temperature as proposed by the Paris Agreement goal (McQueen et al., 2020; Guo et al., 2021; Liu et al., 2021b). The PC industry,

which is an essential ingredient in PCPB mixture preparation (Liu et al., 2020a), is a particularly energy- and CO_2-emission-intensive sector that accounts for approximately 7% of annual global anthropogenic CO_2 emissions (Cao et al., 2020). However, the PCPB application is unlikely to eliminate CO_2 emissions related to the use of PC because of the over-reliance on PC for the current industrial chain and the impracticability of direct replacement of conventional PC agents within the next decades (Habert et al., 2020). Based on the statistics, there are approximately 500 and 6000 Mt of PG stocks present in China (Bao et al., 2017) and worldwide (Li et al., 2022), in which 14% of recycled PG is devoted to the PCPB field application (Ye, 2020) (Fig.7a and b). Considering the continuously growing annual production of PG (see Fig.S6) (Cui et al., 2022), it is vital to understand the PCPB mixture preparation along the top-down cycle (Fig.S2) in future CO_2 emission criteria. Fig.7c shows the assumed carbon footprint of PCPB mixture preparation that reaches 466.0 kg CO_2 for recycling 1 tonne of PG, with the majority (91%) coming from PC production. Accounting for the different recycling scenarios (Fig.7d, e, and f), in 2035, with the increasing generation of PG, the CO_2 emission related to the PCPB binder consumption can reach 2.0-16.7 Mt/year accounting for the 0.2 to 1.9 ‰ overall CO_2 emission in the cement industry of China (Liu et al., 2015, 2021b). Nevertheless, reducing emissions from different binder sources is emphasized as one of the most important technologies but challenging. Many attempts have been applied to efficiently immobilize PG (Min et al., 2021; Jian et al., 2022), but there is a huge gap that still needs to be fulfilled concerning the costs, technical barriers, and actual contributions to hazardous substance retention (Liu et al., 2021b). Furthermore, these alternative binders have not been listed as an efficient methods and standard criteria in any official documents in China yet.

Conversely, researchers proposed that, aside from the CO_2 emissions sources, cement-related materials are significant CO_2 sinks that deliver similar carbon mitigation results (Cao et al., 2020). The abovementioned experimental data demonstrate that carbon capture of PCPB starts at very early hydration (60 mins) and increases with the curing age. Using the quantified weight percentage of calcite, we can accordingly reflect the weight of captured CO_2. From Fig.7c, the dual role of recycling 1 tonne of PG can reach 46.6 and 131.1 kg of CO_2 uptake. Interestingly, in the geochemical modeling (Fig.6), the CO_2 uptake continued even though the calcite was no more precipitate in the system. This is because the pH value is unsuitable for calcite growth, which is usually around 9.4 (Habert et al., 2020), therefore, the carbon presents in the system as unstable forms of bicarbonate complexes (e.g., $CaHCO_3^+$). Further, with the continuous decrease of pH values, the adsorbed CO_2 leads to the formation of carbonic acid in conjunction with CO_3^{2-} and HCO_3^- ions. Herein, we further developed a model to assess the role of additional alkaline agents (2g NaOH in total with respect to 44g of CO_2) in the carbon uptake capacity (Fig.S7), which suggests that the PCPB CO_2 uptake was increased to 161.2 kg accounting for 35% of the entire emission. Then by implementing the full portfolio of PG utilization scenarios, the CO_2 sponge effect is estimated to be 0.20 (Exp), 0.55 (Sim), and

0.68 (NaOH) Mt at a low PG utilization rate (Fig.7f), whereas it can reach by up to 1.67 (Exp), 4.69 (Sim), and 5.76 (NaOH) Mt at a high PG utilization rate (Fig.7d), of which the maximum CO_2 reduction attributing 14% of global commercial carbon capture and storage goal in 2020. Noteworthy, although the traditional electrolytic production of solid NaOH agent is a high cost and carbon footprint process, of which producing 1 tonne of NaOH may bring 0.55 kg CO_2 direct emissions, the low amount of NaOH used in this work implies only a 0.03 Mt CO2 emission increase for recycling 1 tonne of PG (Medina-Martos et al., 2022). Meanwhile, the application of optimized NaOH production processes and the discovery of alternative sodium resources (for instance, seawater desalination brine) can further promisingly lower the attributed carbon emission and broaden the techno-economic feasibility

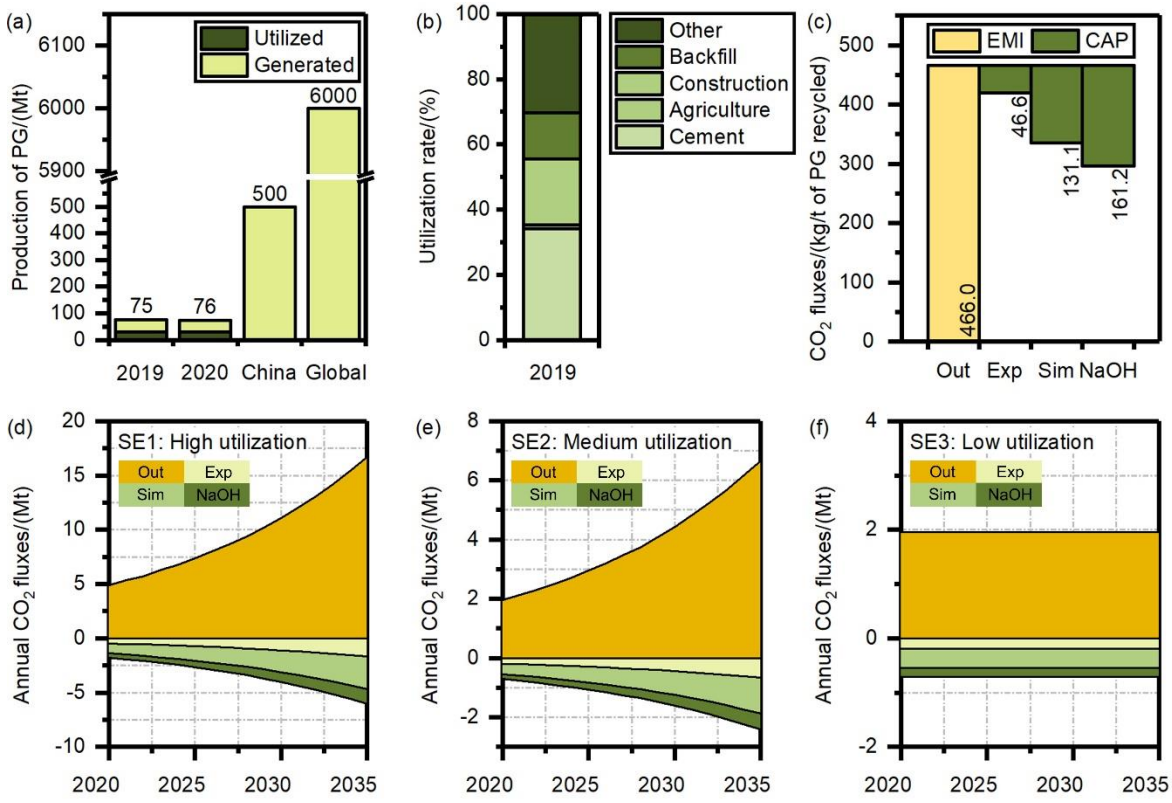

Figure.7. The dual role of PCPB application to carbon emission trend. (a) China's annual production of PG and the estimated stock volume of PG in China and worldwide, (b) PG utilization methods in China in 2019, (c) The CO_2 emissions (EMI) and uptake (CAP) of PCPB mixtures for recycling 1t of PG, of which the OUT indicates the overall CO_2 emission, the CAP is calculated based on the XRD characterization (Exp 46.6), and geochemical modeling presented in Fig.6 (Sim 131.1) and Fig.S7 (NaOH 161.2), (d) the sponge effect of PCPB mixture in the scenarios at high PG utilization rate, (e) the sponge effect of PCPB mixture in the scenarios at medium PG utilization rate, and (f) the sponge effect of PCPB mixture in scenarios at low and constant PG utilization rate.

Notwithstanding, we note that the carbonation of cement is a diffusion-limited process, of which the rate is subject to substantial uncertainties interplay between in-use stock dynamics and atmospheric CO_2 concentrations (Cao et al., 2020; Habert et al., 2020; Assen et al., 2021). Experimental analysis reveals that the carbonation rate of PC samples at ambient conditions can reach 0.04 mm/day (Hernández-Rodríguez et al., 2021), whereas, for the mortar sample, it might be 0.13 mm/day (Habert et al., 2020). Considering the longevity lifetime of the PCPB application (from decades to centuries) (Chen et al., 2017) and its relatively practicable field utilization (Chen et al., 2018), it is clear that future decarbonization is promising, which will become increasingly significant as PG stocks increase. Therefore, necessitating strategies should be adapted to sweep the potential burden in the current PCPB roadmap and intentionally increase the rate of the carbonation process. The previously discussed experiment results indicate that one of the major challenges is from the primary pollutants in PG, phosphates, which can block the surface of cement particles and lower the pH values required for calcite precipitation. Therefore, effective phosphates removal means, for instance, washing pretreatment (Rashad, 2017; Liu et al., 2019b) and sorption (Guo et al., 2020), are needed to improve the reaction rate and achieve the best performance of PCPB CO_2 uptake. Another major issue the geochemical modeling reveals is the maintenance of basic pH values to guarantee carbonate precipitation. Currently, the NaOH is synchronously added into the system by the CO_2 flux, which has shown good performance based on the geochemical modeling. However, it lacks long-term laboratory or field stability tests, which are required to be proven in future studies.

5. Conclusion

This study provides valuable insight to advance understanding the carbon capture and utilization in a net-zero industrialized world, specifically in solid waste in-situ immobilization. In summary, we explored the effect of fluorine and phosphates on the carbon uptake and storage of PCPB applications using multiple experiment techniques and geochemical simulation. Considering the precipitated calcite, we quantified the dual role of PCPB in the CO_2 emission balance. The following conclusions are drawn:

(1) Fluoride is observed to increase the reaction rate at the early ages, with more hydration products and fewer anhydrous cement particles quantified in the experiments. Geochemical modeling reveals that this acceleration is attributed to the formation of the calcium-fluoride complex, which contributes to the calcium source consumption and accordingly promotes the dissolution of clinker phases to maintain the calcium-rich environment. This acceleration may theoretically hold a great promise for shortening the pathway of CO_2 cradle-to-gate balance. Future experimental and long-term work is required to understand exactly the impacts of fluorides on the kinetically controlled carbonation process.

(2) Phosphates adversely affect CO_2 uptake, possibly due to the formation of calcium-phosphate species depositing on cement surfaces and retarding hydration. This immediate precipitation may favor calcium

consumption, but geochemical modeling indicates that it inhibits the conversion from calcium-bearing phases to calcite, conversely favoring the brushite or hydroxyapatite precipitation.

(3) The CO_2 uptake depends strongly on the alkalinity of the PCPB system. The geochemical simulation demonstrates that the continuous and low-concentration NaOH supply can significantly enhance CO_2 capture capacity. However, the simulated results were achieved without real process investigation and there is plenty of scope for significant further improvement.

(4) The carbon footprint assessment shows that, for recycling 1 tonne of PG, PCPB preparation directly releases 466 kg of CO_2 emission. With the growing PG production, the overall CO_2 emission through the PCPB application may reach 16.7 Mt/year, accounting for 1.9 ‰ of CO_2 emissions in the cement industry in China. Simultaneously, the dual role of PCPB could capture between 10% and 35% of CO_2, promisingly reducing net direct emissions by up to 5.76 Mt.

Acknowledgments

This research was funded by the National Natural Science Foundation of China (No. 552104156, 52074351, and No. 52004330), the Science and Technology Innovation Program of Hunan Province (No. 2021RC3125), a scholarship granted by the China Scholarship Council (No.CSC201906370062), and the PRIN project "Mineral reactivity, a key to understand large-scale processes: from rock-forming environments to solid waste recovering/lithification" n. 2017L83S77.

Author Contributions

Yikai Liu: data curation, methodology, software, visualization, writing—original draft

Qiusong Chen: funding acquisition, supervision, writing—original draft

Maria Chiara Dalconi: formal analysis and writing—original draft

Simone Molinari: formal analysis and writing—original draft

Luca Valentini: formal analysis and writing—original draft

Yunming Wang: funding acquisition and resources

Shiyuan Sun: resources and investigation

Peishen Wang: investigation

Gilberto Artioli: funding acquisition, supervision, and methodology.

All the authors discussed the data and agreed on their interpretations. All the co-authors contributed to the final polishing of the manuscript.

Reference

Anbalagan, G., Mukundakumari, S., Murugesan, K.S., and Gunasekaran, S., 2009, Infrared, optical absorption, and EPR spectroscopic studies on natural gypsum: Vibrational Spectroscopy, v. 50, p. 226–230, doi:10.1016/J.VIBSPEC.2008.12.004.

Appelo, C.A.J., Parkhurst, D.L., and Post, V.E.A., 2014, Equations for calculating hydrogeochemical reactions of minerals and gases such as CO2 at high pressures and temperatures: Geochimica et Cosmochimica Acta, v. 125, p. 49–67, doi:10.1016/J.GCA.2013.10.003.

Assen, A.H., Belmabkhout, Y., Adil, K., Lachehab, A., Hassoune, H., and Aggarwal, H., 2021, Advances on CO2 storage. Synthetic porous solids, mineralization and alternative solutions: Chemical Engineering Journal, v. 419, p. 129569, doi:10.1016/J.CEJ.2021.129569.

Bao, W., Zhao, H., Li, H., Li, S., and Lin, W., 2017, Process simulation of mineral carbonation of phosphogypsum with ammonia under increased CO2 pressure: Journal of CO2 Utilization, v. 17, p. 125–136, doi:10.1016/J.JCOU.2016.11.012.

Barzgar, S., Tarik, M., Ludwig, C., and Lothenbach, B., 2021, The effect of equilibration time on Al uptake in C-S-H: Cement and Concrete Research, v. 144, p. 106438, doi:10.1016/J.CEMCONRES.2021.106438.

Belem, T., Benzaazoua, M., and Bussière, B., 2000, Mechanical behaviour of cemented paste backfill: Proceedings of 53rd Candadian Geotechnical Conference,.

Bénard, P., Garrault, S., Nonat, A., and Cau-Dit-Coumes, C., 2005, Hydration process and rheological properties of cement pastes modified by orthophosphate addition: Journal of the European Ceramic Society, v. 25, p. 1877–1883, doi:10.1016/J.JEURCERAMSOC.2004.06.017.

Boudia, S., Zuddas, P., Fernane, F., Fiallo, M., and Sharrock, P., 2018, Mineralogical transformation during hydroxyapatite dissolution in simple aqueous solutions: Chemical Geology, v. 477, p. 85–91, doi:10.1016/J.CHEMGEO.2017.12.007.

Cao, Z., Myers, R.J., Lupton, R.C., Duan, H., Sacchi, R., Zhou, N., Reed Miller, T., Cullen, J.M., Ge, Q., and Liu, G., 2020, The sponge effect and carbon emission mitigation potentials of the global cement cycle: Nature Communications 2020 11:1, v. 11, p. 1–9, doi:10.1038/s41467-020-17583-w.

Chang, N. Bin, Qi, C., and Yang, Y.J., 2012, Optimal expansion of a drinking water infrastructure system with respect to carbon footprint, cost-effectiveness and water demand: Journal of Environmental Management, v. 110, p. 194–206, doi:10.1016/j.jenvman.2012.06.004.

Chen, Q., Zhang, Q., Fourie, A., and Xin, C., 2017, Utilization of phosphogypsum and phosphate tailings for cemented paste backfill: Journal of Environmental Management, v. 201, p. 19–27, doi:10.1016/j.jenvman.2017.06.027.

Chen, Q., Zhang, Q., Qi, C., Fourie, A., and Xiao, C., 2018, Recycling phosphogypsum and construction

demolition waste for cemented paste backfill and its environmental impact: Journal of Cleaner Production, v. 186, p. 418–429, doi:10.1016/j.jclepro.2018.03.131.

Cui, Y., Chang, I.S., Yang, S., Yu, X., Cao, Y., and Wu, J., 2022, A novel dynamic business model to quantify the effects of policy intervention on solid waste recycling industry: A case study on phosphogypsum recycling in Yichang, China: Journal of Cleaner Production, v. 355, p. 131779, doi:10.1016/J.JCLEPRO.2022.131779.

Dehbandi, R., Moore, F., Keshavarzi, B., and Abbasnejad, A., 2017, Fluoride hydrogeochemistry and bioavailability in groundwater and soil of an endemic fluorosis belt, central Iran: Environmental Earth Sciences, v. 76, p. 1–15, doi:10.1007/S12665-017-6489-9/TABLES/3.

Edraki, M., Baumgartl, T., Manlapig, E., Bradshaw, D., Franks, D.M., and Moran, C.J., 2014, Designing mine tailings for better environmental, social and economic outcomes: A review of alternative approaches: Journal of Cleaner Production, v. 84, p. 411–420, doi:10.1016/j.jclepro.2014.04.079.

Gijbels, K., Nguyen, H., Kinnunen, P., Schroeyers, W., Pontikes, Y., Schreurs, S., and Illikainen, M., 2019, Feasibility of incorporating phosphogypsum in ettringite-based binder from ladle slag: Journal of Cleaner Production, v. 237, p. 117793, doi:10.1016/J.JCLEPRO.2019.117793.

Gu, K., and Chen, B., 2020, Loess stabilization using cement, waste phosphogypsum, fly ash and quicklime for self-compacting rammed earth construction: Construction and Building Materials, v. 231, p. 117195, doi:10.1016/J.CONBUILDMAT.2019.117195.

Guo, T., Gu, H., Ma, S., and Wang, N., 2020, Increasing phosphate sorption on barium slag by adding phosphogypsum for non-hazardous treatment: Journal of Environmental Management, v. 270, p. 110823, doi:10.1016/J.JENVMAN.2020.110823.

Guo, B., Tan, Y., Wang, L., Chen, L., Wu, Z., Sasaki, K., Mechtcherine, V., and Tsang, D.C.W., 2021, High-efficiency and low-carbon remediation of zinc contaminated sludge by magnesium oxysulfate cement: Journal of Hazardous Materials, v. 408, p. 124486, doi:10.1016/J.JHAZMAT.2020.124486.

Habert, G., Miller, S.A., John, V.M., Provis, J.L., Favier, A., Horvath, A., and Scrivener, K.L., 2020, Environmental impacts and decarbonization strategies in the cement and concrete industries: Nature Reviews Earth & Environment 2020 1:11, v. 1, p. 559–573, doi:10.1038/s43017-020-0093-3.

Hernández-Rodríguez, A., Orlando, A., Montegrossi, G., Huet, B., Virgili, G., and Vaselli, O., 2021, Experimental analysis on the carbonation rate of Portland cement at room temperature and CO2 partial pressure from 1 to 51 bar: Cement and Concrete Composites, v. 124, p. 104271, doi:10.1016/J.CEMCONCOMP.2021.104271.

Holanda, F. do C., Schmidt, H., and Quarcioni, V.A., 2017, Influence of phosphorus from phosphogypsum on the initial hydration of Portland cement in the presence of superplasticizers: Cement and Concrete Composites, doi:10.1016/j.cemconcomp.2017.07.029.

Holmes, N., Tyrer, M., West, R., Lowe, A., and Kelliher, D., 2022, Using PHREEQC to model cement hydration: Construction and Building Materials, v. 319, p. 126129, doi:10.1016/J.CONBUILDMAT.2021.126129.

Hossain, M.U., Wang, L., Chen, L., Tsang, D.C.W., Ng, S.T., Poon, C.S., and Mechtcherine, V., 2020, Evaluating the environmental impacts of stabilization and solidification technologies for managing hazardous wastes through life cycle assessment: A case study of Hong Kong: Environment International, v. 145, p. 106139, doi:10.1016/J.ENVINT.2020.106139.

Huang, Y., Qian, J., Liu, C., Liu, N., Shen, Y., Ma, Y., Sun, H., and Fan, Y., 2017, Influence of phosphorus impurities on the performances of calcium sulfoaluminate cement: Construction and Building Materials, v. 149, p. 37–44, doi:10.1016/J.CONBUILDMAT.2017.05.028.

Jian, S., Cheng, C., Lv, Y., Wang, C., Tan, H., and Li, B., 2022, Preparation and evaluation of high-fluid backfill materials from construction spoil: Construction and Building Materials, v. 345, p. 128370, doi:10.1016/J.CONBUILDMAT.2022.128370.

Jiang, G., Wu, A., Wang, Y., Wang, Y., and Li, J., 2022, Determination of utilization strategies for hemihydrate phosphogypsum in cemented paste backfill: Used as cementitious material or aggregate: Journal of Environmental Management, v. 308, p. 114687, doi:10.1016/J.JENVMAN.2022.114687.

Jiménez, A., and Prieto, M., 2015, Thermal Stability of Ettringite Exposed to Atmosphere: Implications for the Uptake of Harmful Ions by Cement: Environmental Science and Technology, v. 49, p. 7957–7964, doi:10.1021/ACS.EST.5B00536/ASSET/IMAGES/ES-2015-00536V_M001.GIF.

Li, X., Du, J., Gao, L., He, S., Gan, L., Sun, C., and Shi, Y., 2017, Immobilization of phosphogypsum for cemented paste backfill and its environmental effect: Journal of Cleaner Production, v. 156, p. 137–146, doi:10.1016/j.jclepro.2017.04.046.

Li, B., Li, L., Chen, X., Ma, Y., and Zhou, M., 2022, Modification of phosphogypsum using circulating fluidized bed fly ash and carbide slag for use as cement retarder: Construction and Building Materials, v. 338, p. 127630, doi:10.1016/J.CONBUILDMAT.2022.127630.

Li, X., Zhou, S., Zhou, Y., Min, C., Cao, Z., Du, J., Luo, L., and Shi, Y., 2019a, Durability Evaluation of Phosphogypsum-Based Cemented Backfill Through Drying-Wetting Cycles: Minerals, v. 9, p. 321, doi:10.3390/min9050321.

Li, X., Zhou, Y., Zhu, Q., Zhou, S., Min, C., and Shi, Y., 2019b, Slurry preparation effects on the cemented phosphogypsum backfill through an orthogonal experiment: Minerals, v. 9, doi:10.3390/min9010031.

Liu, Y., Chen, Q., Dalconi, M.C., Molinari, S., Valentini, L., Wang, Y., Sun, S., Wang, P., and Artioli, G., 2022, Enhancing the sustainable immobilization of phosphogypsum by cemented paste backfill with the activation of γ-Al2O3: Construction and Building Materials, v. 347, p. 128624, doi:10.1016/J.CONBUILDMAT.2022.128624.

Liu, Y., Chen, Q., Wang, Y., Zhang, Q., Li, H., Jiang, C., and Qi, C., 2021a, In Situ Remediation of Phosphogypsum with Water-Washing Pre-Treatment Using Cemented Paste Backfill: Rheology Behavior and Damage Evolution: Materials 2021, Vol. 14, Page 6993, v. 14, p. 6993, doi:10.3390/MA14226993.

Liu, Z., Deng, Z., He, G., Wang, H., Zhang, X., Lin, J., Qi, Y., and Liang, X., 2021b, Challenges and opportunities for carbon neutrality in China: Nature Reviews Earth & Environment 2021 3:2, v. 3, p. 141–155, doi:10.1038/s43017-021-00244-x.

Liu, Z., Guan, D., Moore, S., Lee, H., Su, J., and Zhang, Q., 2015, Climate policy: Steps to China's carbon peak: Nature 2015 522:7556, v. 522, p. 279–281, doi:10.1038/522279a.

Liu, L., Xin, J., Qi, C., Jia, H., and Song, K.I.I.L., 2020a, Experimental investigation of mechanical, hydration, microstructure and electrical properties of cemented paste backfill: Construction and Building Materials, doi:10.1016/j.conbuildmat.2020.120137.

Liu, L., Yang, P., Qi, C., Zhang, B., Guo, L., and Song, K.I.I.L., 2019a, An experimental study on the early-age hydration kinetics of cemented paste backfill: Construction and Building Materials, v. 212, p. 283–294, doi:10.1016/J.CONBUILDMAT.2019.03.322.

Liu, Y., Zhang, Q., Chen, Q., Qi, C., Su, Z., and Huang, Z., 2019b, Utilisation of water-washing pre-treated phosphogypsum for cemented paste backfill: Minerals, v. 9, doi:10.3390/min9030175.

Liu, X., Zhong, H., Yang, Y., Yuan, L., and Liu, S., 2020b, Phosphorus removal from wastewater by waste concrete: influence of P concentration and temperature on the product: Environmental Science and Pollution Research, v. 27, p. 10766–10777, doi:10.1007/S11356-019-07577-7/FIGURES/8.

Lothenbach, B., Kulik, D.A., Matschei, T., Balonis, M., Baquerizo, L., Dilnesa, B., Miron, G.D., and Myers, R.J., 2019, Cemdata18: A chemical thermodynamic database for hydrated Portland cements and alkali-activated materials: Cement and Concrete Research, doi:10.1016/j.cemconres.2018.04.018.

Lothenbach, B., Matschei, T., Möschner, G., and Glasser, F.P., 2008a, Thermodynamic modelling of the effect of temperature on the hydration and porosity of Portland cement: Cement and Concrete Research, v. 38, p. 1–18, doi:10.1016/J.CEMCONRES.2007.08.017.

Lothenbach, B., Le Saout, G., Gallucci, E., and Scrivener, K., 2008b, Influence of limestone on the hydration of Portland cements: Cement and Concrete Research, v. 38, p. 848–860, doi:10.1016/J.CEMCONRES.2008.01.002.

Lütke, S.F., Oliveira, M.L.S., Silva, L.F.O., Cadaval, T.R.S., and Dotto, G.L., 2020, Nanominerals assemblages and hazardous elements assessment in phosphogypsum from an abandoned phosphate fertilizer industry: Chemosphere, v. 256, doi:10.1016/j.chemosphere.2020.127138.

Lydersen, E., Salbu, B., Polèo, A.B.S., and Muniz, I.P., 1991, Formation and dissolution kinetics of Al(OH)3 (s) in synthetic freshwater solutions: Water Resources Research, v. 27, p. 351–357,

doi:10.1029/90WR02409.

Maierdan, Y., Cui, Q., Chen, B., Aminul Haque, M., and Yiming, A., 2021, Effect of varying water content and extreme weather conditions on the mechanical performance of sludge bricks solidified/stabilized by hemihydrate phosphogypsum, slag, and cement: Construction and Building Materials, v. 310, p. 125286, doi:10.1016/J.CONBUILDMAT.2021.125286.

Mandel, S., and Tas, A.C., 2010, Brushite (CaHPO4·2H2O) to octacalcium phosphate (Ca8(HPO4)2(PO4)4·5H2O) transformation in DMEM solutions at 36.5 °C: Materials Science and Engineering: C, v. 30, p. 245–254, doi:10.1016/J.MSEC.2009.10.009.

Marchon, D., and Flatt, R.J., 2016, Impact of chemical admixtures on cement hydration: Science and Technology of Concrete Admixtures, p. 279–304, doi:10.1016/B978-0-08-100693-1.00012-6.

Mascarin, L., Ez-zaki, H., Garbin, E., Bediako, M., and Valentini, L., 2022, Mitigating the ecological footprint of alkali-activated calcined clays by waste marble addition: Cement and Concrete Composites, v. 127, p. 104382, doi:10.1016/J.CEMCONCOMP.2021.104382.

Matsuzawa, K., Atarashi, D., Miyauchi, M., and Sakai, E., 2017, Interactions between fluoride ions and cement paste containing superplasticizer: Cement and Concrete Research, v. 91, p. 33–38, doi:10.1016/j.cemconres.2016.10.006.

McQueen, N., Kelemen, P., Dipple, G., Renforth, P., and Wilcox, J., 2020, Ambient weathering of magnesium oxide for CO2 removal from air: Nature Communications, v. 11, p. 1–10, doi:10.1038/s41467-020-16510-3.

Medina-Martos, E., Gálvez-Martos, J.L., Almarza, J., Lirio, C., Iribarren, D., Valente, A., and Dufour, J., 2022, Environmental and economic performance of carbon capture with sodium hydroxide: Journal of CO2 Utilization, v. 60, p. 101991, doi:10.1016/J.JCOU.2022.101991.

Meskini, S., Samdi, A., Ejjaouani, H., and Remmal, T., 2021, Valorization of phosphogypsum as a road material: Stabilizing effect of fly ash and lime additives on strength and durability: Journal of Cleaner Production, doi:10.1016/j.jclepro.2021.129161.

Miller, S.A., Habert, G., Myers, R.J., and Harvey, J.T., 2021, Achieving net zero greenhouse gas emissions in the cement industry via value chain mitigation strategies: One Earth, v. 4, p. 1398–1411, doi:10.1016/J.ONEEAR.2021.09.011.

Min, C., Shi, Y., and Liu, Z., 2021, Properties of cemented phosphogypsum (PG) backfill in case of partially substitution of composite Portland cement by ground granulated blast furnace slag: Construction and Building Materials, doi:10.1016/j.conbuildmat.2021.124786.

Morandeau, A., Thiéry, M., and Dangla, P., 2014, Investigation of the carbonation mechanism of CH and C-S-H in terms of kinetics, microstructure changes and moisture properties: Cement and Concrete Research, v. 56, p. 153–170, doi:10.1016/J.CEMCONRES.2013.11.015.

Padilla-Encinas, P., Fernández-Carrasco, L., Palomo, A., and Fernández-Jiménez, A., 2022, Effect of alkalinity on early-age hydration in calcium sulfoaluminate clinker: Cement and Concrete Research, v. 155, p. 106781, doi:10.1016/J.CEMCONRES.2022.106781.

Parkhurst, D.L., and Appelo, C.A.J., 2013, Description of Input and Examples for PHREEQC Version 3 — A Computer Program for Speciation , Batch-Reaction , One-Dimensional Transport , and Inverse Geochemical Calculations.: U.S. Geological Survey Techniques and Methods, book 6, chapter A43,.

Radwan, M.M., and Heikal, M., 2005, Hydration characteristics of tricalcium aluminate phase in mixes containing β-hemihydate and phosphogypsum: Cement and Concrete Research, v. 35, p. 1601–1608, doi:10.1016/J.CEMCONRES.2004.06.037.

Rashad, A.M., 2017, Phosphogypsum as a construction material: Journal of Cleaner Production, v. 166, p. 732–743, doi:10.1016/j.jclepro.2017.08.049.

Ren, J., Zhang, L., Walkley, B., Black, J.R., and San Nicolas, R., 2022, Degradation resistance of different cementitious materials to phosphoric acid attack at early stage: Cement and Concrete Research, v. 151, doi:10.1016/J.CEMCONRES.2021.106606.

Saadaoui, E., Ghazel, N., Ben Romdhane, C., and Massoudi, N., 2017, Phosphogypsum: potential uses and problems–a review: International Journal of Environmental Studies, doi:10.1080/00207233.2017.1330582.

Saedi, A., Jamshidi-Zanjani, A., and Darban, A.K., 2020, A review on different methods of activating tailings to improve their cementitious property as cemented paste and reusability: Journal of Environmental Management, v. 270, p. 110881, doi:10.1016/j.jenvman.2020.110881.

Salvador, R.P., Cavalaro, S.H.P., Cano, M., and Figueiredo, A.D., 2016, Influence of spraying on the early hydration of accelerated cement pastes: Cement and Concrete Research, v. 88, p. 7–19, doi:10.1016/J.CEMCONRES.2016.06.005.

Scholtzová, E., Kucková, L., Kožíšek, J., and Tunega, D., 2015, Structural and spectroscopic characterization of ettringite mineral –combined DFT and experimental study: Journal of Molecular Structure, v. 1100, p. 215–224, doi:10.1016/J.MOLSTRUC.2015.06.075.

Scrivener, K.L., and Nonat, A., 2011, Hydration of cementitious materials, present and future: Cement and Concrete Research, v. 41, p. 651–665, doi:10.1016/J.CEMCONRES.2011.03.026.

Secco, M., Lampronti, G.I., Schlegel, M.C., Maritan, L., and Zorzi, F., 2015, Degradation processes of reinforced concretes by combined sulfate–phosphate attack: Cement and Concrete Research, v. 68, p. 49–63, doi:10.1016/J.CEMCONRES.2014.10.023.

Shi, Y., Cheng, L., Tao, M., Tong, S. Sen, Yao, X., and Liu, Y., 2021, Using modified quartz sand for phosphate pollution control in cemented phosphogypsum (PG) backfill: Journal of Cleaner Production, doi:10.1016/j.jclepro.2020.124652.

Silva, L.F.O., Oliveira, M.L.S., Crissien, T.J., Santosh, M., Bolivar, J., Shao, L., Dotto, G.L., Gasparotto, J., and Schindler, M., 2022, A review on the environmental impact of phosphogypsum and potential health impacts through the release of nanoparticles: Chemosphere, doi:10.1016/j.chemosphere.2021.131513.

Singh, M., 2003, Effect of phosphatic and fluoride impurities of phosphogypsum on the properties of selenite plaster: Cement and Concrete Research, doi:10.1016/S0008-8846(03)00068-1.

Steiner, S., Lothenbach, B., Proske, T., Borgschulte, A., and Winnefeld, F., 2020, Effect of relative humidity on the carbonation rate of portlandite, calcium silicate hydrates and ettringite: Cement and Concrete Research, v. 135, p. 106116, doi:10.1016/J.CEMCONRES.2020.106116.

Tsioka, M., and Voudrias, E.A., 2020, Comparison of alternative management methods for phosphogypsum waste using life cycle analysis: Journal of Cleaner Production, v. 266, p. 121386, doi:10.1016/j.jclepro.2020.121386.

Wang, F. et al., 2021, Technologies and perspectives for achieving carbon neutrality: The Innovation, v. 2, p. 100180, doi:10.1016/J.XINN.2021.100180.

Wang, F., Kong, X., Jiang, L., and Wang, D., 2020, The acceleration mechanism of nano-C-S-H particles on OPC hydration: Construction and Building Materials, v. 249, p. 118734, doi:10.1016/J.CONBUILDMAT.2020.118734.

Wang, Y., Shi, C., Lei, L., Ma, Y., Liu, J., and Hu, X., 2022, Formulation of an alkali-free accelerator and its effects on hydration and mechanical properties of Portland cement: Cement and Concrete Composites, v. 129, p. 104485, doi:10.1016/J.CEMCONCOMP.2022.104485.

Winnefeld, F., and Lothenbach, B., 2010, Hydration of calcium sulfoaluminate cements — Experimental findings and thermodynamic modelling: Cement and Concrete Research, v. 40, p. 1239–1247, doi:10.1016/J.CEMCONRES.2009.08.014.

Xie, Y., Sun, T., Shui, Z., Ding, C., and Li, W., 2022, The impact of carbonation at different CO2 concentrations on the microstructure of phosphogypsum-based supersulfated cement paste: Construction and Building Materials, v. 340, doi:10.1016/J.CONBUILDMAT.2022.127823.

Xu, J., Fan, L., Xie, Y., and Wu, G., 2019, Recycling-equilibrium strategy for phosphogypsum pollution control in phosphate fertilizer plants: Journal of Cleaner Production, v. 215, p. 175–197, doi:10.1016/j.jclepro.2018.12.236.

Yang, R., and He, T., 2021, The accelerating mechanism of alkali free liquid accelerator based on fluoroaluminate for shotcrete: Construction and Building Materials, v. 274, p. 121830, doi:10.1016/J.CONBUILDMAT.2020.121830.

Yang, Z., Sui, S., Wang, L., Feng, T., Gao, Y., Mu, S., Tang, L., and Jiang, J., 2020, Improving the chloride binding capacity of cement paste by adding nano-Al2O3: The cases of blended cement pastes:

Construction and Building Materials, doi:10.1016/j.conbuildmat.2019.117219.

Ye, X., 2020, Status and situation analysis of phosphogypsum utilization in China in 2019: Phosphate & Compound Fertilizer, v. 35, p. 1–3.

Zarzuela, R., Luna, M., Carrascosa, L.M., Yeste, M.P., Garcia-Lodeiro, I., Blanco-Varela, M.T., Cauqui, M.A., Rodríguez-Izquierdo, J.M., and Mosquera, M.J., 2020, Producing C-S-H gel by reaction between silica oligomers and portlandite: A promising approach to repair cementitious materials: Cement and Concrete Research, v. 130, p. 106008, doi:10.1016/J.CEMCONRES.2020.106008.

Zhang, J., and Scherer, G.W., 2011, Comparison of methods for arresting hydration of cement: Cement and Concrete Research, v. 41, p. 1024–1036, doi:10.1016/J.CEMCONRES.2011.06.003.

Zhao, F., Hu, J., Yang, Y., Xiao, H., and Ma, F., 2022, Cross-Scale Study on Lime Modified Phosphogypsum Cemented Backfill by Fractal Theory: Minerals 2022, Vol. 12, Page 403, v. 12, p. 403, doi:10.3390/MIN12040403.

Zhao, H., Li, H., Bao, W., Wang, C., Li, S., and Lin, W., 2015, Experimental study of enhanced phosphogypsum carbonation with ammonia under increased CO2 pressure: Journal of CO2 Utilization, v. 11, p. 10–19, doi:10.1016/J.JCOU.2014.11.004.

Zhao, Y., Qiu, J., Zhang, S., Guo, Z., Wu, P., Sun, X., and Gu, X., 2021, Low carbon binder modified by calcined quarry dust for cemented paste backfill and the associated environmental assessments: Journal of Environmental Management, v. 300, p. 113760, doi:10.1016/J.JENVMAN.2021.113760.

Zhou, S., Li, X., Zhou, Y., Min, C., and Shi, Y., 2020, Effect of phosphorus on the properties of phosphogypsum-based cemented backfill: Journal of Hazardous Materials, doi:10.1016/j.jhazmat.2020.122993.

Zhou, J., Zheng, K., Liu, Z., and He, F., 2019, Chemical effect of nano-alumina on early-age hydration of Portland cement: Cement and Concrete Research, doi:10.1016/j.cemconres.2018.11.007.

Supporting information for Chapter 6

The sponge effect of phosphogypsum-based cemented paste backfill in the ambient carbon capture with a focus on the early hydration

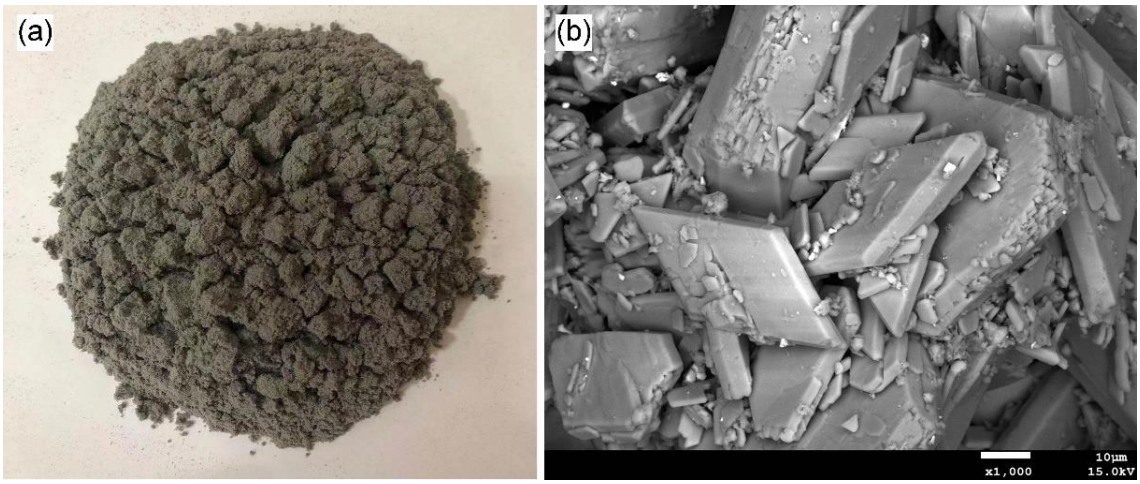

Figure.S1. Images of PG sample. (a) The fresh state of PG and (b) SEM graph of PG demonstrate the presence of gypsum.

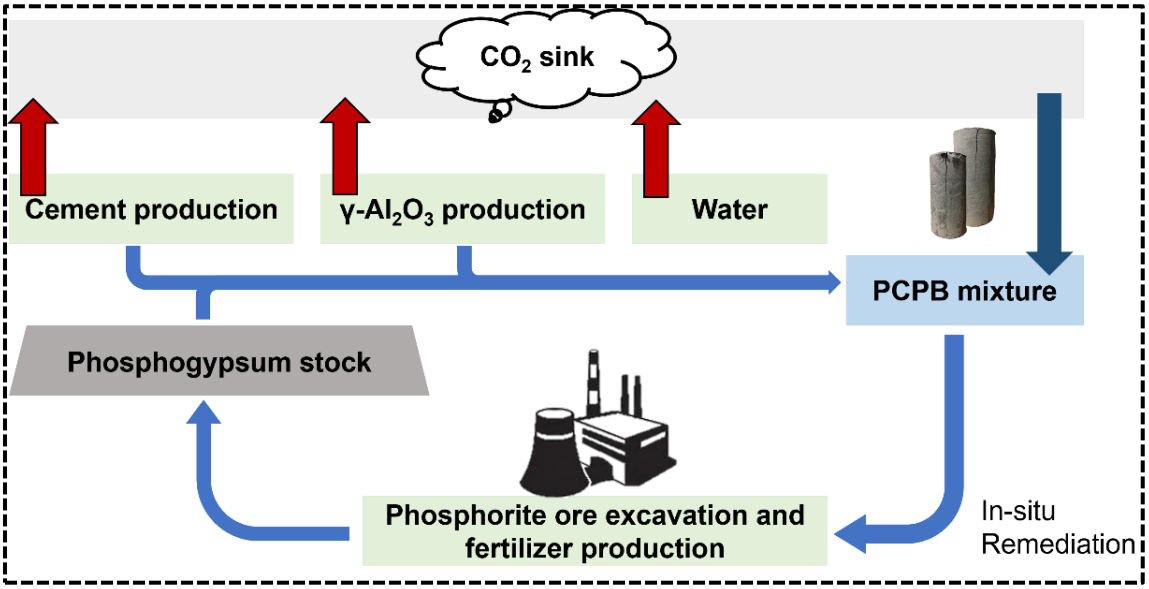

Figure.S2. CO_2 input-output source diagram

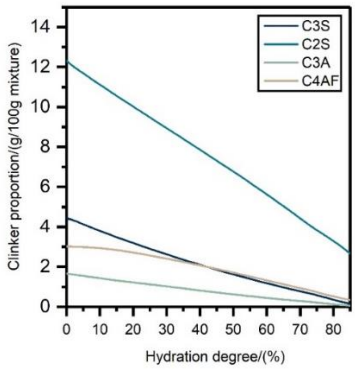

Figure.S3. Estimated hydration degree based on the model proposed by (Lothenbach et al., 2008a, 2008b; Holmes et al., 2022)**.**

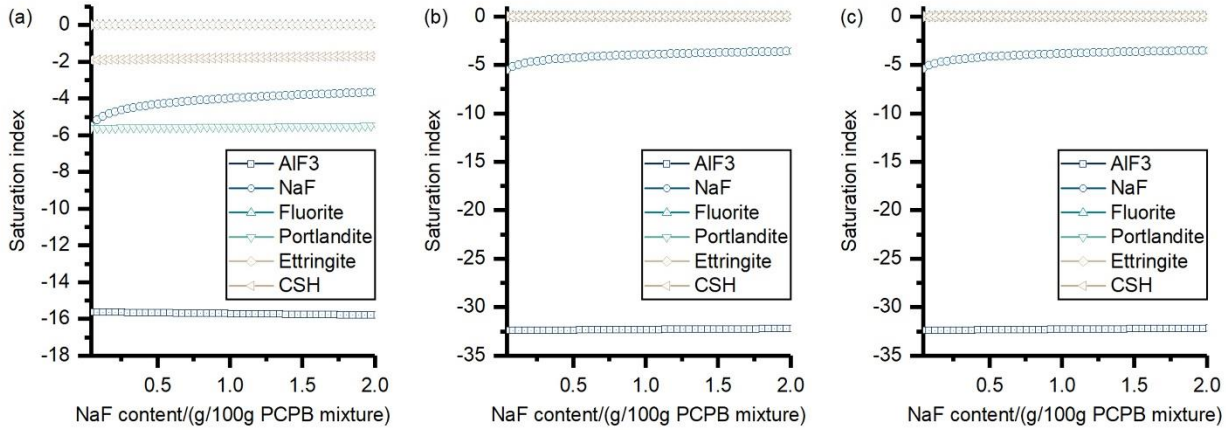

Figure.S4. SI of fluorides and hydration products at hydration degree with the impacts of NaF contents. (a) 5% hydration degree, (b) 20% hydration degree, and (c) 50% hydration degree.

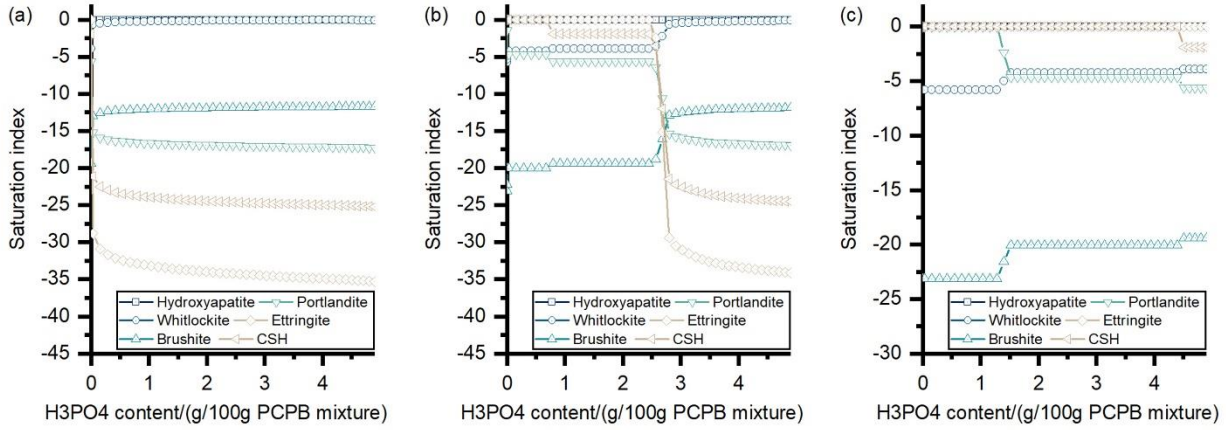

Figure.S5. SI of phosphates and hydration products at hydration degree with the impacts of H_3PO_4 contents. (a) 5% hydration degree, (b) 20% hydration degree, and (c) 50% hydration degree.

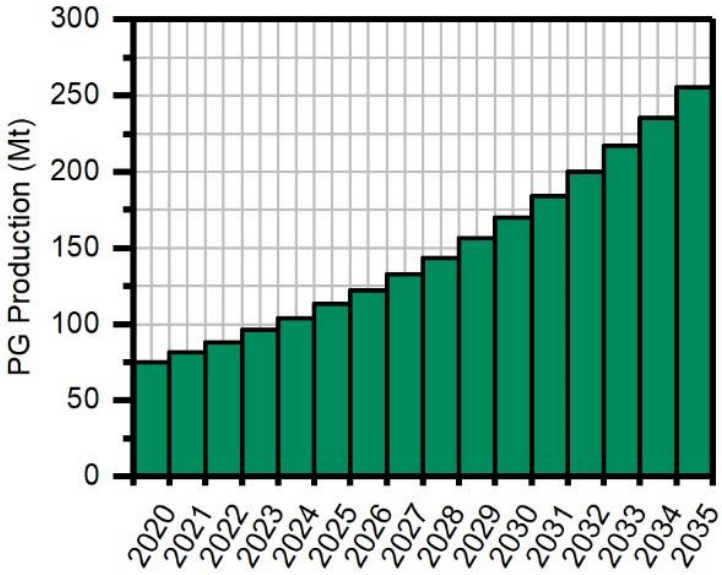

Figure.S6. Estimated PG annual production.

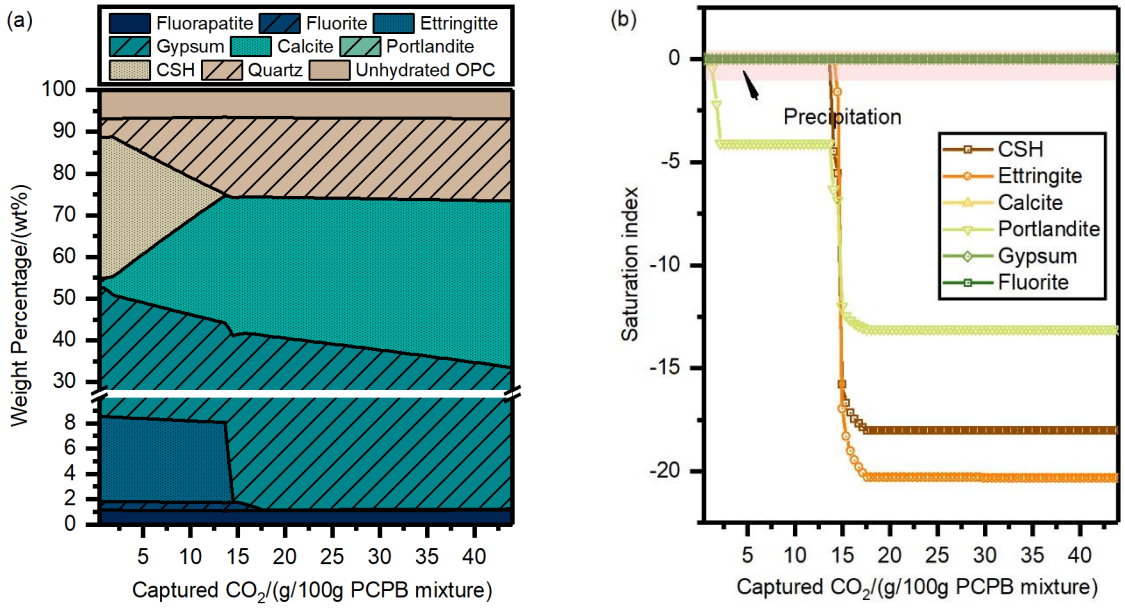

Figure.S7. SI evolution with the H_3PO_4 content of which the hydroxyapatite is included. (a) Weight percentages of the phases and (b) saturation index of the P-bearing phases, portlandite, C-S-H, and ettringite.

Table.S1. Brand of the agents (analytical grade) used in this work.

Agent	Sources
γ-Al_2O_3	Guangzhou nano chemical technology co., Ltd
NaF	Xilong Scientific co., Ltd
P_2O_5	Tianjin Fuchen chemical reagent factory
gypsum	Tianjin Kermal Chemical Reagent Co., Ltd
quartz	Tianjin Kermal Chemical Reagent Co., Ltd

Table.S2. XRD instrument settings

Labels	Parameters
Equipment	Bruker D8 ADVANCE
Radiation source	Copper, Ni filtered
Detector	LYNXEYE XE-T
Geometry	Bragg-Brentano
Soller Slits	2.5
Divergence Slit	0.20
Antiair scatter degree (Å)	2.24
Goniometer_radius	280 mm
2θ range	4 ~ 80 °
Step size	0.02 °
Time per step	28.8 s

Table.S3. The normalized oxide weight percentage of PG and OPC samples.

Species	PG (wt%)	OPC (wt%)
F	0.81	0.00
MgO	0.00	2.31
Al_2O_3	0.71	5.23
SiO_2	5.32	22.72
P_2O_5	1.08	0.00
SO_3	54.10	3.88
K_2O	0.00	0.82
CaO	37.35	60.91
Fe_2O_3	0.63	4.12

Table.S4. Modeling input associated with Fig.6 and S7 (g/100g PCPB mixture)

Phases	Weight percentage
Unhydrated OPC	6.6
Calcite	/
Portlandite	3.5
Quartz	4.2
Gypsum	45.2
Ettringite	6.5
NaF	0.8
H_3PO_4	0.6
Amorphous	32.5

Table.S5. Possible assignments of FTIR spectra

Wavenumber/(cm^{-1})	Possible assignments
510	vibration of Si-O
599	vibration of SO_4
668	vibration of SO_4
873	symmetric stretching vibration of C–O
919	HPO
1004	vibration of SO_4 AND bending vibration of CO_3
1109	vibration of SO_4
1417	Asymmetric stretching of CO_3
1621	υ2 (H2O)
1682	υ2 (H2O)
3400	υ2 (H2O)
3520	υ2 (H2O)

Chapter 7

Conclusions and future perspectives

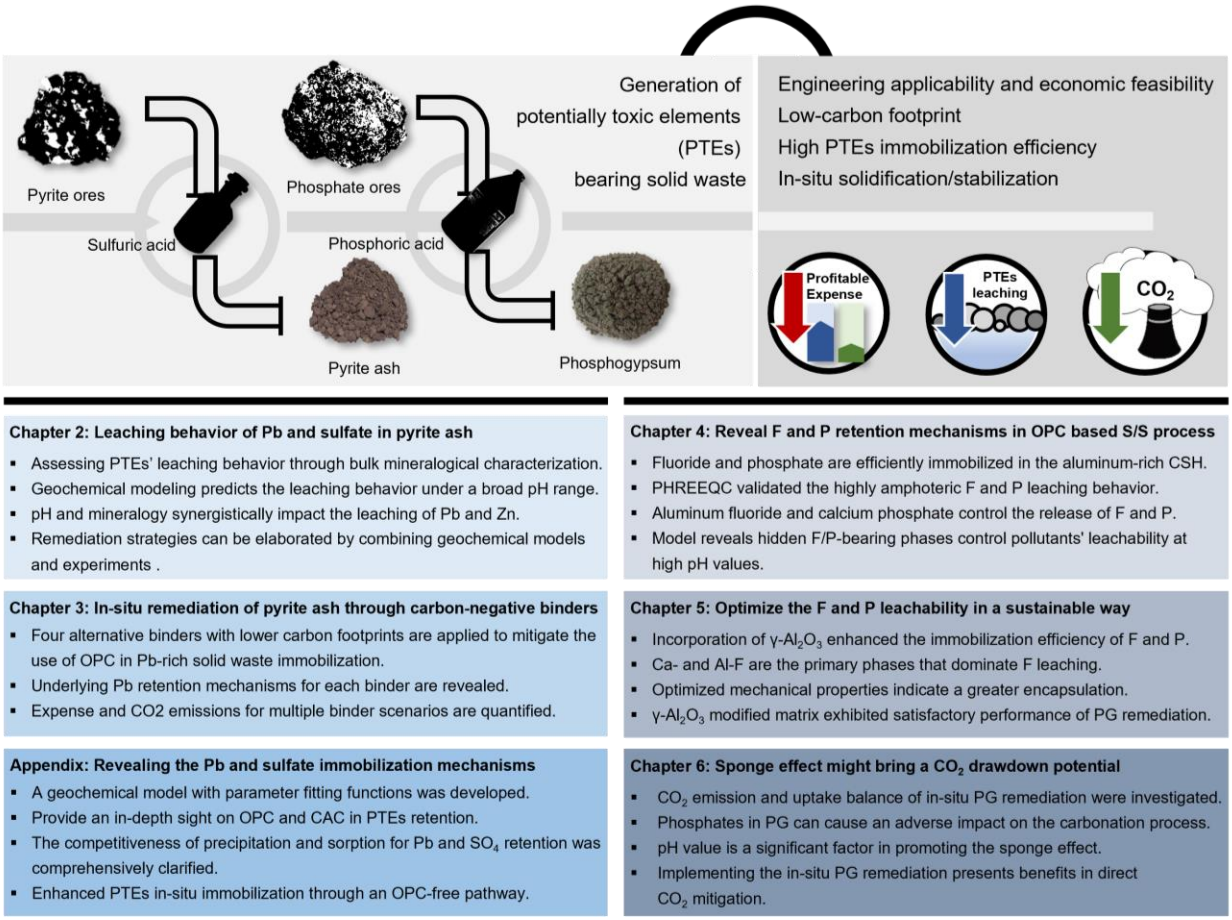

The accumulation of potentially toxic elements (PTEs) in the soil body is a perilous and crucial obstacle to achieving the sustainable stewardship of ecosystems, which has garnered significant attention. Moreover, the PTEs can cause seriously impaired neurological disorders and life-threatening cancers after entering the human body by inadvertently ingesting contaminated soil and contaminated crops. In this work, the application of in-situ solidification/stabilization (S/S) is a promising technology that can treat the PTEs containing solid waste profitably and scalably. Using the low-carbon binders, including CEM III/B, calcium aluminate cement (CAC), mayenite-ground granulated blast-furnace slag (GGBFS) mixture (MAY), alkaline activated GGBFS (ABS), and γ-Al_2O_3, to partially or entirely replace the use of ordinary Portland cement (OPC) has been proven a highly hope strategy that promotes the PTEs remediation efficiency and

bridges the gap between carbon-neutral world rhetoric and the reality of solid waste remediation applications. The developed geochemical modeling has prompted the possibility of an in-depth investigation for in-situ remediation in industrial sites by evaluating the PTEs leachability and the sponge effect of S/S products. The overall findings shed light on the understanding of PTEs immobilization mechanisms in multiple alternative sustainable binders, highlighting the significance of the perspectives of carbon neutrality in the emission-intensive S/S applications and providing new insights into the highly efficient S/S of contaminated wastes. The main conclusions of each chapter are as follows:

In **Chapter 2**, the characterization results demonstrate that Pb and Zn are the most abundant heavy metal pollutants within the collected pyrite ash samples. With the XRD, SEM/EDS, and Raman investigation, anglesite and kintoreite have been confirmed as the primary Pb-bearing crystalline phases, which may be generated from the oxidation of remaining pyrite particles. In addition, the jarosite could be a heavy metal hoster, as the Pb or Zn-incorporated jarosite was characterized along the edge of the hematite particles. The pH-dependent leaching tests and geochemical modeling reveal that the Pb and Zn leachability strongly depends on the pH values of the leachates, with a downward trend towards the near-neutral pH region from 6 to 10. At acid conditions, the increased solubility of Pb is dominated by the dissolution of anglesite and the formation of Pb nitrate complexes, while Zn is controlled by Zn ions and Zn-sulfate complexes in the solution. In contrast, when the pH values move to strong alkaline conditions, the upward trend could be associated with the complexation of aqueous metal hydrates. Noteworthy, the results indicate that even under normal conditions (for instance, normal rainfall), the stockpile of pyrite ash poses a great environmental risk and strongly threatens human health, which only worsens under acidic or alkaline conditions. Herein, integrating profitable and sustainable remediation technologies in the contaminated site is critically essential to prevent further pollution.

In **Chapter 3**, we found that the use of OPC is insufficient for efficient Pb immobilization due to the high alkaline conditions of the soil-binder system resulting from the dissolution of clinker phases, which may interfere with Pb precipitation. Meanwhile, the substantial carbon footprint attributed to OPC production also places critical scrutiny on this scenario. Although the CAC binder incorporation provides a promising Pb immobilization efficiency, the less satisfactory ecological benefits and the relatively high carbon footprint diminish the trial application of CAC. The CEM III/B binder tends to be a comprehensively sustainable and profitable strategy due to its excellent compatibility with Pb and relatively low-carbon nature. The experimental results indicate that aside from the Pb incorporation in the binding matrix similar to the OPC-soil system, the formation of low Ca/Si ratio C-(A)-S-H gel promoted the Pb retention, fulfilling the Pb leachability requirements for reuse as S/S material. Furthermore, the quantified sponge effect of CEM III/B incorporated pellets suggests that it would

promote the achievement of carbon neutrality. Overall, the works in this chapter provided useful guidance for improving the design and application of cement-free pathways for sustainable solid waste amendment, which bridged the gap between carbon-neutral world rhetoric and the reality of solid waste remediation applications.

In **Chapter 4**, based on the conducted XRD characterization, the phosphogypsum used in this work is mainly composed of gypsum, bassanite, and anhydrite generated from the acidulation process and recrystallization process during stockpiling. Minor contents of silicates (quartz, muscovite, and feldspar) and phosphate-containing phase (scorzalite) were quantified, of which the former is attributed to the remained gangue minerals in phosphate rock after acidulation. The detailed SEM investigation demonstrates that the distribution of fluorides and phosphates is likely related to the silicates through incorporation or complexation. In addition, the formation of the Al-Si-F-P-O complex could be attributed to the weathering of aluminosilicates, thus representing a crucial problem for the phosphogypsum repositories due to the fluorides mobilization with the clay soils or clay liners. With the S/S of OPC, the SEM and EMPA investigation indicates that the immobilization of fluorides and phosphates is mainly attributed to the aluminum-rich binding matrix, which could be an aluminum-rich C-S-H gel or a mixture of C-S-H and ettringite. The leaching tests and geochemical modeling reveal that despite a significant reduction of contaminants leaching in the stabilized products being observed, the F and P leaching behavior is still highly amphoteric in both the stabilized and unstabilized phosphogypsum. Mineralogical evidence from simulations points out that calcium phosphate, fluorophosphate, and calcium fluoride are the forms likely to control pollutant release.

In **Chapter 5**, the overall results proved that the utilization of γ-Al2O3 can expand the scalable application of phosphogypsum with a greater pollutants retention capacity (fluoride leaching of OPC-phosphogypsum mixture is 24.1 mg/L at pH 2.1 and γ-Al_2O_3-OPC-phosphogypsum mixture is 1.0 mg/L at pH 1.1) and mechanical properties. The XRD investigation demonstrates that the incorporation of the γ-Al_2O_3 agent in the OPC-phosphogypsum system promoted the precipitation of crystalline ettringite and aluminum-containing amorphous due to the high Al concentration in the pore solution as a result of the rapid dissolution of γ-Al_2O_3. In addition, the compressive strength of γ-Al_2O_3 incorporated samples has been optimized, fulfilling the mechanical strength requirement of engineering applications. Further, similar to the OPC-phosphogypsum system, SEM/EDS results indicate that the Ca-Si-containing phases take the role of F and P retention in the γ-Al_2O_3 incorporated samples. Further, the pH-dependent leaching tests demonstrate that the γ-Al_2O_3 agent decreased the F leaching in acid conditions, even if the harsh acid pH conditions are unsuitable for the stability of hydration products. The geochemical modeling approach provides qualitative support for determining the role of hardly detectable F- and P-containing phases and

describing the amphoteric leaching profiles, highlighting the importance of aluminum components in controlling fluorine leaching at acid conditions through the forms of the AlF complex. Moreover, the quantified carbon footprint for using the γ-Al_2O_3 to partially replace the use of OPC could significantly reduce the total CO_2 emissions of phosphogypsum S/S remediation by approximately 35%, decreasing from 856 to 556 kg CO_2/t, indicating that it could be a promising agent for financially profitable carbon-negative immobilization materials.

In **Chapter 6**, we revealed the impacts of fluorides and phosphates on the early ages of cement hydration and quantified the carbon uptake and storage capacity of the in-situ phosphogypsum remediation. The experimental results suggest that fluorides promote early ages hydration, whereas phosphates tend to bring adverse effects. The former positive influence could be attributed to the calcium-fluoride complex, which accelerates the dissolution of clinker phases to retain a calcium-rich system. In contrast, the retard mechanisms of phosphates are possibly related to the formation of calcium-phosphate coatings, which deposit on cement particle surfaces and accordingly prolong the hydration process. Noteworthy, by comparing the results from the phosphogypsum-based mixtures and control groups, the retard effect of phosphates and acid pH values of phosphogypsum dominate the roles of the seesaw battle, although the acceleration impact of fluorides simultaneously controls the hydration process. The carbon footprint assessment shows that, for recycling 1 tonne of phosphogypsum, the mixture preparation process directly brings 466 kg of CO_2 emission. With the growing demand for phosphates fertilizer, it is estimated that the CO_2 emission may reach 16.7 Mt/year for safeguarding the phosphogypsum reserves, accounting for 1.9 ‰ of CO2 emission in the cement industry in China. Aside from the CO_2 emissions related to the start of life, the sponge effect of the phosphogypsum-based mixture may partially mitigate this considerable carbon footprint. Herein, based on the geochemical modeling approach and the experimentally quantified calcium carbonates fraction, we further evaluated the CO_2 uptake capacity of the systems. The overall findings indicate that alkalinity plays a primary role in controlling the sponge effect. Even with a low concentration but continuous NaOH supply, the CO_2 capture capacity was significantly enhanced. The dual role could capture ranging from 10% to 35% of CO_2 released, promisingly reducing net direct emissions by up to 5.76 Mt, equivalent to approximately 14% of the global commercial carbon capture and storage goal in 2020. The methodology proposed in this work may have an important impact on designing the sustainable solid waste amendment from the perspectives of credible social needs, environmental requirements, and technical feasibility.

Overall, our study provided useful guidance for designing cement-free pathways to facilitate sustainable solid waste management practices, embracing a more carbon-neutral resolution. However, several issues should be carefully addressed before the following broader implementation.

Future works will be required to reveal uncertainties in the stability of disrupted stabilized products and further evaluate the potential eco-toxicity after long-term adopted practices in diverse regional soil hydrology environments. Currently, the determination of the PTEs retention efficacy is primarily based on short-term leaching tests. Although this procedure can partially reflect the resistance of stabilized products to harsh conditions, long-term leaching tests are also essential for ensuring the stability of the structures. Especially considering the concerns from the wide socio-environments underlie the potential audience of these advanced technologies, including the stakeholders, the policymakers, and clients, using multifaceted performance determination to convince the public is an important factor for prioritizing the in-situ remediation.

Another pitfall that could be attributed to the geochemical modeling construction is how to couple the theoretically existing physical encapsulation to the proposed system, which requires fully integrating the multiple mechanisms. The porosity, durability, and integrity of the immobilized products have been widely reported to significantly influence the PTEs retention capacity. The proposed model is mainly based on the bulk chemical characterization of the samples and does not comprehensively consider the influence of physical properties. Herein, the deviation between the experimental leaching data and simulated results is presented in all the studies, which could be partially related to the physical encapsulation. Therefore, the following works on revealing the physical profile would allow a more consistent description of the solid waste-binder systems.

In addition, there is a need for unifying and estimating the adsorption mechanism, which offers a unique opportunity to advance the constructed model. Although in this work, some attempts toward solving this problem rely on the adsorption dataset from chloride, the large gaps between the measurements and predictions emphasize that future research should be conducted on the specific dataset, either through the laboratory (e.g., PTEs adsorption experiments) or simulations (e.g., bid data analysis or machine leaching).

Appendices

Comprehensive understanding of the Pb and sulfates retention in ordinary Portland cement and calcium aluminate cement: clarifying and quantifying the contributions from binders and solid waste.

Yikai Liu[1]; Simone Molinari[1]; Maria Chiara Dalconi[1]; Luca Valentini[1]; Maurizio Pietro Bellotto[2]; Giorgio Ferrari[3]; Roberto Pellay[4]; Graziano Rilievo[5]; Fabio Vianello[5]; Gabriella Salviulo[1]; Gilberto Artioli[1]

1 Department of Geosciences and CIRCe Centre, University of Padua, via G. Gradenigo 6, 35129, Padua, Italy

2 OPIGEO Srl, Montegalda, Vicenza, Italy

3 Mapei S.p.A., via Cafiero 22, 20158, Milan, Italy

4 TEVGroup S.r.l., via Romea 8, 30034, Mira (Venice), Italy

5 Department of Comparative Biomedicine and Food Science, University of Padova, Viale dell'Università 16, 35020 Legnaro, Italy

Abstract

Solidification/stabilization of potentially toxic elements (PTEs) is the biggest challenge raised in the field extrapolation of this technology. While the general PTEs immobilization mechanisms may be revealed based on demanding and broad characterization, there is a need to address quantitatively the underlying mechanisms attributed to each mineralogical phase within the stabilized products. Herein, we proposed a geochemical model with parameter-fitting techniques to reveal the solidification/stabilization of Pb-rich pyrite ash through a traditional (ordinary Portland cement) and an alternative (calcium aluminate cement) binder. We find that ettringite and C-S-H both demonstrate strong affinities for Pb at basic conditions. Partly soluble Pb may be immobilized as $Pb(OH)_2$ when hydration products are insufficient. At acid and neutral conditions, hematite from pyrite ash and newly-formed ferrihydrite are the main controls of Pb, along with anglesite and cerussite precipitation. Thus, this work provides a much-needed complement to this widely-applied technique for detecting PTEs leaching behavior.

1. Introduction

The stockpile of potentially toxic elements (PTEs) containing solid waste is an inevitable consequence of jumping global anthropogenic activities, which has become one of the most widespread and critical problems worldwide (Xia et al., 2019; Wang et al., 2019). Many works have shown that the excessive accumulation of PTEs can cause carcinogenic and poisoning effects on biota, thus harming ecosystems (Sun et al., 2022; Tang et al., 2022). For instance, the intake of Pb can cause various life-threatening cancers (Hou et al., 2020), and the over-inhalation of sulfates may impair the human taste and laxatives (Torres-Martínez et al., 2020). Considering the ubiquitous presence of PTEs in the earth's upper crust (Kumpiene et al., 2019), many attempts have been made to avoid the occasional inhalation or inadvertent ingestion of these contaminants.

The in-situ solidification/stabilization (S/S) is recognized as an efficient and practicable remediation strategy with great potential to be extrapolated in field trials (Contessi et al., 2020; Guo et al., 2021). Generally, ordinary Portland cement (OPC) represents the prevailing binder extensively used in the S/S process (Guo et al., 2017), but recent studies within this decade have highlighted the importance of mitigating the use of OPC in order to entail reaching net-zero emissions and accessing the 2015 Paris Agreement (Yin et al., 2018; Chen et al., 2022c; De Kleijne et al., 2022). Therefore, a growing body of evidence has shown that developing alternative low-carbon binders is a crucial way to reduce the CO_2 emission related to the S/S process being estimated that over 60% of greenhouse gas emission of OPC is from raw material (limestone) calcination reaction (Chen et al., 2022b). The researchers have raised ever-increasing attention to the use of alternative binders for PTEs immobilization, such as kaolinite (Contessi et al., 2020), biochar (Wang et al., 2020), calcium aluminate cement (CAC) (Chen et al., 2021b), granulated blast furnace slag (Wang et al., 2022a). However, unlike the well-established OPC system, the controls of PTEs in alternative pathway immobilized systems remain poorly known (Hossain et al., 2020). The PTEs fate is still a matter of debate despite it is well known that the S/S process diminishes the mobility of the toxic elements predominantly in two manners (1) coprecipitation and adsorption by hydration products and (2) micro- or macro-encapsulation and chemical fixation (Ouhadi et al., 2021). Most importantly, the binder-waste assemblage is highly sensitive to the pH values, which is driven by many factors such as the mineralogical composition, the dissolution of the complexes (e.g., Pb hydroxides and Zn hydroxides), and the interaction with percolating rainwater (Appelo et al., 2014; Yin et al., 2018). Furthermore, the Pb leaching at acid conditions could be several magnitudes (10^4 or 10^5) higher than in neutral pH conditions (Contessi et al., 2020). Therefore, characterizing the PTEs leaching behaviors and the associated mechanisms over a broad pH range is fundamental in tailoring the field application (Malviya and Chaudhary, 2006; Contessi et al., 2020). However, relevant empirical analysis to reveal the underlying mechanisms

responsible for the leaching behavior of constituents remains largely lacking.

Based on several recent undertaken research, the geochemical modeling approach could disentangle how this coupling operates, where insights can be gained through the use of pH-dependent leaching tests coupled with geochemical speciation modeling (Jarošíková et al., 2018; Du et al., 2019; Sun et al., 2019; Chen et al., 2021c). In systemic studies, the dissolution/precipitation equilibrium of the PTEs containing phases and the cementitious assemblages is assumed to be the primary mechanism for the leaching behavior of the PTEs. Although there is strong evidence that the ion exchange and adsorption also play a critical role in controlling the PTEs release, for instance, the Pb could be incorporated into the ettringite structure (Contessi et al., 2021) and adsorbed onto the surface of C-S-H/C-A-S-H gel (Liu et al., 2021; Chen et al., 2022b). The reconstruction of these processes in geochemical modeling is still fragmented and poorly constrained (Vega-Garcia et al., 2021; Zavarin et al., 2022). This is because the representativeness of the modeling is limited by the amount of available data from the thermodynamic database (Lu et al., 2022; Holmes et al., 2022). These knowledge gaps hinder the development of a fundamental understanding of the controls on PTEs liberation and migration.

To contribute to filling in these gaps, the main objectives of this work are: (1) elucidate the roles of traditional (OPC) and alternative (CAC) binders in Pb retention to investigate the possibility of using cement-free pathways to reduce the great greenhouse gas emissions associated with OPC application and (2) integrate the insights of adsorption and ion exchange mechanisms controlling Pb mobilization. To achieve these goals, pyrite ash (PA) was characterized to explore its mineralogical composition and the source of Pb. Subsequently, the Pb retention performance of S/S immobilized PA in both traditional and alternative ways is evaluated by X-ray diffraction (XRD) analyses, scanning electron microscopy/energy dispersive spectroscopy (SEM/EDS) investigation, and pH-dependent leaching tests. Further, the PA-binder assemblages after the leaching tests were collected to quantify mineral phase dissolution and formation repricipitation. Finally, with the thorough characterization of the partitioning of chemical species, we constructed geochemical modeling coupled with the Parameter Estimation software (PEST). The Pb leaching behavior and the associated modeled retention mechanisms and experimental observations should be as close as possible. The result of this paper demonstrates the feasibility of using the cement-free pathway to immobilize the PA and, indeed, mitigate the use of OPC. Further, it provides a reliable methodology to guide the development and test the plausibility of conceptual and numerical models of Pb mobilization and transport, even with a limited dataset, which may help improve the in-situ application of S/S technologies.

2. Materials and methods

2.1. Sampling and pelletization process

The PA is collected from an abandoned factory in Ancona, Italy, which was devoted to the pyrite (FeS_2) roasting process to produce sulfuric acid. Before the following S/S process, the sample was air-dried and passed through a 2 mm mesh sieve. The binders used in this work are OPC (CEM I 52.5 R, Barbetti S.p.A., Italy) and CAC (Gorkal 70, Mapei S.p.A., Italy). The high-performance S/S process® (Bonomo et al., 2009; Contessi et al., 2020) was applied to pelletize the PA and binder. The exact mixture proportion is given in Table.1, with the water-to-solid (binder+PA) ratio being kept at 0.23, which is within the typical range (approximately 0.2) in the S/S process for contaminated solid matrices (Wang et al., 2022b). After pelletization, the samples were sealed in plastic bags for 28 days under ambient conditions and then sieved to a diameter range between 2 and 10 mm (Fig.S1).

Table.1. The components proportion of pellets (wt%)

Label	PA (dry)	OPC (dry)	CAC (dry)	Water	Water/Solid ratio
OPP	65.2	16.4	-	18.4	0.23
CAP	64.9	-	16.3	18.8	0.23

*Note: the solid represents the weight accumulation of binder (OPC or CAC) and PA

2.2. Characterization methods

The mineral phases of selected samples were identified by X-ray diffraction (Malvern Panalytical X'Pert Pro diffractometer, UK) with a stepwise of 0.02° and a scanning range of 3° to 84° 2θ. Samples were ground in an agate mortar and micronized in a McCrone micronizing mill for 5 mins. To quantify the amorphous content in the pellets, 10 wt% of zincite (ACS Reagent, Thermo Fisher Scientific Inc., Waltham, USA) was mixed with the powdered samples as an internal standard. SEM/EDS investigation (CamScan MX3000, Applied Beams, USA) was used to characterize the polished and carbon-coated PA, OPP, and CAP samples.

2.3. Leaching procedures and ions concentration determination

The pH-dependent leaching tests were performed on the sieved soil following the EN 14429:2015 (British Standards Institution, 2015) standard, consisting of a series of parallel batch extractions tests with increasing pH values. The analytical reagent nitric acid (HNO_3) or sodium hydroxide (NaOH) was used to adjust the pH values of the leachate. The collected eluates were filtered at 0.45 μm and analyzed for element concentrations (Pb, Al, Fe, and SO_4) by ICP-MS. The amount of acid/basic agent used for the pH-dependent leaching tests is given in Fig.S3.

2.4. Geochemical modeling construction

PHREEQC (Dijkstra et al., 2002; Parkhurst and Appelo, 2013; Appelo et al., 2014) and PEST++ (Doherty, 2015) software were used to calculate the thermodynamically stable phases and identify the possible retention mechanisms (precipitation, adsorption, and ion exchange) during the leaching tests. The databases

applied in this work include the cement-specific database CEMDATA18 (Lothenbach et al., 2019) and the extended database PHREEQCDAT (Appelo et al., 2014). A schematic of the developed modeling algorithms is shown in Fig.1.

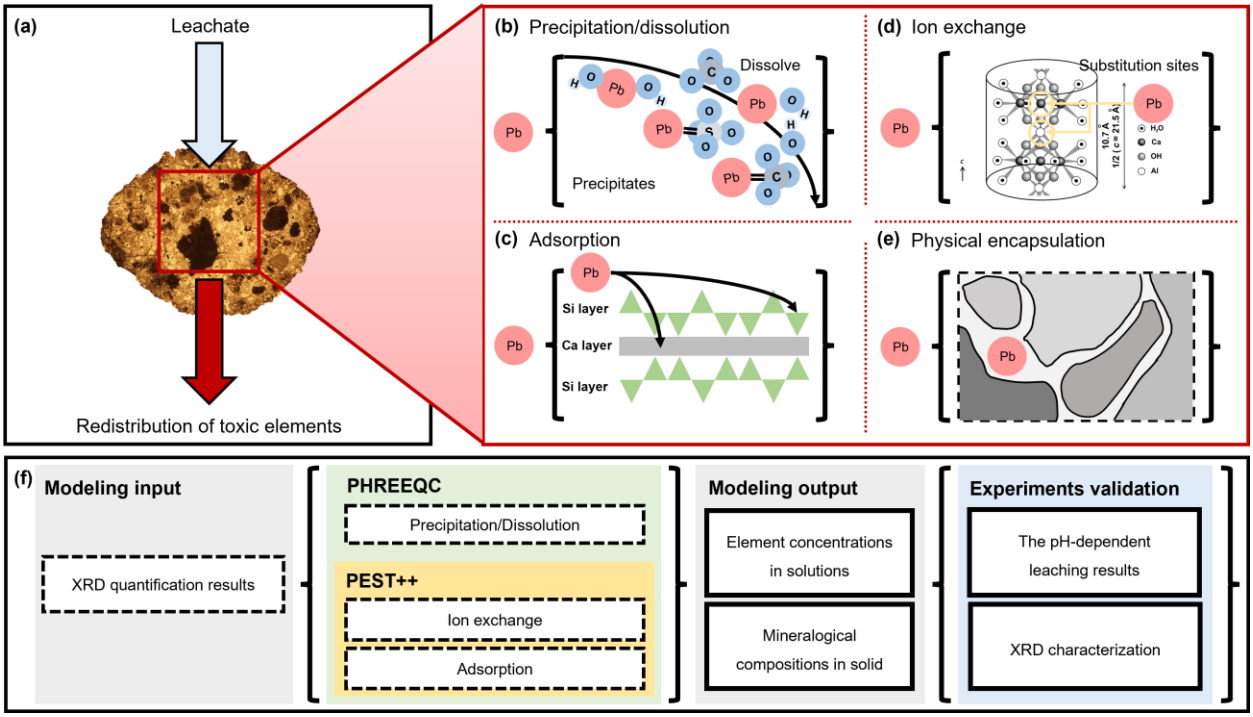

Figure.1. The Pb retention mechanisms and the framework of the forward modeling construction. (a) the optical microscope image of CAP, (b) precipitation/dissolution of Pb-bearing phases, (c) adsorption of Pb on C-S-H layers, (d) ion exchange of Pb to the ettringite (the ettringite image is from Puppala et al. (2018)), (e) physical encapsulation of the Pb, and (f) the simulation framework.

The solid phases input, indicating the pellets mineralogical compositions, in the simulation construction is based on the XRD quantification results and the SEM/EDS observations of OPP and CAP samples. In addition, nitric acid and sodium hydroxide were added to the solution phases aiming to define acid/basic buffering in the leaching tests. Using the abovementioned database, the equilibrium state of possible Pb-bearing phases in OPP and CAP systems was estimated (Fig.1b). The PEST++ was incorporated to simulate the roles of adsorption mechanisms of C-S-H, jarosite, and hematite (Fig.S2) and ion exchange mechanisms of ettringite (Fig.1d) of Pb immobilization (Guo et al., 2017; Gabarrón et al., 2018; Shi et al., 2022). The estimated output of the overall simulation is the concentration of the elements in the leachates, validated by experimental results from the pH-dependent leaching tests and ICP analyses. In addition, the residues of OPP and CAP samples after leaching tests were collected and characterized through XRD to further verify the modeling by comparison with the solid phase compositions in the residues.

3. Results

3.1. Characterization of the PA samples

The XRD pattern (Fig.2a) and SEM/EDS micrograph (Fig.2b) of PA samples display the typical mineralogical compositions of roasted pyrite, mainly constituted by hematite (Fe_2O_3), gypsum ($CaSO_4 \cdot 2H_2O$) and jarosite ($KFe_3(SO_4)_2(OH)_6$) (Oliveira et al., 2012). The Pb is mainly present as anglesite ($PbSO_4$) and kintoreite ($PbFe_3(PO_4)(SO_4)(OH)_6$), typical phases usually found in weathered PA storages (Parbhakar-Fox, 2016). Further, the EDS spot analyses indicate that aside from anglesite and kintoreite, the presence of Pb in PA is also related to Ca, Fe, and Si (Fig.1d) (Gabarrón et al., 2018).

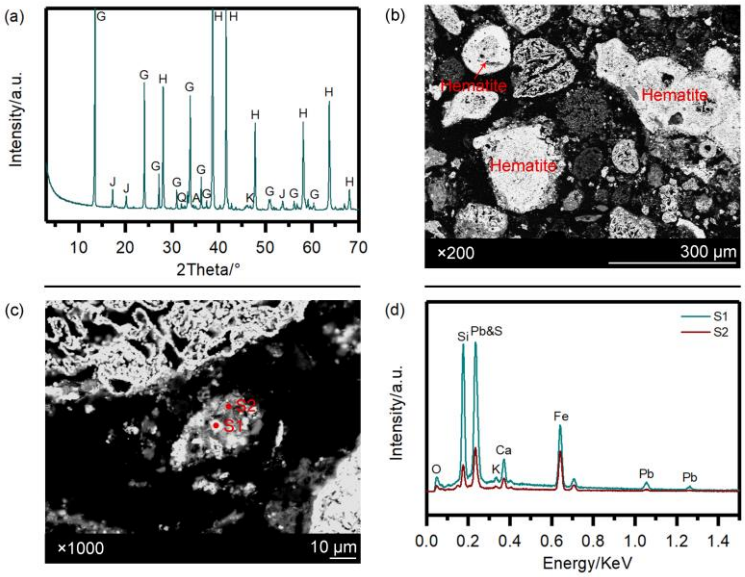

Figure.2. The mineralogical and BSE images of the PA sample. (a) XRD pattern of the PA powder, (b) BSE image indicates the different topographical form of hematite, (c) BSE image demonstrates the Pb incorporation in complexes assemblage, and (d) EDS patterns related to the points marked in image c. A: anglesite, G: gypsum, H: hematite, J: jarosite, K: kintoreite, Q: quartz.

3.2. Characterization of the OPP and CAP samples

The XRD diffractograms and the quantification results (Fig.3) show that ettringite is the primary crystalline hydration product (4.5 wt%) detected in the OPP samples. The observed calcite (6.1 wt%) could be attributed to portlandite carbonation at early ages when the cement-based sample is exposed to the ambient atmosphere (Steiner et al., 2020). By subtracting the known amount of ZnO fraction, the amorphous content is quantified as 24.4 wt%, which is composed of the C-S-H gel (Contessi et al., 2020). Hematite (45.5 wt%), gypsum (9.2 wt%), and jarosite (3.1 wt%), originating from the PA samples, are still present in the stabilized OPP pellets. The Pb-bearing phases demonstrate different fates as the anglesite is totally dissolved, whereas the kintoreite (0.4 wt%) remained in the OPP matrix. Regarding the CAP pellets, massive ettringite (15.4 wt%) and gibbsite (5.5 wt%) fractions are identified due to the CAC binder providing more aluminate. In

turn, the weight percentages of sulfate-bearing minerals, gypsum (4.5 wt%) and jarosite (2.3 wt%) decrease compared to the OPP pellets. The dissolved gypsum and jarosite act as sulfate sources for the ettringite precipitation. Further, the amorphous content in CAP pellets is quantified as 10.5 wt%, which may be primarily attributed to the amorphous $Al(OH)_3$ or CAH gel as the C-(A)-S-H gel is estimated that would not precipitate in the CAC incorporated system (Klaus et al., 2013; Qoku et al., 2022).

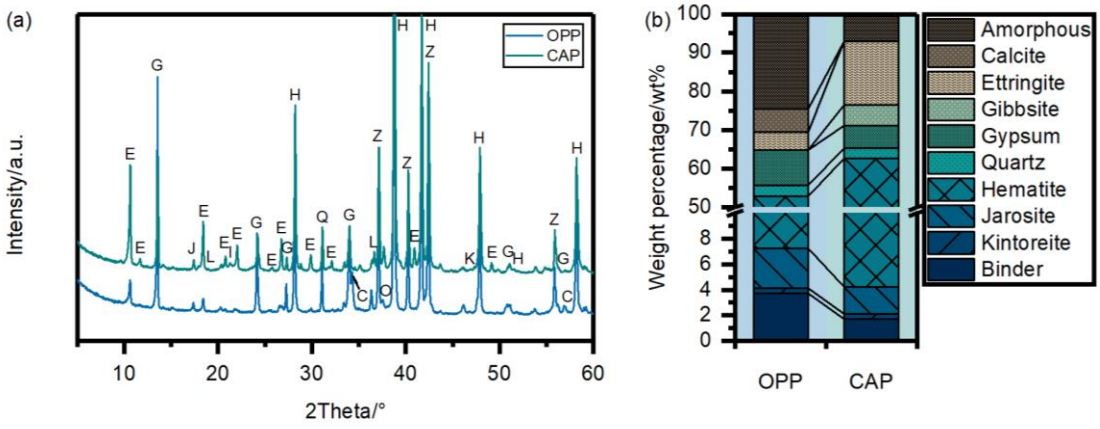

Figure.3. The XRD investigation of the OPP and CAP samples. (a) XRD patterns and (b) The quantification results. C: calcite, E: ettringite, G: gypsum, H: hematite, I: Gibbsite, J: jarosite, K: kintoreite, L: gehlenite, O: alite and/or belite, Q: quartz, Z: zincite. Binder in Fig.2b indicates the sum fraction of alite and belite in OPP samples and the fraction of gehlenite in CAP samples.

The SEM/EDS (Fig.4) images of OPP samples ascertained the presence of unhydrated clinker particles (rectangle-marked particles in Fig.4b) and hematite particles (bright assemblages), which are embedded in an apparently continuous gel matrix (Ca and Si present area, see Fig.4d and e) connecting the unreacted portions. The Pb distribution (Fig.4c) is homogeneously dispersed within the cementitious matrices, with a slight enrichment along the edge of unhydrated cement particles (red rectangle in Fig.4c) and in the body of porous hematite particles (yellow rectangle in Fig.4c and f). The preference for Pb concentration in the unreacted cement particles could be attributed to the formation of pozzolanic reaction products, such as C-S-H, of which the Pb incorporation in the C-S-H structure through linkages to Si–O chains has been widely reported (Guo et al., 2017; Contessi et al., 2020).

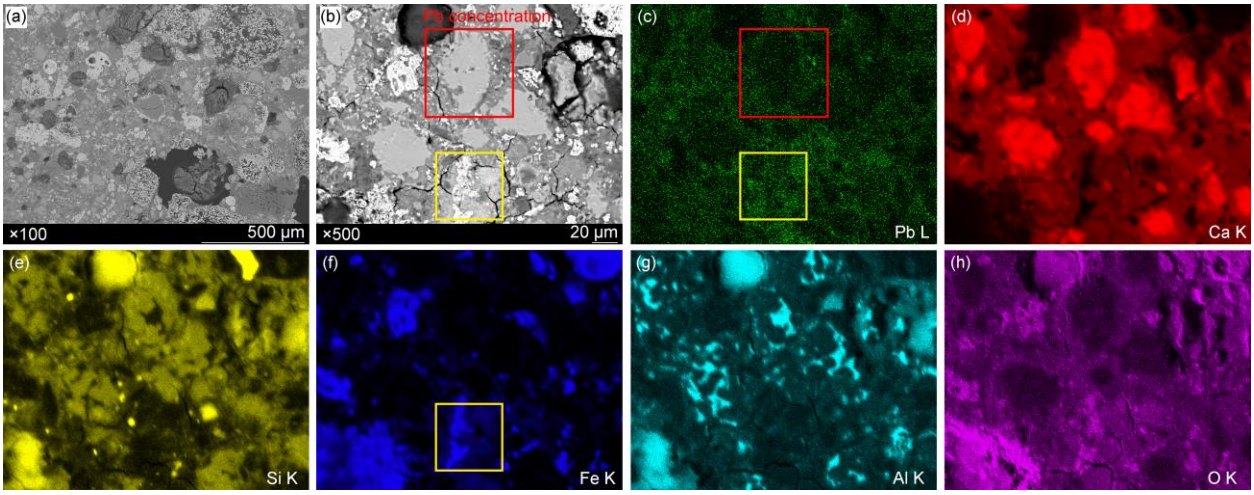

Figure.4. SEM/BSE images of OPP samples. (a) backscattered microscopy image of OPP sample, (b) images demonstrating the presence of unreacted hematite and clinker phases, (c) elemental mapping of Pb, (d) Ca, (e) Si, (f) Fe, (g) Al, and (h) O.

Fig.5a reveals that the ettringite, along with the cementitious matrix, supports the microstructure of CAP samples, surrounded by hematite and unhydrated particles. Similar to the OPP samples, Pb was mainly found in the hydration matrix. However, small particles characterized by a marked Pbenrichment can be observed in the matrix (bright particles in Fig.5b and marked circular area in Fig.5c), possibly corresponding to anglesite (Fig.5h). The Si distribution is not equal along the different binder scenarios (Fig.5e), which is relatively less proportion in CAP, ascertained the finding as the C-(A)-S-H is not the primary reaction product. In addition, Pb is found incorporated in the Fe sulfates assemblages (dash rectangle marked area in Fig.S4a). From the qualitative EDS quantification results (Fig.S4b), the relatively high fraction of Pb (23.8-25.1wt%), Fe (40.9-42.5wt%), and S (18.2-19.9wt%) suggest the mixtures are probably plumbojarosite ($Pb_{0.5}Fe_3(SO_4)_2(OH)_6$) because of the weight percentages of detected K (0.7-0.8 wt%) and Na (0.4-0.9 wt%) are much lower, which are the characteristic elements for confirming potassium/sodium-jarosite ($K/NaFe_3(SO_4)_2(OH)_6$). However, the formation and presence of plumbojarosite are still not clear. Some works suggest that it can remain in neutral and basic conditions, for instance, at high pH values and high-Ca concentrations environment, which is sufficient for portlandite saturation, the Ca-precipitation (portlandite and/or calcite) can block the plumbojarosite aggregates and accordingly lower the dissolution rate (Chen et al., 2021a; Hoeber and Steinlechner, 2021). But this mineral is prone to form and keep stable under harsh acid and high-Pb concentration conditions (Forray et al., 2010; Deng et al., 2022; Helser and Cappuyns, 2022).

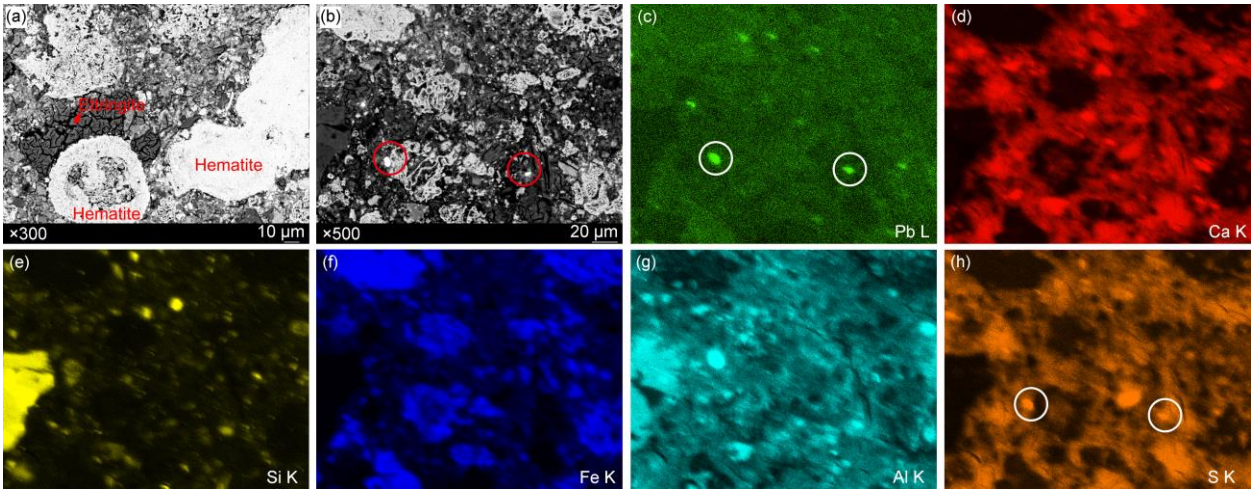

Figure.5. SEM images of CAP samples. (a) backscattered microscopy image of CAP sample, (b) image demonstrating the presence of lead sulfates, (c) elemental mapping of Pb, (d) Ca, (e) Si, (f) Fe, (g) Al, and (h) S.

3.3. Leaching behavior of Pb and sulfates from the pH-dependent leaching tests and modeling

To reveal the PTEs immobilization efficiency of the OPP and CAP pellets, the leaching behaviors of Pb and sulfates at different pH values were investigated (Fig.6). The amount of HNO_3 and NaOH agent solution used to reach the target pH values are given in Fig.S3. The detected pH value of CAP pellets (pH 9.8) is slightly lower compared to OPP pellets (pH 10.9) and is consistent with results reported in the literature (Contessi et al., 2020; Calgaro et al., 2021). Concerning the Pb leaching (Fig.6a and b), both scenarios show amphoteric leaching behavior, where the minimum Pb leachability of OPP (2.3 µg/L) and CAP (4.4 µg/L) pellets were observed at pH 11.4 and 10.2, respectively. Although the Pb retention efficiency of the CAP sample is slightly lower than the traditional OPP sample at moderate alkaline conditions, the Pb retention capacity of CAP at highly-acidic and -alkaline conditions is more satisfactory than the OPP samples. When the pH value decreases below 4, the detected Pb concentration of OPP is 43000 µg/L (pH 3.3), whereas the highest value (12000 µg/L) for CAP was found at pH 11.8. The estimated Pb release from OPP and CAP modeling also ascertained their experimentally determined amphoteric characteristic, as the highest Pb concentration was observed at harsh acid conditions (pH<4) and the lowest is presented at moderate alkaline conditions (pH from 7-11).

Contrary to the Pb leaching behavior, the sulfate releasing is close to a steady dissolution state for both scenarios, varying from 600 to 970 mg/L in the studied pH range (Fig.6c and d). However, the simulation of sulfate leaching of OPP samples at basic and neutral conditions is less satisfactory than the estimation at acid conditions. With the increase of pH values, the sulfates concentration from the modeling gradually increased (pH approximately at 7 to 10) and then remained stable under alkaline conditions, but an order

of magnitude higher than the experimental results (e.g., 7.3×10^3 and 8.4×10^2 mg/L at pH of 12.9, Fig.6c).

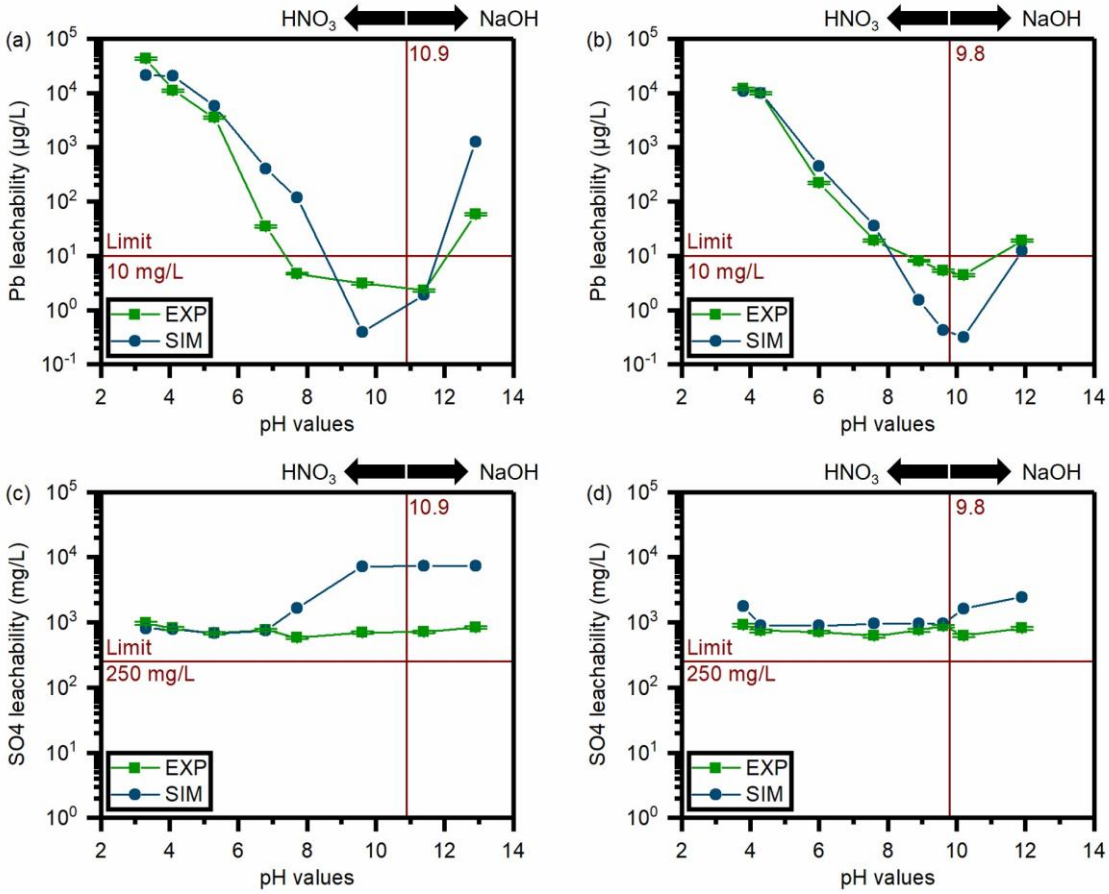

Figure.6. The pH-dependent leaching tests of Pb and sulfates. (a) The leaching behavior of Pb in OPP samples, (b) The leaching behavior of Pb in CAP samples, (c) The leaching behavior of sulfates in OPP samples, and (d) The leaching behavior of sulfates in CAP samples. EXP and SIM indicate the leaching results from experiments and simulation, respectively. 10.9 and 9.8 represent the detected pH value of the OPP and CAP pellets, using deionized water as the leachate. The limit of Pb concentration is from, whereas the sulfate limit is from. HNO_3 and NaOH mean the buffering agent used to reach the target pH values.

3.4. Quantification of Pb and sulfates existence on OPP and CAP pellets.

Fig.7 gives the quantitative results of the Pb and sulfates-bearing species of OPP and CAP under the studied pH ranges. At alkaline pH conditions (pH > 8), the immobilization of Pb in the OPP samples mainly relies on the adsorption and ion exchange of C-S-H and ettringite (Fig.7a). With the decrease in pH values, the neutral pH conditions are no more suitable for the equilibrium of C-S-H and ettringite. Therefore, the adsorbed Pb is gradually released as a consequence of the dissolution of hydration products. Then the

soluble Pb precipitates as cerussite or is partially immobilized by the ferrihydrite and hematite. At acid conditions (pH <5), the Pb immobilization is attributed to the anglesite precipitation and hematite adsorption. However, non-negligible amounts of Pb remain soluble in pore solutions, as the leaching tests (Fig.6a) ascertained that the Pb leachability at the pH of 3.3 is a thousand times higher than the specified limit. In Fig.7b, the Pb retention of CAP samples at alkaline conditions is primarily assigned to the adsorption and ion exchange with ettringite and hematite or precipitation as $Pb(OH)_2$. At neutral pH conditions (pH 7 to 8), Pb leachability is dominated by hematite and ferrihydrite adsorption. Then Pb partially redissolves and reprecipitates as cerussite and anglesite, as well as a portion of soluble Pb remains in the pore solution in the forms of Pb^{2+}, $PbNO_3^-$, and $PbSO_{4(aq)}$ when the pH shifts to acid conditions. From Fig.7c and d, the sulfates variation of OPP and CAP samples demonstrate a similar trend in acidic conditions (pH approximately from 3 to 7). In these conditions, sulfate mainly precipitates as jarosite, anglesite, and gypsum. Whereas gypsum is the principal sulfate-bearing phase at pH values ranging from 7 to 9. The ettringite fraction increases at the basic conditions, which is suitable for the hydration products' stability.

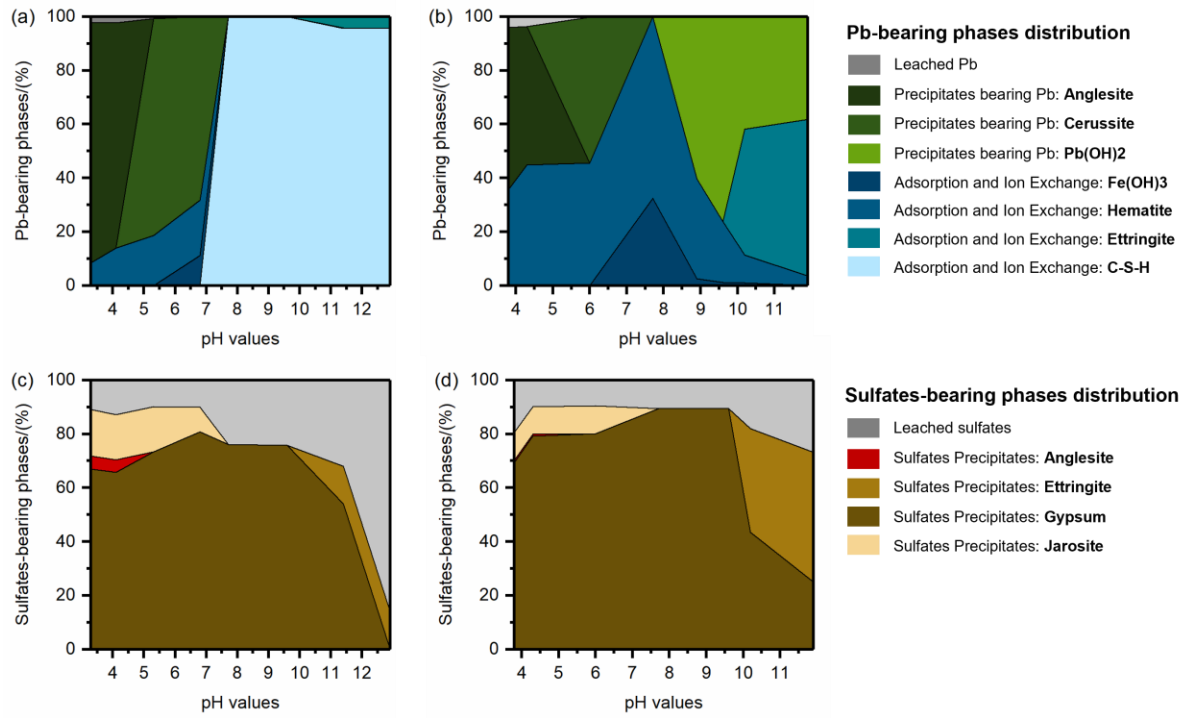

Figure.7. The simulated PTEs-bearing phases variation as a function of pH values. (a) the variation of the Pb-bearing species in OPP samples, (b) the variation of the Pb-bearing species in CAP samples, (c) the variation of the sulfates-bearing species in OPP samples, and (d) the variation of the sulfates-bearing species in CAP samples.

3.5. Validation of the modeling construction: mineralogical characterization of the residues.

Fig.8 and S5 show the XRD quantification results from the collected OPP residues after the leaching tests at pH values of 3.3, 5.3, and 12.9 and the solid phase quantification results from the simulation. The XRD mineralogical analyses and geochemical modeling confirm the dissolution of ettringite and portlandite with decreasing pH values, whereas gypsum and jarosite are prone to precipitate at acid conditions. However, the estimation of carbonates (calcite and vaterite) equilibrium in the modeling is less satisfactory. From the XRD quantification, carbonates are present in the OPP residues in the broad pH range studied, but the geochemical modeling indicates that the precipitation of carbonates can only be observed at highly alkaline conditions (pH 12.9, 1.2 wt%). In addition, the experimentally quantified amorphous fraction in the residues varies from 15.4 to 30.4 wt%. This observation can be better explained by the modeling results, as the amorphous fraction at basic conditions is mainly composed of C-S-H, as well as a minor content of ferrihydrite. With the acid addition, these constituents decrease gradually afterward due to the continuous dissolution, whereas the amorphous fraction is mainly assigned to amorphous silicates dissolved from the C-S-H matrices (Gutberlet et al., 2015) and precipitated $Al(OH)_3$.

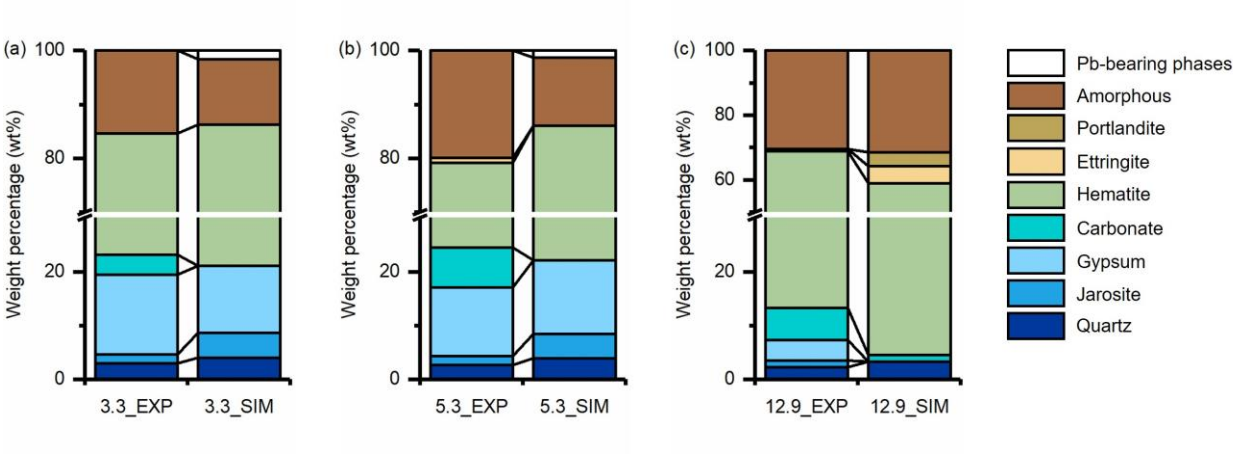

Figure.8. The quantified mineralogical assemblages of the collected OPP residues from the XRD patterns and Phreeqc models and the correlated deviation. The leachate pH values at (a) 3.3, (b) 5.3, and (c) 12.9. The abbreviation "EXP" indicates the quantified mineralogical compositions from XRD. The abbreviation "SIM" means the quantified mineralogical compositions from modeling. The "Pb-bearing phases" is the accumulation of weight percentages of anglesite, cerussite, hydrocerussite, and $Pb(OH)_2$. The "amorphous" represents the experimentally quantified amorphous fraction in XRD (EXP), whereas, in simulation (SIM), it is the sum of the estimated amorphous silicates dissolved from the C-S-H matrices, amorphous C-S-H gel, amorphous $Fe(OH)_3$, and amorphous $Al(OH)_3$.

The mineralogical analyses of CAP residues performed by XRD and geochemical modeling are shown in Fig.9 and S6. Similar to the OCP characterization, the primary crystalline hydration product ettringite in

CAP residues favorably precipitates in alkaline conditions. Ettringite is identified at the basic pH range (12.3 wt%, pH 11.9) while less preserved towards the neutral pH range (5.1 wt%, pH 6.0). Gypsum is found in all the CAP residue samples even though the weight percentage decreases from basic to acid conditions (from 11.3 to 7.0 wt%, pH from 3.8 to 11.9). In addition, the experimentally characterized aluminates (amorphous $Al(OH)_3$ and crystalline gibbsite) are in a relatively constant fraction range (22.6 to 24.7 wt%). The simulation also reflects this trend, but the quantified aluminates weight percentages are only half of the experiments, with a range of 11.1 to 12.1 wt%. Carbonates in CAP residues are only found at the pH value of 11.9, with 1.4 and 0.9 wt% being quantified in EXP and SIM, respectively.

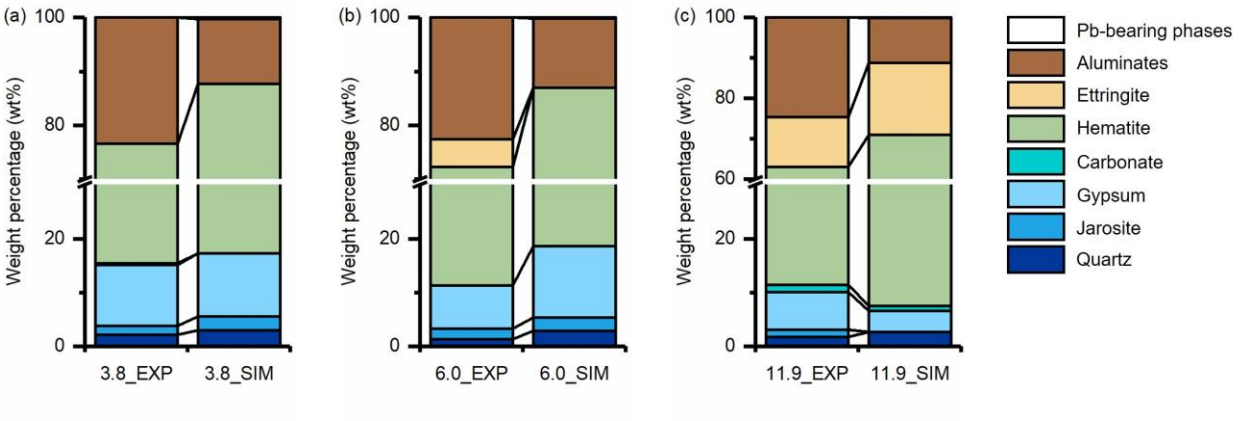

Figure.9. The quantified mineralogical assemblages of the collected CAP residues from the XRD patterns and Phreeqc models and the correlated deviation. The leachate pH values at (a) 3.8, (b) 6.0, and (c) 11.9. The abbreviation "EXP" indicates the quantified mineralogical compositions from XRD. The abbreviation "SIM" means the quantified mineralogical compositions from modeling. The "Pb-bearing phases" is the accumulation of weight percentages of anglesite, cerussite, hydrocerussite, and $Pb(OH)_2$. The "aluminates" in EXP represent the experimentally quantified amorphous fraction and gibbsite in XRD, and in SIM, indicates the accumulation of amorphous $Al(OH)_3$ and crystalline gibbsite.

4. Discussion

Although the general PTEs retention mechanisms have been discussed and studied for many years (Chen et al., 2009; Guo et al., 2017; Contessi et al., 2020; Hossain et al., 2020), it is always challenging to quantify and clarify the exact roles of cementitious phases in PTEs immobilization. This is because the leaching of PTEs in the stabilized products is dominated by multiple physico-chemical parameters, such as the physical protection from the hardened cementitious matrices (Halim et al., 2005), the dynamic changes in solid and liquid compositions (Dijkstra et al., 2006; Zavarin et al., 2022), and the inherent variability of PTEs-bearing

phases due to the different binder scenarios (Contessi et al., 2020; Zhang et al., 2021). Traditionally, the reliability of the thermodynamic database is the major limitation in the forward geochemical modeling construction when building such a complex and dynamic process. Furthermore, without additional mineral composition fitting (e.g., normalization coefficient and fraction adjustment), leachability estimation in many case studies is deficient (Cornelis et al., 2012; Helser and Cappuyns, 2021; Pang et al., 2022; Liu et al., 2022; Chen et al., 2022a). In the combined model presented here, adsorption and ion exchange of PTEs in multiple species from original solid waste (hematite, jarosite, and ferrihydrite) and incorporated binder phases (ettringite, C-S-H, and amorphous $Al(OH)_3$) are revealed, as well as the mechanisms of precipitation/dissolution.

In the OPP samples simulation, the retention of Pb at basic pH values is mainly controlled by the ettringite and C-S-H. Regarding the previous works without the adsorption estimation, the Pb stabilization at higher pH values is predominantly assigned to sparingly-soluble compound precipitations (e.g., hydrocerussite and $Pb(OH)_2$) (Solpuker et al., 2014; Bobirică et al., 2018; Tangviroon et al., 2020). However, the SEM results (Fig.4c) validate the Pb incorporation into the C-S-H as the Pb is concentrated along the edge of cement particles with a preference for Ca and Si-enriched area. Although the Pb incorporation in ettringite is not directly observed in this work, the structural substitution of Pb in ettringite has been extensively reported (Gougar et al., 1996; Contessi et al., 2021; Wang and Wang, 2022). This indicates that the fate of Pb in the OPP matrices is to be directly sorbed by the C-S-H, forming Pb-enriched outer rings distributed around the cement particles (Wang and Wang, 2022). The increase in pH values (from 10.9 to 12.9) is well-known to affect the solubility of hydration products slightly. Therefore, the Pb incorporation should be preserved in an alkaline environment, whereas such an assumption of hydroxide constitution is only under plausible theoretical consideration. Further experimental verification is required to support this hypothesis. With the pH values moving to neutral conditions, the prediction (Fig.7a) indicates that the valley of the amphoteric Pb leaching curve (Fig.6a) is dominated by precipitation of anglesite and cerussite and adsorption by hematite and ferrihydrite. However, other studies thought that the enhanced Pb immobilization is mainly related to the physical protection from the hardened cementitious phases, which efficiently prevents the Pb-bearing phases getting contact with the leachate (Halim et al., 2005; Martens et al., 2010; Solpuker et al., 2014; Berthomier et al., 2021). Therefore, to give a better representation of Pb leachability, Solpuker et al., (2014) estimated that only 10% of the phases would take part in the dissolution/precipitation process when the pH values of the system are lower than 11, similar specific leaching coefficients of 31% and 40% are also introduced in the work of Halim et al., (2005) and Berthomier et al., (2021), respectively. The Pb speciation of OPP samples at acid conditions (pH<5, Fig.7a) is likewise the previous investigations (Contessi et al., 2020; Chukwura and Hursthouse, 2020) as anglesite precipitation is the primary Pb-bearing phase in equilibrium, and due to the high acidity of the system, a

considerable amount of soluble Pb would release to the solution.

Regarding the Pb immobilization in CAP samples at basic conditions (Fig.7b), this is not surprising that ettringite is the main contributor, with approximately 58% of Pb stabilized by ettringite approximately ten times higher than the relative percentage in OPP samples (4%, pH 12.9). In addition, although the adsorption of amorphous $Al(OH)_3$ is defined in the CAP modeling system, 38% of Pb is stabilized as $Pb(OH)_2$ precipitation at the pH value of 11.9, unlike the OPP systems, most redissolved Pb is trapped by C-S-H (Fig.7a). This conversion is possibly assigned to the relatively low Pb concentrations in both systems, as the Pb fraction is lower than 1 wt%. When the concentrations exceed the maximum Pb host capacity, referring to different Pb hosters, the sorption capacity of the overall system may reach a saturation point and no more soluble Pb can be attached to the hosters' surface. Accordingly, the precipitation would control the Pb immobilization, and Pb hydroxides are subsequently formulated. Therefore, in the OPP system, the high specific surface area and the layered structure of C-S-H make the maximum sorption capacity preference for the Pb incorporation. Wang and Wang (2022) report a similar finding, as the primary fate of Pb is directly sorbed and/or encapsulated by C-S-H, but probably insignificant Pb hydroxides may precipitate when the Pb concentration at the specific area exceeds the saturation point. By contrast, in the CAP system, the specific surface area of amorphous $Al(OH)_3$ defined in the modeling is much lower than the C-S-H (Table.S2), giving the overall system a relatively low sorption capacity compared to OPP samples. Herein the Pb favors the hoster of ettringite and hydroxide precipitation. Another interesting difference is that when the pH values are slightly acidic (pH from 4 to 7), Pb in CAP dissolved from the ferrihydrite surface and partially precipitated as cerussite and anglesite. However, the relative Pb content captured by hematite is steadily at 45% (Fig.7d), which ascertains the assumption of overall system maximum adsorption capacity. Because of the physical protection defined in this work, the total amount of Pb input within CAP samples is estimated to be only a quarter of OPP samples (Table.S2). Therefore, after all the active binding sites of hematite are occupied by Pb, the remaining soluble Pb reacts with the sulfates dissolved from the ettringite and slightly dissolved CO_2 from the atmospheric air. But since the amount of Pb defined in OPP samples is higher than CAP, more soluble Pb would be released to the pore solution and generate more Pb-bearing phases precipitation. Consequently, different Pb retention mechanisms were shown.

To further quantify the relative Pb host capacities (ion exchange and adsorption) of the phases defined in modeling, excluding the effects of estimated physical protection, we calculated the relative capacities of each phase in the studied pH range (Fig.10). The results reveal that the cementitious matrices (ettringite and C-S-H) have greater Pb capacities compared to the phases from PA samples (hematite, jarosite, and ferrihydrite). Obviously, the enhanced Pb capacity of cementitious matrices is more efficient at high pH

conditions due to their inherent solubility and sensitivity to pH (Fig.10a and b). When the cementitious matrices cannot effectively stabilize all the soluble Pb in the system, hematite and ferrihydrite take the responsibility in turn (Fig.10c and d). Similar experimental findings were also reported in the literature (Vu et al., 2013; Lu et al., 2020). In fact, without solidification/stabilization, the Pb incorporation into the iron (oxyhydr)oxides takes place between near neutral and alkaline pH. Moreover, Pb can only be released from the iron phases at highly acidic conditions (pH <2) or during reductive dissolution (e.g., if the colloids are buried within anaerobic sediments) (Vu et al., 2013; Lu et al., 2020).

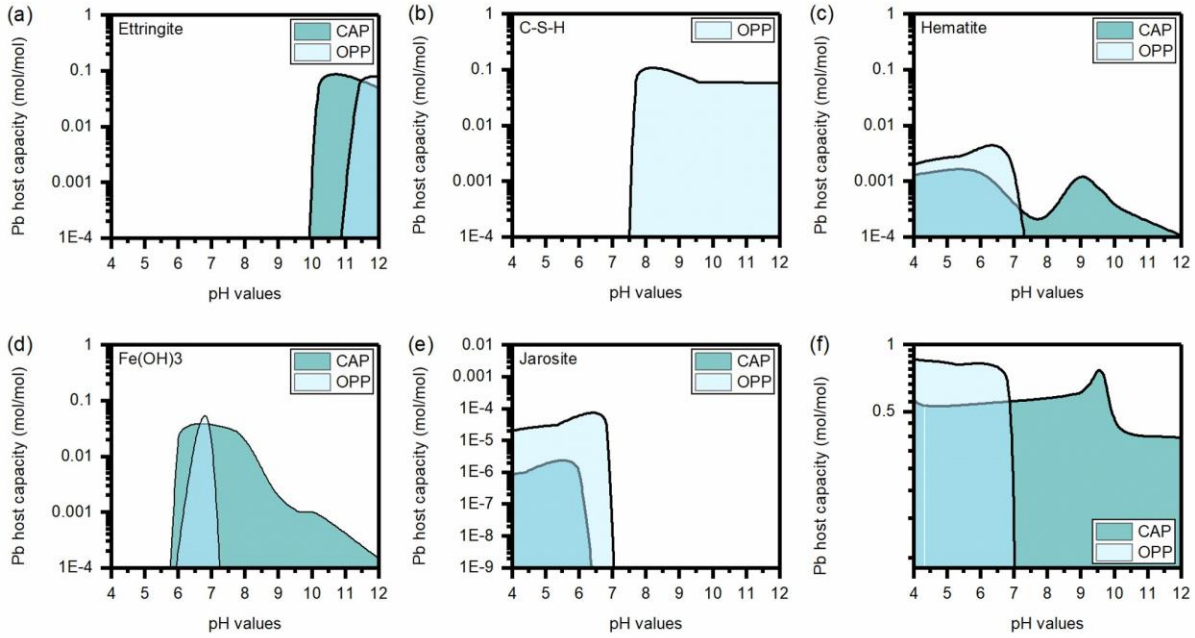

Figure.10. The relative Pb host capacities of multiple phases in OPP and CAP (mol/mol). (a) ettringite, (b) C-S-H, only present in OPP samples, (c) hematite, (d) $Fe(OH)_3$, (e) jarosite, and (f) Pb-precipitations. Note that the Pb host capacities with adsorption and ion exchange are calculated by dividing the mole content of adsorped Pb by the mole content of attributed phases. (e.g., 1 mol of Pb is adsorped by 10 mol C-S-H, then the Pb host capacity is 0.1 mol/mol). The Pb host capacity in image f indicates the mole percentage of anglesite, cerussite, and $Pb(OH)_2$ with respect to the immobilized Pb.

Noteworthy, despite the current simulation conforms to the experimental Pb leaching profile (Fig.6a and b) and the variation of mineralogical composition (Fig.8 and 9), there are some limitations to our interpretation, such as the estimation of carbonates and sulfates dissolution/precipitation in this pH range which still needs to be further investigated and optimized. The overestimation of carbonates could be partially attributed to the kinetic of calcite dissolution. Although the pH decrease is one of the critical factors controlling the

dissolution of the carbonates, both the porosity and the concentration gradient in the local aqueous phase conditions can also be essential mechanisms when applied in natural systems, as the previous investigation indicates that the calcite fluctuates between the period of precipitation and dissolution (Matteo et al., 2018). Concerning the sulfate leaching, the estimation in both CAP and OPP profiles in acid conditions is fairly acceptable. However, the release in OPP samples at basic conditions is not disaggregated in this research (Fig.6c). This behavior can be explained by the sulfate equilibrium dominated by the ettringite and gypsum. At highly alkaline conditions, the overall modeling system favors the ettringite precipitation. Therefore, the sulfate vacuity in the system facilitates the gypsum dissolution to provide the additional sulfate for ettringite forming. However, in real cases, ettringite formation and dissolution is also kinetic controlling process (Winnefeld and Lothenbach, 2010). Consequently, the overrated ettringite fraction and underestimated gypsum fraction were observed in both scenarios (Fig.8c and 9c).

Altogether, our developed method enables a better understanding of the PTEs immobilization roles of the main hydration products and inherent phases in solid waste, which is hardly revealed by the experimental techniques. In turn, understanding the extent of this role variation will allow for more accurate and reliable design for the in-situ remediation industry in a relatively cost-downdrawn pathway. The implication of these results underscores the importance of not only predicting and clarifying the PTEs immobilization amounts as a function of pH values but also highlighting the essential question of how the stabilized products would help the PTEs retention when the field conditions are under harsh or unsuitable conditions. For example, when the pH of the rainfall and groundwater changes with the season or anthropogenic activities, the predicted concentrations of dissolved PTEs could be used to forecast whether secondary pollution will occur.

5. Conclusion

This study explores the exact role of the PTEs immobilization capacity of cementitious phases and solid wastes phases in a broad pH range. The Pb-rich PA waste was stabilized in traditional (OPC) and alternative (CAC) binders to optimize the Pb leachability due to the sensitive durability of OPC and mitigate the CO_2 emission attributed to OPC production. The experimental and modeling investigations accordingly reveal the solidification/stabilization mechanisms of each scenario. The following conclusions can be drawn based on the results obtained from the experiment and modeling.

(1) Both scenarios demonstrate high retention of Pb at neutral and alkaline pH conditions, approximately from 7 to 11. The use of CAC binder effectively enhanced the Pb retention capacity of the stabilized products, especially in harsh acid conditions, with only a quarter of Pb concentration detected in CAP samples (11000 μg/L) compared to OPP samples (43000 μg/L). Experiments reveal that Pb incorporation in OPP samples is mainly related to the C-S-H with a preference in Ca and Si-rich areas along the cement particles, whereas the Pb is homogeneously distributed in the CAP samples.

(2) Geochemical modeling reveals that C-S-H adsorption is the primary Pb immobilization role of OPP samples at basic conditions, with a 0.1 mol/mol Pb retention capacity that can be reached. When the pH is unsuitable for C-S-H precipitation, cerussite and anglesite precipitation is the main control of the Pb leachability, as well as a minor content of soluble Pb is adsorbed by hematite and ferrihydrite.

(3) Regarding the CAP samples, $Pb(OH)_2$ precipitation and ettringite coexisting are the dominant control for Pb in alkaline environments. An approximately 0.1 mol/mol Pb host capacity was estimated for ettringite which is equivalent to C-S-H. However, the roles of hematite and ferrihydrite adsorption on Pb are observed in a broader pH range compared to OPP samples. Likewise, the cerussite and anglesite precipitation shows stronger affinities for Pb immobilization in acid conditions.

(4) The sulfate release in both cases is at a steady state, varying from 600 to 900 mg/L in all experiments conducted. The modeling shows that sulfate retention is controlled by the dissolution and precipitation of anglesite, gypsum, ettringite, and jarosite. But the estimation of sulfate leachability is fairly limited, especially at OPP samples, which might be influenced by the kinetic of ettringite equilibrium. Further work is in progress to coincide with the impacts of the kinetics of the discussed phases for PTEs immobilization.

Reference

Appelo, C.A.J., Parkhurst, D.L., and Post, V.E.A., 2014, Equations for calculating hydrogeochemical reactions of minerals and gases such as CO2 at high pressures and temperatures: Geochimica et Cosmochimica Acta, v. 125, p. 49–67, doi:10.1016/J.GCA.2013.10.003.

Berthomier, M., Lors, C., Damidot, D., De Larrard, T., Guérandel, C., and Bertron, A., 2021, Leaching of CEM III paste by demineralised or mineralised water at pH 7 in relation with aluminium release in drinking water network: Cement and Concrete Research, v. 143, doi:10.1016/J.CEMCONRES.2021.106399.

Bobirică, C., Long, D.T., Parsons, M.J., Stănescu, R., and Voice, T.C., 2018, Examination of the influence of dissolved halite (NaCl) on the leaching of lead (Pb) from cement-based solidified wastes: Journal of Material Cycles and Waste Management, v. 20, p. 59–70, doi:10.1007/S10163-016-0552-6/FIGURES/8.

Bonomo, L., Careghini, A., Dastoli, S., De Propris, L., Ferrari, G., Gabellini, M., and Saponaro, S., 2009, Feasibility studies for the treatment and reuse of contaminated marine sediments: https://doi.org/10.1080/09593330902990105, v. 30, p. 817–823, doi:10.1080/09593330902990105.

Calgaro, L., Contessi, S., Bonetto, A., Badetti, E., Ferrari, G., Artioli, G., and Marcomini, A., 2021, Calcium aluminate cement as an alternative to ordinary Portland cement for the remediation of heavy metals contaminated soil: mechanisms and performance: Journal of Soils and Sediments, doi:10.1007/s11368-020-02859-x.

Chen, J., Fu, C., Mao, T., Shen, Y., Li, M., Lin, X., Li, X., and Yan, J., 2022a, Study on the accelerated carbonation of MSWI fly ash under ultrasonic excitation: CO2 capture, heavy metals solidification, mechanism and geochemical modelling: Chemical Engineering Journal, v. 450, p. 138418, doi:10.1016/J.CEJ.2022.138418.

Chen, K., Jin, X., Guo, C., He, C., Zhang, Y., Gao, K., Lu, G., and Dang, Z., 2021a, Reductive dissolution of Pb-Zn jarosite under near-neutral conditions: Chemical Geology, v. 579, p. 120338, doi:10.1016/J.CHEMGEO.2021.120338.

Chen, Q.Y., Tyrer, M., Hills, C.D., Yang, X.M., and Carey, P., 2009, Immobilisation of heavy metal in cement-based solidification/stabilisation: A review: Waste Management, doi:10.1016/j.wasman.2008.01.019.

Chen, L., Wang, Y.S., Wang, L., Zhang, Y., Li, J., Tong, L., Hu, Q., Dai, J.G., and Tsang, D.C.W., 2021b, Stabilisation/solidification of municipal solid waste incineration fly ash by phosphate-enhanced calcium aluminate cement: Journal of Hazardous Materials, v. 408, p. 124404, doi:10.1016/J.JHAZMAT.2020.124404.

Chen, L., Wang, L., Zhang, Y., Ruan, S., Mechtcherine, V., and Tsang, D.C.W., 2022b, Roles of biochar in

cement-based stabilization/solidification of municipal solid waste incineration fly ash: Chemical Engineering Journal, v. 430, p. 132972, doi:10.1016/J.CEJ.2021.132972.

Chen, Z., Zhang, P., Brown, K.G., Branch, J.L., van der Sloot, H.A., Meeussen, J.C.L., Delapp, R.C., Um, W., and Kosson, D.S., 2021c, Development of a Geochemical Speciation Model for Use in Evaluating Leaching from a Cementitious Radioactive Waste Form: Environmental Science and Technology, v. 55, p. 8642–8653, doi:10.1021/ACS.EST.0C06227/ASSET/IMAGES/LARGE/ES0C06227_0007.JPEG.

Chen, L., Zhang, Y., Wang, L., Ruan, S., Chen, J., Li, H., Yang, J., Mechtcherine, V., and Tsang, D.C.W., 2022c, Biochar-augmented carbon-negative concrete: Chemical Engineering Journal, v. 431, p. 133946, doi:10.1016/j.cej.2021.133946.

Chukwura, U.O., and Hursthouse, A.S., 2020, Evaluating controls on potentially toxic element release in circum-neutral mine water: a case study from the abandoned Pb–Zn mines of Leadhills and Wanlockhead, South of Scotland, United Kingdom: Environmental Earth Sciences, v. 79, p. 1–13, doi:10.1007/S12665-020-09108-X/FIGURES/5.

Contessi, S., Calgaro, L., Dalconi, M.C., Bonetto, A., Bellotto, M. Pietro, Ferrari, G., Marcomini, A., and Artioli, G., 2020, Stabilization of lead contaminated soil with traditional and alternative binders: Journal of Hazardous Materials, doi:10.1016/j.jhazmat.2019.120990.

Contessi, S., Dalconi, M.C., Pollastri, S., Calgaro, L., Meneghini, C., Ferrari, G., Marcomini, A., and Artioli, G., 2021, Cement-stabilized contaminated soil: Understanding Pb retention with XANES and Raman spectroscopy: Science of The Total Environment, v. 752, p. 141826, doi:10.1016/J.SCITOTENV.2020.141826.

Cornelis, G., Etschmann, B., Van Gerven, T., and Vandecasteele, C., 2012, Mechanisms and modelling of antimonate leaching in hydrated cement paste suspensions: Cement and Concrete Research, v. 42, p. 1307–1316, doi:10.1016/J.CEMCONRES.2012.06.004.

Deng, H., Tian, C., Li, L., Liang, Y., Yan, S., Hu, M., Xu, W., Lin, Z., and Chai, L., 2022, Microinteraction Analysis between Heavy Metals and Coexisting Phases in Heavy Metal Containing Solid Wastes: ACS ES&T Engineering, v. 2, p. 547–563, doi:10.1021/ACSESTENGG.1C00343.

Dijkstra, J.J., Van der Sloot, H.A., and Comans, R.N.J., 2002, Process identification and model development of contaminant transport in MSWI bottom ash: Waste Management, v. 22, p. 531–541, doi:10.1016/S0956-053X(01)00034-4.

Dijkstra, J.J., Van Der Sloot, H.A., and Comans, R.N.J., 2006, The leaching of major and trace elements from MSWI bottom ash as a function of pH and time: Applied Geochemistry, v. 21, p. 335–351, doi:10.1016/J.APGEOCHEM.2005.11.003.

Doherty, J., 2015, Calibration and Uncertainty Analysis for Complex Environmental Models PEST:

complete theory and what it means for modelling the real world:, www.pesthomepage.org (accessed August 2022).

Du, B., Li, J., Fang, W., and Liu, J., 2019, Comparison of long-term stability under natural ageing between cement solidified and chelator-stabilised MSWI fly ash: Environmental Pollution, v. 250, p. 68–78, doi:10.1016/J.ENVPOL.2019.03.124.

Forray, F.L., Smith, A.M.L., Drouet, C., Navrotsky, A., Wright, K., Hudson-Edwards, K.A., and Dubbin, W.E., 2010, Synthesis, characterization and thermochemistry of a Pb-jarosite: Geochimica et Cosmochimica Acta, v. 74, p. 215–224, doi:10.1016/J.GCA.2009.09.033.

Gabarrón, M., Babur, O., Soriano-Disla, J.M., Faz, A., and Acosta, J.A., 2018, Composition and risk assessment of roasted pyrite ash from fertiliser production: Chemosphere, v. 209, p. 277–285, doi:10.1016/J.CHEMOSPHERE.2018.06.109.

Gougar, M.L.D., Scheetz, B.E., and Roy, D.M., 1996, Ettringite and C S H Portland cement phases for waste ion immobilization: A review: Waste Management, v. 16, p. 295–303, doi:10.1016/S0956-053X(96)00072-4.

Guo, B., Liu, B., Yang, J., and Zhang, S., 2017, The mechanisms of heavy metal immobilization by cementitious material treatments and thermal treatments: A review: Journal of Environmental Management, v. 193, p. 410–422, doi:10.1016/j.jenvman.2017.02.026.

Guo, B., Tan, Y., Wang, L., Chen, L., Wu, Z., Sasaki, K., Mechtcherine, V., and Tsang, D.C.W., 2021, High-efficiency and low-carbon remediation of zinc contaminated sludge by magnesium oxysulfate cement: Journal of Hazardous Materials, v. 408, p. 124486, doi:10.1016/J.JHAZMAT.2020.124486.

Gutberlet, T., Hilbig, H., and Beddoe, R.E., 2015, Acid attack on hydrated cement - Effect of mineral acids on the degradation process: Cement and Concrete Research, doi:10.1016/j.cemconres.2015.03.011.

Halim, C.E., Short, S.A., Scott, J.A., Amal, R., and Low, G., 2005, Modelling the leaching of Pb, Cd, As, and Cr from cementitious waste using PHREEQC: Journal of Hazardous Materials, v. 125, p. 45–61, doi:10.1016/j.jhazmat.2005.05.046.

Helser, J., and Cappuyns, V., 2022, Acid generation potential and kinetics of metal(loid) release from resuspended sulfidic mine waste: Journal of Environmental Chemical Engineering, v. 10, p. 108158, doi:10.1016/J.JECE.2022.108158.

Helser, J., and Cappuyns, V., 2021, Trace elements leaching from PbZn mine waste (Plombières, Belgium) and environmental implications: Journal of Geochemical Exploration, v. 220, p. 106659, doi:10.1016/J.GEXPLO.2020.106659.

Hoeber, L., and Steinlechner, S., 2021, A comprehensive review of processing strategies for iron precipitation residues from zinc hydrometallurgy: Cleaner Engineering and Technology, v. 4, p. 100214, doi:10.1016/J.CLET.2021.100214.

Holmes, N., Tyrer, M., West, R., Lowe, A., and Kelliher, D., 2022, Using PHREEQC to model cement hydration: Construction and Building Materials, v. 319, p. 126129, doi:10.1016/J.CONBUILDMAT.2021.126129.

Hossain, M.U., Wang, L., Chen, L., Tsang, D.C.W., Ng, S.T., Poon, C.S., and Mechtcherine, V., 2020, Evaluating the environmental impacts of stabilization and solidification technologies for managing hazardous wastes through life cycle assessment: A case study of Hong Kong: Environment International, v. 145, p. 106139, doi:10.1016/J.ENVINT.2020.106139.

Hou, D., O'Connor, D., Igalavithana, A.D., Alessi, D.S., Luo, J., Tsang, D.C.W., Sparks, D.L., Yamauchi, Y., Rinklebe, J., and Ok, Y.S., 2020, Metal contamination and bioremediation of agricultural soils for food safety and sustainability: Nature Reviews Earth & Environment 2020 1:7, v. 1, p. 366–381, doi:10.1038/s43017-020-0061-y.

Jarošíková, A., Ettler, V., Mihaljevič, M., Drahota, P., Culka, A., and Racek, M., 2018, Characterization and pH-dependent environmental stability of arsenic trioxide-containing copper smelter flue dust: Journal of Environmental Management, v. 209, p. 71–80, doi:10.1016/J.JENVMAN.2017.12.044.

Klaus, S.R., Neubauer, J., and Goetz-Neunhoeffer, F., 2013, Hydration kinetics of CA2 and CA—Investigations performed on a synthetic calcium aluminate cement: Cement and Concrete Research, v. 43, p. 62–69, doi:10.1016/J.CEMCONRES.2012.09.005.

De Kleijne, K., Hanssen, S. V, Van Dinteren, L., Huijbregts, M.A.J., Van Zelm, R., and De Coninck, H., 2022, Limits to Paris compatibility of CO 2 capture and utilization: One Earth, v. 5, p. 168–185, doi:10.1016/j.oneear.2022.01.006.

Kumpiene, J., Antelo, J., Brännvall, E., Carabante, I., Ek, K., Komárek, M., Söderberg, C., and Wårell, L., 2019, In situ chemical stabilization of trace element-contaminated soil – Field demonstrations and barriers to transition from laboratory to the field – A review: Applied Geochemistry, v. 100, p. 335–351, doi:10.1016/J.APGEOCHEM.2018.12.003.

Liu, Y., Chen, Q., Dalconi, M.C., Molinari, S., Valentini, L., Wang, Y., Sun, S., Wang, P., and Artioli, G., 2022, Retention of phosphorus and fluorine in phosphogypsum for cemented paste backfill: Experimental and numerical simulation studies: Environmental Research, p. 113775, doi:10.1016/J.ENVRES.2022.113775.

Liu, S., Cui, S., Guo, H., Wang, Y., and Zheng, Y., 2021, Adsorption of Lead Ion from Wastewater Using Non-Crystal Hydrated Calcium Silicate Gel: Materials 2021, Vol. 14, Page 842, v. 14, p. 842, doi:10.3390/MA14040842.

Lothenbach, B., Kulik, D.A., Matschei, T., Balonis, M., Baquerizo, L., Dilnesa, B., Miron, G.D., and Myers, R.J., 2019, Cemdata18: A chemical thermodynamic database for hydrated Portland cements and alkali-activated materials: Cement and Concrete Research, doi:10.1016/j.cemconres.2018.04.018.

Lu, Y., Hu, S., Liang, Z., Zhu, M., Wang, Z., Wang, X., Liang, Y., Dang, Z., and Shi, Z., 2020, Incorporation of Pb(ii) into hematite during ferrihydrite transformation: Environmental Science: Nano, v. 7, p. 829–841, doi:10.1039/C9EN01355E.

Lu, P., Zhang, G., Apps, J., and Zhu, C., 2022, Comparison of thermodynamic data files for PHREEQC: Earth-Science Reviews, v. 225, p. 103888, doi:10.1016/J.EARSCIREV.2021.103888.

Malviya, R., and Chaudhary, R., 2006, Factors affecting hazardous waste solidification/stabilization: A review: Journal of Hazardous Materials, v. 137, p. 267–276, doi:10.1016/J.JHAZMAT.2006.01.065.

Martens, E., Jacques, D., Van Gerven, T., Wang, L., and Mallants, D., 2010, Geochemical modeling of leaching of Ca, Mg, Al, and Pb from cementitious waste forms: Cement and Concrete Research, v. 40, p. 1298–1305, doi:10.1016/J.CEMCONRES.2010.01.007.

Matteo, E.N., Huet, B., Jové-Colón, C.F., and Scherer, G.W., 2018, Experimental and modeling study of calcium carbonate precipitation and its effects on the degradation of oil well cement during carbonated brine exposure: Cement and Concrete Research, v. 113, p. 1–12, doi:10.1016/J.CEMCONRES.2018.03.016.

Oliveira, M.L.S., Ward, C.R., Izquierdo, M., Sampaio, C.H., de Brum, I.A.S., Kautzmann, R.M., Sabedot, S., Querol, X., and Silva, L.F.O., 2012, Chemical composition and minerals in pyrite ash of an abandoned sulphuric acid production plant: Science of The Total Environment, v. 430, p. 34–47, doi:10.1016/J.SCITOTENV.2012.04.046.

Ouhadi, V.R., Yong, R.N., and Deiranlou, M., 2021, Enhancement of cement-based solidification/stabilization of a lead-contaminated smectite clay: Journal of Hazardous Materials, v. 403, p. 123969, doi:10.1016/J.JHAZMAT.2020.123969.

Pang, L., Wang, D., Wang, H., An, M., and Wang, Q., 2022, Occurrence and leaching behaviors of heavy-metal elements in metallurgical slags: Construction and Building Materials, v. 330, p. 127268, doi:10.1016/J.CONBUILDMAT.2022.127268.

Parbhakar-Fox, A., 2016, Geoenvironmental Characterisation of Heap Leach Materials at Abandoned Mines: Croydon Au-Mines, QLD, Australia: Minerals 2016, Vol. 6, Page 52, v. 6, p. 52, doi:10.3390/MIN6020052.

Parkhurst, D.L., and Appelo, C.A.J., 2013, Description of Input and Examples for PHREEQC Version 3 — A Computer Program for Speciation , Batch-Reaction , One-Dimensional Transport , and Inverse Geochemical Calculations.: U.S. Geological Survey Techniques and Methods, book 6, chapter A43,.

Puppala, A.J., Talluri, N., Congress, S.S.C., and Gaily, A., 2018, Ettringite induced heaving in stabilized high sulfate soils: Innovative Infrastructure Solutions, v. 3, p. 1–12, doi:10.1007/S41062-018-0179-7/FIGURES/10.

Qoku, E., Bier, T.A., Schmidt, G., and Skibsted, J., 2022, Impact of sulphate source on the hydration of

ternary pastes of Portland cement, calcium aluminate cement and calcium sulphate: Cement and Concrete Composites, v. 131, p. 104502, doi:10.1016/J.CEMCONCOMP.2022.104502.

Shi, M., Min, X., Tian, C., Hao, T., Zhu, S., Ge, Y., Wang, Q., Yan, X., and Lin, Z., 2022, Mechanisms of Pb(II) coprecipitation with natrojarosite and its behavior during acid dissolution: Journal of Environmental Sciences, v. 122, p. 128–137, doi:10.1016/J.JES.2021.10.006.

Solpuker, U., Sheets, J., Kim, Y., and Schwartz, F.W., 2014, Leaching potential of pervious concrete and immobilization of Cu, Pb and Zn using pervious concrete: Journal of Contaminant Hydrology, doi:10.1016/j.jconhyd.2014.03.002.

Steiner, S., Lothenbach, B., Proske, T., Borgschulte, A., and Winnefeld, F., 2020, Effect of relative humidity on the carbonation rate of portlandite, calcium silicate hydrates and ettringite: Cement and Concrete Research, v. 135, p. 106116, doi:10.1016/J.CEMCONRES.2020.106116.

Sun, Z., Vollpracht, A., and van der Sloot, H.A., 2019, pH dependent leaching characterization of major and trace elements from fly ash and metakaolin geopolymers: Cement and Concrete Research, v. 125, p. 105889, doi:10.1016/J.CEMCONRES.2019.105889.

Sun, J., Wang, L., Yu, J., Guo, B., Chen, L., Zhang, Y., Wang, D., Shen, Z., and Tsang, D.C.W., 2022, Cytotoxicity of stabilized/solidified municipal solid waste incineration fly ash: Journal of Hazardous Materials, v. 424, p. 127369, doi:10.1016/J.JHAZMAT.2021.127369.

Tang, W., Guo, B., Li, Z., Zhao, X., and Gu, X., 2022, Flooding and drainage induced abiotic reactions control metal solubility in soil of a contaminated industrial site: Chemosphere, v. 297, p. 134032, doi:10.1016/J.CHEMOSPHERE.2022.134032.

Tangviroon, P. et al., 2020, Immobilization of Lead and Zinc Leached from Mining Residual Materials in Kabwe, Zambia: Possibility of Chemical Immobilization by Dolomite, Calcined Dolomite, and Magnesium Oxide: Minerals 2020, Vol. 10, Page 763, v. 10, p. 763, doi:10.3390/MIN10090763.

Torres-Martínez, J.A., Mora, A., Knappett, P.S.K., Ornelas-Soto, N., and Mahlknecht, J., 2020, Tracking nitrate and sulfate sources in groundwater of an urbanized valley using a multi-tracer approach combined with a Bayesian isotope mixing model: Water Research, v. 182, p. 115962, doi:10.1016/J.WATRES.2020.115962.

Vega-Garcia, P., Schwerd, R., Schwitalla, C., Johann, S., Scherer, C., and Helmreich, B., 2021, Leaching prediction for vertical test panels coated with plaster and mortars exposed under real conditions by a PHREEQC leaching model: Chemosphere, v. 280, p. 130657, doi:10.1016/J.CHEMOSPHERE.2021.130657.

Vu, H.P., Shaw, S., Brinza, L., and Benning, L.G., 2013, Partitioning of Pb(II) during goethite and hematite crystallization: Implications for Pb transport in natural systems: Applied Geochemistry, v. 39, p. 119–128, doi:10.1016/J.APGEOCHEM.2013.10.001.

Wang, L., Chen, L., Tsang, D.C.W., Guo, B., Yang, J., Shen, Z., Hou, D., Ok, Y.S., and Poon, C.S., 2020, Biochar as green additives in cement-based composites with carbon dioxide curing: Journal of Cleaner Production, v. 258, p. 120678, doi:10.1016/J.JCLEPRO.2020.120678.

Wang, L., Cho, D.W., Tsang, D.C.W., Cao, X., Hou, D., Shen, Z., Alessi, D.S., Ok, Y.S., and Poon, C.S., 2019, Green remediation of As and Pb contaminated soil using cement-free clay-based stabilization/solidification: Environment International, v. 126, p. 336–345, doi:10.1016/J.ENVINT.2019.02.057.

Wang, H., Ju, C., Zhou, M., Chen, J., Dong, Y., and Hou, H., 2022a, Sustainable and efficient stabilization/solidification of Pb, Cr, and Cd in lead-zinc tailings by using highly reactive pozzolanic solid waste: Journal of Environmental Management, v. 306, p. 114473, doi:10.1016/J.JENVMAN.2022.114473.

Wang, Q., Li, J. shan, Xue, Q., and Poon, C.S., 2022b, Immobilization and recycling of contaminated marine sediments in cement-based materials incorporating iron-biochar composites: Journal of Hazardous Materials, v. 435, p. 128971, doi:10.1016/J.JHAZMAT.2022.128971.

Wang, D., and Wang, Q., 2022, Clarifying and quantifying the immobilization capacity of cement pastes on heavy metals: Cement and Concrete Research, v. 161, p. 106945, doi:10.1016/J.CEMCONRES.2022.106945.

Winnefeld, F., and Lothenbach, B., 2010, Hydration of calcium sulfoaluminate cements — Experimental findings and thermodynamic modelling: Cement and Concrete Research, v. 40, p. 1239–1247, doi:10.1016/J.CEMCONRES.2009.08.014.

Xia, W.Y., Du, Y.J., Li, F.S., Li, C.P., Yan, X.L., Arulrajah, A., Wang, F., and Song, D.J., 2019, In-situ solidification/stabilization of heavy metals contaminated site soil using a dry jet mixing method and new hydroxyapatite based binder: Journal of Hazardous Materials, doi:10.1016/j.jhazmat.2019.02.031.

Yin, K., Ahamed, A., and Lisak, G., 2018, Environmental perspectives of recycling various combustion ashes in cement production – A review: Waste Management, v. 78, p. 401–416, doi:10.1016/J.WASMAN.2018.06.012.

Zavarin, M. et al., 2022, Community Data Mining Approach for Surface Complexation Database Development: Environmental Science and Technology, v. 56, p. 2827–2838, doi:10.1021/ACS.EST.1C07109/ASSET/IMAGES/LARGE/ES1C07109_0006.JPEG.

Zhang, Y., Labianca, C., Chen, L., De Gisi, S., Notarnicola, M., Guo, B., Sun, J., Ding, S., and Wang, L., 2021, Sustainable ex-situ remediation of contaminated sediment: A review: Environmental Pollution, v. 287, p. 117333, doi:10.1016/J.ENVPOL.2021.117333.

Supporting information for Appendices

Comprehensive understanding of the Pb and sulfates retention in ordinary Portland cement and calcium aluminate cement: clarifying and quantifying the contributions from binders and solid waste.

Yikai Liu[1]; Simone Molinari[1]; Maria Chiara Dalconi[1]; Luca Valentini[1]; Maurizio Pietro Bellotto[2]; Giorgio Ferrari[3]; Roberto Pellay[4]; Graziano Rilievo[5]; Fabio Vianello[5]; Gabriella Salviulo[1]; Gilberto Artioli[1]

1 Department of Geosciences and CIRCe Centre, University of Padua, via G. Gradenigo 6, 35129, Padua, Italy

2 OPIGEO Srl, Montegalda, Vicenza, Italy

3 Mapei S.p.A., via Cafiero 22, 20158, Milan, Italy

4 TEVGroup S.r.l., via Romea 8, 30034, Mira (Venice), Italy

5 Department of Comparative Biomedicine and Food Science, University of Padova, Viale dell'Università 16, 35020 Legnaro, Italy

Table.S1. XRD instrument settings.

Parameters	Settings
Radiation source	Cobalt
Detector	X'Celerator detector
Geometry	Bragg-Brentano geometry
Optics	Soller slits 0.04 rad.; Bragg-Brentano^{HD}
2θ range	3-84°
Step size	0.017°
Time per step	100 s

Table.S2. PHREEQC modeling input.

Phases	Minerals	Equilibrium equitions	Log k	Initial input OPP (mol/100g)[a]	Initial input CAP (mol/100g)
Ca	Gypsum	$CaSO_4{\cdot}2H_2O = Ca^{2+} + SO_4^{2-} + 2H_2O$	-4.6	0.0534	0.0394
	Bassanite	$CaSO_4{\cdot}0.5H_2O = Ca^{2+} + SO_4^{2-} + 0.5H_2O$	-3.9	0.0000	0.0000
	Anhydrite	$CaSO_4 = Ca^{2+} + SO_4^{2-}$	-4.4	0.0000	0.0000
	Portlandite	$Ca(OH)_2 + 2H^+ = Ca^{2+} + 2H_2O$	22.8	0.0129	0.0089
	Calcite	$CaCO_3 = CO_3^{2-} + Ca^{2+}$	-8.5	0.0000	0.0000
	Aragonite	$CaCO_3 = CO_3^{2-} + Ca^{2+}$	-8.4	0.0000	0.0000
	Vaterite	$CaCO_3 = CO_3^{2-} + Ca^{2+}$	-7.9	0.0000	0.0000
	C-S-H	$Ca_2Si_2O_{6.6436}H_{1.2872}{:}1.7542H_2O + 4.0H^+ = 2.0Ca^{2+} + 4.3978H_2O + 2SiO_2$	17.3	0.0703	0.0000
	Gahlenite	$Ca_2Al_2SiO_7 + 10\ H^+ = 2Al^{3+} + SiO_2 + 2Ca^{2+} + 5H_2O$	56.8	0.0000	0.0000
	Ettringite	$Ca_6Al_2(SO_4)_3(OH)_{12}{\cdot}26H_2O + 12H^+ = 2Al^{3+} + 3SO_4^{2-} + 6Ca^{2+} + 38H_2O$	56.7	0.0036	0.0151
Pb	$Pb(OH)_2$	$Pb(OH)_2 + 2H^+ = Pb^{2+} + 2H_2O$	8.2	0.0042	0.0013
	$PbSO_4$	$PbSO_4 = Pb^{2+} + SO_4^{2-}$	-7.8	0.0000	0.0000
	Jarosite(Pb)	$Pb_{0.5}Fe_3(SO_4)_2(OH)_6 + 6H^+ = 3Fe^{3+} + 0.5Pb^{2+} + 2SO_4^{2-} + 6H_2O$	-8.1	0.0000	0.0000
	Litharge	$PbO + 2H^+ = Pb^{2+} + H_2O$	12.6	0.0000	0.0000
	Cerrusite	$PbCO_3 + H^+ = HCO_3^- + Pb^{2+}$	-3.2	0.0000	0.0000
	Hydrocerrusite	$Pb_3(CO_3)_2(OH)_2 + 4\ H^+ = 2H_2O + 2HCO_3^- + 3Pb^{2+}$	1.9	0.0000	0.0000
Others	Thenardite	$Na_2SO_4 = SO_4^{2-} + 2\ Na^+$	-0.3	0.0000	0.0000
	Quartz	$SiO_2 = SiO_2$	-3.7	0.0000	0.0481
	Periclase	$MgO + 2H^+ = Mg^{2+} + H_2O$	21.5	0.0074	0.0000
	Jarosite	$KFe_3(SO_4)_2(OH) + 6\ H+ = 3Fe^{3+} + K^+ + 2SO_4^{2-} + 6\ H2O$	-14.8	0.0066	0.0049
	Gibbsite	$Al(OH)_3 + 3H^+ = Al^{3+} + 3H_2O$	8.1	0.0000	0.0285
	Hematite	$Fe_2O_3 + 6H^+ = 2\ Fe^{3+} + 3H_2O$	-4.0	0.2849	0.4217
	$Fe(OH)_{3(a)}$[c]	$Fe(OH)_3 + 3H^+ = Fe^{3+} + 3H_2O$	4.9	0.0000	0.0000
	$Al(OH)_{3(a)}$	$Al(OH)_3 + 3H^+ = Al^{3+} + 3H_2O$	10.80	0.0000	0.1040
Surface	Ettringite	$Pb^{2+} + 2SITE^- = PbSITE_2$	Estimate	-	-
	C-S-H	$Hco\_wOH + Pb^{2+} = Hco\_wOPb^+ + H^+$	Estimate	-	-
		$Hco\_sOH + Pb^{2+} = Hco\_sOPb^+ + H^+$	Estimate		
	Jarosite	$Hjo\_sOH + Pb^{2+} = Hjo\_sO\ Pb^+ + H^+$	Estimate	-	-
	Hematite	$Hho\_sOH + Pb^{2+} = Hho\_sOPb^+ + H^+$	Estimate	-	-
	$Fe(OH)_{3(a)}$	$Hfo\_sOH + Pb^{2+} = Hfo\_sOPb^+ + H+$	4.7	-	-
		$Hfo\_wOH + Pb^{2+} = Hfo\_wOPb^+ + H+$	0.3		
	$Al(OH)_{3(a)}$	$Hao\_wOH + Pb^{2+} = Hao\_wOPb^+ + H^+$	Estimate	-	-
		$Hao\_sOH + Pb^{2+} = Hao\_sOPb^+ + H^+$	Estimate		

Notes: [a] The mole concentration of the minerals for 100 grams of the soil and [b] The maximum mole content of the phase that can dissolve in the solution.

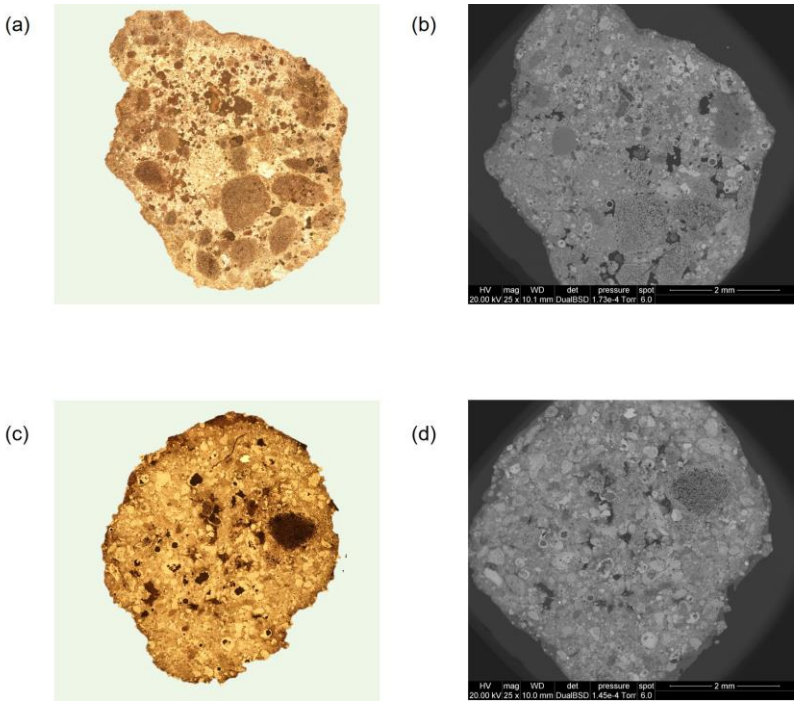

Figure.S1. OPP and CAP pellets. (a) opticale microscope image of OPP sample, (b) SEM image of OPP samples, (c) opticale microscope image of CAP sample, and (d) SEM image of CAP samples

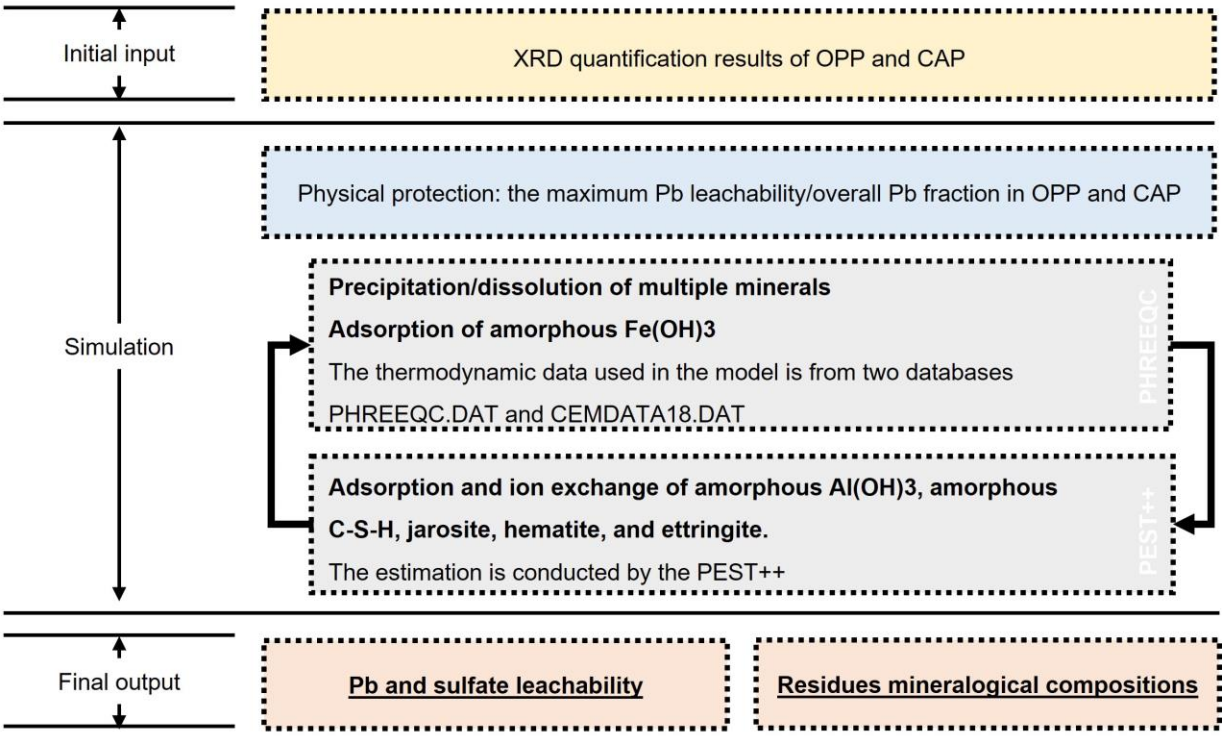

Figure.S2. Model establishment scheme.

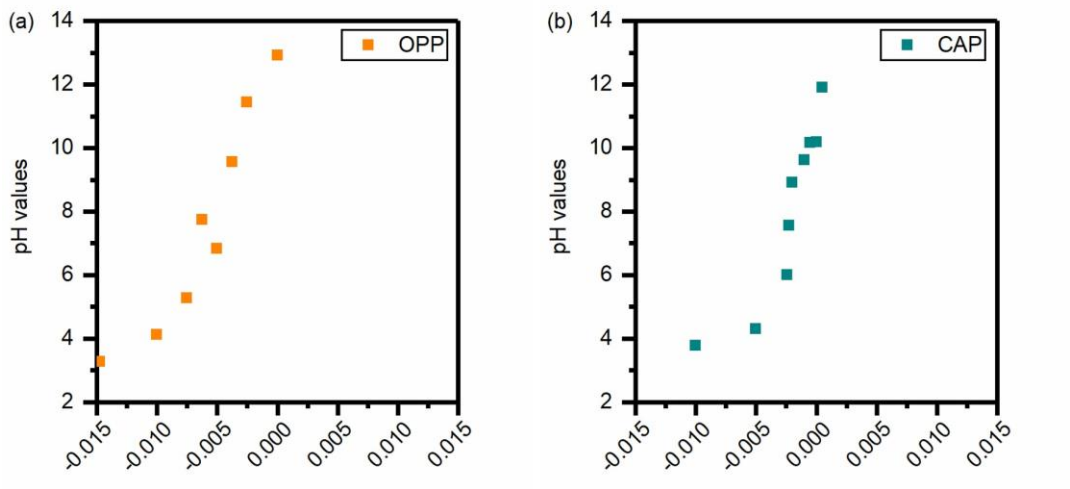

Figure.S3. Buffering capacity of OPP and CAP samples.

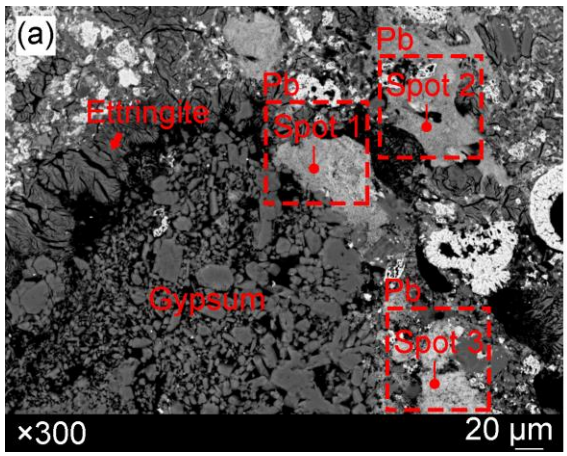

(b)

Element (wt%)	Spot1	Spot2	Spot3
O K	9.7	7.0	9.0
NaK	0.9	0.6	0.4
AlK	0.5	6.3	0.8
SiK	0.2	1.2	1.1
S K	19.9	18.2	19.9
K K	0.7	0.7	0.8
CaK	0.9	1.4	0.7
FeK	42.2	40.9	42.5
PbL	25.1	23.8	25.0

Figure.S4. SEM/EDS analysis of CAP samples revealing the presence of Pb-Fe sulfates. (a) BSE image and (b) EDS qualitative quantification results of the marked spots.

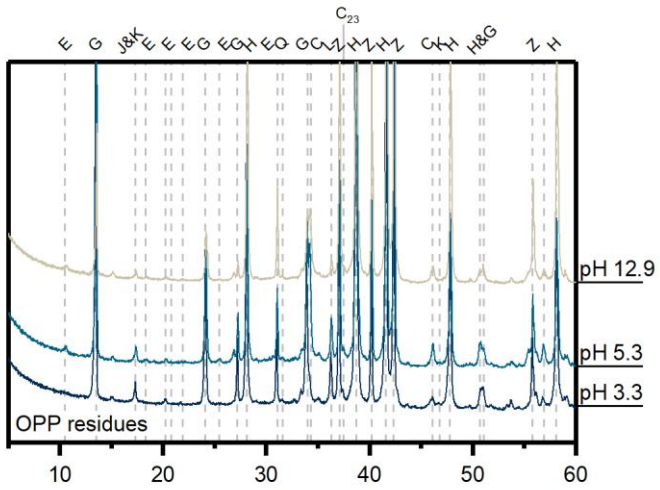

Figure.S5. XRD spectra of the analyzed OPP residues. E: ettringite, G: gypsum, J: jarosite, K: kintoreite, H: hematite, Q: quartz, Z: zincite, C, Calcite, C23, alite and belite, and L: periclase.

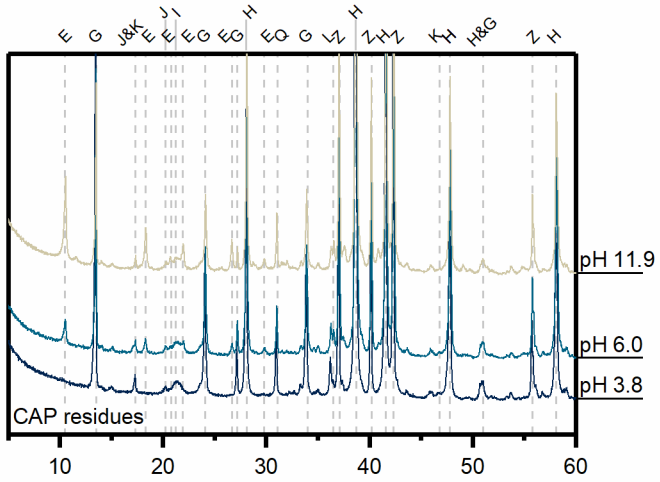

Figure.S6. XRD spectra of the analyzed CAP residues. E: ettringite, G: gypsum, J: jarosite, K: kintoreite, H: hematite, Q: quartz, Z: zincite, L: gehlenite, and I: gibbsite.

Acknowledgment

I am grateful to my amazing and kind advisors: Gilberto Artioli, Maria Chiara Dalconi, and Simone Molinari. Meanwhile, I would like to say special thanks to Luca Valentini. Their guidance and mentorship have helped me a lot in my thesis writing and shaped me to be a real researcher. In the past three years, I have learned a lot about cementitious systems and scientific writing from them. I do hope this knowledge will remain with me in my future research and career.

Also, I want to say thanks to my colleagues, Ludovico, Alessandro, and Giulia, who helped me a lot with the sample preparation and characterization experiments at the beginning of my Ph.D. In addition, I would like to thank Graziano, Maurizio, and Giorgio, who kindly offered me a hand with the leaching experiments, the binder preparation, and the equipment.

I would like to thank my collaborators in China: Qiusong Chen and Shiyuan Sun. Their kind help and effort proceed my Ph.D. project a huge step during the COVID quarantine period.

Outside of the department, I shared a lot of good memories with a close circle of friends in Italy. I want to thank their caring and sharing. Last, I am grateful to my family for their unconditional love and support.

Good luck!